UNIVERSITY OF CALIFORNIA SAN DIEGO

Characterization of Large Diameter Reinforcement Under Large Strain Cyclic Reversals

A dissertation submitted in partial satisfaction of the requirements for the degree of Doctor of Philosophy

in

Structural Engineering

by

Rodrigo Carreno Vallejos

Committee in charge:

Professor José I. Restrepo, Chair
Professor Yehuda Bock
Professor Joel P. Conte
Professor Hyonny Kim
Professor David Sandwell
Professor P. Benson Shing

2018

The Dissertation of Rodrigo Carreno Vallejos is approved, and it is acceptable in quality and form for publication on microfilm and electronically:

Chair

University of California San Diego

2018

DEDICATION

To my parents, Pedro and Eliana, and my sister Valeria,

whose support made this journey possible.

EPIGRAPH

Engineering is the art of modeling materials we do not wholly understand, into shapes we cannot precisely analyze so as to withstand forces we cannot properly assess, in such a way that the public has no reason to suspect the extent of our ignorance.

A.R. Dykes

TABLE OF CONTENTS

LIST OF SYMBOLS

A	Instantaneous cross-sectional area
A_0	Initial cross-sectional area of element
A_g	(Gross) section area of column
$C\ (\%)$	Carbon content
$CE(\%)$	Equivalent carbon content, as defined in Section 6.4 of ASTM A706
D	Column diameter
DI	Damage index for fatigue life of reinforcement
E^*_{sec}	Secant post-yield modulus measured from coupon tensile test
E_0	Elastic Young's Modulus
E_T	Tangent modulus
E_a	Tangent modulus at the beginning of the Bauschinger effect
E_b	Tangent modulus at the end of the Bauschinger effect
E_{eff}, E_r	Effective (reduced) modulus
I	Section moment of inertia
L	Length of buckled element. Also, column shear span
L_D	Horizontal distance between vertical linear potentiometers on column deformation panels
L_R	Distance to extreme longitudinal bar from column centerline
L_i	Gage length of vertical linear potentiometer on i^{th} row of column deformation panels
L_p	Equivalent plastic hinge length
$L_{p\varepsilon}$	Smeared strain compatible equivalent plastic hinge length
M	Material constant. Also, column section bending moment

MFR	Steel Manufacturer
M_{cr}	Column section cracking moment
M_p	Section plastic moment
M_y	Column section bending moment at first yield
N	Axial force
N_0	Reversal number
$2N_f$	Number of reversals to failure
$\boldsymbol{P_1, P_2, P_3, P_4}$	Coordinates of control points in Bezier curve
P_{cr}	Critical buckling load
P_T	Critical buckling load according to tangent modulus theory
R_0	Menegotto-Pinto model parameter for Bauschinger effect
R_a, R_b	Rebar lug radii
T/Y	Tensile-to-yield strength ratio
U_T	Toughness from tensile test
$U_{rel}^{i,j}$	Relative toughness of coupon i under strain history j
$\bar{U}_{rel}$	Average relative toughness of coupons in the same category
V	Element volume
W_a, W_b	Material constants
W_{fT}	Total dissipated energy
W_y	Dissipated elastic energy
Z	Axis in the vertical direction

a_1	Isotropic hardening parameter of *STEEL02*, defining stress shift in compression
a_2	Isotropic hardening parameter of *STEEL02*, defining stress shift in compression
a_3	Isotropic hardening parameter of *STEEL02*, defining stress shift in tension
a_4	Isotropic hardening parameter of *STEEL02*, defining stress shift in tension
$\hat{a}_1$	Isotropic hardening parameter of the model from Filippou's formulation
$\hat{a}_2$	Isotropic hardening parameter of the model from Filippou's formulation
$\bar{a}_1$	Average of calibrated values of a_1 from every tested coupon
$\bar{a}_3$	Average of calibrated values of a_3 from every tested coupon
b	Post-yield strain hardening ratio in *STEEL02*
c	Fatigue ductility exponent
c_0, c_1, c_2	Plane equation parameters
c_1	Slope of smeared to local strain amplitude ratio, λ_{CR}
cR_1	Curvature variation parameter of Bauschinger curve after each reversal
cR_2	Curvature variation parameter of Bauschinger curve after each reversal
d	Cross section depth
d_{CR}	Distance between centers of rotation in the buckled reinforcement
d_{POI}	Distance between points of inflection in buckled reinforcement
$d_{b\ell}$	Diameter of longitudinal reinforcement
d_{bn}	Nominal diameter of longitudinal reinforcement
e	Initial lateral deformation of reinforcement

e_{norm}	Error between measured and predicted stress-strain response, normalized by the optimal error using the calibrated parameters
error	Square root of sum of squares (SRSS) of the difference between measured and predicted stress response, normalized by the measured stress response
$\overline{e}_i$	Average estimation error of user i
$f(\varepsilon)$	Steel stress at strain ε
$f_c^{'}$	Compressive strength of concrete
f'_s	True stress of steel
$f_u^{'}$	Expected steel uniform stress (tension)
f_u^{*}	Expected steel uniform stress (compression)
f_y^H	Yield strength identified in hysteretic response at high strain rate ($\dot{\varepsilon}$ =0.02/sec)
f_y^L	Yield strength identified in hysteretic response at low strain rate ($\dot{\varepsilon}$ = 0.001/sec)
$f_y^{'}$	Expected yield strength
f_a	Stress at the beginning of the Bauschinger curve
f_b	Stress at the end of the Bauschinger curve
f_{cr}	Critical buckling stress
$f_{in\text{-}house}$	Characteristic stress measured by in-house testing
$f_{m,i}$	Experimental stress measured at step i of the hysteretic response
f_{max}	Magnitude of maximum stress (Tension or compression)
f_{mill}	Characteristic stress indicated in mill certificate
$f_{p,i}$	Stress predicted by the material model for step i of the hysteretic response

f_r	Stress at reversal strain ε_r in cyclic hysteretic response
f_s	Engineering stress of steel
$f_{sh,1}$	Stress at strain $\varepsilon_{sh,1}$
f_{suc}	Steel uniform stress in compression
f_u	Steel uniform stress (tension)
f_{vK}	Peak compressive Stress (von Karman Stress)
f_y	Yield strength
$f_y^{calibrated}$	Optimal yield stress after calibrating the material model to experimental response
$f_y^{identified}$	Yield stress identified from visual inspection of the stress-strain response
$f_{y,\ell}$	Yield stress of longitudinal reinforcement
$f_{y,t}$	Yield stress of transverse reinforcement
$\overline{f}_y$	Average yield strength of coupons under the same category
g_r	Gap between bar deformations
h_r	Height of rebar deformation
$k_{e\text{-}bb}$	Transverse reinforcement factor for computation of $\Delta_{\text{bb-calc}}$
ℓ	Instantaneous length of element
ℓ_0	Initial length of element
$\ell_{c,0}$	Initial surface crack length
$\ell_{c,f}$	Final surface crack length at failure
n	Number of vertical displacement sensors
n_{bar}	Number of longitudinal bars in the section
$\hat{n}, \hat{n}_0$	Normal unit vectors

q	Reduction factor for critical load in formulation by Papia
r	Rebar lug radius
s	On center spacing between hoops
s_r	Average bar deformation spacing
v_0	Lateral deflection of buckled columns
w_1, w_2, w_3, w_4	Weight factors for control points in Bezier curve
w_i	Weight of estimate from user i in weighted average
w_{method}	Weight for method used to identify d_{POI}
$\boldsymbol{x_{opt}}$	Vector of model properties that minimize the error between measured and predicted stress-strain response
Δ	Coefficient of variation (c.o.v) of data set: σ/μ
Δ_{bb}	Lateral displacement of column when long. Reinforcement reaches ε_{bb}
$\Delta_{bb\text{-}calc}$	Estimation of Δ_{bb} according to Berry and Eberhard
$\Delta\varepsilon_{E\text{-}C}$	Engesser-Considère strain amplitude: ε_{st}-$\varepsilon_{E\text{-}C}$
$\Delta\varepsilon_{kv}$	Strain amplitude in concave fiber: ε_{st}-ε_{kv}
$\Delta\varepsilon_p$	Plastic strain range
$\Delta\varepsilon_{t\text{-}c}$	Smeared strain amplitude: ε_{st}-ε_{sc}
$\Delta\varepsilon_{vK}$	von Karman strain amplitude: ε_{st}-ε_{vK}
$\Delta\ell$	Change in length of element from its initial length
Δ_y	Lateral displacement of column at yield
$\boldsymbol{\Delta x_{opt}}$	Vector added to $\mathbf{x_{opt}}$ to perturbate the predicted stress-strain response
Ω	Area under Bauschinger curve in interval [0,0.1] in normalized coordinates (Dodd-Restrepo constitutive stress-strain relationship)

Ω_{fac}	Bauschinger effect shape factor
α	Linear factor for computation of L_p
α_c	Correction factor between machined and unmachined coupons for model parameters E and b in Menegotto-Pinto constitutive stress-strain relationship
α_s	Stiffness of hoops as defined by Papia et al. (1988)
β	Linear factor for computation of L_p
δL_i	Measured displacement by North East, North West, South East or South West vertical displacement sensor on i^{th} row of column deformation panels
ε	Engineering strain
ε'	Natural strain
ε^*	Strain where 90% of tensile strength of steel is reached in a tensile test
$\varepsilon'_0(1)$	Maximum compressive plastic strain in natural coordinates
$\varepsilon'_0(2)$	Maximum tensile plastic strain in natural coordinates
$\varepsilon'_{peak,comp}$	Maximum compressive strain in natural coordinates
$\varepsilon'_{peak,tens}$	Maximum tensile strain in natural coordinates
ε'_u	Steel uniform strain (tension) in natural coordinates
ε_{CR}	Smeared strain between centers of rotation of the buckled shape
$\varepsilon_{E\text{-}C}$	Strain at onset of buckling (Engesser-Considère strain)
ε_{amp}	Total strain amplitude
ε_a	Strain at the beginning of the Bauschinger curve
ε_b	Strain at the end of the Bauschinger curve
ε_{ave}	Average strain at plane origin

ε_{bar}	Smeared strain at extreme column longitudinal steel bar
ε_{bb}	Buckling strain
ε_{c}	Extreme compressed fiber smeared strain
ε_{cr}	Strain corresponding to f_{cr}
ε_{kv}	Strain in fiber in the concave side of the critical section of the buckled shape
ε_{kx}	Strain in fiber in the convex side of the critical section of the buckled shape
ε_{max}	Maximum strain from strain history
ε_{min}	Minimum strain from strain history
ε_{rejoin}	Strain where Bauschinger curve rejoins a previous curve or the backbone of the material in the Dodd-Restrepo stress-strain relationship
ε_{r}	Reversal strain in cyclic hysteretic response
ε_{s}	Smeared axial strain from North East, North West, South East or South West vertical displacement sensors on column deformation panels
ε_{sc}	Maximum smeared strain in compression
ε_{sh}	Steel strain at onset of strain hardening in the backbone curve
$\varepsilon_{sh,\ell}$	Strain at the onset of strain hardening for longitudinal reinforcement
$\varepsilon_{sh,t}$	Strain at the onset of strain hardening for transverse reinforcement
ε_{st}	Smeared strain demand in tension
ε_{u}	Steel uniform strain (tension)
$\varepsilon_{u\ell}$	Uniform strain in longitudinal reinforcement
ε_{u}^{R}	Reduced uniformed strain as defined in Caltrans SDC (2013)
ε_{ut}	Uniform strain in transverse hoops
ε_{vK}	Strain where the peak compressive stress is reached (von Karman Strain)

ε_y	Steel yield strain
ε_z	Strain in the Z direction
$\dot{\varepsilon}$	Rate/speed of the strain history
θ	Angle of rotation
θ_f	Column fixed-end rotation
λ	Transverse reinforcement configuration factor for Δ_y
λ_1	Auxiliary variable in the original formulation of the Bauschinger effect
λ_2	Auxiliary variable in the original formulation of the Bauschinger effect
λ_{POI}	Ratio between strain amplitude in concave side, $\Delta\varepsilon_{kv}$, and smeared strain amplitude between points of inflection, $\Delta\varepsilon_{POI}$, in buckled bar
λ_{CR}	Ratio between strain amplitude in concave side, $\Delta\varepsilon_{kv}$, and smeared strain amplitude between centers of rotation, $\Delta\varepsilon_{CR}$, in buckled bar
μ	Mean value of data set
μ_s	Coefficient of friction
ξ	Linear factor for computation of L_p
ρ_{eff}	"Effective" volumetric transverse ratio $\rho_s f_{ys}/f'_c$
ρ_s	Volumetric ratio of transverse reinforcement
ρ_ℓ	Longitudinal reinforcement ratio
σ	Standard deviation of dataset
σ'	True stress
σ'_a	True stress range
σ'_f	Fatigue strength coefficient
σ_a	Stress range
τ	E_T/E_0

ϕ	Section curvature
ϕ_k	Peak curvature at cracking
$\phi_{p\text{-}bb}$	Plastic curvature in RC column when long. reinforcement reaches ε_{bb}
ϕ_y	Yield curvature
$\overline{\phi}$	Smeared curvature

LIST OF FIGURES

LIST OF TABLES

ACKNOWLEDGMENTS

I would like to thank Professor Restrepo and Professor Conte, who have taught me so much, their support and advice has helped me to grow both as a researcher and as a person.

My deepest gratitude also to my fellow graduate students: Koorosh Lotfizadeh, Adel Mashayekh, Rodrigo Astroza, Gabriele Guerrini, Yong Li, Yujia Liu, David Duck, Arpit Nema, Michelle Chen and Gulen Ozkula, to name a few. I will always be grateful for their guidance and friendship throughout the years.

Thanks to the Powell lab staff: Dr. Chris Latham, Darren McKay, Michael Sanders, Noah Aldrich and Abdullah Hamid for their invaluable help and advice during the experimental part of this work.

Also, I would like to thank the SE department staff, especially Yvonne Wollmann, Debra Bomar, and Lindsay Walton, without their help I would not have made it to this point.

I would also like to express my gratitude to the Chilean National Commission for Scientific and Technological Research (CONICYT) for the graduate fellowship (BecasChile) that supported the first four years of my doctoral program. I also thank the Department of Structural Engineering at UCSD for the financial support provided in the last years of my program.

Finally, I want to thank the members of my committee for the time they dedicated and their valuable contribution to define the objectives for this dissertation.

This study was made possible by funding from the California Department of Transportation under contract No. 65A0502. Technical input from Dr. Charles Sikorsky, Ray Zelinski, and Fadel Alameddine was greatly appreciated.

Chapter 2, in part, is a reprint of the material as it appears in *SSRP Report 17/10: Plastic buckling-straightening fatigue of large Diameter reinforcing steel bars*, 2018. Duck, David; Carreño, Rodrigo; and Restrepo, José I. The dissertation author co-authored this material.

Chapter 3, in full, has been submitted for publication of the material as it may appear in *Material Model Parameters for the Giuffrè-Menegotto-Pinto Uniaxial Steel Stress-Strain Model*, ASCE Journal of Structural Engineering, 2018. Carreño, Rodrigo; Lotfizadeh, Koorosh; Conte, Joel P.; and Restrepo, José I. The dissertation author was the primary investigator and author of this paper.

Chapter 4, in full, is currently being prepared for submission for publication of the material. Carreño, Rodrigo; Lotfizadeh, Koorosh; Conte, Joel P.; and Restrepo, José I. The dissertation author was the primary investigator and author of this paper.

Chapter 5, in full, is a reprint of the material as it appears in *SSRP Report 17/10: Plastic buckling-straightening fatigue of large Diameter reinforcing steel bars*, 2018. Duck, David; Carreño, Rodrigo; and Restrepo, José I. The dissertation author was a co-author of the report.

Chapter 6, in full, is a reprint of the material as it appears in *SSRP Report 17/10: Plastic buckling-straightening fatigue of large Diameter reinforcing steel bars*, 2018.

Duck, David; Carreño, Rodrigo; and Restrepo, José I. The dissertation author was a co-author of this report and first author of the specific Chapter.

Chapter 7, in full, is a reprint of the material as it appears in SSRP Report 17/10: *Plastic buckling-straightening fatigue of large Diameter reinforcing steel bars*, 2018. Duck, David; Carreño, Rodrigo; and Restrepo, José I. The dissertation author was a co-author for this report and first author of the specific Chapter.

VITA

2008	Bachelor in Engineering Science, Civil Engineering.
	University of Chile
2009	Civil Engineer in Structures and Construction
	University of Chile
2009 – 2011	Project Engineer
	Ruben Boroschek and Associates, Santiago, Chile.
2014	Master of Science in Structural Engineering
	University of California, San Diego
2014 – 2016	Teaching Assistant, Department of Structural Engineering.
	University of California, San Diego
2016-2018	Research Assistant
	University of California, San Diego
2018	Doctor of Philosophy in Structural Engineering
	University of California, San Diego

PUBLICATIONS

Boroschek, R., & **Carreño, R.** (2011). Period variations in a shear wall building due to earthquake shaking. *5th international conference on Structural Health Monitoring of Intelligent Infrastructure (SHMII-5), Cancun, Mexico,* (pp. 11-15).

Carreño, R., & Boroschek, R. L. (2011). Modal parameter variations due to earthquakes of different intensities. *Civil Engineering Topics, Volume 4*, 321-333.

Carreño, R., & Restrepo, J. I. (in-preparation). Plastic Buckling-Straightening Fatigue Limit State for Longitudinal Reinforcement in Circular Bridge Columns.

Carreño, R., Lotfizadeh, K., Conte, J. P., & Restrepo, J. I. (under-review). Material Model Parameters for the Giuffrè-Menegotto-Pinto Uniaxial Steel Stress-Strain Model.

Carreño, R., Lotfizadeh, K., Conte, J. P., & Restrepo, J. I. (in-preparation). Implementation of Improved Dodd-Restrepo Constitutive Stress-strain relationship.

Çelebi, M., Sereci, M., Boroschek, R., **Carreño, R.**, & Bonelli, P. (2013). Identifying the Dynamic Characteristics of a Dual Core-Wall and Frame Building in Chile Using Aftershocks of the 27 February 2010 (Mw= 8.8) Maule, Chile, Earthquake. *Earthquake Spectra, 29*, 1233-1254.

Çelebi, M., Sereci, M., Boroschek, R., **Carreño, R.**, & Bonelli, P. (2013). Preliminary Identification of Dynamic Characteristics of a Unique Building in Chile Following 27 February 2010 (Mw= 8.8) Earthquake. In *Nondestructive Testing of Materials and Structures* (pp. 1071-1077). Springer.

Duck, D. E., **Carreño, R**., & Restrepo, J. I. (2018). *SSRP-17/10: Plastic Buckling-Straightening Fatigue of Large Diameter Reinforcing Steel Bars (Vol I & II).* University of California, San Diego. La Jolla: Dept. of Structural Engineering.

ABSTRACT OF THE DISSERTATION

Characterization of Large Diameter Reinforcement Under
Large Strain Cyclic Reversals

by

Rodrigo Carreno Vallejos

Doctor of Philosophy in Structural Engineering

University of California San Diego, 2018

Professor José I. Restrepo, Chair

To resist strong intensity earthquakes, the design of reinforced concrete members often relies on well-detailed plastic hinge regions for a ductile response. Within these plastic hinges, large strain deformations are expected in both the concrete

and steel reinforcement. In the case of ordinary bridge columns, experimental testing of full-scale specimens has shown that fracture of longitudinal reinforcement, following visible plastic buckling is a common failure mode in the plastic hinge of columns designed according Caltrans' Seismic Design Criteria (SDC). This type of failure is defined herein as "Plastic Buckling-Straightening Fatigue" (PBSF), as the name "Low-cycle fatigue" commonly used for it is inconsistent with limitations set forth by ASTM standards for this phenomenon. The mechanism under which the PBSF type of failure occurs starts with micro-cracks developing at the root of bar deformations, in the concave side of a buckled bar, which start to propagate for an abrupt fracture when the bar stretches. Knowing the process under which the fracture occurs, the buckling behavior of the longitudinal reinforcement, considering the effect of material properties and the configuration of transverse hoops is studied, evaluating the fatigue life of the bars. Based on the regression of multiple Finite Element Model results, a simple design and verification procedure is proposed to control the PBSF limit state in ordinary bridge columns, recommended for inclusion in Caltrans SDC specifications.

The use of large diameter reinforcement has proven an effective method to expedite the construction process of reinforced concrete bridges (Marsh, et al., 2011). The fatigue life of large bars however, has not been well documented yet, with the use of large diameter reinforcement in seismic regions limited to #11 bars vertical members in most ordinary bridges. For this research work, a series of Grade 60 #18 bars were tested under large amplitude cyclic strain histories, evaluating the fatigue life of the reinforcement for different length to diameter ratios and amplitude of deformations. The

tests performed herein correspond to the first successful examination of the response under large amplitude strain reversals, including the fracture under PBSF, for reinforcement of this size.

Chapter 1.

INTRODUCTION

1.1. Motivation

The structural design of most ordinary bridges in California rely on plastic hinges to provide a ductile response under high intensity earthquakes. This plastic hinge is capacity designed to develop and maintain the desired inelastic mechanism.

In the past two decades, the California Department of Transportation, Caltrans, has funded multiple experimental efforts to assess and improve the seismic design provisions for ordinary bridges (see Caltrans SDC, 2013). In 2010 a full-scale reinforced concrete bridge column, designed according to Caltrans provisions (SDC v1.6, 2010), was tested at the Large High-Performance Outdoor Shake Table (LHPOST) at UC San Diego. The column design showed satisfactory results, with good structural integrity of the element after multiple design-level earthquakes. The column was later subjected to higher than design level shaking until failure, at which point a significant number of longitudinal bars

fractured after buckling or showed clear signs of buckling. The failure mode observed in this test is consistent with results observed in other experimental efforts (Goodnight et al. 2015) and suggests the deformation capacity of ordinary bridge columns may be limited by post-buckling fracture of longitudinal reinforcement in the plastic hinge region. This type of failure however, is not included explicitly in Caltrans specifications (SDC v1.7, 2013) for column design. The term "low-cycle fatigue" has been commonly used for this type of failure, despite violating the explicit limitation against buckling placed by ASTM E606 (2012) for strain-controlled fatigue testing. The name "Plastic Buckling-Straightening Fatigue" (PBSF) is used instead when referring to the post-buckling fracture of longitudinal bars observed in tested bridge columns (Schoettler et al. 2012).

In the quest for "Accelerated Bridge Construction" (ABC), Caltrans has encouraged the development of new construction techniques, including the use of precast concrete construction. The use of large diameter reinforcement, such as #18 bars, could significantly expedite the construction process, however a wide gap in knowledge exists on the behavior of such reinforcement under large cylic strain histories (Marsh et al., 2011). A big concern is the "low cycle fatigue" life of large bars, as experimental work has shown a reduction in the fatigue life with increasing bar size (Brown and Kunnath, 2004). Previous research efforts to characterize the cyclic behavior of #18 Grade 60 reinforcement have been largely unsuccessful due to problems with the loading apparatus. Because of this, the experimental assessment of the fatigue life of this type of reinforcement would be a significant contribution to current research efforts aimed at Accelerated Bridge Construction.

1.2. Objectives and Scope

The research work presented herein focuses on the behavior of steel reinforcement in ductile reinforced concrete members subjected to cyclic loads, particularly for ordinary bridge columns located in high seismicity regions. An initial part of the research focused on the calibration of parameters from two commonly used constitutive stress-strain relationships for steel reinforcement, the Giuffrè-Menegotto-Pinto and Dodd-Restrepo models. This study was carried out to fullfil the need, by researchers and engineering professionals alike, for an appropriate set of model parameters representing the behavior of steel reinforcement manufactured under current ASTM standards (A615, 2016, and A706, 2016). Additionally, given the absence of a stable implementation of the constitutive stress-strain relationship by Dodd and Restrepo in structural analysis software available to the author, an improved version of the model, including a closed-form solution for the Bauschinger effect, was implemented and made available to researchers and engineering professionals via the OpenSees software framework.

Extensive experimental work was also performed on #18 Grade 60 bars, characterizing its fatigue life under cyclic loading. The goal of this project, funded by the California Department of Transportation, was to assess how viable is the use of large diameter reinforcement for ordinary bridge columns in seismic regions. The use of large reinforcement is one of the main lines of research for Accelerated Bridge Construction, thus several authors have attempted similar work. The cyclic tests carried out for this project however, were the first of its kind, as previous attempts by other authors have been largely unsuccessful, due to issues with the loading apparatus.

Plastic Buckling-Straightening Fatigue (PBSF), also know as “low-cycle fatigue”, is a common failure mode for the plastic hinge region of bridge columns and other ductile reinforced concrete elements. In this phenomenon, after the bar buckles, micro-cracks develop at the root of the deformations in the concave side (Restrepo et al. 1993, see Figure 2.1), which then propagate as the bar stretches, leading to a brittle fracture. The final part of this research studies the buckling phenomenon and its effect on the fatigue life of the reinforcement from an engineering design perspective.

Although its influence is well recognized (Bresler and Gilbert, 1961; Mander et al. 1984), the effect of transverse reinforcement in the post-buckling response of longitudinal reinforcement has yet to be quantified. Furthermore, few authors consider the buckled shape of longitudinal bars within reinforced concrete elements spanning multiple sets of hoops (Papia et al. 1988), as observed in experimental tests (Schoettler et al. 2012). A study based on finite element model results was performed to assess, by means of simple equations, the effect of the reinforcement configuration and material properties in the buckling and subsequent fracture of longitudinal reinforcement. Using these simple equations, a design and verification procedure was then recommended for inclusion into Caltrans’ Seismic Design Criteria (SDC) for ordinary bridge columns.

1.3. Outline

This section presents a brief description of the eight chapters included in this dissertation:

- Chapter 1: Introduction

  This chapter details the objectives, scope, and motivations of the research work, including an outline of the content presented in the dissertation.

- Chapter 2: Literature Review

  A detailed description of the research efforts in the study of plastic buckling of reinforcing bars is presented in this chapter.

- Chapter 3: Calibration of GMP Constitutive Stress-strain Relationship for Reinforcing Steel

  This chapter describes the research work done to establish a set of model parameters for the Giuffrè-Menegotto-Pinto (GMP) constitutive stress-strain relationship calibrated for Grade 60 Reinforcing steel, manufactured according to ASTM A615 and A706 standards.

- Chapter 4: Improved Implementation of the Constitutive Stress-Strain Relationship by Dodd and Restrepo for Reinforcing Steel.

  In this chapter an improved formulation of the constitutive stress-strain relationship by Dodd and Restrepo is implemented into OpenSees and tested on

large scale structural models. A calibration of the model parameters, similar to the one performed on the GMP constitutive stress-strain relationship (Chapter 3) is performed to characterize Grade 60 ASTM A615 and A706 reinforcing steel.

- Chapter 5: Experimental Work on Large Diameter Reinforcement

  Description of the design, implementation and main results of the cyclic testing of #18 Grade 60, ASTM A706 reinforcing steel bars. This chapter includes, among other things, the design of the loading apparatus, the selection of the loading protocols, the steps to prepare and test each specimen, and the main results obtained.

- Chapter 6: Longitudinal Bar-Hoop Interaction in Circular Columns

  This chapter describes a series of regression analyses, based on finite element results, to find the correlation between the reinforcement configuration and material properties of reinforcing steel with the plastic buckling behavior of the longitudinal reinforcement. Regression equations were introduced to predict geometric properties (e.g. the distance between points of inflection, d_{POI}) and relation between smeared and local strains of the buckled reinforcement.

- Chapter 7: Design and Verification Procedures for Plastic Buckling-Straightening Fatigue (PBSF) of Longitudinal Reinforcement.

Based on the regression equations found in Chapter 6, a design and verification methodology are introduced for circular bridge columns to prevent premature Plastic buckling and subsequent fracture of longitudinal reinforcement. The proposed method is then verified by column test results found in the literature.

- Chapter 8: Conclusions

  Description of the main findings of this research and future work.

Chapter 2.

LITERATURE REVIEW

2.1. General

Buckling and straightening of longitudinal reinforcement in the plastic hinge of bridge columns can be caused by the dynamic response of a bridge during earthquake input. Such phenomena can have a significant impact on the deformation capacity and ductility of these elements. Buckling and straightening results in "low-cycle" fatigue in those regions of the buckled bar where the curvature reaches the peak. Crack initiation, as seen in Figure 2.1, is believed to be dependent on factors like the geometry of the deformations, including local defects at the root of the bar deformations arising during the rolling process and the pattern of the deformations. On the other hand, crack propagation is believed to be dependent on the strain history and temperature of the bar at the onset of buckling, among various other parameters. This Chapter reviews the existing literature relevant to the plastic buckling of longitudinal reinforcement and, to a lesser extent, the fatigue life of reinforcing bars.

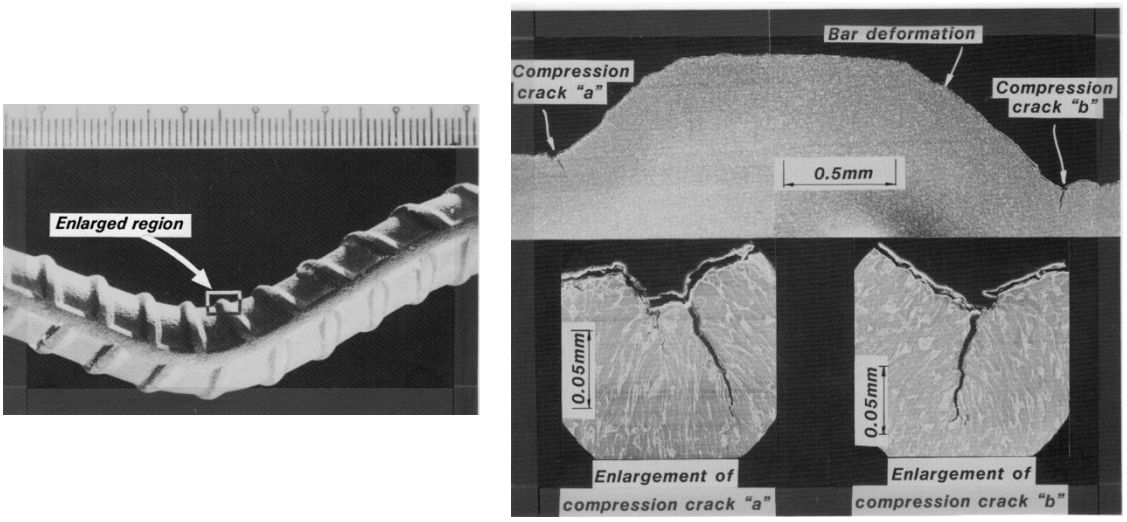

(a) (b)

Figure 2.1. Electron Microscope Image of a Longitudinal Section of a Deformed Reinforcing Bar After Buckling Showing Crack Initiation: (a) Buckled Longitudinal Bar (scale in mm.); (b) Cracks at the Bar Deformation Roots (Restrepo-Posada et al., 1994)

2.2. Plastic Buckling of Longitudinal Reinforcement

The first mathematical formulation of the buckling phenomenon was introduced by Euler in 1757 (Oldfather, et al. 1933). Under the assumption of a linear-elastic material, Euler found the critical axial load under which a column will develop lateral deformations,

$$P_{cr} = \frac{\pi^2 \cdot E_0 I}{L^2} \qquad 2.1$$

Where E_0 is the elastic Young's Modulus, I is the moment of inertia of the section, L is the length between supports, and P_{cr} is the critical load for the onset of buckling.

More than a century after Euler, Engesser (1889) and Considère (1891) began to study the buckling phenomenon. They proposed formulations similar to Euler's critical load, replacing the elastic Young's Modulus by either a tangent (Engesser, see Equation

2.2a) or effective stiffness (Considère, Equation 2.2b), as a way to calculate the critical plastic buckling load, see Figure 2.2.

$$P_{cr} = \frac{\pi^2 \cdot E_T I}{L^2} \quad \text{(a)}$$
$$P_{cr} = \frac{\pi^2 \cdot E_{eff} I}{L^2} \quad \text{(b)} \qquad 2.2$$

Where E_T is the tangent modulus, and E_{eff} the effective (or reduced) modulus, satisfying the condition $E_T \leq E_{eff} \leq E_0$, although Considère did not specify a formulation for E_{eff}.

Research work into critical load leading to plastic buckling was continued by von Karman (1910), who introduced the concept of double-modulus (see Equation 2.3). This concept accounts for the effect of strain bifurcation, where some fibers in the cross section begin to decompress (unload) while the others continue deforming in compression, developing a curvature in the bar, see Figure 2.3.

Although von Karman's formulation was theoretically more accurate than any previous work, many researchers found the tangent-modulus theory (Engesser, 1889) to be more consistent with experimental results (Templin, et al., 1938).

$$P_{cr} = \frac{\pi^2 E_r I}{L^2} \text{ (a)} \qquad E_r = \frac{E_0 \cdot I_1 + E_T \cdot I_2}{I_1 + I_2} \text{ (b)} \qquad 2.3$$

where E_r is the reduced modulus (double modulus), $I_1$and I_2 are the moments of inertia of the segments of the section being decompressed and compressed (after bifurcation takes place), respectively.

The controversy between both Engesser-Considère tangent modulus and von Karman's double-modulus theories, which appear correct but led to different plastic buckling loads, was not resolved until 1946, when Shanley published his historical paper "The Column Paradox". In this paper Shanley demonstrated that both formulations were in fact correct, but each represented a different state of the plastic buckling process (Shanley F. R., 2012). By assuming that a short column has additional axial load capacity after the onset of buckling, thanks to post-yield hardening of the material, it was possible to have bending without any strain reversal, which was the main assumption in the double-modulus theory. Because of this, the tangent modulus predicts the load at the onset of buckling, while the double-modulus returns the maximum capacity of the buckled element if the tangent modulus remains constant.

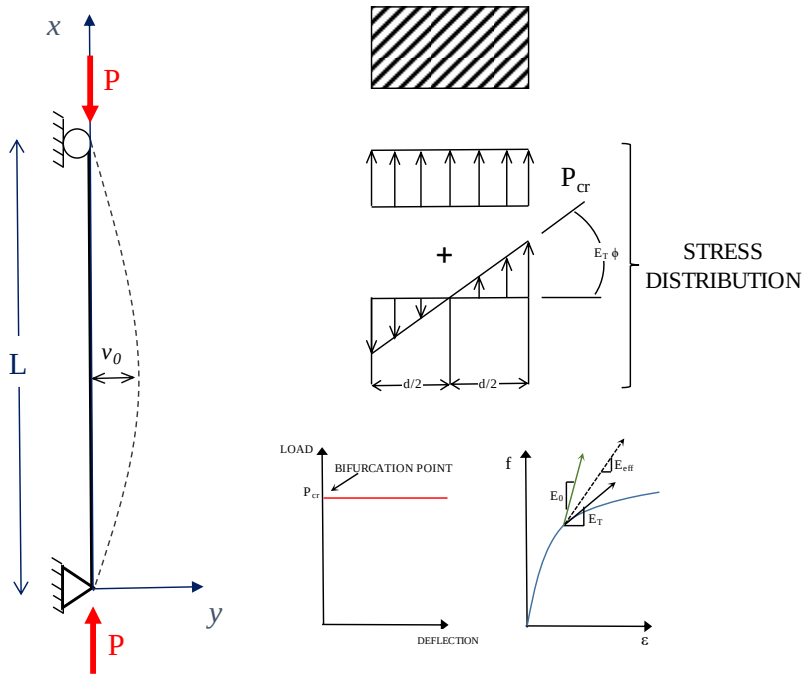

Figure 2.2. Engesser-Considère Buckling Formulation (Chen and Lui, 1987)

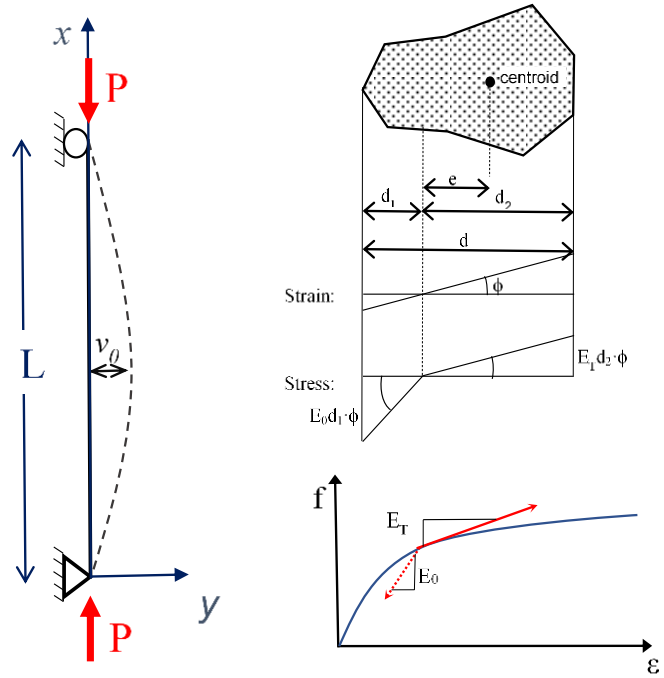

Figure 2.3. Double Modulus Formulation by von Karman (Chen and Lui, 1987)

To prove his formulation, Shanley analyzed the simple case of a two-legged hinge column, in which the hinge is a unit "cell" formed by two small axial elements (Shanley, 2012), see Figure 2.4. By equating the internal and external moment, the critical load can be easily defined as,

$$P_{cr} = P_T \cdot \left[1 + \frac{1}{\frac{d}{2 \cdot v_0} + \frac{1+\tau}{1-\tau}} \right] \qquad 2.4$$

Where $P_T = \frac{A \cdot d}{L} E_T$ and $\tau = \frac{E_T}{E_0}$, with A the area of the deformable cell, d the distance between the two legs in the cell, and v_0 the lateral deformation of the column, see Figure 2.4 and Figure 2.5.

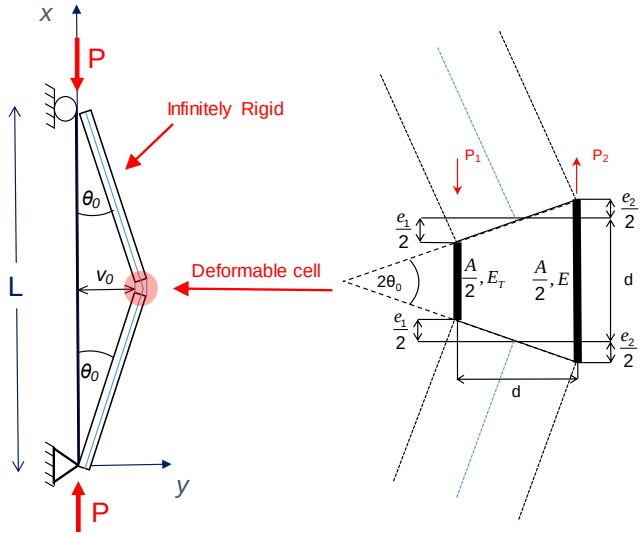

Figure 2.4. Shanley's Simplified Two-Flange Column (Shanley, 1947)

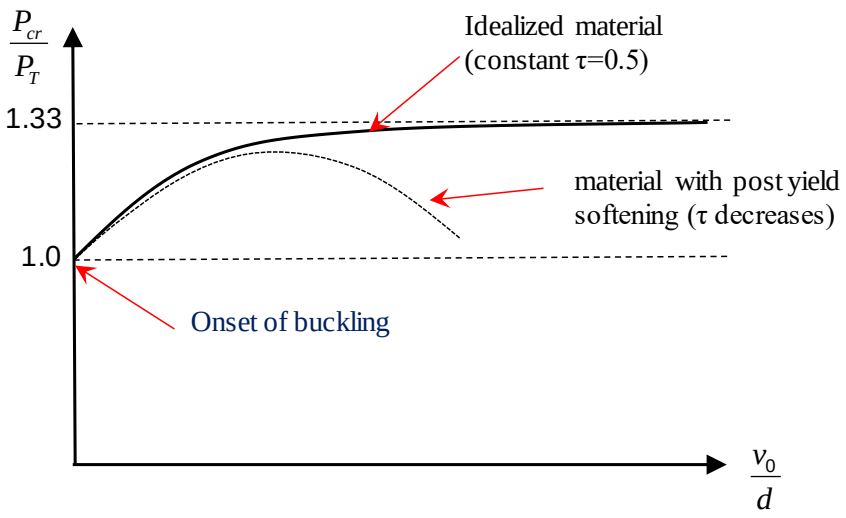

Figure 2.5. Variation of Column Load Capacity (Normalized by Load at Onset of Buckling) vs Lateral Deformation (Shanley, 1947)

Following Shanley's demonstration, extensive experimental work by several authors (Madsen, 1941; Osgood, 1951) focused on the effect of residual stresses in steel columns, resulting in significant advances in the understanding of the behavior of these elements.

Bresler and Gilbert (1961) developed some of the earliest work on critical loads in reinforcing steel, and were the first proponents of a maximum tie spacing to ensure the stability of longitudinal reinforcing bars, based on tangent modulus theory.

One of the first closed-form solutions for the hysteretic response of a pinned column under axial load, including the effect of buckling, was developed by Nonaka (1973), under the simplifying assumption the material was elastoplastic. Papadrakakis and Loukakis (1988) extended this formulation for partially restrained imperfect bars with various end conditions, using a piece-wise linear approximation of the axial force-moment interaction curve of the section. These formulations rely on the plastic-hinge (lumped plasticity)

concept and cannot predict the decrease in carrying capacity of the column after the first cycle of loading, which is mostly attributed to the spread of plasticity near the plastic hinges. Both the original and extended formulations were developed analytically, without experimental verification.

Mander et al. (1984) conducted monotonic tests on reinforcing bars at different slenderness ratios, and proposed a modification to the double modulus theory to account for the onset of buckling observed experimentally when the longitudinal reinforcement yields in compression, see Figure 2.6. This modified double modulus theory uses a secant modulus E'_T, defined in Equation 2.5, instead of the tangent modulus E_T to compute the critical load P_{cr} (see Equation 2.3).

$$E_T^{'} = \frac{f_{cr} - f(\varepsilon_{cr} - \varepsilon_{sh})}{\varepsilon_{sh}} \qquad 2.5$$

Where f_{cr} is the critical buckling stress (P_{cr}/A), ε_{sh} the steel strain at onset of strain hardening, ε_{cr} the strain corresponding to f_{cr}, and $f(\varepsilon_{cr}-\varepsilon_{sh})$ is the steel stress at strain of $\varepsilon_{cr}-\varepsilon_{sh}$.

Another finding by Mander et al. (1984) was that a limit spacing of approximately six bar diameters is a suitable ratio to preclude premature longitudinal bar buckling and to ensure the desired ductility is reached. The spacing limitation resulted from the modified double modulus theory (see Equation 2.5), by imposing the critical buckling stress f_{cr} to match the steel tension stress at a strain of 5%, well within the plastic-zone of the material,

$$\frac{s}{d_{bn}} = 1.5 \cdot \sqrt{\frac{E_r}{f_{cr}}} \qquad 2.6$$

where d_{bn} is the nominal diameter of the longitudinal reinforcement, and s the spacing between hoops.

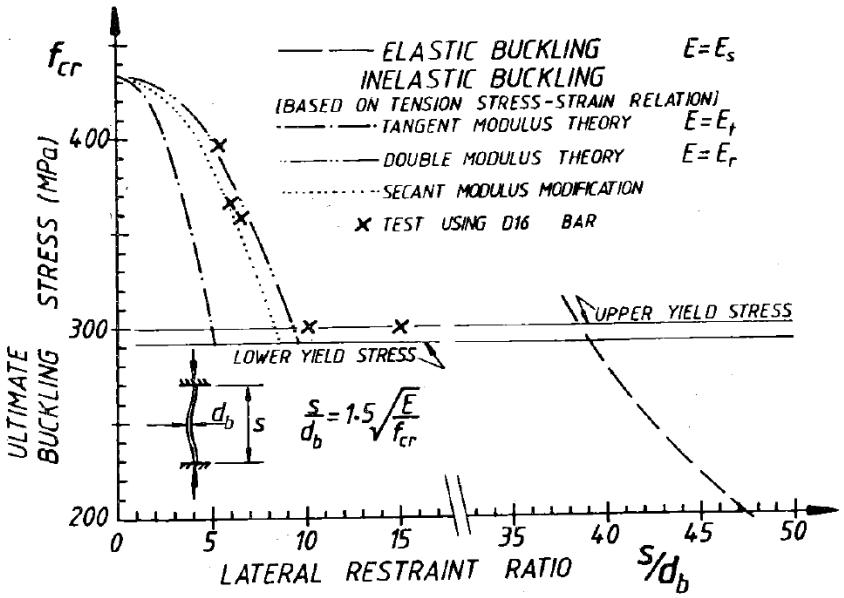

Figure 2.6. Test Results Compared with Theoretical Predictions (Mander et al., 1984)

Mander et al.'s formulation assumed the transverse reinforcement was stiff enough to limit bar buckling between consecutive sets of hoops, for an effective buckling length of *s/2*, Figure 2.7.

Zahn et al. (1985) extended Mander et al. work by testing the spacing limit (Equation 2.6) for different steel grades, and developed diagrams for the maximum spacing allowed for a given critical stress, f_{cr}, and strain, ε_{cr}, see Figure 2.8 and Figure 2.9. A linear formulation of the critical strain and stress for $s/d_{b\ell} \geq 4$ (at lower slenderness levels the

buckling effect is negligible) is also shown in the figures, closely matching experimental results.

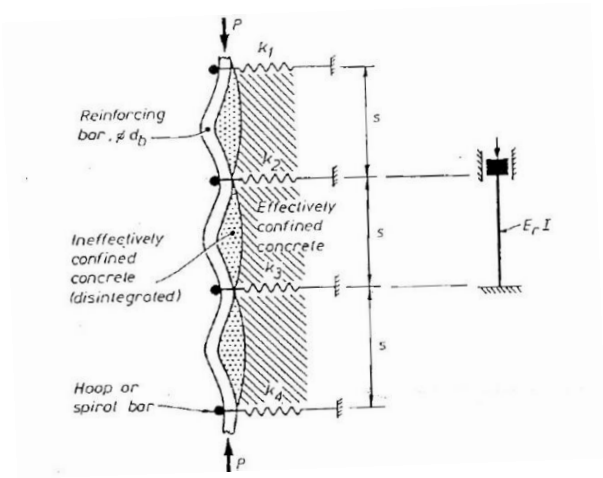

Figure 2.7. Model for Buckling of Longitudinal Reinforcement in a Cage Proposed by Zhan et al. (1985)

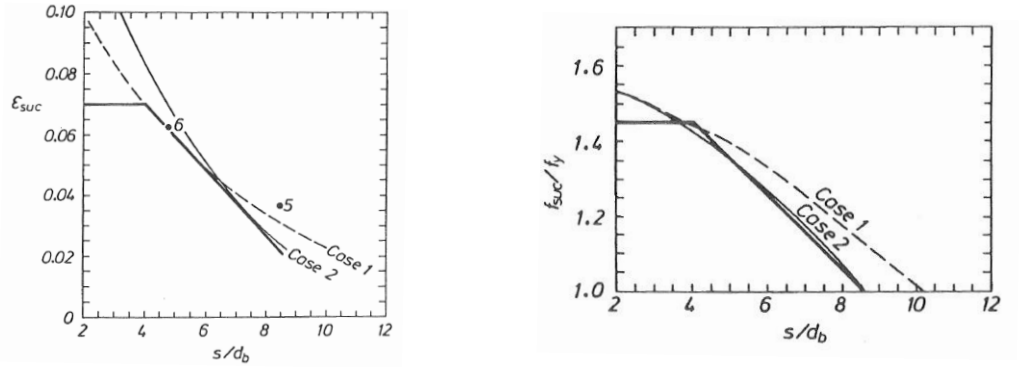

(a) (b)

Figure 2.8. Ultimate Compressive Strain and Stress vs Hoop Spacing. Grade 275 MPa Steel (Zahn, 1985): (a) Buckling Strain ε_{suc} vs Hoop Spacing; (b) Normalized Buckling Stress f_{suc}/f_y vs Hoop Spacing

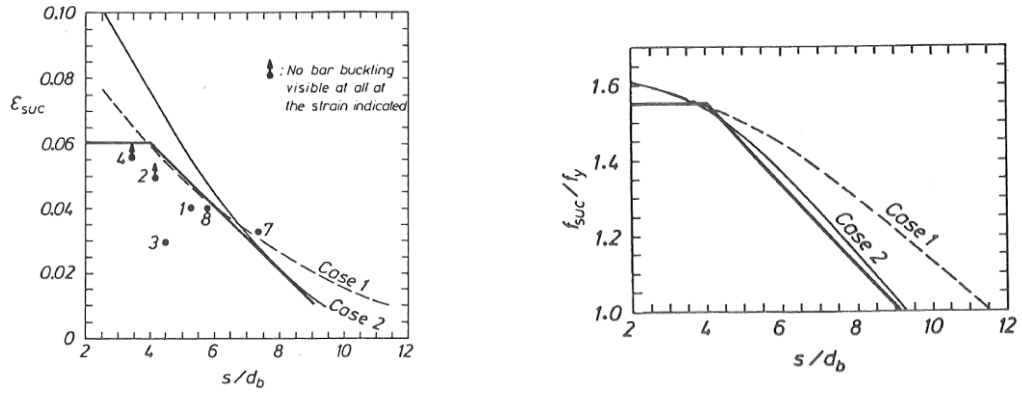

(a) (b)

Figure 2.9. Ultimate Compressive Strain and Stress vs Hoop Spacing. Grade 380 MPa Steel (Zahn, 1985): (a) Buckling Strain ε_{suc} vs Hoop Spacing; (b) Normalized Buckling Stress f_{suc}/f_y vs Hoop Spacing

In his work, Zahn et al. observed that in some tests the bars tended to buckle across several hoops, especially for $s/d_{b\ell} \leq 4$, but did not consider those cases in the analysis. Also, since the formulation assumes monotonic load, Zahn et al. suggested a correction for cyclic loading, where the compressive strains are increased to an equivalent monotonic strain as a function of the compressive axial load. According to him, the predicted results with this correction were likely unreliable, and therefore the simplistic monotonic formulation was recommended.

Tanaka et al. (1990), continuing the work of Mander et al. and that of Zahn et al., studied the buckling of reinforcement across multiple hoops, see Figure 2.10. They determined analytically the capacity of 90° hook ties and peripheral hoops to prevent buckling of longitudinal reinforcement. The analyses included the effects of core concrete expansion (Poisson effect) and initial imperfections of the longitudinal reinforcement.

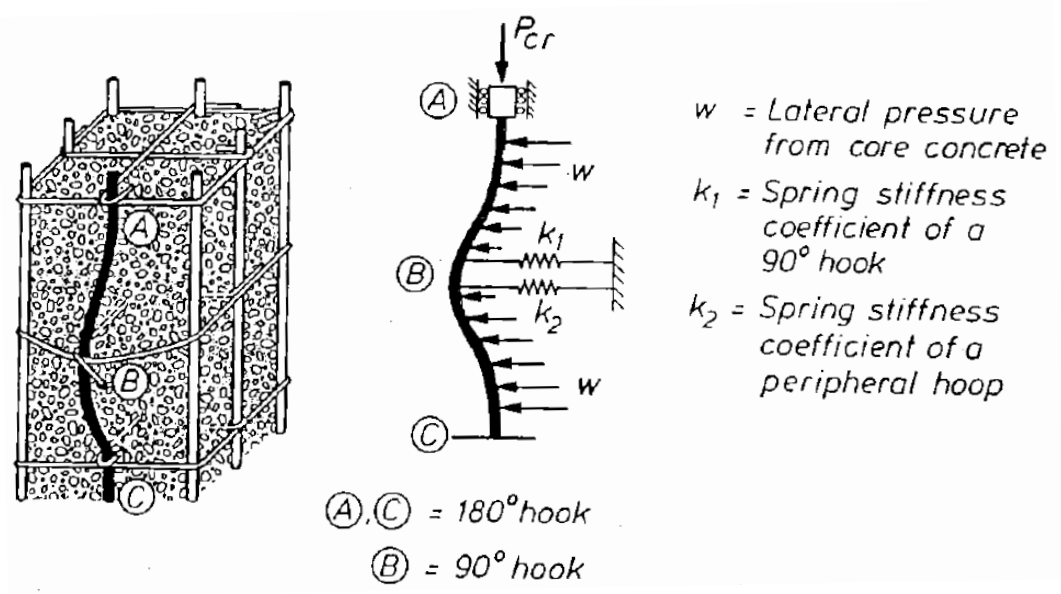

(a) (b)

Figure 2.10. Buckling of Intermediate Longitudinal Bar Restrained by Cross Ties with 90° and 135° or 180° (Tanaka et al., 1990): (a) Buckled Shape; (b) Buckling Model

Papia et al. (1988) studied the critical load of longitudinal reinforcement considering a buckled bar could span multiple sets of hoops. They modeled the hoops as linear-elastic and used Bernoulli-Euler beam elements to represent the longitudinal reinforcement, see Figure 2.11a. The addition of appropriate boundary conditions, including a restriction for elements bending into the core concrete, complete the system of equations required to determine the critical buckling load. Figure 2.11b shows the resulting critical load, P_c, normalized by the critical load of a hinged segment between consecutive hoops ($P_0 = \pi^2 EI/s^2$), versus the ratio between the stiffness of the hoops and the shear stiffness of the longitudinal bars (α_s and EI/s^3 respectively). Results from the formulation consistently overestimated critical loads obtained experimentally, which was attributed to geometric and mechanical imperfections of the real specimens. Based on the average error

between analytical and experimental results, Papia et al. suggested reducing the predicted critical load by a factor q =1.2.

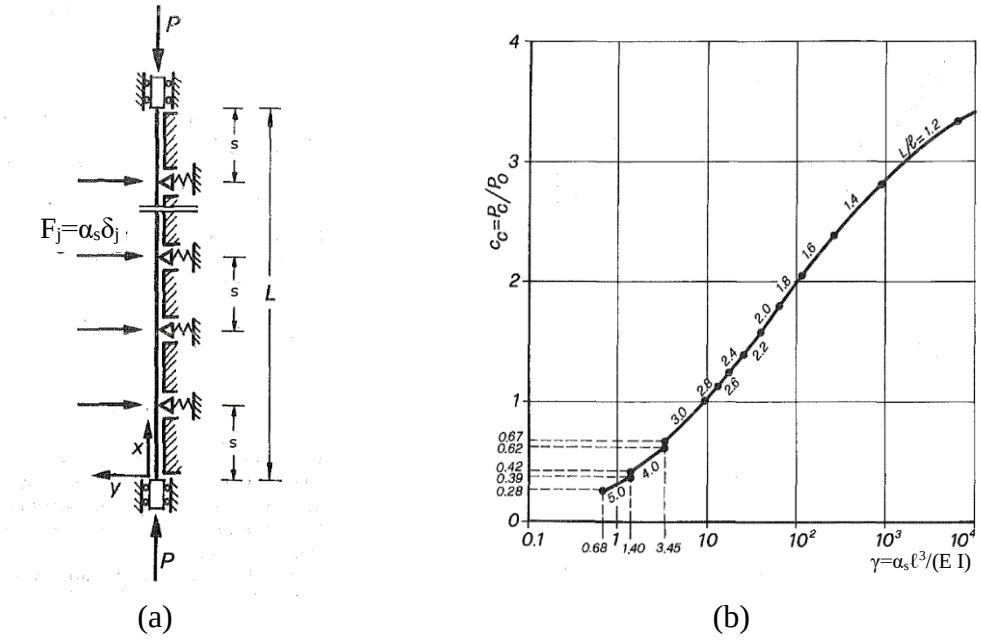

(a) (b)

Figure 2.11. Analysis Model and Critical Load Result Diagram (Papia et al. 1988): (a) Mechanical Model; (b) Normalized Critical Load vs γ Parameter

Although initial studies on the buckling of reinforcing steel focused on the critical load rather than the post-critical behavior, Mau and El-Mabsout (1989) carried out a series of parametric analyses. They used beam-column elements to predict the post-buckling stress-strain response of reinforcement at different slenderness levels. Their results closely matched previous experimental results for reinforcement under monotonic load, see Figure 2.12.

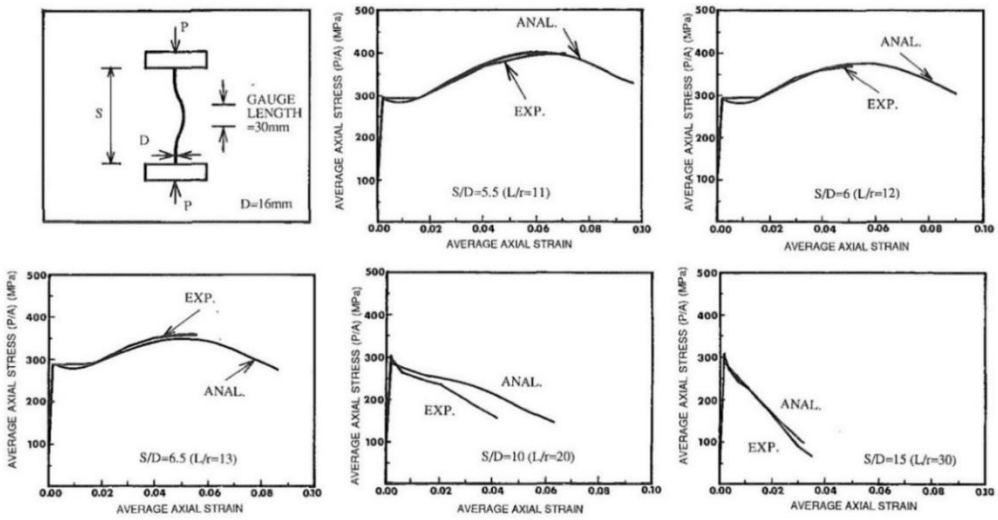

Figure 2.12. Comparison of Experimental Results and Analytical Results (Mau and El-Mabsout, 1989)

Monti and Nuti (1992) created a simple, yet effective model for the cyclic response of steel including inelastic buckling, calibrated experimentally in terms of the slenderness ratio $s/d_{b\ell}$. Their initial conclusion was that inelastic buckling develops under the condition: $s/d_{b\ell} > 5$. The model was tested under both symmetric and anti-symmetric strain histories, showing significant improvement in the fit of experimental results for $s/d_{b\ell} > 5$, compared to typically used material models that do not include buckling, see Figure 2.13. Like the model by Menegotto and Pinto (1973) on which it is based, the formulation by Monti and Nuti (1992) overestimated the stress response following a partial unloading and reloading, this issue was later resolved by Fragiadakis et al. (2008), see Figure 2.14.

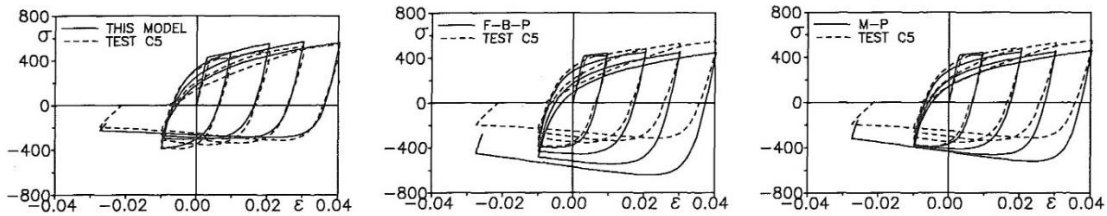

(a) (b) (c)

Figure 2.13. Comparison between Experimental and Analytical Models for Asymmetric strain history. $s/d_{b\ell}$ = 11 (Monti and Nuti, 1992): (a) Monti- Nuti; (b) Filippou-Bertero-Popov; (c) Menegotto and Pinto

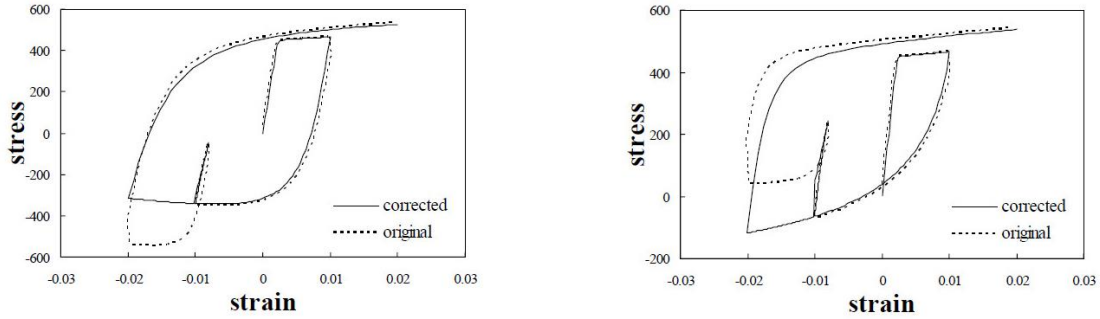

(a) (b)

Figure 2.14. Corrected and Uncorrected Stress-Strain Paths (Fragiadakis et al., 2008): (a) $s/d_{b\ell}$ = 12; (b) $s/d_{b\ell}$ = 6

Gomes and Appleton (1997) also developed a simple model for inelastic buckling for steel reinforcement by combining the Menegotto-Pinto formulation and a lumped plasticity mechanism in the buckled reinforcement, see Figure 2.15. The model assumed the plastic model of the bar is not dependent on the axial force and that buckling concentrates between consecutive hoops.

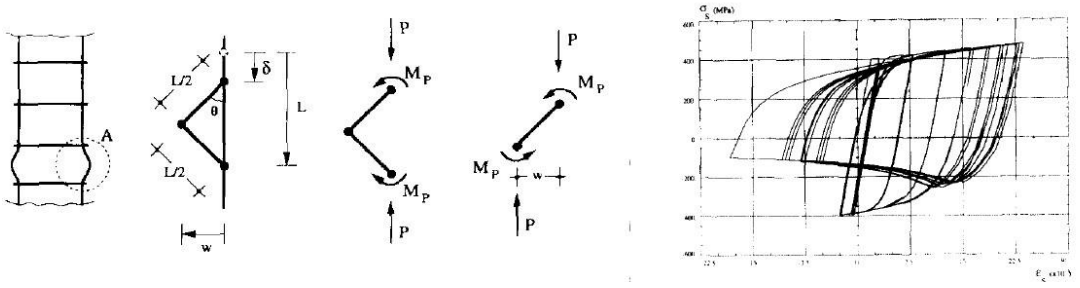

(a) (b)

Figure 2.15. Buckling Model by Gomes and Appleton (1997): (a) Equilibrium of Buckled Longitudinal Bar; (b) Stress-Strain Response of the Model

Rodriguez et al. (1999) performed a series of monotonic and cyclic tests on steel reinforcing bars conforming to most of the ASTM A706 requirements, with aspect ratios of 2.5, 4, 6, and 8. Based on moment-curvature analyses of typical column sections, values of 1 and 2.3 for the ratio between maximum tensile and compressive strains (ε_m^+, ε_m^- respectively) were used for the cyclic strain histories. The onset of buckling during the cyclic tests was defined from the strain readings on opposite sides of the specimen, compared to the peak strains reached in the corresponding cycle, (ε_m^+ and ε_m^-). They proposed a procedure to predict the onset of buckling based on the plastic strain following the largest reversal from tension, ε_0^+ , see Figure 2.16, and the critical stress, f_p, calculated from reduced modulus theory, see Equation 2.3. This research assumed buckling occurs between consecutive hoops and did not address the post-buckling behavior, and the critical stress, f_p, was calculated from reduced modulus theory, see Figure 2.16.

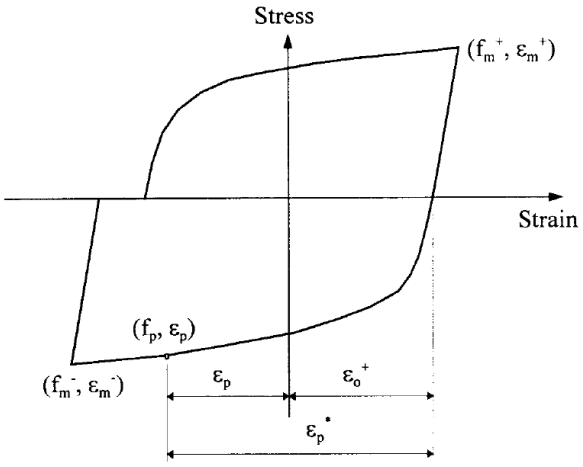

Figure 2.16. Cyclic Stress Strain Curve for Steel (Rodriguez et al. 1999)

El-Bahy et al. (1999) tested six reinforced concrete circular bridge piers under monotonic and cyclic loading to obtain their relevant force-deformation and "low-cycle" fatigue characteristics. Constant amplitude cycles of displacement amplitudes ranging from a corresponding 2 percent lateral drift up to 7 percent were used. The authors conclude that, under sequences of predominantly low amplitude cycles, a confinement failure is more probable, while for predominantly high amplitude inelastic cycles, buckling and "low-cycle" fatigue fracture of the longitudinal reinforcement is more likely.

Bayrak and Sheikh (2001) studied the effect of buckling in the longitudinal reinforcement at the section level, developing a procedure to predict the monotonic moment-curvature response in the plastic hinge of a RC column. The procedure relies on experimental results for the lateral load due to expansion of the concrete core, and the stress-strain response of longitudinal reinforcement between hoops (in between hoops, the bond between concrete and steel is lost after the onset of buckling). For this purpose, Bayrak and Sheikh tested 56 #6 steel specimens at multiple slenderness ratios (from $s/d_{b\ell}$=4

to $s/d_{b\ell}$ = 10) and initial imperfection ratios (from $e/d_{b\ell}$ = 0 to $e/d_{b\ell}$ = 0.03, with e the initial lateral deformation of the reinforcement) under monotonic load. The moment-curvature results from this procedure showed a better fit to experimental data compared to conventional section analyses, Figure 2.17.

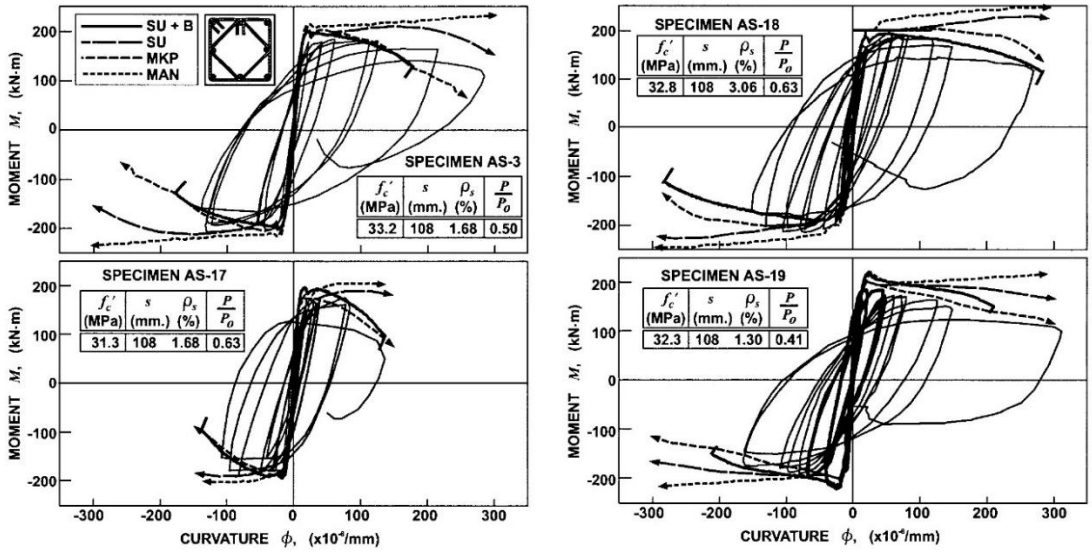

Figure 2.17. Experimental and Predicted Moment-Curvature Response. SU: Sheikh and Uzumeri; MKP: Kent and Park; MAN: Mander; SU+B: Bayrak and Sheikh (2001)

Dhakal and Maekawa (2002) ran several finite element simulations of the buckling response of bare reinforcing bars (without core concrete or transverse reinforcement interaction). Through a parametric study, they found the product $s / d_{b\ell} \cdot \sqrt{f_y}$ (f_y: yield stress), can accurately define the post-buckling behavior of reinforcing steel, not just the slenderness ratio $s/d_{b\ell}$, as stated by Monti and Nuti, 1992. A model for the monotonic post-buckling response was suggested, see Figure 2.18, which could be used as an envelope for the Menegotto and Pinto cyclic model. The model was tested against experimental response

originally recorded by Monti and Nuti, see Figure 2.19. Kunnath et al. (2009) implemented a material model including the effects of buckling, "low-cycle" fatigue and cyclic degradation; using the formulation by Dhakal and Maekawa for the buckling effect. The material model is currently implemented in OpenSees as *ReinforcingSteel*.

Moyer and Kowalsky (2003) showed experimentally how the buckling of reinforcement is dependent on the level of tensile strains the bars are initially subjected to, an observation first made by Wang and Restrepo (1996) in their work on columns confined with fiberglass/epoxy jackets, see Figure 2.20. The relationship can be explained as follows: for a longitudinal bar to buckle, a large tensile strain is first required to open the cracks in the surrounding concrete; at the following loading reversal, the reinforcing bar represents the sole source of compression capacity until the cracks close, if the critical load is reached before then, the bar will start to buckle.

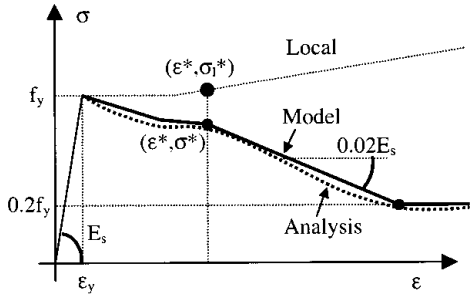

Figure 2.18. Proposed Model by Dhakal and Maekawa (2002)

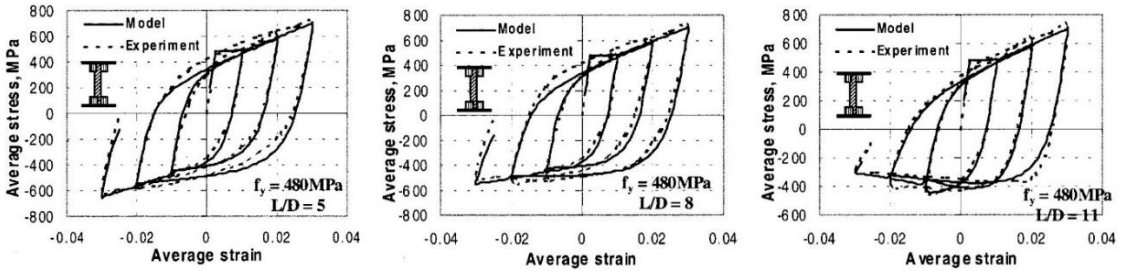

Figure 2.19. Comparison of Analytical and Experimental Hysteretic Response (Dhakal and Maekawa, 2002)

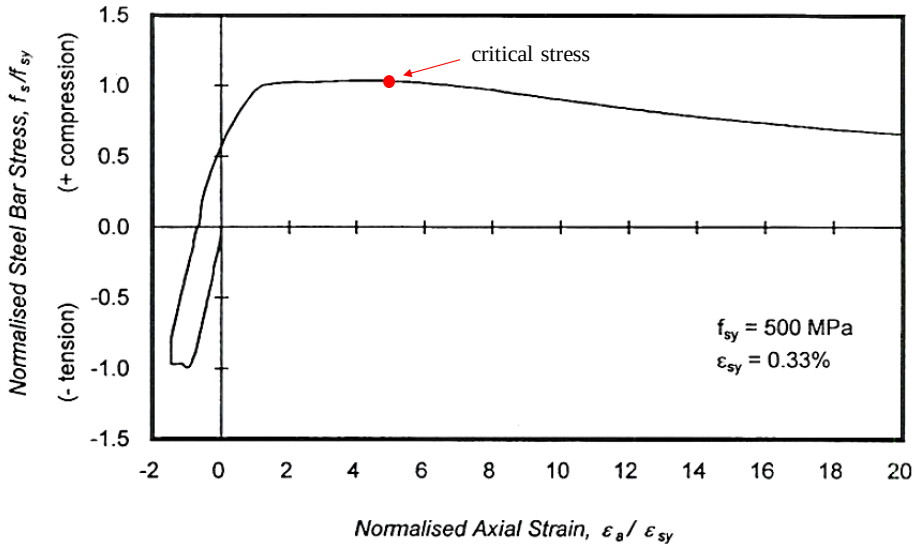

Figure 2.20. Inelastic Buckling Behavior of Grade 430 Deformed Reinforcing bar with Aspect Ratio $s/d_{b\ell}$=9 (Wang and Restrepo, 1996)

Bae et al. (2005) tested 162 #8 and #10 bars under monotonic load for multiple combinations of slenderness ratio and initial lateral imperfection ratio. Using the experimental results to model the relationship between axial stress, lateral displacement, and axial strain, a simple monotonic material model, suitable for fiber discretization

models, was developed and tested against experimental data with satisfactory results, see Figure 2.21.

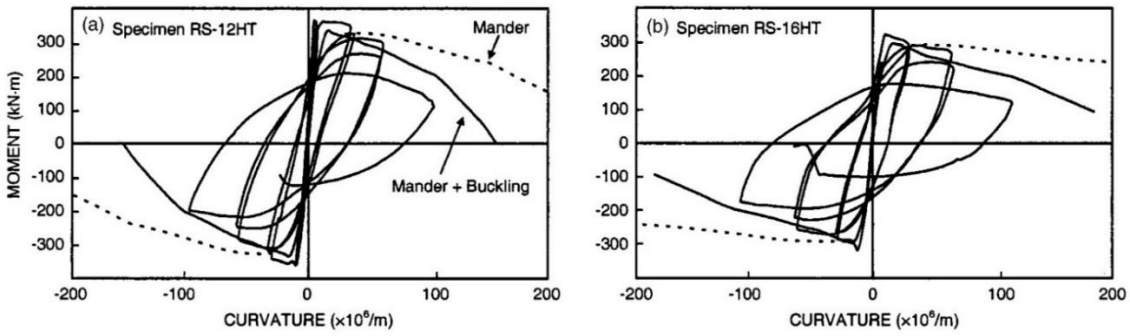

Figure 2.21. Experimental and Predicted Moment-Curvature Response (Bae et al., 2005)

Berry and Eberhard (2005) proposed a procedure for earthquake engineering practice to estimate the lateral deformation at which a RC column reaches the onset of buckling, which represents an important performance state of the system. The method combines experimental formulations for the yield displacement (Priestley et al. 2003), plastic hinge length (Mattock, 1967), strain of steel at onset of buckling, and plastic curvature (Berry, 2003). The resulting lateral deformation equation depends on five constants, see Equation 2.7, calibrated from a database of experimental results from 104 columns tested under cyclic load:

$$\frac{\Delta_{bb}}{\Delta_y} = 1 + \frac{3E_o}{\lambda f_y} C_0 (1 + C_1 \rho_{eff}) \left(1 + C_2 \frac{P}{A_g f_c'} \right)^{-1} \times \left(\frac{D}{L} + C_3 + C_4 \frac{D}{L} \frac{f_y d_{b\ell}}{D} \right) \qquad 2.7$$

Where Δ_{bb} is the predicted lateral displacement at the onset of bar buckling, Δ_y the lateral displacement at yield, C_0 through C_4 are the calibrated constants, L and D are the length and diameter of the column, λ is a constant dependent on the type of transverse reinforcement, and $\rho_{eff} = f_y/f'_c$ the effective volumetric transverse ratio.

From the calibration analysis, Berry and Eberhard (2005) proposed the following equation,

$$\frac{\Delta_{bb\text{-}calc}}{L}(\%) = 3.25\left(1 + k_{e\text{-}bb}\rho_{eff}\frac{d_{b\ell}}{D}\right)\left(1 - \frac{P}{A_g f'_c}\right)\left(1 + \frac{L}{10D}\right) \qquad 2.8$$

With $k_{e\text{-}bb} = 40$ for rectangular-reinforced column, 150 for spiral-reinforced column, and 0.0 when $s/d_{b\ell} > 6$. The ratio between experimental and predicted results for Δ_{bb} resulted in a mean of 1.0 and standard deviation of 25%.

Cosenza and Prota (2006) performed extensive experimental work on the monotonic response of smooth steel bars under a wide range of slenderness ratios, from $s/d_{b\ell} = 5$ to $s/d_{b\ell} = 70$. They defined threshold values of $s/d_{b\ell}$ for the type of response to be expected: from plastic behavior without buckling for $s/d_{b\ell} < 5$, to elastic buckling for $s/d_{b\ell} > 20$. Smooth reinforcement and large slenderness ratios are representative of the typical reinforcement in RC structures built in the 1960s. This work was expanded by Prota et al. (2009) with the study of the cyclic response of smooth bars under multiple slenderness ratios. The study found the cyclic behavior to be heavily influenced by the loading history (in particular, the maximum plastic elongation and hysteretic energy dissipated) besides

$s/d_{b\ell}$. The study also found that most material models available could not capture the response of specimens with $s/d_{b\ell} > 8$.

Massone and Moroder (2009) proposed a plastic model based on early unpublished work by Restrepo (2007). In it, an initial imperfection is introduced to the reinforcement and the deformations concentrate in four plastic hinge locations along the buckled bar, see Figure 2.22.

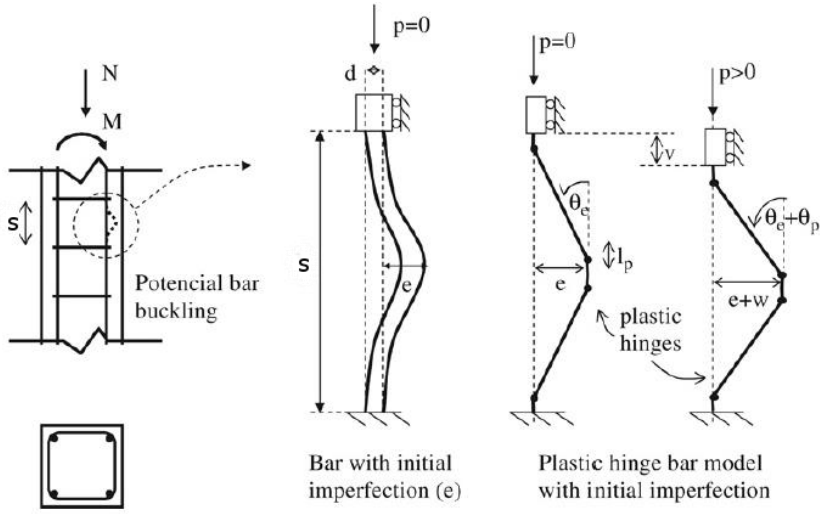

Figure 2.22. Mechanical model for Bar Buckling. Massone and Moroder, 2008

Zong et al. (2013) defined a post-buckling envelope curve similar to the formulation by Dhakal and Maekawa (2002), calibrating the model using simulation results from the finite element software LS-DYNA. The interaction with transverse reinforcement was included using the bar-with-spring model developed by Zong (2011).

Feng et al. (2014) proposed a two-step numerical method to predict the occurrence of longitudinal bar buckling under seismic load. First, a fiber-based finite element model is used to obtain the response of the full structural element under seismic excitation. The

resulting strain history in the plastic hinge zone is used as input in a second finite element model, developed in the software Abaqus, which includes the interaction with the concrete core and transverse reinforcement, see Figure 2.23. This procedure accurately predicted the observed onset of buckling of three experimental tests.

Kashani et al. (2015) did a comprehensive experimental testing on ninety reinforcing bars under "low-cycle" fatigue strain history with various slenderness ratios, diameters, yield strengths and surface roughness (deformed and smooth bars). The deformed reinforcing bars were B500B and B460 for the smooth bars. Aspect ratios of 5, 8, 10, 12, and 15 were used with strain amplitudes ranging from 1-5% for 12 mm bars and 1-4% for 16 mm bars. Their work shows that crack initiation due to fatigue testing occurs earlier for bars with larger aspect ratios and that cracks start at the concave face of the buckled bars. They suggest that, when a bar buckles, the total strain amplitude at the concave face of the bar increases due to combined axial and bending deformation. Once formed, fatigue cracks propagate away from the transverse rib into the body of the bar normal to the bar axis, suggesting that the largest stresses lie in the longitudinal direction of the bar. Also, a reduction in "low-cycle" fatigue life is noted for larger diameter bars.

Yang et al. (2016) developed a modified version of the Gomes-Appleton model using four plastic hinge locations, improving the prediction of the original model, especially for small slenderness ratios ($s/d_{b\ell}$).

Analytical models of the post-buckling behavior can be divided into three main categories: beam-column elements, material models, and geometric formulations. Beam-column element models rely on Bernoulli-Euler beam theory to analyze the post-buckling

behavior. Initial work by Mau and El-Mabsout (1989), Nonaka (1973), Papadrakakis and Loukakis (1988), among others, assumed fixed ends of the reinforcement at the transverse ties.

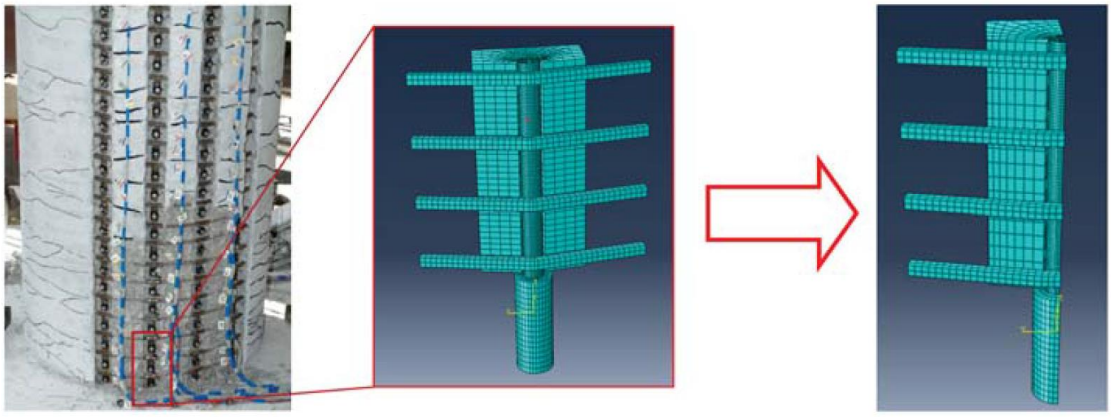

Figure 2.23. Geometry of the Plastic Hinge Zone Model in Abaqus (Feng et al. 2014)

Material models account for the nonlinear response through various simplifications, calibrating their formulation using computer simulations (e.g. Dhakal and Maekawa, 2002) or experimental results (e.g. Monti and Nuti, 1992).

Geometric models address the non-linear geometric compatibility directly, using finite element analysis or a plastic mechanism model. The finite element model approach has been investigated by several authors (e.g. Nakamura and Higai 2002, and Feng et.al 2014). The accuracy of the results from this method are, however, at the expense of high computational demand, making them unpractical for the modeling of full scale systems.

Plastic mechanism models are based on concentrated plasticity theory, such as the work by Engesser- Considère, von Karman, and Shanley. The simplified models by Gomes

and Appleton (1997), and Papadrakakis and Loukakis (1988), also incorporate concentrated plasticity in their formulation.

The experimental efforts of several authors (Bayrak and Sheikh 2001, Bae et al. 2005, Cosenza and Prota 2006), have enabled the development of a comprehensive database, available for the verification of analytical models of buckling, although results for large diameter reinforcement under cyclic loading are still scarce.

2.3. Fatigue Life of Reinforcing Bars

The fatigue phenomenon is of great importance to the response of reinforced concrete (RC) members when subjected to large deflections during an earthquake. While numerous studies have focused on studying and characterizing such phenomenon, there is very limited data on the fatigue characterization of large-diameter steel bars. The purpose of this section is to briefly cover the fundamental concepts of fatigue and the various methods used to characterize the fatigue life of steel reinforcement.

Fatigue can be defined as a degradation of mechanical properties leading to failure under cyclic loading (Meyers and Chawla, 2009). From mechanics of materials, the two principal methods for material deformation and failure are crack growth and dislocations, as well as plastic flow. As high stress concentrations occur at the tip of cracks, the mechanism of fracture can involve plastic deformation at such locations. A material which allows plastic deformations to take place at the cracks is “tough”, otherwise, the material is “brittle”. Deformation processing, such as rolling, forging, and extrusion involve substantial plastic deformation and the response of the material will depend on its plastic

behavior during such processes. The material properties of steel are also highly affected by heat treatment. Quenching produces a hard, martensitic structure, which is gradually softened by tempering treatments at higher temperatures. On the other hand, the annealed structure is ductile, but results in a low yield stress.

2.3.1. Fatigue Process

As previously mentioned, fatigue can be defined as a degradation of mechanical properties leading to failure of a material under cyclic loading. Typically, the failure under cyclic loading occurs at much lower stress levels than the strength measured under monotonic loading. The study of cyclic behavior can be divided into three classes: the stress-life approach, the strain-life approach, and the fracture mechanics approach.

The stress-life approach is useful when stresses and strains mainly remain in the elastic range. The main drawback of this approach is the inability to distinguish between the initiation and propagation phases of fatigue life. For elastic-plastic materials, such as reinforcing steel, this approach is used when dealing with high-cycle fatigue (1,000 cycles or more to failure). The strain-life approach is useful when there is a significant amount of plastic strain and is the basis of this research. The fatigue life is typically quite short under these conditions and is referred to as low-cycle fatigue (less than 1,000 cycles to failure). In the fracture mechanics approach, estimates of the life spent in propagating a crack from an initial size to larger size, or to the critical failure, are determined.

The first step in the fatigue process in most materials corresponds to crack nucleation at singularities or discontinuities. Discontinuities may be on the surface or in the interior of the material. The singularities can be structural (such as inclusions or second-

phase particles) or geometrical (such as scratches or steps). The explanation of preferential nucleation of fatigue cracks at surfaces perhaps resides in the fact that plastic deformation is easier there and that slip steps form on the surface (Meyers and Chawla, 2009). While slip steps alone can be responsible for initiating cracks, they can also interact with existing structural or geometric defects to produce cracks. In metals, surface singularities may be present from the beginning or may develop during cyclic deformation, such as the formation of intrusions and extrusions at what are called the persistent slip bands (PSBs). Figure 2.24 illustrates the fatigue crack nucleation at slip bands. As loading takes place, slip occurs on a favorably oriented plane and, during unloading, reverse slip occurs on a parallel plane, since slip of the original plane is inhibited due to hardening or due to the oxidation of the newly formed free surface. The first cyclic slip may create an extrusion or an intrusion at the surface. An intrusion may grow and form a crack by continued plastic deformation during subsequent cycles. At large stress or strain amplitudes, as much as 90% of a material's fatigue life is consumed in the growth or propagation of a crack (Meyers and Chawla, 2009).

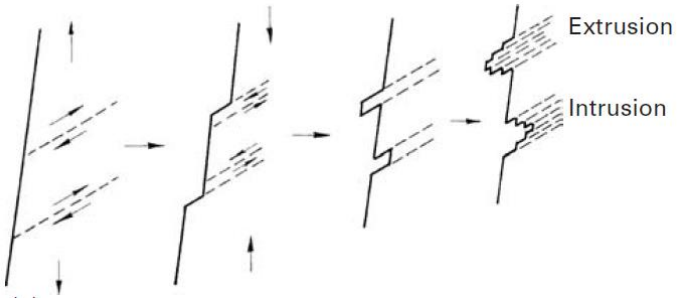

Figure 2.24. Fatigue Crack Nucleation (Meyers and Chawla, 2009)

2.3.2. Effects of Bar Geometry

Hanson et al. (1968) performed two series of fatigue tests on No. 8 bar embedded in rectangular concrete beams. They suggest that the radii at the base of the lugs should be approximately equal to the height of the lugs to obtain good fatigue characteristics. An increase in lug radius at the base increases the fatigue strength of steel reinforcement. They also conclude that the fatigue strength of the bars is not necessarily improved by terminating the transverse lugs before they reach the longitudinal ribs.

Kokubu and Okamura (1969) performed a series of high-cycle fatigue tests on reinforced concrete beams using different types of high-strength #6 and #8 deformed bars. They concluded that the most influential factor governing the high-cycle fatigue of deformed bars is the degree of change in slope at the base of the lug. However, they note that if arcs with radii of 5 or more times the height of the lugs are used, bonding between the bar and concrete is impaired. To reduce this effect, they suggest abruptly changing the slope of a lug at a point about one-third up the lug such that the upper half will be vertically.

MacGregor et al. (1971) carried out high-cycle fatigue tests on RC beams reinforced with a single #5, #8, or #10 bar. Such bars had two longitudinal ribs, parallel transverse lugs inclined at about 75 degrees to the bar axis, and all lugs merged into the longitudinal ribs. They conclude that, for design purposes, the fatigue strength of hot-rolled deformed reinforcing bars is not affected by changes in the tensile strength of the bars. They also note a small decrease in the fatigue strength with an increase in the diameter of the bar.

The effects of bar deformations were studied by Fei and Darwin (1999). They tested #4 and #5 bars in air and showed that deformations cause high stress concentrations at the root and serve as potential fatigue crack initiators. Also, that the ratio of the lug base radius to the lug height (r/h) has a significant influence on the stress concentration at the base of deformations. They conclude that bar diameter has a significant effect on the fatigue strength of bars, with larger bars having a reduced fatigue strength.

2.4. Gaps in Knowledge

Significant progress has been made over the years in the understanding and prediction of buckling of reinforcement in the plastic hinge region of reinforced concrete members. However, an accurate and efficient formulation of this effect, capable of integrating this phenomenon in simulations of large scale models, has yet to be developed. Currently, efficient buckling formulations available for fiber-based finite element models assume, for simplicity, that the transverse reinforcement constrains lateral deformations between adjacent hoops, despite experimental results showing otherwise. More accurate material models, which include the interaction between longitudinal, transverse reinforcement and the core concrete, have computational requirements that make them unsuitable for the modeling of large scale systems.

Little is known about the development of micro-cracks in buckled reinforcing steel bars. As previously noted, all damage processes have typically been simply lumped as “low-cycle” fatigue, which only considers the number of cycles and strain amplitude in most formulations of this phenomenon.

Definition of strain alone poses an interesting and rarely explored problem. Should the strain amplitude used to determine the low-fatigue of the bars be defined at the global level, at the local level, or at the microscopic level? The problem of defining strain at the local level alone is that the buckling observed in test samples is slightly different from the buckling observed in longitudinal bars in columns, so such formulation can contain a significant bias. The definition of strain at the microscopic level would also pose a problem as it would only be meaningful within a metallurgist perspective. Perhaps the best engineering approach is to establish relationships between global and local strains and relate strain amplitude and damage between these two strain definitions.

Chapter 2, in part, is a reprint of the material as it appears in *SSRP Report 17/10: Plastic buckling-straightening fatigue of large Diameter reinforcing steel bars*, 2018. Duck, David; Carreño, Rodrigo; and Restrepo, José I. The dissertation author co-authored this material.

Chapter 3.

CALIBRATION OF GIUFFRÈ-MENEGOTTO-PINTO CONSTITUTIVE STRESS-STRAIN RELATIONSHIP FOR REINFORCING STEEL

3.1. Abstract

The uniaxial Giuffrè-Menegotto-Pinto constitutive steel model is widely used in non-linear modeling of reinforced concrete elements. However, parameters required in this constitutive stress-strain relationship are not easily identifiable from mechanical tests. An extensive literature review shows that most authors use the parameters recommended during the early development of the constitutive model. The authors of this paper believe that a calibration of the model parameters to steel manufactured in accordance with ASTM A615 and A706 would be a significant contribution to researchers and engineering professionals.

A series of cyclic stress-strain tests were performed on thirty-six reinforcing steel Grade 60 ASTM A615 and A706 coupons. To obtain data about statistical variability, bars were sourced from three different manufacturers. Test results were used to calibrate the model parameters, which were then verified using a set of validation reversed cyclic stress-strain tests. The strain rate effects were analyzed using equivalent cyclic coupon tests at

rates of 0.001/sec and 0.02/sec. Final calibration results are presented in terms of expected values, prediction intervals, and correlation functions between the model properties.

3.2. Introduction

The Giuffrè-Menegotto-Pinto (GMP) constitutive stress-strain relationship has been widely used in the modeling of the non-linear response of reinforcing steel under cyclic loading. The model, as first described by Giuffrè and Pinto (1970), was based on the non-linear stress-strain relation proposed by Goldberg and Richard (1963), and incorporated the effect of plastic deformations on the Bauschinger effect (Bauschinger, 1886) observed in steel coupons tested experimentally. The resulting constitutive stress-strain relationship, although still relatively simple, could effectively replicate stress-strain responses observed experimentally. Giuffrè and Pinto (1970) proposed a set of parameter values for the constitutive stress-strain relationship based on the cyclic response of a single 10 mm diameter coupon tested under symmetric tension-compression cycles up to ±0.75%. The formulation was further improved by Menegotto and Pinto (1973), and subsequently used by multiple authors due to its simplicity and accuracy predicting the response of reinforcing steel (Stanton and McNiven, 1979, and Ciampi et al. 1982). The model provided better predictions of the stress-strain response compared to other formulations available, such as the bilinear and those proposed by Ramberg and Osgood (1943) and Dafalias (1975).

Filippou et al. (1983) later incorporated the effect of isotropic hardening into the constitutive stress-strain relationship, given the relevance of this phenomenon in the steel response at higher strain amplitudes. Additional improvements of the model have been

implemented by other authors since then (Monti and Nuti 1992, Dhakal and Maekawa 2002, Bosco et al. 2016, Kolozvari et al. 2018). However, the formulation by Filippou et al. (1983), or some variation of it, is often preferred in the modeling of reinforced concrete systems, given its reliable results and reduction of convergence issues in non-linear analyses.

A quick literature review shows the widespread use of the GMP constitutive stress-strain relationship in the modeling of a variety of reinforced concrete structures (Mitra and Lowes, 2007, Bao et al. 2008, Haselton et al. 2008, Mullapudi and Ayoub, 2010, Lu and Panagiotou, 2013). However, despite the widespread use of the constitutive stress-strain relationship, the material parameters used by most authors are often based on the original values specified by Giuffrè and Pinto (1970) and Filippou et al. (1983). For this reason, the authors believe a set of calibrated parameters for reinforcing steel specifications currently used, such as ASTM A615 (2016) and A706 (2016), represents a useful contribution to the work of researchers and engineering practitioners alike. A limited study is thus performed herein, using #4 Grade 60 reinforcing bars satisfying the ASTM A615 and A706 standards from three different manufacturers. To facilitate the experimental procedure, the coupons used for the calibration and cyclic testing were machined at mid-length to a 9 mm diameter and 2:1 aspect ratio. Although some noticeable differences between tensile test results of machined and unmachined coupons are observed and analyzed herein, the results for calibrated parameters presented in this article are based on the response of machined coupons.

The effect of strain rate in the cyclic response of the reinforcing bars and calibrated parameters of the constitutive stress-strain relationship is also investigated. Though multiple studies on strain rate effects have been performed on reinforcing bars (Manjoine 1944, Mirza and MacGregor 1979, Restrepo-Posada et al. 1994), the scope of such studies have mainly focused on the monotonic response.

The Open System for Earthquake Engineering Simulation, or OpenSees (McKenna et al. 2000) is a popular software framework for the modeling of large structural systems. This article focuses in the GMP constitutive stress-strain relationship implemented in OpenSees as *STEEL02*.

3.3. Testing Procedure

3.3.1. Description of Test Coupons

Two straight, never coiled #4 bars of equal length – 4.6 meters – were acquired from three different steel mills, labeled henceforth as mills A, B and C. Each bar was manufactured to comply with the specifications for Grade 60 ASTM A615 or A706. The selection of specimens allows a limited study on the variability of the stress-strain response for the given Grade, bar size, and ASTM standards.

From each bar, a series of 250 mm long coupons were extracted for testing. Such coupons were classified into six groups with six coupons each, divided by manufacturer and ASTM specification, Table 3.1. The bars were machined at the center to ensure a uniform cross section and define the location of the failure mode, Figure 3.1. The machined

portion of the bars had a length to diameter ratio of 2 to minimize the effects of nonlinear geometry in the hysteretic response (Mander, 1983, Bae et al. 2005).

Three additional coupons from each steel batch, two unmachined and one machined to the same specifications in Figure 3.1, were subjected to a pure tension test until failure.

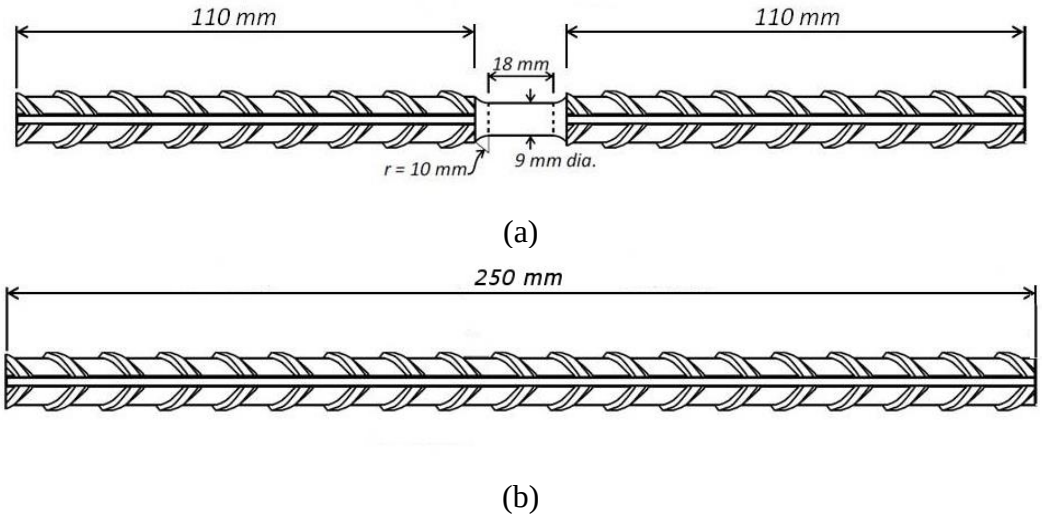

Figure 3.1. Test Coupons Used for Testing: (a) Machined #4 Coupon used in Cyclic and Tensile Tests; (b) Unmachined #4 Coupon Used for Tensile Tests Only

Table 3.1 summarizes the properties of each steel category, including the mechanical properties indicated by the manufacturer and the results from in-house testing of unmachined coupons (average of the two coupons per steel category). As noted on the table, the characteristic stresses from in-house testing are consistently below the value indicated by the manufacturer, with an average difference of 7%. The observed difference lies within the expected range considering strain rate effects, given the common practice by U.S manufacturers of testing bars at high strain rate, as confirmed by metallurgists from two major U.S. mills, whose products were used for this study.

Table 3.1. Mechanical Properties of the Coupons

			MILL CERTIFICATE		IN-HOUSE TEST (UNMACHINED)		COMPARISON $(f_{mill} - f_{in\text{-}house}) / f_{mill}$	
COUPONS	MILL	ASTM	Yield Strength (MPa)	Tensile Strength (MPa)	Yield Strength (MPa)	Tensile Strength (MPa)	Yield Strength (%)	Tensile Strength (%)
A61 & A62	A	A615	474	741	445	720	6.1%	2.9%
B61 & B62	B	A615	503	731	487	725	3.3%	0.8%
B71 & B72	B	A706	453	631	438	626	2.9%	0.7%
A71 & A72	A	A706	492	687	440	660	10.5%	4.0%
C71 & C72	C	A706	492	641	414	576	15.7%	10.1%
C61 & C62	C	A615	608	707	525	638	13.6%	9.9%

Tensile tests for machined coupons exhibited differences in the mechanical properties with respect to the unmachined coupons, see Table 3.2. One reason for this difference is the unknown cross-section area of unmachined coupons, with the nominal value for the bar size differing from the actual value by as much as 10%, whereas the cross-section area for machined coupons can be measured very accurately. Also, the variable cross-section area along unmachined coupons results in a non-uniform strain distribution in the longitudinal direction, as strains concentrate between bar deformations, where the cross-section area is smallest. Moreover, the hot-rolling process to manufacture reinforcing bars can produce different material properties between the center and the surface of each bar, given the temperature gradients while cooling and the rearrangement of grains on the surface of the rolled bars. Finally, the machining process can produce additional changes in the mechanical properties of the material, as heating and cooling of the surface of the coupon may harden the material, an effect that could not be measured.

Table 3.2. In-house Test Results for Unmachined and Machined Coupons

		UNMACHINED					MACHINED				
CATEGORY	ASTM	f_y (MPa)	ε_{sh} (%)	ε_u (%)	f_u (MPa)	f_u/f_y	f_y (MPa)	ε_{sh} (%)	ε_u (%)	f_u (MPa)	f_u/f_y
A6	A615	445	0.74	9.4	720	1.62	438	0.37	10.4	839	1.91
B6	A615	487	1.16	9.6	725	1.49	537	0.78	11.0	837	1.56
B7	A706	438	1.26	11.6	626	1.43	483	0.66	14.3	724	1.50
A7	A706	440	0.82	10.6	660	1.50	475	0.42	12.1	765	1.61
C7	A706	414	1.40	10.6	576	1.39	430	1.26	16.2	653	1.52
C6	A615	525	1.34	8.8	638	1.21	522	1.80	14.1	690	1.32

The in-house tension test results show not only a significant difference between yield and tensile strengths of machined and unmachined coupons, but also a large contrast in the uniform strain, ε_u, justified by the non-uniform strain distribution in the longitudinal direction of unmachined coupons. Furthermore, the difference between tensile to yield strength ratios, f_u/f_y, suggests that machined and unmachined coupon results differ not only due to the assumed cross-section area, but also from a change in material properties between the center and the surface of the bar.

For the cyclic testing and parameter calibration in this study, the use of machined coupons was preferred because the geometrical non-linear response is practically eliminated, allowing only material non-linearities contribute to the hysteretic response.

Table 3.3 shows the chemical composition of each steel category as indicated by the manufacturers. The steel sets were sorted by their carbon content in descending order. Table 3.1 through Table 3.3 show that every steel category satisfies the mechanical properties and chemical composition set forth in the ASTM standards they were manufactured for, ASTM A615 (2016) and A706 (2016).

Table 3.3. Chemical Composition of the Coupons

CATEGORY	C (%)	Mn (%)	Cu (%)	Ni (%)	Cr (%)	V (%)	Mo (%)	P (%)	S (%)	Si (%)	CE (%)
A6X	0.42	1.13	0.23	0.11	0.18	0.0046	0.023	0.009	0.036	0.2	0.64
B6X	0.42	1.14	0.24	0.08	0.07	-	0.017	0.014	0.035	0.2	0.62
B7X	0.28	1.21	0.3	0.09	0.13	0.023	0.02	0.006	0.025	0.18	0.51
A7X	0.28	1.2	0.29	0.11	0.11	0.027	0.025	0.014	0.04	0.21	0.50
C7X	0.27	1.1	0.31	0.12	0.12	0.001	0.028	0.012	0.041	0.21	0.47
C6X	0.26	0.75	0.34	0.11	0.11	0.001	0.02	0.015	0.038	0.21	0.44

3.3.2. Instrumentation

All machined test coupons were outfitted with two diametrically opposed 5 mm high-yield electrical foil strain gages in the machined region for cyclic testing, see Figure 3.2, to record a smeared longitudinal strain along the cross section and identify the onset of buckling. In tensile tests, strains were measured with a high-precision extensometer instead. All tests were performed using a 500 kN MTS Universal Testing Machine, Load Unit model 318.50 (MTS Systems Corporation 2009), at the Charles Lee Powell Laboratories at the University of California in San Diego.

Figure 3.2. Application of Strain Gages to Machined Coupons

3.3.3. Strain Histories

The machined coupons were tested under four different cyclic strain histories (SH1, SH2, SH3, and SH4), at a nominal strain rate of 0.001/sec, see Figure 3.3. Additionally, two machined coupons per steel category were tested under strain histories SH1 and SH2 at a strain rate of 0.02/sec, to evaluate strain rate effects, see Figure 3.4. Data was collected at 256 Hz and time stamped.

The selected "high" strain rate, at 0.02/sec, is consistent with the average rates recorded experimentally during seismic testing. In particular, the strain response of reinforcement in the plastic-hinge region of a full-scale bridge column, tested under seismic demands exceeding the design level, was used as a reference (Schoettler et al. 2012). The reduction in the nominal rate by a factor of 20 for the "low" strain rate (0.001/sec), is significant enough to display strain rate effects in the hysteretic response, and sufficiently large to keep the duration of each test within a few minutes, see Figure 3.3. Quasi-static strain rates (1E-5/sec – 1E-4/sec) were not used given the duration of testing, and the discrepancy of such rates with those experienced by reinforcing bars during seismic excitation.

Instead of traditional "sawtooth" shape strain histories, randomized strain histories, similar to those observed experimentally in reinforcing steel during seismic tests (Schoettler et al. 2012), were preferred for testing in this study. Furthermore, the selected strain histories represent a variety of response conditions, including high amplitude strain reversals (see strain histories SH1, SH3, and SH4), medium level reversals (SH2), multiple unloading/reloading reversals (SH1, SH3, and SH4), histories skewed towards positive or

negative strains (SH1 and SH3 respectively), etc. By selecting these histories, the material model and the calibrated parameters suggested for it, are evaluated under conditions similar to those in a seismic event, unlike more traditional "sawtooth" shaped and incremental amplitude strain histories.

Figure 3.3 and Figure 3.4 show the strain histories used for cyclic testing. The magnitude of strains was limited to ±5% during testing, within the range of strains experienced by reinforcing bars during seismic shaking, and where the strain gages attached to the specimens provide reliable readings. Strain history SH3 was generated by changing the sign of strain history SH1, Figure 3.3c.

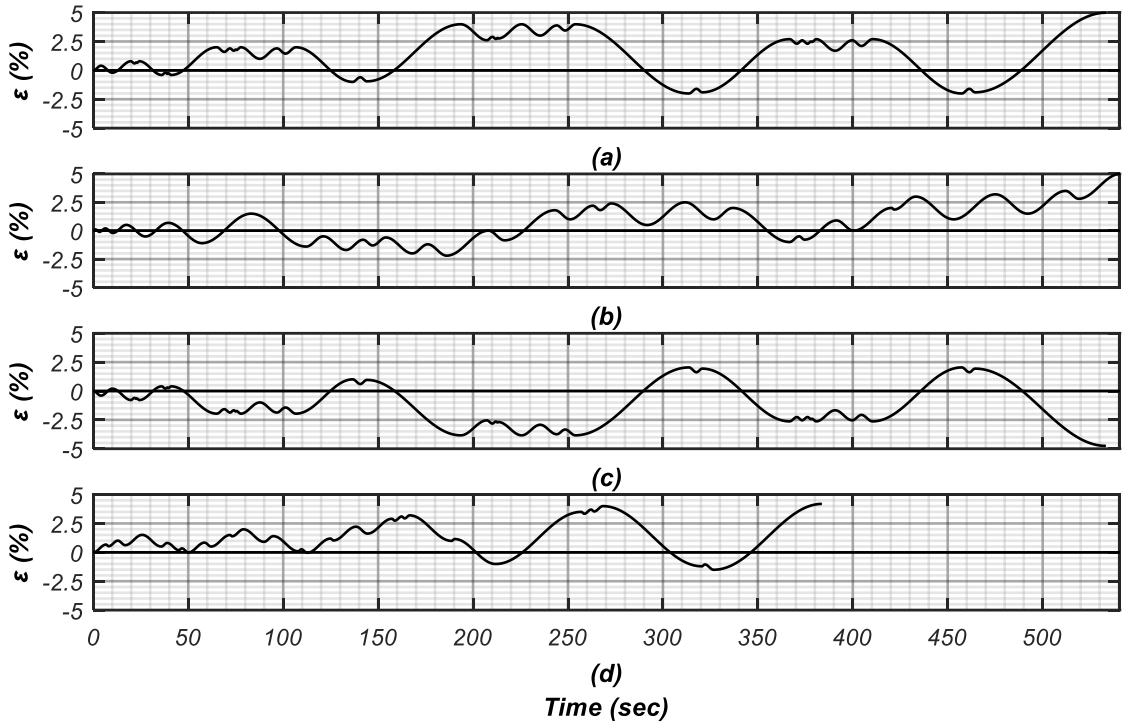

Figure 3.3. Strain histories with nominal strain rate = 0.001 (1/sec) used for testing: (a) SH1-L; (b) SH2-L; (c) SH3-L; (d) SH4-L

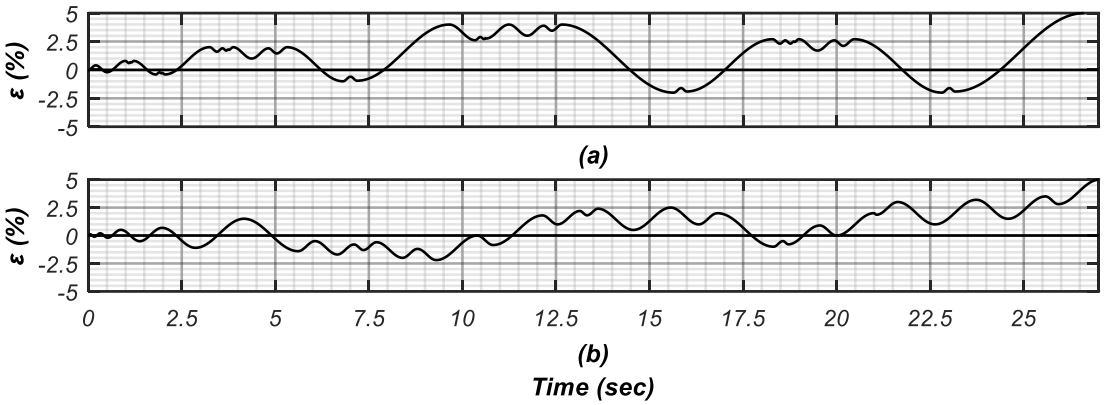

Figure 3.4. Strain histories with nominal strain rate = 0.02 (1/sec) used for testing: (a) SH1-H; (b) SH2-H

3.3.4. Coupon Identification

The coupons were labeled according to their manufacturer, the ASTM code they comply with, and the strain history used for testing. Each strain history was assigned to a specimen number, see Table 3.4. Strain history "T" corresponds to monotonic tension until failure for unmachined and machined coupons, while the remaining strain histories refer to cyclic loading.

Table 3.4. Coupon Identification for Each Strain History

Strain Histories	Coupon #	Cross-Section
T	1	Unmachined
T	2	Unmachined
T	3	Machined
SH1-L	4	Machined
SH2-L	5	Machined
SH3-L	6	Machined
SH4-L	7	Machined
SH1-H	8	Machined
SH2-H	9	Machined

The following labeling scheme was used for each coupon:

[MANUFACTURER]+[ASTM CODE]+[COUPON # FROM TABLE 3] 3.1

For example, an ASTM A706 machined coupon from manufacturer B, tested under strain history SH3 at "low" strain-rate is labeled as B76 (= [B]+[7]+[6]).

3.4. Experimental Results

3.4.1. Tensile Tests

In the monotonic tension tests, a commercial clip-on extensometer measured the deformations, while the cyclic tests used diametrically opposed strain gauges to detect the onset of buckling. Figure 3.5 shows the stress-strain response in axial tension for one machined and two unmachined coupons per steel category. The average strain rate of these tests was 0.001/sec.

Results from Figure 3.5 confirm the differences in the response of machined and unmachined coupons detailed in the Description of Test Coupons section. Besides the differences in ductility and magnitude of yield and tensile strength, the machined coupons also show a significant reduction in the extent of the yield plateau, see ε_{sh} in Table 3.2. Although the source of this effect is not fully understood, it is suspected that the machining process, due to the heating and subsequent cooling of the surface of the coupons, may cause some hardening in the material.

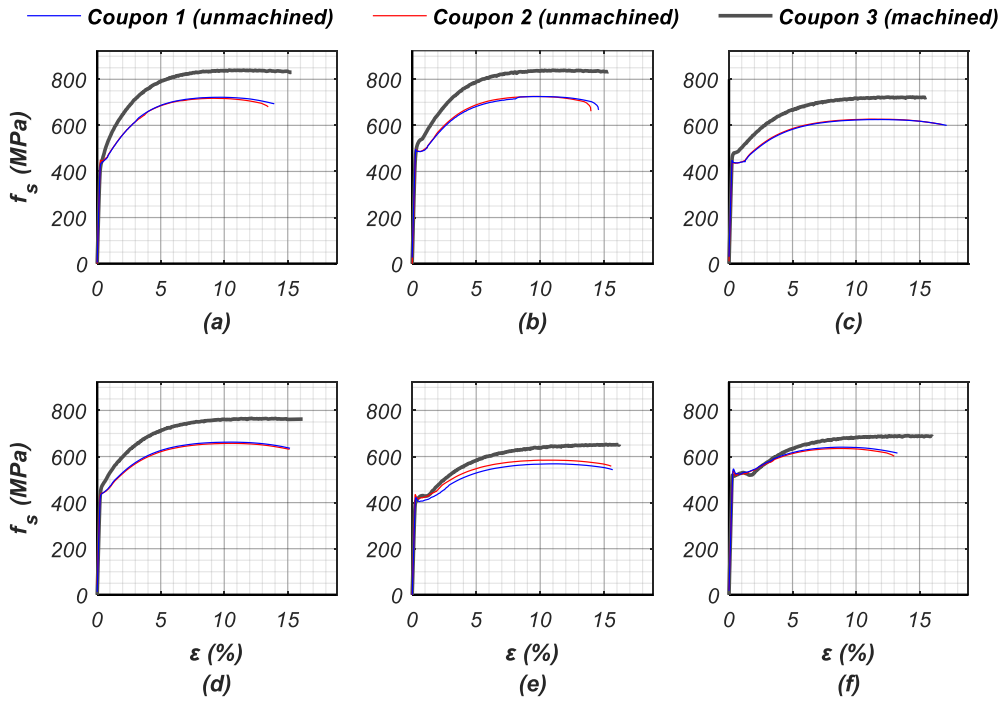

Figure 3.5. Axial Tension Test Results for all Steel Categories: (a) A63;(b) B63; (c) B73; (d) A73; (e) C73; (f) C63

Figure 3.5 also shows a significant difference in the response of coupons from different manufacturers. In ASTM A615 machined coupons, the observed difference in yield and tensile strength between manufactures is as much as 23% for each parameter, with the tensile to yield strength ratio, f_u/f_y, ranging from 1.32 to 1.91, see Table 3.2. For ASTM A706 specimens, given the more stringent requirements for the chemical composition and mechanical properties of the standard, the maximum observed difference in yield and tensile strength is reduced to 12% and 17% respectively, with a narrower range for the strength ratio, f_u/f_y, between 1.50 and 1.61, see Table 3.2.

In terms of toughness, U_T, defined in Equation 3.2, specimens from each ASTM standard showed similar variability between manufacturers. The observed average

toughness of ASTM A706 coupons was 10% greater than that observed for the ASTM A615 coupons, see Table 3.5.

$$U_T = \int_0^{\varepsilon_u} f(\varepsilon) \cdot \mathrm{d}\varepsilon \qquad 3.2$$

Where U_T is the toughness, ε and f are the strain and stress of the material, and ε_u is the uniform strain.

Table 3.5. Toughness from In-House Tension Tests

SPECIMEN	ASTM	U_T (J/cm^3)
A63	A615	76.7
B63	A615	81.8
B73	A706	94.1
A73	A706	83.4
C73	A706	95.3
C63	A615	88.8

3.4.2. Cyclic Tests

Following the tensile tests, four machined specimens per steel category were axially loaded under the "low" strain rate histories detailed in Figure 3.3. For a preliminary analysis of the stress-strain responses Table 3.6 shows, for each steel category, the average stress at yield and the average relative deformation energy (that is, the energy normalized by the mean value between specimens under the same strain history, see Equation 3.3).

The average yield strength from cyclic responses, see $\overline{f}_y$ in Table 3.6, is in most cases within 5% of the observed value from monotonic tests, see f_y of machined specimens in Table 3.2. In steel category A6 however, the observed difference in yield strength increases to 12%. These results are consistent with monotonic and cyclic tests having an equivalent nominal strain rate. Also, in each steel category f_y remained stable between

loading histories, as observed in the coefficient of variation (c.o.v.) under 3% for all cases, see Table 3.6.

$$U_{rel}^{i,j} = \frac{\int_{SH\ j} f_i \cdot d\varepsilon_i}{\frac{1}{N}\sum_{k=1}^{N} \int_{SH\ j} f_k \cdot d\varepsilon_k} \qquad 3.3$$

Where $U_{rel}^{i,j}$ is the relative toughness of specimen *i* under strain history *SH j*, f_i and ε_i are the corresponding stress and strain histories of specimen *i*, and *N* is the number of specimens from all steel categories subjected to strain history *j*.

Table 3.6. Average Cyclic Test Properties per Steel Category (Strain rate = 0.001/sec)

CATEGORY	$\bar{f}_y$ (MPa) (c.o.v.)	$\bar{U}_{rel}$ (J/cm^3) (c.o.v.)
A6	490 (2.8%)	1.02 (1.1%)
B6	548 (0.6%)	1.06 (0.9%)
B7	484 (2.6%)	1 (0.7%)
A7	493 (2.5%)	1.05 (0.4%)
C7	421 (0.4%)	0.91 (1.4%)
C6	519 (1.3%)	0.96 (1.1%)

Results for U_{rel} show that the relative hysteretic energy dissipated by each steel category remains stable for different loading histories, as noted by the small c.o.v. values in Table 3.6. The observed range of deformation energies is however small, between 0.91

and 1.06. As expected with strain histories of large amplitude, U_{rel} is highly correlated to the tensile strength of the material, f_u, as seen in the results from monotonic tests in tension, see Figure 3.6.

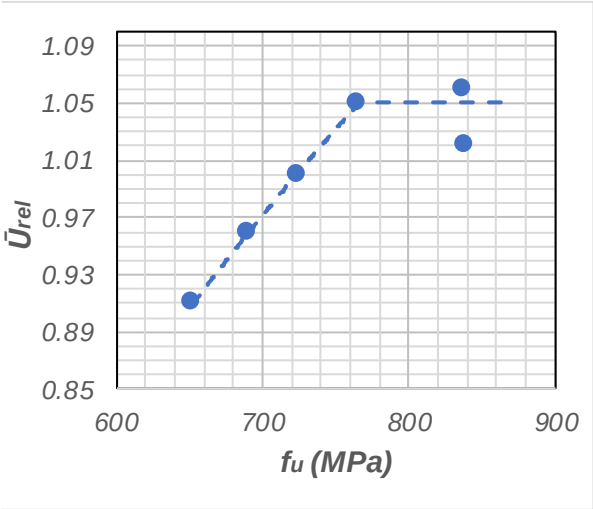

Figure 3.6. Tensile Strength, f_u vs Average Relative Deformation Energy, $\bar{U}_{rel}$, from Cyclic Tests

To illustrate the difference in the response of the steel types under study, Figure 3.7 shows the stress-strain response of each specimen tested under strain history SH1-L, including the maximum stress, $|f_{max}|$, and hysteretic energy, U, of each response. As seen in the figure, the stress-strain responses can be clearly differentiated between steel types, both in terms of stress magnitude and shape of hysteretic loops.

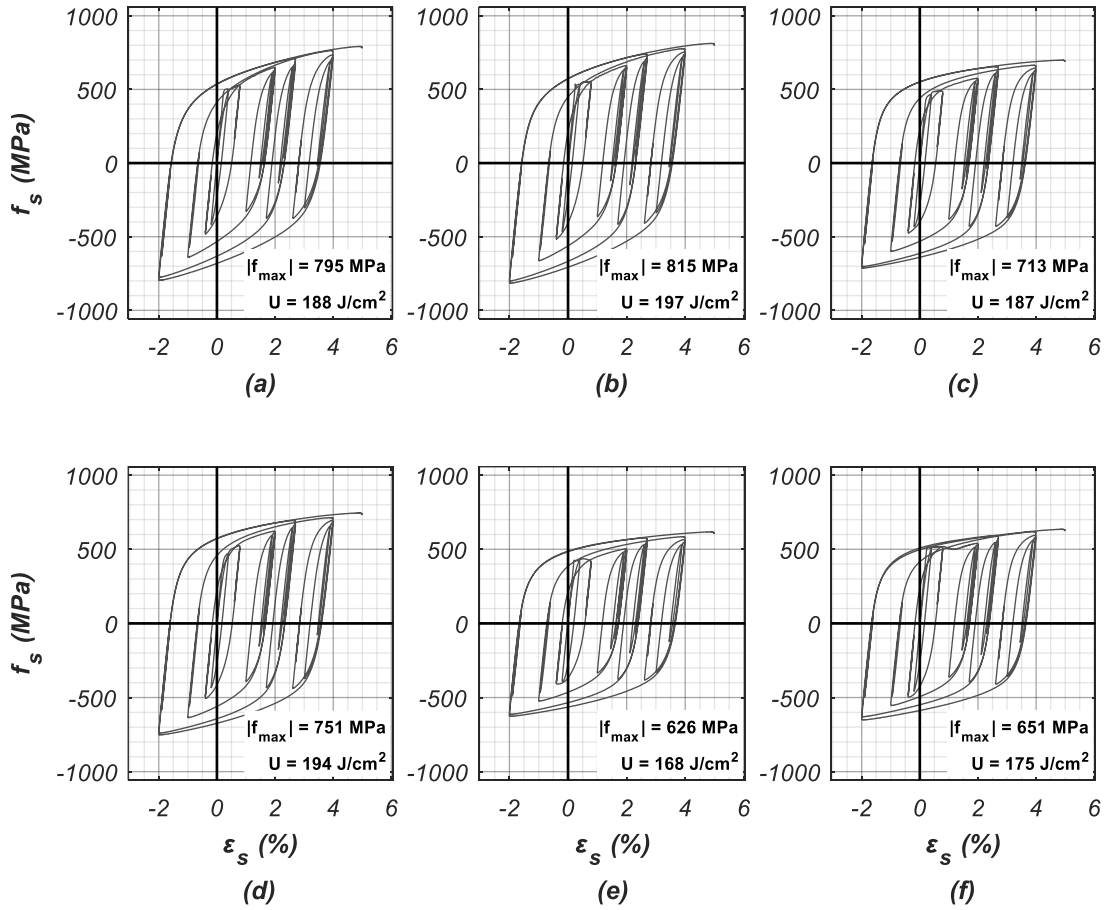

Figure 3.7. Cyclic Response for Strain History SH1-L: (a) A64; (b) B64;(c) B74;(d) A74;(e) C74; (f) C64

3.4.3. Strain Rate Effects

Strain rate effects are examined using the response from two cyclic strain histories (SH1 and SH2), tested at "Low" and "High" nominal strain rates, corresponding to $\dot{\varepsilon}$=0.001/sec and $\dot{\varepsilon}$=0.02/sec respectively. Figure 3.8 compares the stress-strain response of two equivalent specimens from category C6 under strain history SH1 at the two nominal rates. As observed in Figure 3.8, an increase in the strain rate correlates with a higher yield

stress (see top-left corner of the figure) which, in Figure 3.8, corresponds to a 12% increase, the largest difference observed between all the tested steel categories.

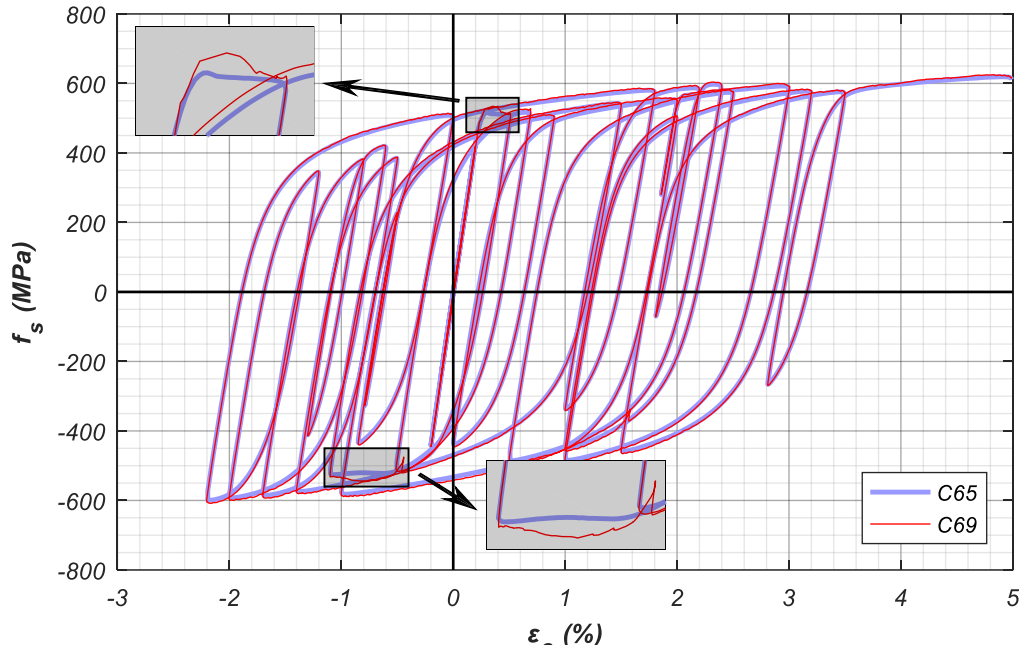

Figure 3.8. Effect of Strain Rate in Hysteretic Response. C65 at $\dot{\varepsilon}$ = 0.001/sec and C69 at $\dot{\varepsilon}$ = 0.02/sec

Table 3.7 shows the measured yield strength in all coupons subjected to strain histories SH1 and SH2 at the two nominal rates. In all but steel category A6, the yield strength increases with larger strain rates, which is consistent with findings from other authors (Manjoine, 1944; Atalay et al. 1972; Mirza & MacGregor, 1979; Restrepo-Posada et al. 1994).

Besides the variation in the yield strength, the effect of strain rate in the cyclic stress-strain response of the tested coupons is very small, at a normalized least-squared difference, defined in Equation 3.4, under 3% in all cases, see Table 3.8. Because of this,

the hysteretic responses under high strain rate (Coupons 8 and 9 as per Table 3.4) were not considered in the subsequent calibration of the model parameters.

$$\text{Difference}=\sqrt{\frac{\sum_{i=1}^{n}\left(f_{\dot{\varepsilon}=0.001/\text{sec}}-f_{\dot{\varepsilon}=0.02/\text{sec}}\right)^2}{\sum_{i=1}^{n}f_{\dot{\varepsilon}=0.001/\text{sec}}^2}} \qquad 3.4$$

Where $f_{\dot{\varepsilon}=0.001/\text{sec}}$ is the stress measured at strain rate $\dot{\varepsilon}$ = 0.001/sec at strain step *i*, and $f_{\dot{\varepsilon}=0.02/\text{sec}}$ the corresponding stress measured at a strain rate $\dot{\varepsilon}$ = 0.02/sec.

Table 3.7. Strain Rate Effect on Measured Yield Strength

Category	Measured Yield Strength (MPa)				$(f_y^H - f_y^L)/f_y^L$ (%)
	SH1-L (0.001/sec)	SH1-H (0.02/sec)	SH2-L (0.001/sec)	SH2-H (0.02/sec)	
A6	502.3	486.8	503.8	486.8	-3.2%
B6	550.0	571.9	544.8	567.8	4.1%
B7	486.5	500.9	476.1	500.9	4.1%
A7	471.5	504.4	500.0	504.4	3.9%
C7	421.1	452.9	421.1	452.9	7.6%
C6	515.1	552.5	510.6	570.0	9.4%

Table 3.8. Normalized Least-Squared Difference of Stress-Strain Response at two Different Strain Rates

Category	Normalized Least-Squared Difference (%)	
	SH1	SH2
A6	2.2	2.31
B6	1.79	1.94
B7	1.88	1.78
A7	2.83	2.16
C7	2.72	2.29
C6	3.00	1.36

3.5. Description of the Constitutive Model

The Giuffrè-Menegotto-Pinto model (Menegotto and Pinto, 1973), implemented into OpenSees as *STEEL02*, is a uniaxial constitutive stress-strain relationship for the modeling of reinforcing steel in structural concrete members. This section provides a description of the material model, detailing the role of each parameter to be calibrated.

STEEL02 is defined by ten model parameters: E_0, f_y, b, R_0, cR_1, cR_2, a_1, a_2, a_3, and a_4, see the Notation section for the description.

The material model is represented by Equation 3.5, (Giuffrè & Pinto, 1970)

$$f^* = b\,\varepsilon^* + \frac{(1-b)\,\varepsilon^*}{\left(1+\left|\varepsilon^*\right|^R\right)^{\frac{1}{R}}} \qquad 3.5$$

Where ε^* and f^* are the normalized strain and stress, see Equation 3.6 and 3.7.

$$\varepsilon^* = \frac{\varepsilon - \varepsilon_r}{\varepsilon_0 - \varepsilon_r} \qquad 3.6$$

$$f^* = \frac{f - f_r}{f_0 - f_r} \qquad 3.7$$

Based on Equation 3.5, the material model computes the stress for a given strain from a smooth transition between two linear asymptotes: one with slope E_0 for the elastic response, followed by the post-yield response, with a slope $E_1 = b \cdot E_0$. The linear asymptotes are updated at each strain reversal, with the elastic asymptote originating from the reversal point (ε_r, f_r) and intersecting the post-yield asymptote at the updated yield point (ε_0, f_0), see Figure 3.9.

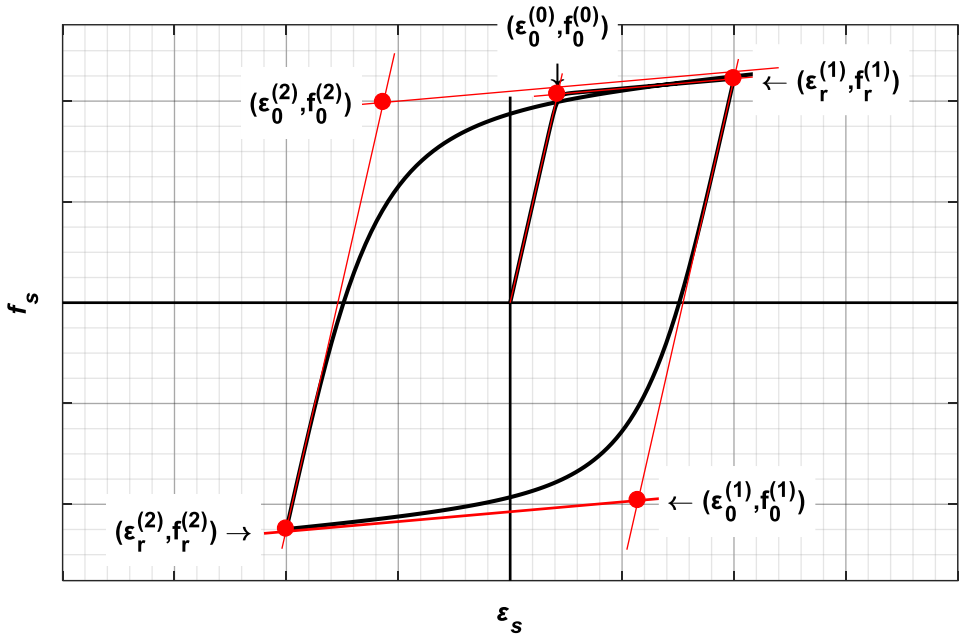

Figure 3.9. Asymptote Update Between Reversals

The transition between asymptotes has a curvature defined by the parameter *R*, a state variable of the model that changes at each strain reversal. *R* is dependent on the strain distance between the latest reversal point and the maximum excursion in the loading direction after the reversal, see Equation 3.8 and Figure 3.10.

$$R = R_0 \cdot \left(1 - \frac{cR_1 \cdot \xi}{cR_2 + \xi}\right) \quad R(\xi) > 0 \tag{3.8}$$

Where ξ is a normalized measure of the plastic strain, defined as follows:

$$\xi = \left| \frac{\varepsilon_r - \varepsilon_p}{\varepsilon_y} \right| \tag{3.9}$$

Where ε_p is the maximum recorded strain excursion in the loading direction after the reversal at ε_r.

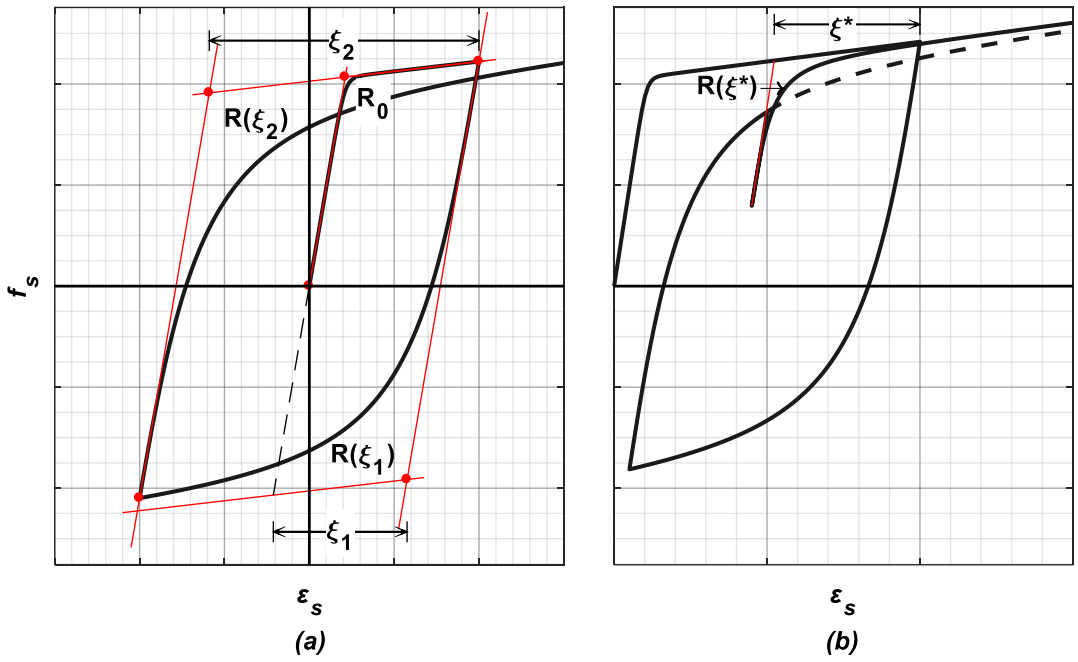

Figure 3.10. Change in Parameter R Defining Curvature of Bauschinger Curve: (a) Definition of *R(ξ)*; (b) Partial Unloading and Reloading

The location of the yield point (ε_0, f_0), depends on the previous reversal point (ε_r, f_r), and the effect of isotropic hardening, which is implemented as a parallel shift of the post-yield asymptote by a stress f_{st}, see Figure 3.11.

The Isotropic Hardening in *STEEL02* is implemented by two equations, one per loading direction. Equation 3.10 and 3.11 show the stress shift for isotropic hardening in tension and compression respectively.

$$f_{st} = f_y \cdot a_3 \cdot \left(\frac{\varepsilon_p^{\max} - \varepsilon_p^{\min}}{2 \cdot a_4 \cdot \varepsilon_y} \right)^{0.8} \qquad 3.10$$

$$f_{st} = f_y \cdot a_1 \cdot \left(\frac{\varepsilon_p^{\max} - \varepsilon_p^{\min}}{2 \cdot a_2 \cdot \varepsilon_y} \right)^{0.8} \qquad 3.11$$

Where ε_y is the original yield strain, $\varepsilon_p^{\min}$ and $\varepsilon_p^{\max}$ are the minimum and maximum recorded strains at the latest strain reversal.

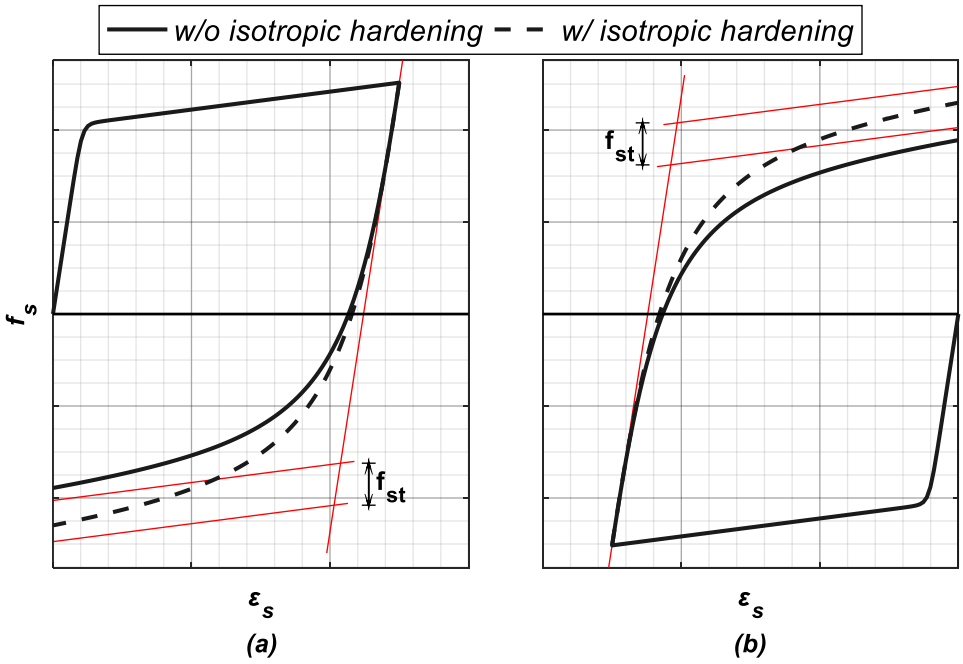

Figure 3.11. Stress Shift of Hardening Asymptote: (a) Isotropic Hardening in Compression ($a_1 \neq 0$); (b) Isotropic Hardening in Tension ($a_3 \neq 0$)

The isotropic hardening in *STEEL02* differs from the original formulation by Filippou et al. (1983), which defined a single equation for the stress shift in tension and compression, Equation 3.12. In this formulation, the stress shift depended on the maximum strain in absolute value in either direction, see ε_{max} in Equation 3.13.

$$f_{st} = \max\left(f_y \cdot a_1 \cdot \left(\frac{\varepsilon_{\max}}{\varepsilon_y} - a_2 \right), 0 \right) \qquad 3.12$$

Where a_1 and a_2 are the isotropic hardening parameters of the original formulation and

$$\varepsilon_{\max} = \max(\varepsilon_p^{\max}, -\varepsilon_p^{\min}) \qquad 3.13$$

The isotropic hardening formula defined by Filippou et al. 1983 specifies a minimum ductility for the onset of isotropic hardening through a_2, unlike the formulation from OpenSees (see Equations 3.10 and 3.11).

3.6. Parameter calibration

3.6.1. Preliminary Analysis

From Equations 3.10 and 3.11, it is observed that the strain hardening effect, as defined by the constitutive stress-strain relationship under study (*STEEL02*), can be defined by a single parameter relation for each loading direction: $a_3 / (a_4)^{0.8}$ and $a_1 / (a_2)^{0.8}$ for tension and compression respectively. Because of this, the four isotropic hardening parameters in the model can be simplified into only two independent variables, a_1 and a_3, by keeping a_2 and a_4 constant.

Preliminary optimization analyses also show a high correlation between R_0 and cR_1, variables controlling the curvature of the Bauschinger curve, see $R(\xi)$ in Equation 3.8. This results in significant variations in the optimal values found for parameters R_0 and cR_1, depending on the initial estimates. The different (R_0, cR_1) pairs obtained however, result in equivalent functions $R(\xi)$ for $\xi > 1$, corresponding to the most common domain of the function in a non-linear stress-strain response. Figure 3.12 shows an example of four (R_0, cR_1) combinations yielding almost identical hysteretic responses using the constitutive stress-strain relationship. Because of this the calibration analysis is simplified, without losing much generality of the material model, by assuming R_0 is constant. A value $R_0 = 20$

was selected, both to represent the sharp slope change at the yield plateau of the material and to maintain consistency with typical values used in the literature for this parameter.

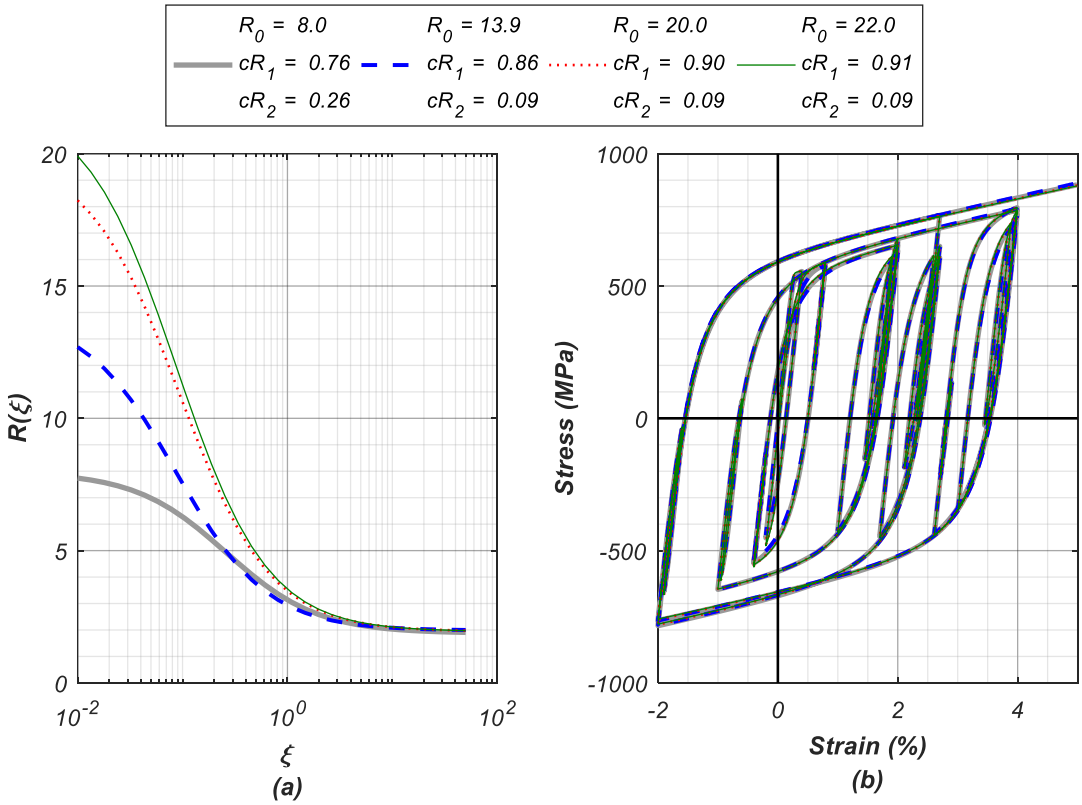

Figure 3.12. Example of "Equivalent" (R_0, cR_1) Combinations in GMP's Constitutive Stress-strain relationship: (a) Curvature of Transition between Asymptotes, R, vs Normalized Accumulated Plastic Deformation, ξ. (b) Hysteretic Response of the Model for each (R_0, cR_1) Combination

3.6.2. Optimization Algorithm

Material model parameters were calibrated from the stress-strain records of coupons tested under low strain-rate histories, see Figure 3.3, using a normalized least-squares error optimization between measured and predicted hysteretic response. The error used was defined as follows:

$$error(x) = \sqrt{\frac{\sum_{i=1}^{n} \left(f_{m,i} - f_{p,i}(x) \right)^2}{\sum_{i=1}^{n} f_{m,i}^2}} \qquad 3.14$$

Where $f_{m,i}$ is the measured stress at the i^{th} strain step, **x** is a vector with the parameters of the constitutive stress-strain relationship, and $f_{p,i}(\mathbf{x})$ is the stress predicted by the material model in the i^{th} strain step.

Estimates of the Young's Modulus, E, and yield strength, f_y, were identified from the hysteretic response of each coupon used in the calibration. The modulus E was identified using linear interpolation of the initial elastic cycles, while the yield strength was computed by averaging the stresses measured in the yield plateau region. During the optimization analyses E was kept constant, while f_y was further optimized to account for the discrepancy between the definition of f_y in the material model and the value identified in the measured stress-strain response. Reasonable upper and lower bounds for each material property were also defined to expedite the calibration process.

Calibration analyses were performed using MATLAB's Optimization Toolbox (2016) for constrained multivariate functions. Several algorithms available in the toolbox, including the *interior-point*, *trust-region-reflective*, *active-set* and *sqp* (MathWorks, 2018), were compared in terms of speed, stability of results, and magnitude of the optimal error. The *interior-point* algorithm (Byrd et al. 1999), which is based on a logarithmic *barrier function* to impose the upper and lower limits of each parameter, was chosen as the best alternative. From multiple optimizations tests, the *interior-point* algorithm was the most stable to changes in the initial conditions and gave the smallest errors.

3.6.3. Calibration Results

The calibration analyses on each stress-strain response produced an average fit error, as defined by Equation 3.14, of only 5.4%. The goodness-of-fit achieved at this error level can be appreciated from the response comparisons in Figure 3.13 and Figure 3.14.

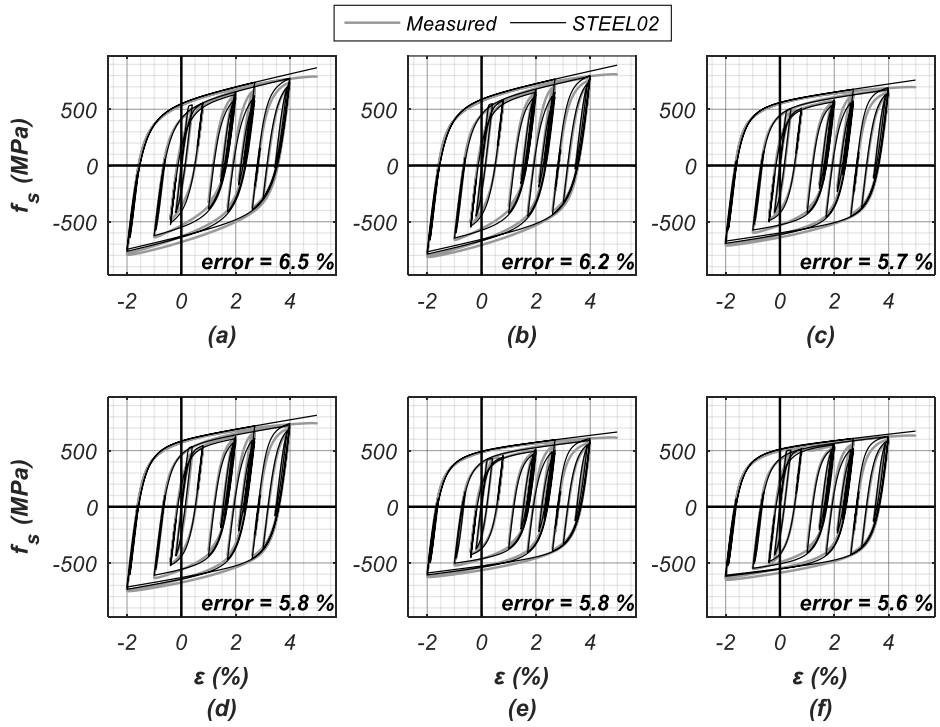

Figure 3.13. Measured vs Predicted Stress-Strain Response: (a) A64; (b) B64; (c) B74; (d) A74; (e) C74; (f) C64

Comparison between measured and predicted responses for the different strain histories exposes some of the limitations of the material model, among them the inability to capture the change in hardening of the material at large strains; the symmetry of the model in engineering coordinates, when the actual material is only symmetric in natural/true coordinates (Dodd and Restrepo, 1995); and the un-realistic Unloading-Reloading behavior depicted in Figure 3.10b, also seen in Figure 3.14d.

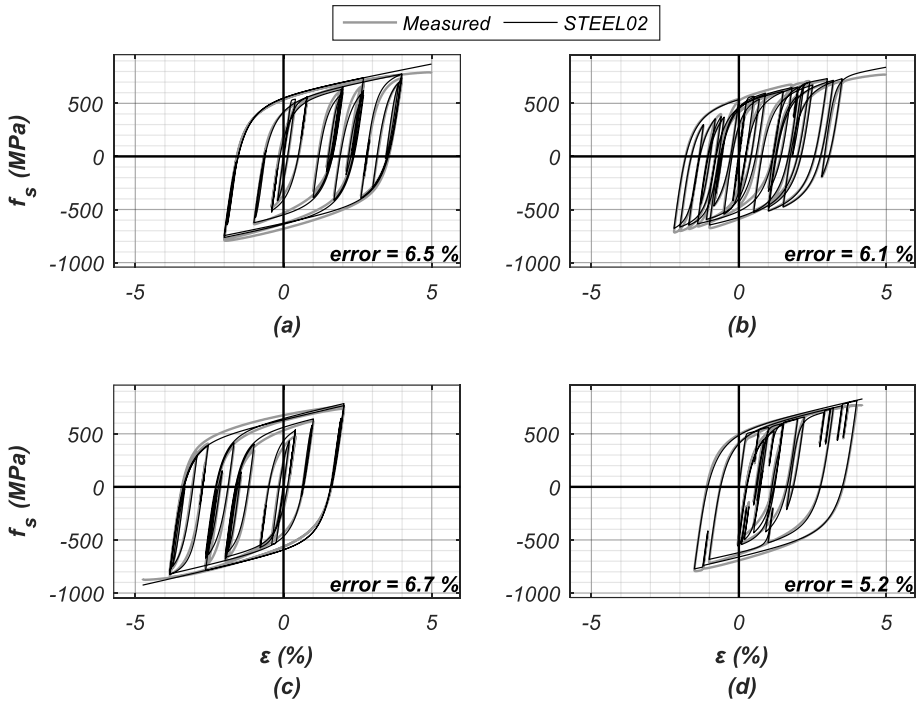

Figure 3.14. Measured vs Predicted Stress-Strain Response: (a) A64; (b) A65; (c) A66; (d) A67

Table 3.9 summarizes the results of the calibration process of each steel type under low rate cyclic tests (SHX-L, see Table 3.4), in terms of average values and coefficients of variation (c.o.v). Figure 3.15 shows the calibration results in a box-plot representation.

Table 3.9. Average and Coefficient of Variation of Calibrated Model Properties

Category	E (GPa) (c.o.v.)	f_y (MPa) (c.o.v.)	b (c.o.v.)	cR_1 (c.o.v.)	cR_2 (c.o.v.)	a_1 (c.o.v.)	a_3 (c.o.v.)
A6	211 (1.5%)	524 (4.2%)	0.027 (8.8%)	0.904 (0.6%)	0.07 (24.2%)	0.04 (36.1%)	0.027 (29.1%)
B6	217 (1.4%)	544 (4%)	0.025 (7.5%)	0.898 (0.5%)	0.07 (16.5%)	0.039 (31.8%)	0.029 (28.6%)
B7	215 (1.9%)	484 (3.9%)	0.016 (8.5%)	0.895 (0.3%)	0.08 (22.3%)	0.038 (30.5%)	0.03 (21.7%)
A7	212 (1.6%)	518 (4.2%)	0.019 (9.6%)	0.891 (0.6%)	0.08 (19.5%)	0.04 (29.9%)	0.032 (24.6%)
C7	214 (0.9%)	423 (3.7%)	0.014 (9.5%)	0.906 (0.4%)	0.08 (19.7%)	0.035 (28.1%)	0.029 (22%)
C6	218 (1.1%)	505 (4.1%)	0.013 (11.7%)	0.9 (0.6%)	0.08 (12.3%)	0.018 (57.7%)	0.013 (59.8%)

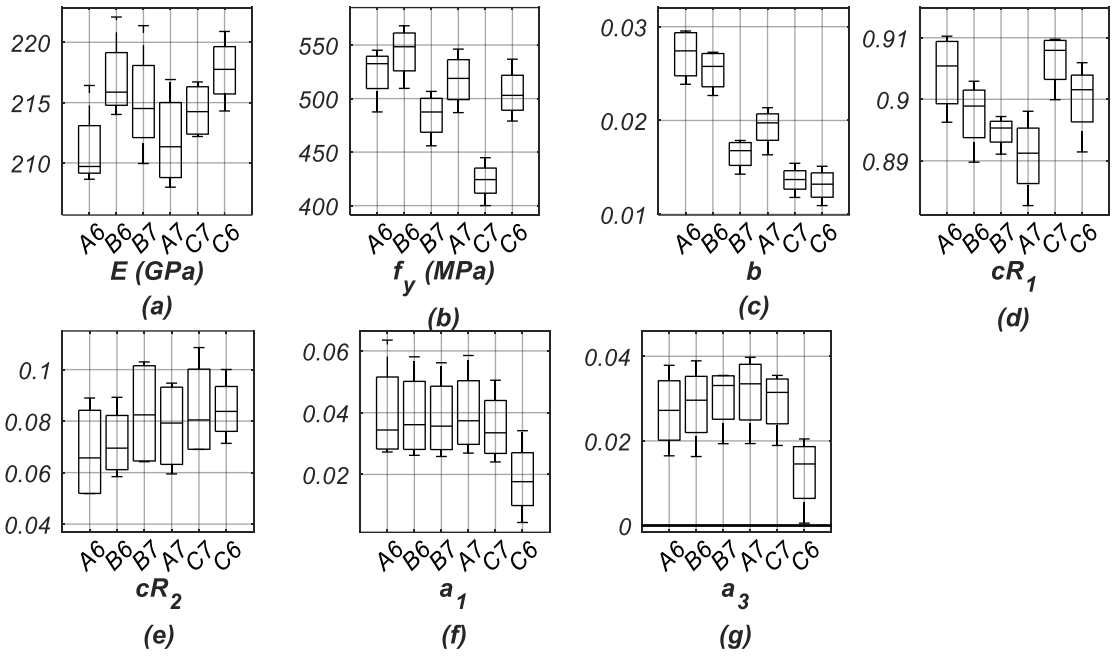

Figure 3.15. Box Plot of Calibrated Parameters: (a) E; (b) f_y; (c) b; (d) cR_1; (e) cR_2; (f) a_1; (g) a_3

In Figure 3.15, the central line in each box represents the median of the calibrated property, the bottom and top edges of the box are the 25th and 75th percentiles, and the whiskers extend to the maximum and minimum values obtained. Since the results are based on only four data points per steel category, the statistical significance of these results is only limited.

Several observations can be made from the results in Table 3.9 and Figure 3.15 for each calibrated parameter. For example, the Young's modulus, E, shows, as expected, very small variability within each steel category, with an average c.o.v. of only 1.4%. Furthermore, the average value of E is almost identical in between categories, with of only a 3% difference between the most extreme categories (A6 and C6, see Table 3.9). It is important to remark the limitations of the statistical results obtained within steel categories

for each material parameter (e.g. E, f_y, b, cR_1), given the small number of specimens tested per category.

In the case of f_y, there is also a very small variability within each category, with an average c.o.v. of 4%. However, in between categories the yield stress can differ significantly, despite all coupons being specified by their manufacturers as Grade 60, by as much as 29% between the average of categories B6 and C7. It is also observed that the calibrated values of f_y in Table 3.9 differ from the values initially identified from the yield plateau in the hysteretic responses, see Table 3.6. The average difference is however small, with the ratio of calibrated over identified yield stress, $f_y^{calibrated} / f_y^{identified}$, between 0.97 and 1.07.

The post-yield slope ratio, b, displays a larger variability within each category, with an average c.o.v. of 9.3%. Despite the variance of the results within categories, the difference between steel types is still clear, with average values ranging from 0.013 to 0.027. Noting that steel categories in Figure 3.15 are sorted by carbon content, C (%), a correlation between b and C (%) and, to a lesser extent, between cR_1 and C (%) can be observed.

Of all calibrated model parameters, cR_1, which controls the shape of the Bauschinger curve, is the most stable within each steel category, as observed from the average c.o.v. at 0.5%. Furthermore, the values obtained for cR_1 range in a narrow window between 0.88 and 0.91. The small variability of cR_1 is justified by the high sensitivity of the hysteretic response of the material model to this parameter, as seen in the Sensitivity

Analysis section. As mentioned in the Preliminary Analysis, cR_1 is highly correlated to the parameter R_0, assumed constant and equal to 20 during the calibration.

The second parameter controlling the shape of the Bauschinger curve, cR_2, has significant dispersion within each material category, with an average c.o.v. of 19%. The large dispersion of the values identified suggests the use of a constant cR_2 for all steel types.

Finally, parameters accounting for isotropic hardening show the largest variability within steel categories, with an average c.o.v. of 36% and 31% for a_1 and a_3 respectively. Except for category C6, the mean values per category remain stable around overall averages of $\bar{a}_1$=0.038 and $\bar{a}_3$=0.029. Additionally, most coupons showed larger isotropic hardening in compression than tension ($a_1 > a_3$, with an average a_1/a_3 = 1.6), which compensates for the increased cross-section area of the coupon in compression, not accounted for by engineering stresses (Dodd and Restrepo, 1995). In the calibration analysis, only when the strain history was skewed towards negative values, see SH3 in Figure 3.3, a_3 became larger than a_1, however, this type of strain history is uncommon in reinforcing bars, which are usually intended to undergo large tensile deformations.

3.6.4. Sensitivity Analysis

The sensitivity of the material model to parameter variations is assessed via the relative increment in the error, as defined in Equation 3.14, resulting from a relative variation in each material parameter independently. Figure 3.16 shows, for example, the effect of a 10% increment/reduction of each material property on the predicted stress-strain response for a simple strain history.

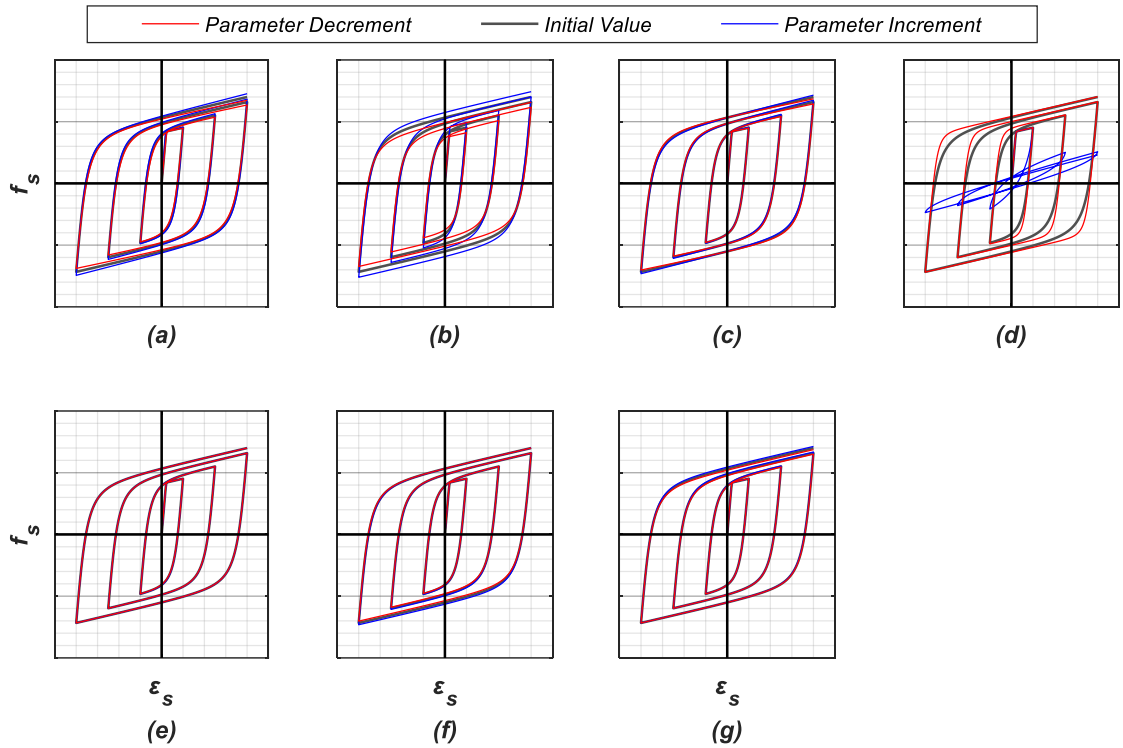

Figure 3.16. Effect of 10% Variation in Each Material Property on the Predicted Stress-Strain Response: (a) E; (b) f_y; (c) b; (d) cR_1; (e) cR_2; (f) a_1; (g) a_3

As Figure 3.16d shows, the hysteretic response is most sensitive to parameter cR_1, whereas parameter cR_2 has the least noticeable effect, see Figure 3.16e.

For each stress-strain record, the material model parameters were perturbed independently by up to 25% above and below their optimal values. The error was then normalized by the minimum error from the optimization of the corresponding record, given by:

$$e_{norm} = \frac{error\left(\mathbf{x}_{\mathbf{opt}} + \Delta\mathbf{x}_{\mathbf{opt}}\right)}{error\left(\mathbf{x}_{\mathbf{opt}}\right)} \qquad 3.15$$

Where e_{norm} is the normalized error, $\mathbf{x_{opt}}$ is a vector with the calibrated parameters of the material model, and $\mathbf{\Delta x_{opt}}$ is a vector with a perturbation of the parameters. Figure 3.17 and Figure 3.18 show for each calibrated parameter the average of the sensitivity analysis of all stress-strain records processed.

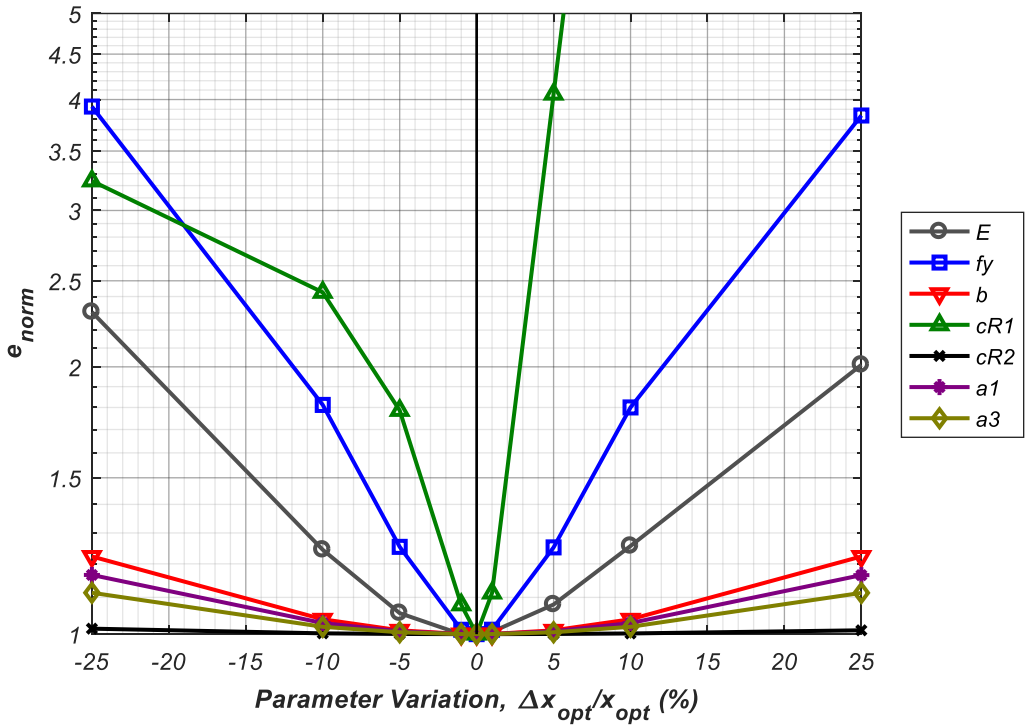

Figure 3.17. Average Sensitivity Analysis Results Between Stress-Strain Records. Normalized Error vs Relative Variation of Calibrated Parameters

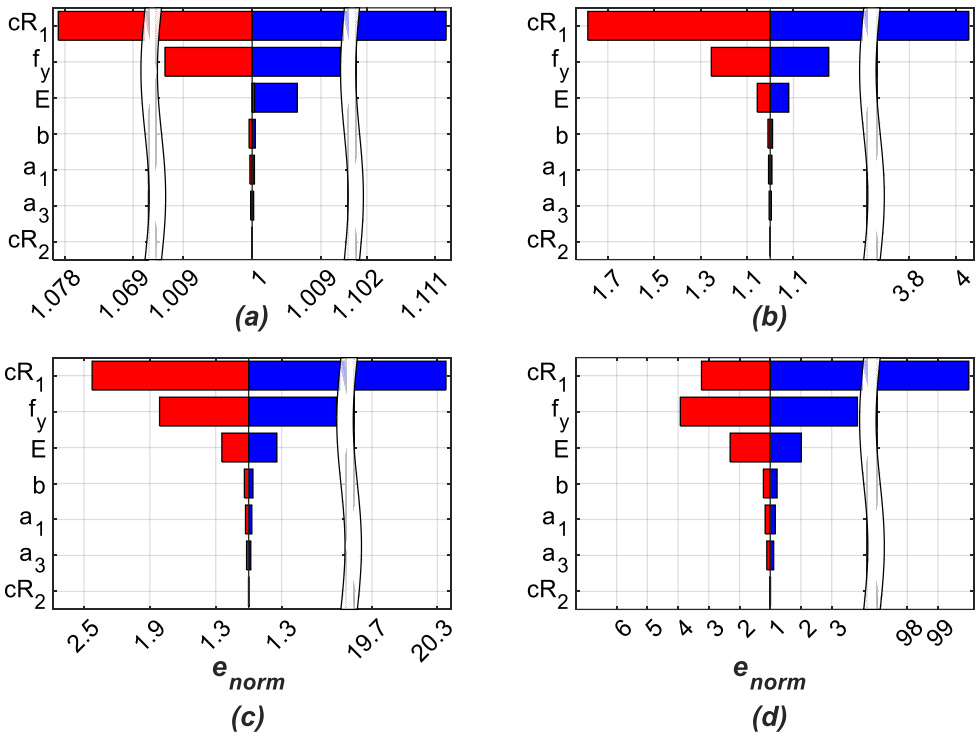

Figure 3.18. Average Sensitivity Analysis Results Between Stress-Strain Records. Tornado Diagram of Normalized Error vs Relative Variation of Calibrated Parameters: (a) 1.0 % Variation; (b) 5.0% Variation; (c) 10% Variation; (d) 25% Variation

As observed in the sensitivity analysis results, equivalent variations of the model parameters can have widely different effects on the predicted stress-strain response. For example, changes in cR_2 of as much as 25% only produce a 1% increment in the normalized error, e_{norm}, while equivalent variations in parameter cR_1 can raise the error more than a hundredfold, see Figure 3.18d.

Based on the sensitivity analysis, model parameters can be classified into two main groups: low-sensitivity variables, which include cR_2, the post-yield slope ratio, b, and strain hardening parameters a_1 and a_3; and high-sensitivity variables, including the Young's modulus, E, yield stress, f_y, and cR_1.

As observed in Figure 3.17 and Figure 3.18, in most model parameters the effect of perturbations around the calibrated values is symmetric, with similar increments in the normalized error, e_{norm}, whether the variable is increased or reduced. In the case of cR_1 however, sensitivity analysis shows much larger error increments when cR_1 is overestimated. This behavior originates in the formulation of the material model, which imposes an upper limit for cR_1 around 1 for the curvature of the Bauschinger curve to be well-defined, as specified by the condition $R(\xi)>0$ in Equation 3.8.

Among variables causing the largest effects, E and cR_1 show very small difference in between the analyzed steel categories, as discussed in the Calibration Results section. This condition greatly simplifies defining an estimate for these variables. Only the yield stress, f_y, combines high sensitivity over the stress-strain response with high variability between steel categories. Because of this, a proper estimation of f_y is essential for a good prediction of the hysteretic response using this constitutive stress-strain relationship.

3.6.5. Proposed Model Parameters

This section describes the statistical analysis for the determination of an all-purpose set of calibrated model properties, to accurately predict the hysteretic response of reinforcing steel bars.

The Young's Modulus, E, found to have a small variability both within and in-between steel categories, see Table 3.9, did not show any correlation to other material properties. Furthermore, an ANOVA analysis (Montgomery and Runger, 2010) showed no difference between the mean values of E for the two ASTM specifications considered in

this study (A615 and A706). Based on these results, the use of a constant value of E would be sufficient to attain a good fit of the hysteretic response of ASTM A615 and A706 bars. The average Young's modulus for all machined coupons, at E = 215 GPa, represents the actual modulus of the material, given a well-known cross-section area, see Figure 3.19. However, since the common practice is to use nominal cross-section areas to model reinforcement, a correction factor α_c = 0.94, the average ratio of E from the tensile tests of machined and unmachined coupons, see Figure 3.5, is applied to E, resulting in a proposed value for the parameter E = 202 GPa (29,300 ksi).

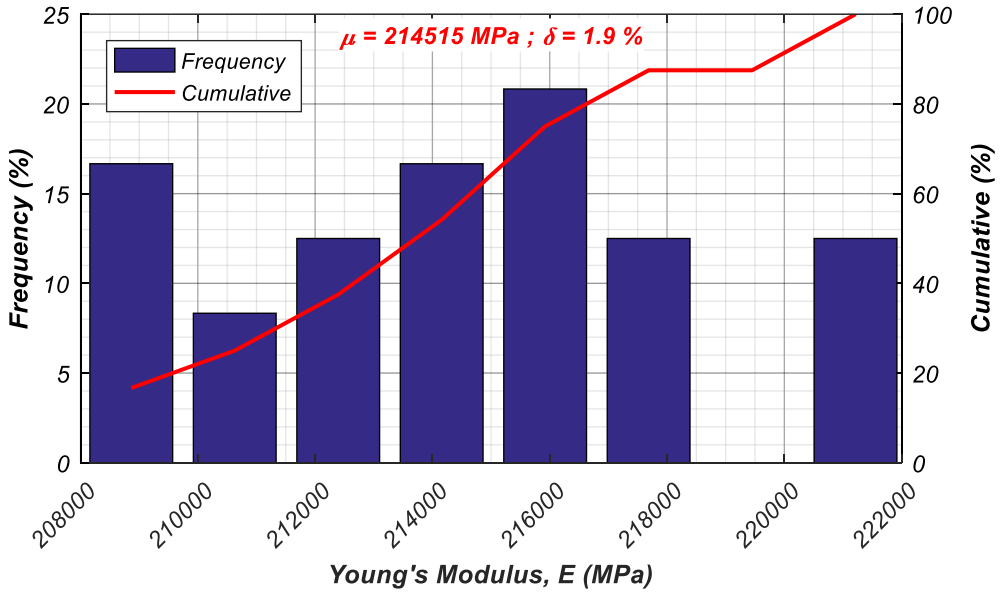

Figure 3.19. Histogram of Calibrated Values for the Young's Modulus, *E*, in Machined Coupons

Similar to the Young's Modulus, the parameters controlling the shape of the Bauschinger curve, cR_1 and cR_2, showed a limited correlation to other material properties. Furthermore, an ANOVA analysis of both parameters showed no difference in between the results for ASTM A615 and A706 coupons. Given these conditions, a constant value cR_1=

0.9 and cR_2=0.08, corresponding to the average for all tested coupons, is proposed, see Figure 3.20.

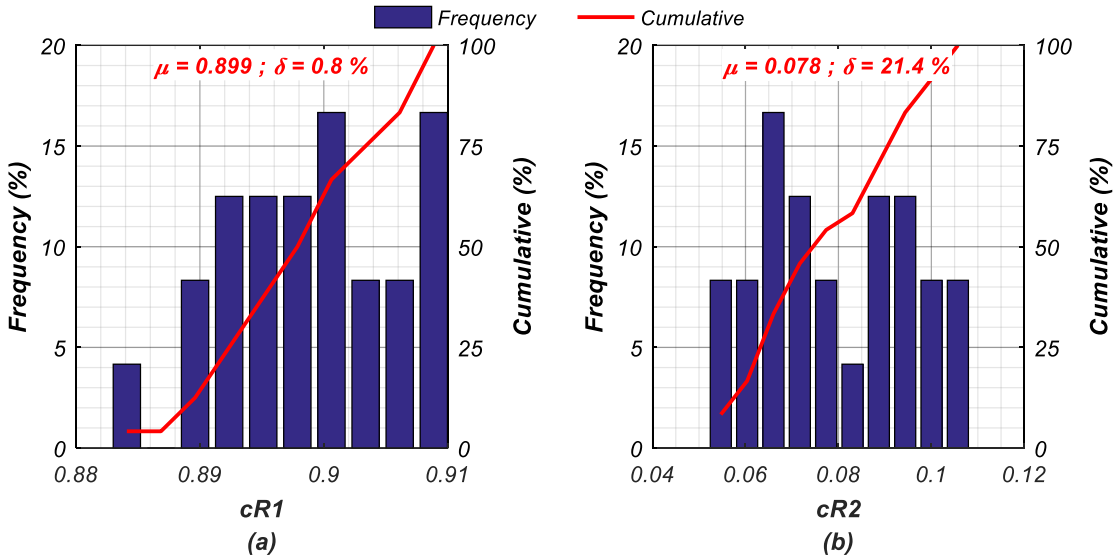

Figure 3.20. Histogram of Calibrated Values for Bauschinger Curve Parameters: (a) cR_1; (b) cR_2

The isotropic hardening parameters, a_1 and a_3, are the last set of model properties for which the use of a constant value is proposed, a_1= 0.039 and a_3= 0.029, given their limited correlation to mechanical properties of the material. Additionally, a negligible difference is found between the results from the two ASTM standards considered, as per an ANOVA analysis. As noted in the Calibration Results section, for a strain history biased towards negative values (see SH3 in Figure 3.3), the isotropic hardening factor for tension, a_3, becomes larger than the one for compression, a_1. For this case, although uncommon in reinforced concrete elements, the recommended values for a_1 and a_3 can be interchanged

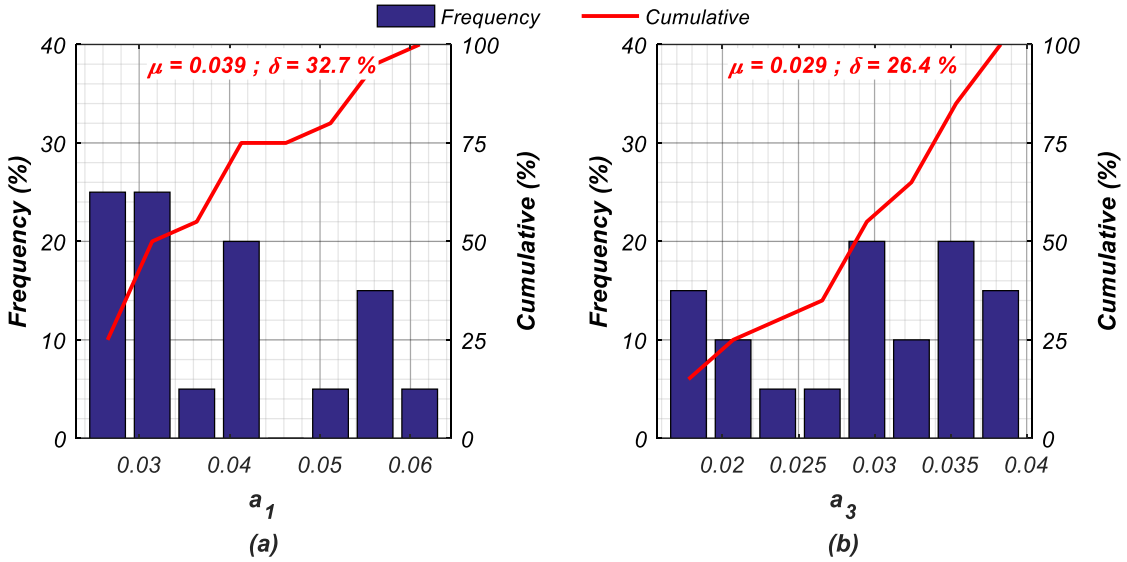

Figure 3.21. Histogram of Calibrated Isotropic Hardening Factors: (a) a_1; (b) a_3.

The post-yield slope ratio, b, was the only parameter showing a clear correlation to the chemical composition of the material and, as expected from the definition of the parameter, with the measured tensile strength, f_u.

Based on Figure 3.22, when the tensile strength of the material, f_u, is known, the post-yield slope ratio, b, can be best estimated using Equation 3.16.

$$b = 7.5 \cdot 10^{-5} \cdot f_u \text{ (MPa)} - 0.037 > 0 \qquad 3.16$$

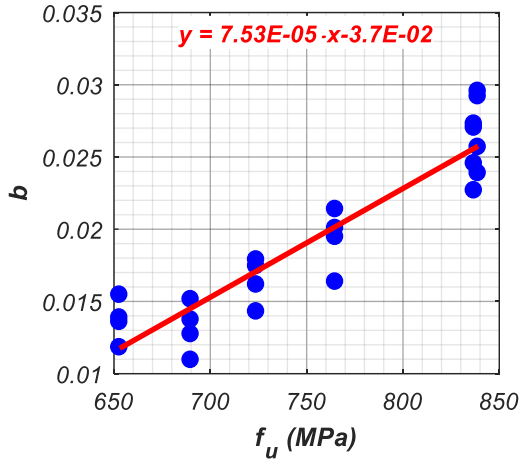

Figure 3.22. Correlation Analysis of Post-Yield Slope Ratio in Machined Coupons

In practice, however, the value of f_u is likely unknown (for suggested values of f_u, see Table 3.11). For these cases, a constant value of b, dependent on the ASTM standard is proposed: b = 0.016 for ASTM A706 and b = 0.025 for ASTM A615 machined coupons. As with the Young's modulus, E, a correction factor is required for b to account for the difference between machined and unmachined coupons. In the case of b, this difference is not related to the cross-section area of the coupons, but to the change in ductility, measured through ε_u, and variation in the yield to tensile strength ratio, f_u/f_y. Using the ratio between the post-yield secant modulus, as defined in Equation 3.17, from the tensile tests of unmachined and machined coupons, results in a correction factor α_c= 0.78 for both ASTM A706 and A615 coupons, see Table 3.10, resulting in values of b of 0.012 and 0.02, respectively.

$$E^*_{\text{sec}} = \frac{0.9 \cdot f_u - f_y}{\varepsilon^* - \varepsilon_y} \qquad 3.17$$

Where E^*_{sec} is the secant stiffness of the tensile response of the material between the onset of yield (ε_y, f_y) and the stress-strain point where 90% of the tensile strength is reached (ε^*,$0.9 \cdot f_u$).

Table 3.10. Secant Post-Yield Modulus from Tensile Tests of Machined and Unmachined Coupons

Category	Unmachined			Machined			E^*_{sec} ratio Unmachined/Machined
	ε^* (%)	$0.9 \cdot f_u$ (MPa)	E^*_{sec} (MPa)	ε^* (%)	$0.9 \cdot f_u$ (MPa)	E^*_{sec} (MPa)	
A6	3.7	648	5879	3.9	756	8670	0.68
B6	3.8	653	4697	3.9	756	5992	0.78
B7	4.1	564	3291	4.3	651	4132	0.80
A7	3.7	594	4476	4.1	689	5536	0.81
C7	4.1	519	2748	5.2	588	3174	0.87
C6	3.1	574	1775	4.4	622	2405	0.74

As mentioned in the Sensitivity Analysis section, the yield strength of the material, f_y, not only has a significant effect on the predicted hysteretic response of the model but can also differ considerably between manufacturers. Furthermore, regression analyses of f_y did not show a correlation to other mechanical properties of the material. Because of this, a statistically significant sample size of reinforcing bars yield strengths is required for an accurate estimate of the parameter. Due to the limited experimental information collected in this study, the author consulted a comprehensive survey of mechanical properties of reinforcing bars performed at the University of Kansas (Bournonville et al. 2004). Based on this survey, the recommended average yield strength for ASTM A615 Gr 60 bars is f_y = 480 MPa, while the corresponding value for A706 Gr 60 specimens is 476 MPa. Table 3.11 includes additional statistical information extracted from this study for reference.

Table 3.11. Yield and Tensile Strength Distribution Results (Bournonville et al. 2004)

	A615 Gr 60		A706 Gr60	
	f_y (MPa)	f_u (MPa)	f_y (MPa)	f_u (MPa)
Average	480	728	477	656
c.o.v.	7.2%	6.3%	5.3%	5.2%
Percentiles				
5	437	663	437	598
10	444	680	444	613
25	457	699	458	635
median	473	724	475	657
75	495	749	493	679
90	526	776	510	701
95	550	798	522	713

Based on the proposed values for the material model parameters summarized in Table 3.12, along with typical parameter values used in the literature, the error between measured and predicted stress-strain response of the coupons used in the calibration analysis is computed. The histogram in Figure 3.23 shows the error distribution using the proposed model parameters (without the correction factors included in E and b for unmachined bars).

Table 3.12. Proposed Material Model Parameters (Unmachined Reinforcing Bars)

Parameter	Proposed value	Typical values used (Filippou et al. 1983, Menegotto and Pinto, 1973)
E	202 GPa (29,300 ksi)	205 GPa
f_y	480 MPa (69.6 ksi) (A615 steel) 476 MPa (69.0 ksi) (A706 steel)	420 MPa*
b	0.02 (A615 steel) 0.012 (A706 steel)	0.02
R_0	20	20
cR_1	0.9	0.925
cR_2	0.08	0.15
a_1	0.039	0.01†
a_2	1.0	7‡
a_3	0.029	-
a_4	1.0	-

As seen in Figure 3.23, the fit error with the proposed model properties is, on average, twice the minimum error obtained from the calibration of the individual records. Despite the error increment, the calibrated material model properties still result in a reasonable match of the hysteretic response. Figure 3.24 compares the measured and predicted response with the proposed parameter values (without correction factors in E and b for unmachined bars) for steel category C7 which, along with category C6, resulted in the largest error magnitude.

* Nominal yield strength for Grade 60 steel. This value is usually replaced by expected yield strength values or tensile test results

† Value of isotropic hardening parameter $\hat{a}_1$ from the original formulation by Filippou et al. (1983), see Equation 3.12

‡ Value of isotropic hardening parameter $\hat{a}_2$ from the original formulation by Filippou et al. (1983), see Equation 3.12

The relatively large error in the stress-strain fit of category C7, compared to other categories under study, is justified by the difference between the proposed yield strength, f_y=476 MPa, and the optimal value for the category, f_y=423 MPa. Figure 3.25 shows the stress-strain response comparison after changing the proposed yield strength to f_y = 420 MPa. The change in the yield strength alone reduced the average stress-strain error using the proposed material model properties from 14% to 6.8%.

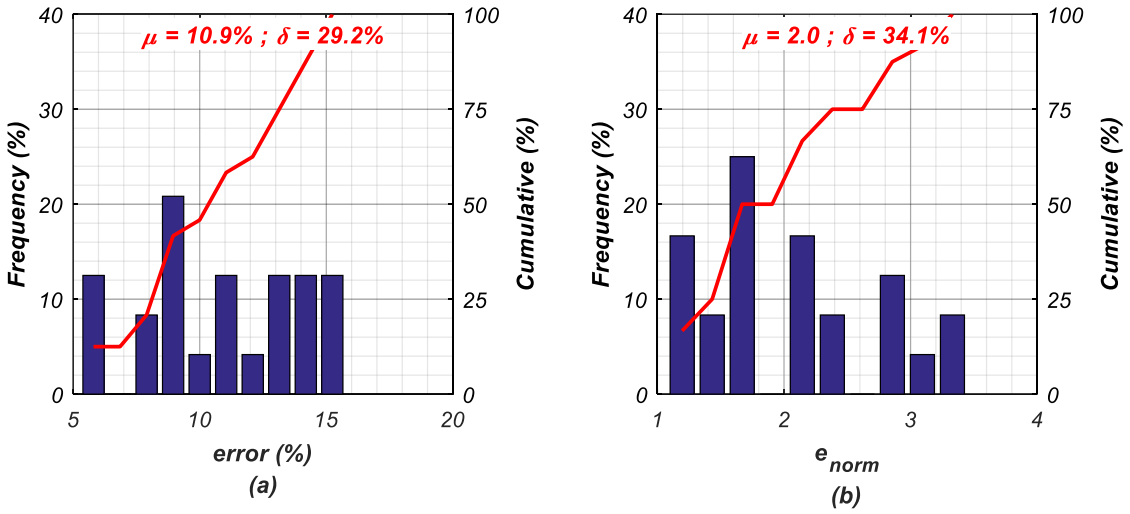

Figure 3.23. Histogram of Error Between Measured Stress-Strain Response and Material Model with Proposed Material Model Properties: (a) Fit Error; (b) Fit Error Normalized by Optimal Error

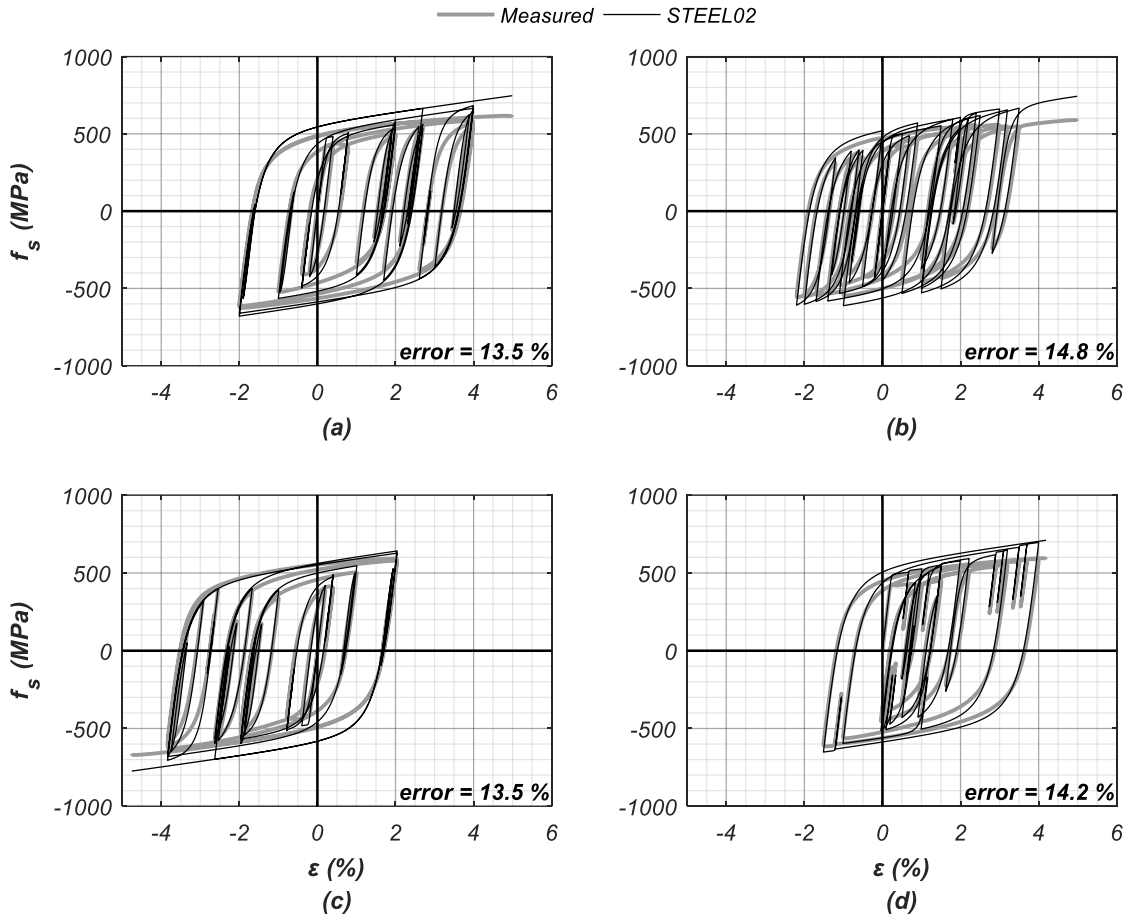

Figure 3.24. Measured vs Predicted Stress-Strain Response Using Proposed Material Model Parameters: (a) C74; (b) C75; (c) C76; (d) C77

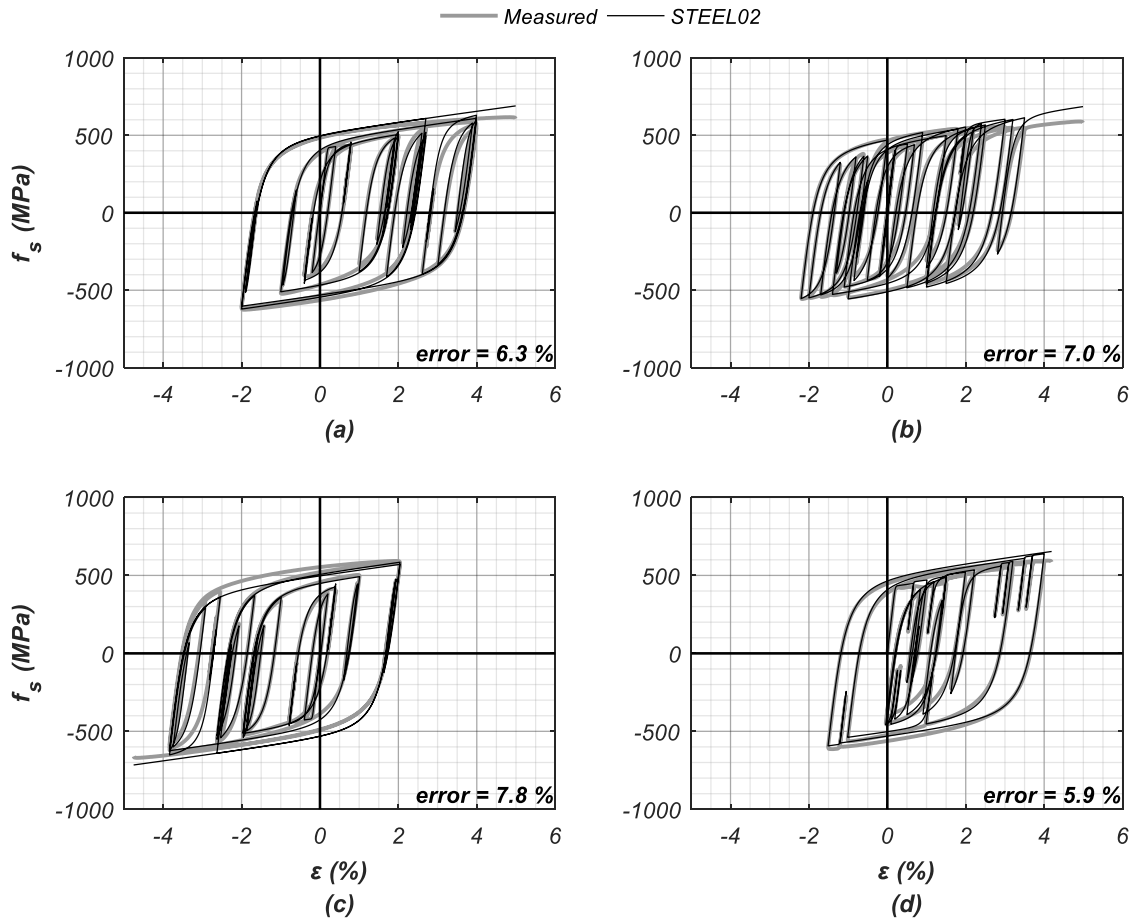

Figure 3.25. Measured vs Predicted Stress-Strain Response Using Proposed Material Model Parameters and Optimal Yield Strength for the Category: (a) C74; (b) C75; (c) C76; (d) C77

3.6.6. Verification of Results

The verification of the proposed parameters for the constitutive stress-strain relationship, see Table 3.12, is performed using experimental results collected from cyclic tests on #4 ASTM A706 unmachined coupons. The coupons in these tests belong to a different batch of reinforcement than the coupons used for calibration.

For this separate study, a series of #4 bars were tested under cyclic load at the Charles Lee Powell Laboratories at the University of California in San Diego, to evaluate

the effect of buckling in coupons with different length to diameter ratio. Two of the coupons were tested at an unbraced length of $3d_{b\ell}$, for which the effect of non-linear geometry is still small. Figure 3.26 compares the measured and predicted stress-strain responses for these two coupons. The fit error using the proposed model properties remain small, at 10.5% and 8.8% for coupons 1 and 2 respectively. For both coupons, a noticeable difference in the peak stress in tension is observed, with the predicted response exceeding the measured value by up to 16%. This difference, as well as the magnitude of the fit errors, is justified by the smaller than average yield strength of the coupons, measured at f_y = 440 MPa from tensile tests.

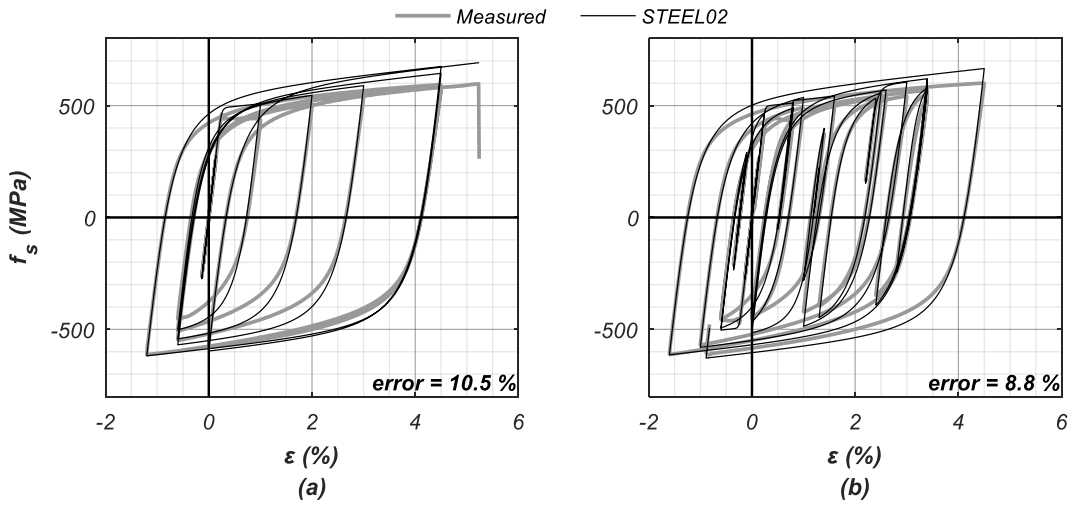

Figure 3.26. Measured vs Predicted Stress-Strain Response Using Proposed Material Model Properties for two ASTM A706 Coupons Not Used in Calibration: (a) Coupon 1; (b) Coupon 2

3.7. Conclusions

A study to calibrate the Giuffre-Menegotto-Pinto (GMP) steel model to the hysteretic response of reinforcing bars manufactured in accordance to ASTM A615 (2016) and A706 (2016) standards is performed. A batch of thirty-six #4 Grade 60 bars, from three different manufacturers and complying with one of two ASTM specifications (A615 or A706) were tested under different cyclic strain histories. The selection of specimens allows a limited study on the variability of the stress-strain response and calibrated material parameters for the Grade, bar size and ASTM standards tested. It is noted that the results presented herein, including the calibrated parameters for the constitutive stress-strain relationship, are based on the cyclic response of machined coupons. Such coupons were used because they practically remove geometrical non-linearities, leaving only material non-linearities in the hysteretic response. Three additional coupons, two unmachined and one machined, per steel category were tested under monotonic tension until failure.

In each of the six steel categories studied, four coupons were tested under "low" strain rate, $\dot{\varepsilon}$=0.001/sec, while the remaining two were tested under "high" strain rate, $\dot{\varepsilon}$=0.02/sec. Comparative analysis between coupons tested under equivalent strain histories at different strain rates showed no significant difference in the hysteretic response, with the exception of the observed yield strength at the yield plateau, which increased up to 12% at the higher strain rate.

A detailed formulation of the material model is presented herein. Using the definition of the parameters, it was reasoned that the number of model properties to

calibrate can be reduced from 10 to 7 without losing accuracy in the model, by fixing parameters R_0, a_2 and a_4.

Preliminary calibration results showed some limitations of the material model, such as symmetric stress-strain response in engineering coordinates, unlike the actual material, with symmetric behavior only in natural coordinates.

A sensitivity analysis evaluated the increase in the error with perturbations of the calibrated model properties. Material model parameters were divided into two groups: low-sensitivity variables, including cR_2, b, a_1 and a_3; and high-sensitivity variables, including E, f_y and cR_1. Among the high-sensitivity variables, only f_y showed significant variability between steel categories, with the rest remaining almost constant.

For parameters E, cR_1, cR_2, a_1 and a_3, a unique value was proposed regardless of the ASTM standard of the reinforcement. For the post-yield slope ratio, b, a correlation to the tensile strength, f_u, was found, but given the limited material information available in practice, a value of b was proposed for each ASTM standard. Given the different response observed between machined and unmachined coupons in tensile tests, a correction factor for model parameters E and b, calibrated from machined bars, was suggested to model unmachined bars used in practice. For the yield strength, f_y, an average value was proposed for each ASTM standard. However, given the significant variability of f_y, combined with high sensitivity of the predicted hysteretic response, it is recommended to perform a sensitivity analysis of this variable when using the GMP steel model. For this purpose, some useful statistical results were extracted from a comprehensive survey of mechanical properties of reinforcing bars made at the University of Kansas, (Bournonville et al. 2004).

The proposed model parameters were verified using test data from a separate study, whose results were not used in the calibration analysis. The predicted response using the proposed material model properties, at an error below 11%, matched satisfactorily the measured stress-strain response.

Chapter 3, in full, has been submitted for publication of the material as it may appear in *Material Model Parameters for the Giuffrè-Menegotto-Pinto Uniaxial Steel Stress-Strain Model*, ASCE Journal of Structural Engineering, 2018. Carreño, Rodrigo; Lotfizadeh, Koorosh; Conte, Joel P.; and Restrepo, José I. The dissertation author was the primary investigator and author of this paper.

Chapter 4.

IMPROVED IMPLEMENTATION OF THE CONSTITUTIVE STRESS-STRAIN RELATIONSHIP BY DODD AND RESTREPO FOR REINFORCING STEEL

4.1. Abstract

The uniaxial constitutive stress-strain relationship developed by Dodd and Restrepo at the University of Canterbury, New Zealand, is widely used to represent the hysteretic response of reinforcing steel bars. The model has many advantages over other constitutive models. Among them, it is defined by recognizable mechanical properties of the material, represents all branches of the monotonic response, accounts for the Poisson effect, and considers the reduction in uniform strain capacity during cyclic loading. The model, however, also presents some disadvantages due to the relative complexity of the formulation and unreliable implementations available to use. In this paper, a new implementation of the model is incorporated into OpenSees, with some additions and corrections to increase the reliability and robustness of the model, making it suitable for the analysis of large scale structures. A calibration analysis of the parameters of the model is also presented, and verified, to further facilitate its future use.

4.2. Introduction

The Dodd-Restrepo model (Dodd and Restrepo, 1995), is a popular constitutive stress-strain relationship for the hysteretic response of reinforcing steel. The model has multiple advantages over other popular material formulations, such as the Giuffrè-Menegotto-Pinto model (Menegotto and Pinto, 1973). Among these advantages is the ability to represent the different branches of the monotonic response (Mander, 1983), the use of natural coordinates (Nadai, 1950) to account for the Poisson effect, the easily identifiable material properties used as model parameters, and accounting for the reduction in the magnitude of the elastic modulus and uniform strain capacity, ε_u, due to plastic deformations.

One disadvantage of the constitutive stress-strain relationship preventing its widespread use in the research and engineering practice community is its relative complexity, with computational implementations of the model being scarce. The lack of a closed form solution for the Bauschinger effect, and the use of an iterative process instead, is somehow inefficient and subject to convergence issues. The model is also not defined past the uniform strain, ε_u, with an abrupt loss of capacity beyond this point, which causes additional convergence problems in the model. The constitutive stress-strain relationship also returns tangent stiffness values close to zero at large strains and the yield Plateau which, although consistent with the actual behavior of the material, can cause convergence issues in structural models, particularly those using flexibility-based members (e.g. force-based beam-column elements).

Other authors have added improvements to the model by incorporating phenomena like buckling and low-cycle fatigue (Kim and Koutromanos, 2016). However, working implementations of these models are not readily available in commonly used structural analysis software (e.g. OpenSees), therefore the stability and accuracy of such implementations has yet to be assessed.

This paper introduces a new formulation of the material model that includes a closed form expression for the Bauschinger effect, a post-necking response, and several improvements on the stability of the algorithm, which has been tested on several large-scale structural models.

A calibration analysis is performed over the stress-strain response of ASTM A615 and A706 Grade 60 reinforcing steel coupons, sourced from different U.S. manufacturers, introducing a set of recommended model parameters.

4.3. Original model formulation

This section presents a summary of the original model formulation (Dodd and Restrepo, 1995). One of the main features of the Dodd-Restrepo model is the internal use of natural strains (Nadai, 1950), ε'_s, and true stresses, f'_s, thus incorporating the Poisson effect. Experimental results show a symmetric stress-strain behavior of reinforcing steel under ε'_s-f'_s coordinates, unlike in engineering strain, ε_s, and stress, f_s, see Figure 4.1. Definitions of uniaxial strain and uniaxial stress for an element in each coordinate system can be found in Equation 4.1.

$$\varepsilon_s = \frac{\ell - \ell_0}{\ell_0} \quad \text{(a)} \qquad \varepsilon'_s = \int_{\ell_0}^{\ell} \frac{d\ell}{\ell} = \ln\left(\frac{\ell}{\ell_0}\right) \quad \text{(b)}$$

$$f_s = \frac{N}{A_0} \quad \text{(c)} \qquad f'_s = \frac{N}{A} \quad \text{(d)} \qquad 4.1$$

Where ℓ_0 and ℓ are the initial and instantaneous length of the uniaxial element, A_0 and A are the initial and instantaneous cross-section area, and N is the axial force applied.

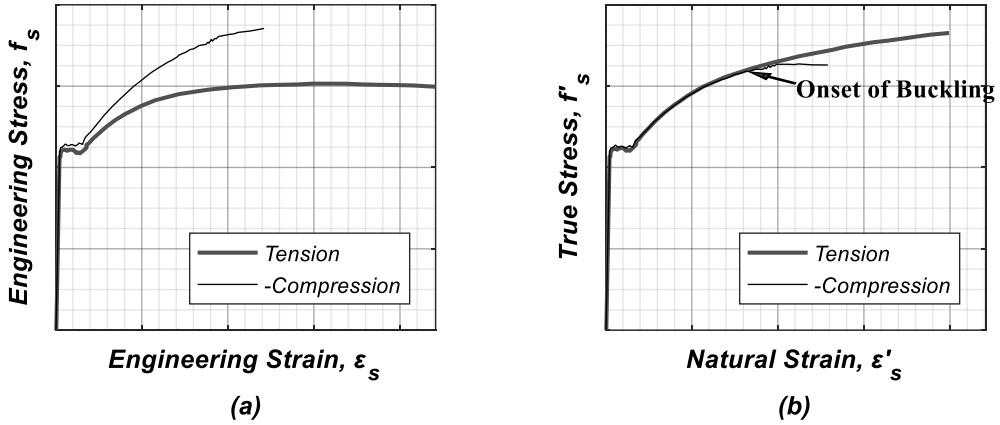

Figure 4.1. Sample Backbone Curve of Reinforcing Steel in Tension and Compression: (a) Engineering Strain vs Engineering Stress; (b) Natural Strain vs True Stress (Dodd and Restrepo, 1995)

Transformations of strain, stress, and tangent modulus between coordinate systems are based on parameter definitions, see Equation 4.1, and the assumption of incompressible material ($A \cdot \ell = A_0 \cdot \ell_0$), which is reasonable under plastic deformations:

$$\varepsilon_s = e^{\varepsilon'_s} - 1 \quad \text{(a)} \qquad f_s = \frac{f'_s}{e^{\varepsilon'_s}} \quad \text{(b)} \qquad E_t = \frac{df_s}{d\varepsilon_s} = \left(\frac{df'_s}{d\varepsilon'_s} - f'_s\right) \cdot e^{-2\cdot\varepsilon'_s} \quad \text{(c)}$$

$$\varepsilon'_s = \ln(1+\varepsilon_s) \quad \text{(d)} \qquad f'_s = f_s \cdot (1+\varepsilon_s) \quad \text{(e)} \qquad E'_t = \frac{df'_s}{d\varepsilon'_s} = \left(\frac{df_s}{d\varepsilon_s} + \frac{f_s}{1+\varepsilon_s}\right) \cdot (1+\varepsilon_s)^2 \quad \text{(f)} \qquad 4.2$$

The original formulation by Dodd and Restrepo (1995) was defined by eight parameters: E_0, f_y, ε_{sh}, ε_u, f_u, $\varepsilon_{sh,1}$, $f_{sh,1}$, and Ω_{fac}, see notation section for the full description. Most of the model parameters can be extracted from the backbone curve of the material, as seen in Figure 4.2. Only Ω_{fac}, which controls the hysteretic energy under the curve, requires additional information, and has been associated to the Carbon content of the material (Dodd and Restrepo, 1995).

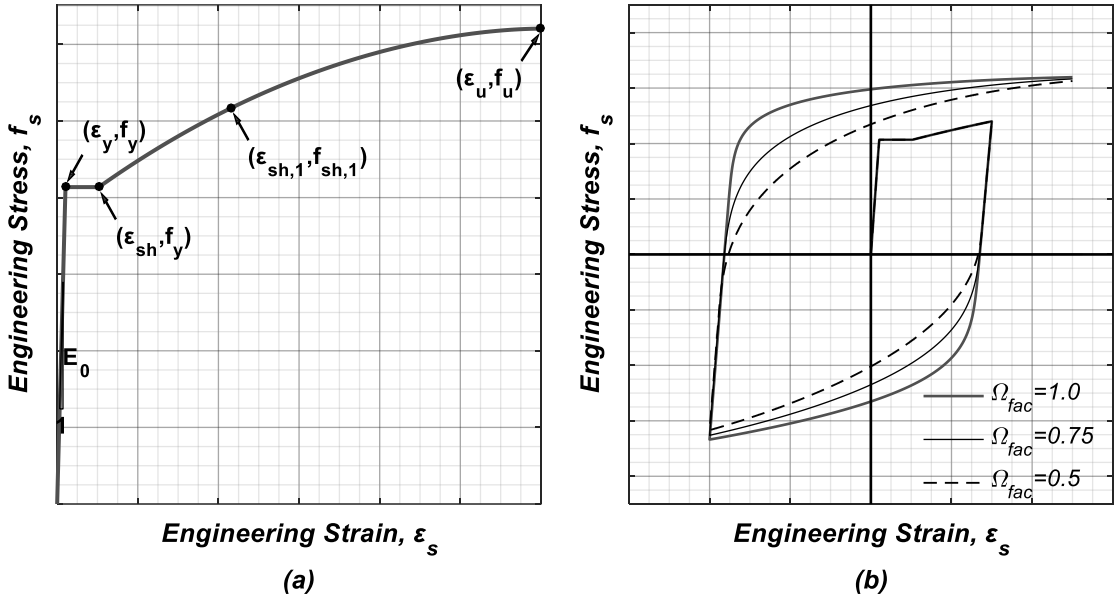

Figure 4.2. Parameters of the Material Model: (a) Parameters Extracted from Backbone Curve; (b) Shape of the Bauschinger Effect

4.3.1. Backbone Curve of the Model

In mild steel, the backbone curve can be divided into four regions: (1) Linear-Elastic branch; (2) Yield Plateau; (3) Post-Hardening region; and (4) Post-Ultimate stress zone, see Figure 4.3. Based on the formulation by Mander (1983), the Dodd-Restrepo model considers only the three initial regions of the backbone curve, see Equation 4.3, as the Post-Ultimate stress zone does not have a well-defined strain measure: beyond the

uniform strain, ε'_u, elongations concentrate in a small portion of the bar, a phenomenon known as necking, making the strain measure dependent on the gage length, see Figure 4.3.

$$f'_s = \begin{cases} E_0 \cdot \varepsilon'_s & \text{if } -\varepsilon'_y \le \varepsilon'_s \le \varepsilon'_y \\ s \cdot f_y \cdot e^{s \cdot \varepsilon'_s} & \text{else if } s \cdot \varepsilon'_y \le s \cdot \varepsilon'_s \le s \cdot \varepsilon'_{sh} \\ s \cdot c_1 \cdot \left[\dfrac{\varepsilon'_u - s \cdot \varepsilon'_s}{\varepsilon'_u - \varepsilon'_{sh}} \right]^P - s \cdot f'_u \cdot (\varepsilon'_u - s \cdot \varepsilon'_s) + s \cdot f'_u & \text{else if } s \cdot \varepsilon'_{sh} \le s \cdot \varepsilon'_s \le s \cdot \varepsilon'_u \\ 0 & \text{otherwise} \end{cases} \quad 4.3$$

Where s corresponds to the sign of strain ε'_s, c_1 is defined in Equation 4.4, and the exponent $P > 1$ is generated to intersect with $(\varepsilon'_{sh,1}, f'_{sh,1})$ in the strain hardening branch, resulting in Equation 4.5.

$$c_1 = f_y \cdot e^{\varepsilon'_{sh}} + f'_u \cdot (\varepsilon'_u - \varepsilon'_{sh}) - f'_u \quad 4.4$$

$$P = \frac{\ln\left(\dfrac{f'_{sh,1} + f'_u \cdot (\varepsilon'_u - \varepsilon'_{sh,1}) - f'_u}{c_1} \right)}{\ln\left(\dfrac{\varepsilon'_u - \varepsilon'_{sh,1}}{\varepsilon'_u - \varepsilon'_{sh}} \right)} \quad 4.5$$

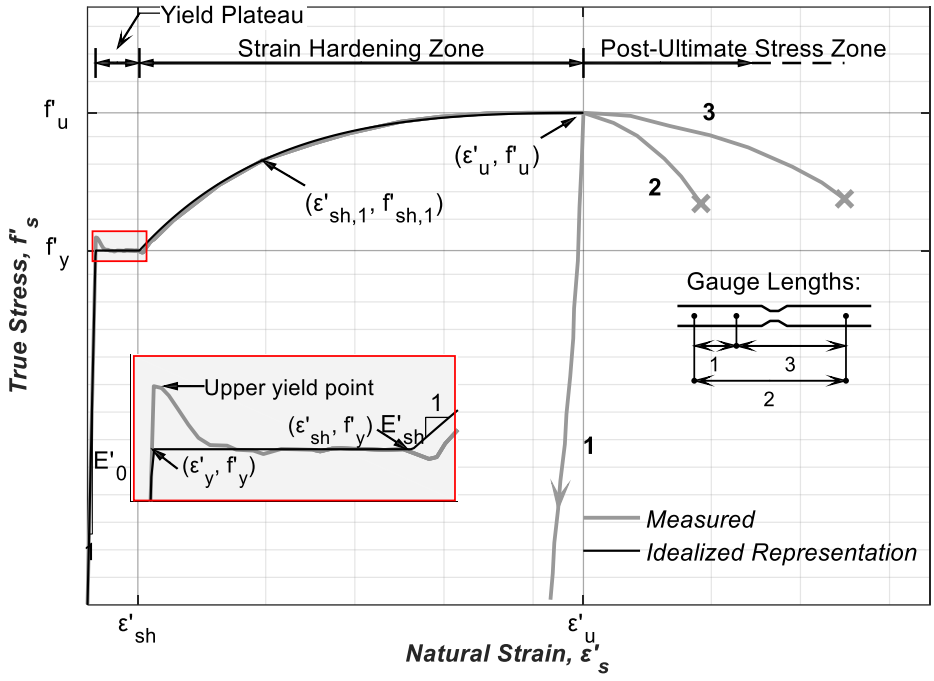

Figure 4.3. Backbone Curve of the Dodd-Restrepo Model

4.3.2. Response Following First Strain Reversal

Once the material undergoes plastic deformations in the backbone curve, the post-reversal response of the model is divided into three branches: **(i)** a linear unloading branch; **(ii)** a Bauschinger curve, transitioning from the end of branch (i) to the boundary conditions defined by a previous reversal; and **(iii)** The shifted backbone (see iii-a in Equation 4.6), or a Bauschinger curve converging to the shifted uniform strain (see iii-b in Equation 4.6).

$$f'_s = \begin{cases} \text{(i)} & E'_u \cdot (\varepsilon'_s - \varepsilon'_r) + f'_r & \text{if } s\cdot\varepsilon'_r \le s\cdot\varepsilon'_s \le s\cdot\varepsilon'_a \\ \text{(ii)} & \text{bausch}(\varepsilon'_s, \varepsilon'_a, \varepsilon'_{rejoin}) & \text{else if } s\cdot\varepsilon'_a < s\cdot\varepsilon'_s \le s\cdot\varepsilon'_{rejoin} \\ \text{(iii-a)} & \text{backbone}(\varepsilon'_s - \varepsilon'_0(K)) & \text{else if } \max\left(\left|\varepsilon'_0(K)\right|\right) \le \varepsilon'_{sh} - \varepsilon'_y \\ \text{(iii-b)} & \text{bausch}\left(\varepsilon'_s, \varepsilon'_{rejoin}, s\cdot\varepsilon'_u + \varepsilon'_0(K)\right) & \text{otherwise} \end{cases} \quad 4.6$$

Where (ε'_r, f'_r) are the coordinates of the last reversal point, E'_u is current elastic modulus, which decreases with the magnitude of plastic deformations (see ε'_M in Equation

4.7), ε'_a is the strain at the end of the linear unloading (see Equation 4.8 and Figure 4.4). ε'_{rejoin} is the strain where the Bauschinger curve rejoins either a previous Bauschinger curve or a shifted backbone (see (iii-a) and (iii-b) in Equation 4.6 respectively). ε'_0 is a two-element state variable with the plastic strain accumulated for tension and compression, Equation 4.9, and K is an index dependent on the direction of loading following the reversal, s. The function *backbone(x)*, used after a reversal from the yield plateau, corresponds to Equation 4.3. *bausch(x,y,z)* corresponds to the iterative process computing the Bauschinger curve between the boundary conditions (strain, stress and tangent modulus) defined by y and z.

$$E'_u = E_0 \cdot \left(0.82 + \frac{1}{5.55 + 1000 \cdot \varepsilon'_M} \right) \quad \text{(a)} \qquad \varepsilon'_M = \max(-\varepsilon'_0(1), \varepsilon'_0(2)) \quad \text{(b)} \qquad 4.7$$

$$\varepsilon'_a = \varepsilon'_r + s \cdot \frac{f_y}{E'_u} \qquad 4.8$$

$$\varepsilon'_0(K) = \varepsilon'_r - f'_r / E'_u \qquad \text{if } s \cdot \varepsilon'_0(K) > s \cdot (\varepsilon'_r - f'_r / E'_u) \qquad 4.9$$

The strain ε'_{rejoin} is defined by the preceding reversal history of the material. The constitutive stress-strain relationship defines three types of reversals: major, minor and simple, for more details refer to Dodd and Restrepo (1995).

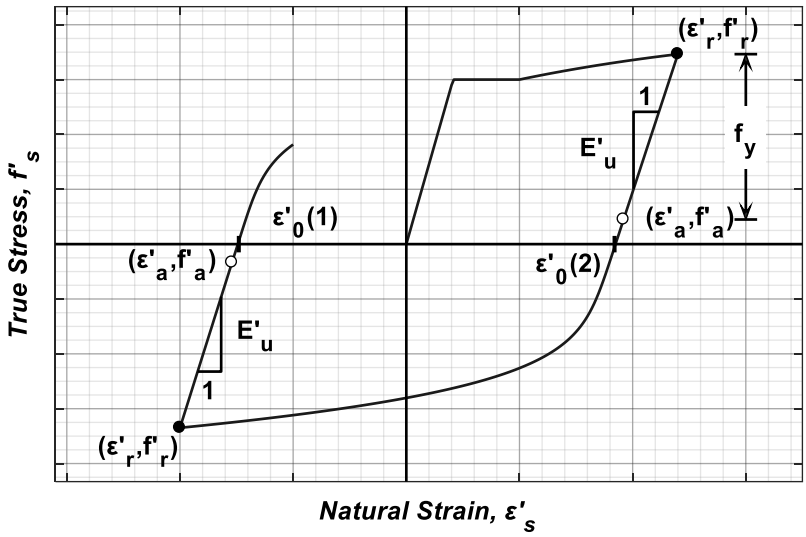

Figure 4.4. Post-Reversal Linear Unloading

4.3.3. Bauschinger Effect

Once the boundary conditions at both ends of the curve are determined (Point a: ε_a, f_a, E_a and Point b: ε_b, f_b, E_b), the original formulation of the model (Dodd and Restrepo, 1995) suggests an iterative process to generate a curve satisfying the boundary conditions, including an extra variable to control the hysteretic energy. In this process, the natural strain/true stress coordinates of the curve (ε'_s,f'_s) are transformed, in two steps, into a coordinate system ($\hat{\varepsilon}_s$, $\hat{f}_s$) where the curve can be approximated by a power function, see Figure 4.5 and Equation 4.10.

$$\hat{\varepsilon}_s = \frac{f'_s - f'_a - E'_a \cdot (\varepsilon'_s - \varepsilon'_a)}{f'_b - f'_a - E'_a \cdot (\varepsilon'_b - \varepsilon'_a)} \quad \text{(a)} \qquad \hat{f}_s = \frac{f'_s - f'_a - E'_b \cdot (\varepsilon'_s - \varepsilon'_a)}{f'_b - f'_a - E'_b \cdot (\varepsilon'_b - \varepsilon'_a)} \quad \text{(b)} \quad 4.10$$

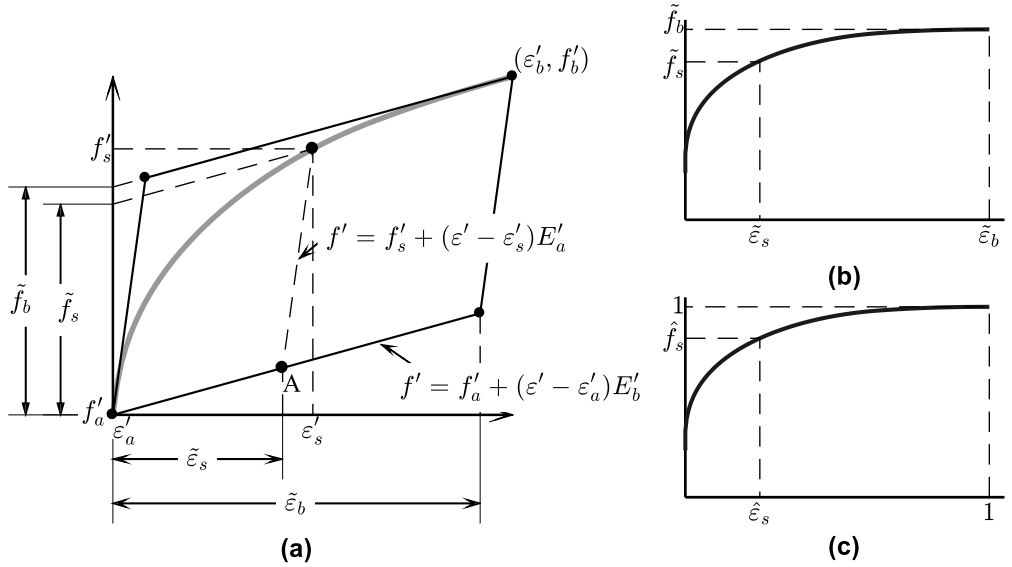

Figure 4.5. Coordinate Transformation of Bauschinger Curve: (a) Natural Strain – True Stress Coordinates; (b) Transformed Coordinates; (c) Normalized Coordinates

From Equation 4.10, a stress-strain relation in normalized coordinates is obtained as follows:

$$\hat{f}_s = \hat{\varepsilon}_s \cdot \lambda_1 + \lambda_2 \qquad 4.11$$

Where:

$$\lambda_1 = \frac{f'_b - f'_a - E'_a \cdot (\varepsilon'_b - \varepsilon'_a)}{f'_b - f'_a - E'_b \cdot (\varepsilon'_b - \varepsilon'_a)} \quad \text{(a)}$$

$$\lambda_2 = \frac{(E'_a - E'_b) \cdot (\varepsilon'_s - \varepsilon'_a)}{f'_b - f'_a - E'_b \cdot (\varepsilon'_b - \varepsilon'_a)} \quad \text{(b)} \qquad 4.12$$

The power function in Equation 4.13 satisfies the boundary conditions and the concave shape required of the Bauschinger curve in normalized coordinates, see Figure 4.6.

$$\hat{f}_s = \left(1 - (1 - \hat{\varepsilon}_s)^2\right)^Q \qquad 4.13$$

Where $Q \in [0,1]$ controls the area under the power function, and was calibrated to match an empirical estimate of the area under the stress-strain curve, Ω, see Equation 4.14 and 4.15.

$$\Omega = \int_0^{0.1} \hat{f}_s \cdot d\hat{\varepsilon}_s \approx \left[0.001 + \frac{0.00108}{1.043 - \left(\varepsilon'_p / \varepsilon'_u \right)} \right] \cdot \left(\frac{f'_p}{f'_t} - 0.69 \right) \cdot \frac{1}{0.18} + 0.085 \qquad 4.14$$

Where $\varepsilon'_p/\varepsilon'_u$ and f'_p/f'_t are non-dimensional variables defined as per Figure 4.7.

$$Q = 56.689 \cdot \left(\Omega_{fac} \cdot \Omega - 0.077 \right)^2 - 4.921 \cdot \left(\Omega_{fac} \cdot \Omega - 0.077 \right) + 0.1 \qquad 4.15$$
$$0.06 \le Q \le 0.3$$

As seen in Equation 4.16, the parameter Ω_{fac} in the constitutive stress-strain relationship is used to scale the empirical factor Ω for the computation of the exponent Q.

Replacing Equation 4.13 in 4.11 results in a non-linear equation for the normalized strain, $\hat{\varepsilon}_s$, which can be solved iteratively using the Newton-Raphson algorithm as follows:

$$\hat{\varepsilon}_s^{(i+1)} = \hat{\varepsilon}_s^{(i)} - \frac{\left(1 - \left(1 - \hat{\varepsilon}_s^{(i)} \right)^2 \right)^Q - \lambda_1 \cdot \hat{\varepsilon}_s^{(i)} - \lambda_2}{2 \cdot Q \cdot \left(1 - \left(1 - \hat{\varepsilon}_s^{(i)} \right)^2 \right)^{Q-1} \cdot \left(1 - \hat{\varepsilon}_s^{(i)} \right) - \lambda_1} \qquad 4.16$$

With a recommended initial estimate $\hat{\varepsilon}_s^{(0)} = \left(\varepsilon'_s - \varepsilon'_a \right) / \left(\varepsilon'_b - \varepsilon'_a \right)$. For small values of $\hat{\varepsilon}_s$, the Newton-Raphson algorithm may not converge, thus a bisection algorithm is recommended for cases where $\hat{\varepsilon}^{(0)}$ is less than 0.2.

Once convergence of the normalized strain $\hat{\varepsilon}_s^{(i)}$ is achieved, the corresponding normalized stress, $\hat{f}_s$, is computed from Equation 4.13 evaluated at $\hat{\varepsilon}_s^{(i)}$. The natural coordinates, ε'_s and f'_s, can then be computed by solving a linear system of equations based

on Equations 4.10a and 4.10b. The tangent modulus, *E'*$_s$, is computed using the chain rule of differentiation as follows:

$$\frac{d\hat{f}_s}{d\hat{\varepsilon}_s} = 2 \cdot Q \cdot \left(1-\left(1-\hat{\varepsilon}_s\right)^2\right)^{Q-1} \cdot \left(1-\hat{\varepsilon}_s\right) \quad \text{(a)}$$

$$\frac{d\tilde{f}_s}{d\tilde{\varepsilon}_s} = \frac{d\hat{f}_s}{d\hat{\varepsilon}_s} \cdot \frac{\left(f'_b - f'_a - E'_b \cdot \left(\varepsilon'_b - \varepsilon'_a\right)\right) \cdot \left(E'_a - E'_b\right)}{E'_a \cdot \left(\varepsilon'_b - \varepsilon'_a\right) - \left(f'_b - f'_a\right)} \quad \text{(b)} \qquad 4.17$$

$$E'_s = \frac{df'_s}{d\varepsilon'_s} = \frac{d\tilde{f}_s}{d\tilde{\varepsilon}_s} \cdot \frac{E'_a - E'_b}{E'_a - E'_b + \frac{d\tilde{f}_s}{d\tilde{\varepsilon}_s}} + E_b \quad \text{(c)}$$

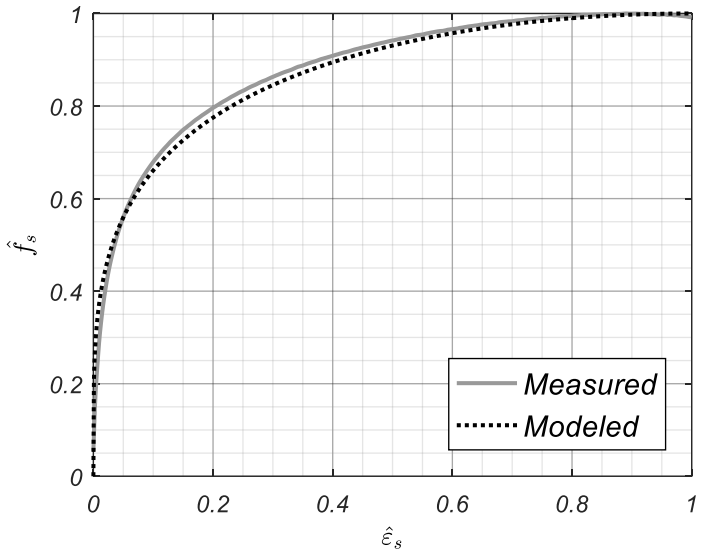

Figure 4.6. Experimental Bauschinger Curve vs Power Function Approximation in Normalized Stress-Strain Coordinates

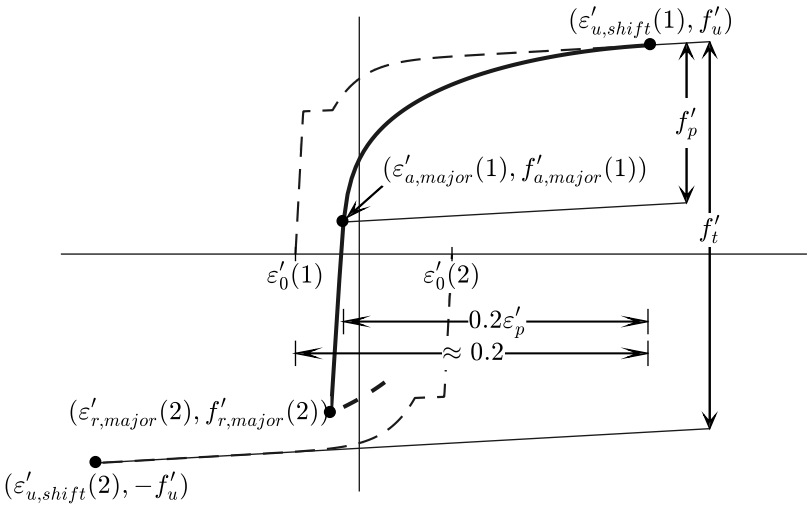

Figure 4.7. Non-Dimensional Variables for Empirical Formulation of the Area Under the Bauschinger Curve, *Ω*, Following a Major Reversal

4.4. Features Implemented

4.4.1. Closed-Form Bauschinger Curve

The search for a closed-form solution of the Bauschinger effect in the Dodd-Restrepo constitutive stress-strain relationship has found little success since the model was first introduced (Dodd and Restrepo-Posada, 1995). The main challenge was to find a continuously differentiable curve (class C^1, see Krantz, 1999) that not only satisfies the required boundary conditions for strain, stress and tangent modulus, but also maintains the sign for the curvature and has a parameter to control the area under the curve. Kim and Koutromanos (2016) recently developed a closed-form formulation for the Bauschinger effect using non-uniform rational b-splines, also known as NURBS (Piegl and Tiller, 1997). Their approach defines the Bauschinger curve as two NURBS segments connected at a characteristic point in the curve, ($\varepsilon'_{char}, f'_{char}$). The strain, stress, and tangent modulus

of this characteristic point is defined to match the area under the curve, Ω, as defined in Equation 4.14 in the original formulation by Dodd and Restrepo. However, a computer implementation of the model by Kim and Koutromanos (2016), which also includes the effects of inelastic buckling and low-cycle fatigue, was not available in any non-linear analysis tool accessible to the authors (e.g. OpenSees, McKenna et al., 2000). Because of this, the accuracy and stability of the model could not be initially assessed, thus a partial implementation of it was incorporated into the authors' computer code for OpenSees, to compare with the results of the approach presented in this article.

An alternative closed-form solution for the Bauschinger effect, using parametric Bezier curves (Bezier, 1970), is presented herein.

A Bezier curve of order n is defined by $n+1$ control points, $\mathbf{P_0}$ to $\mathbf{P_n}$ which, combined with polynomials of the independent parameter t, generate a curve in the space containing the control points, see Equation 4.18 and Figure 4.8.

$$C(t) = \sum_{i=0}^{n} B_{i,n}(t) \cdot \mathbf{P}_i \qquad 4.18$$

Where $\underline{t} \in [0,1]$ is the independent parameter and $B_{i,n}(t)$ is the i^{th} Bernstein polynomial of order n (Bernstein, 1912), see Equation 4.19.

$$B_{i,n}(t) = \binom{n}{i} \cdot t^i \cdot (1-t)^{n-i} \qquad 4.19$$

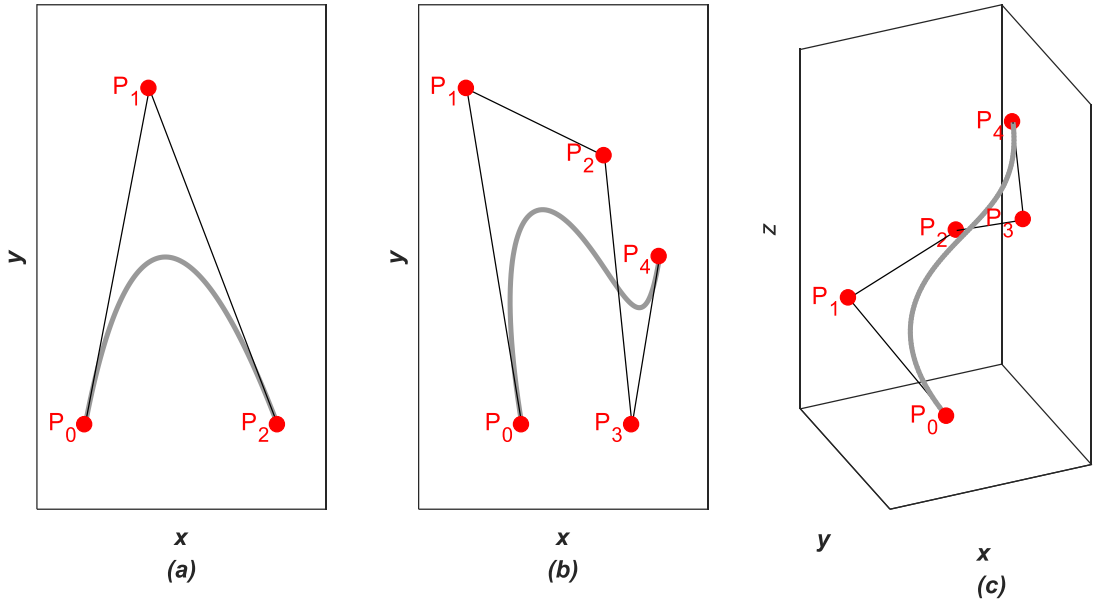

Figure 4.8. Sample Bezier Curves: (a) Quadratic (n=2) Bezier in 2D Space; (b) 4th Order Bezier in 2D Space; (c) 4th Order Bezier in 3D Space

Since a given set of control points defines a unique Bezier curve, additional control over the shape can be achieved using weight factors, w_i, as defined for Rational Bezier functions, see Equation 4.20 and Figure 4.9.

$$C(t)=\frac{\sum_{i=0}^{n} B_{i,p}(t)\cdot w_i \cdot \mathbf{P_i}}{\sum_{i=0}^{n} B_{i,p}(t)\cdot w_i} \qquad 4.20$$

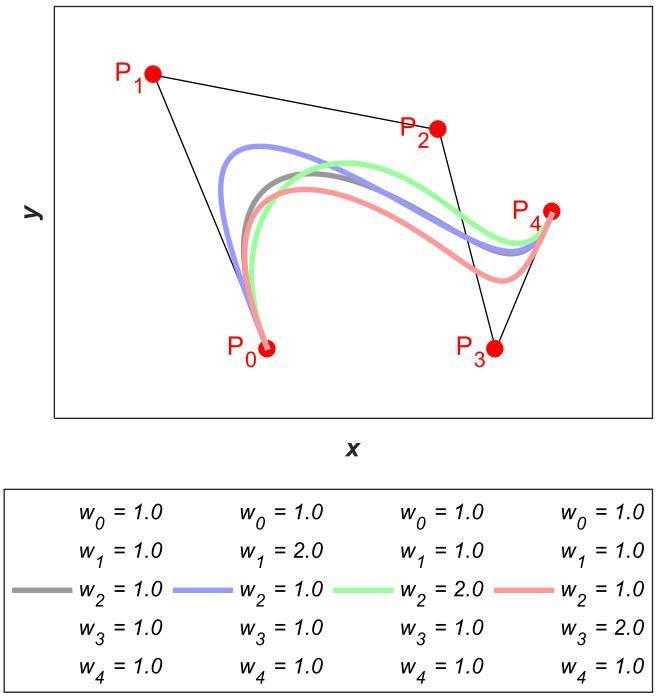

Figure 4.9. Effect of Weight Factors in Rational Bezier Curve with Fixed Control Points

For the Bauschinger effect, the control points of the Bezier curve belong to the two-dimensional strain-stress space (i.e. $\mathbf{P_i} = (\varepsilon_i, f_i)$). Following the analysis of different Bezier curves of order 2 and higher, a cubic rational Bezier (n=3) showed the best fit for the Bauschinger effect, see Equation 4.21.

$$C(t) = \frac{(1-t)^3 \cdot w_0 \mathbf{P_0} + 3 \cdot (1-t)^2 t \cdot w_1 \mathbf{P_1} + 3 \cdot (1-t) t^2 \cdot w_2 \mathbf{P_2} + t^3 w_3 \mathbf{P_3}}{(1-t)^3 \cdot w_0 + 3 \cdot (1-t)^2 t \cdot w_1 + 3 \cdot (1-t) t^2 \cdot w_2 + t^3 w_3} \qquad 4.21$$

Where points $\mathbf{P_0}$ and $\mathbf{P_3}$ are the ends of the curve, while $\mathbf{P_1}$ and $\mathbf{P_2}$ are intermediate points along the two asymptotes, defined by the stress-strain coordinates and tangent modulus at each end point, see Figure 4.10.

As seen in the diagram in Figure 4.10, to satisfy the boundary conditions of the Bauschinger effect, the control points of the Bezier curve are defined as follow:

$$
\begin{aligned}
\mathbf{P_0} &= \left(\varepsilon_a,\, f_a\right) \\
\mathbf{P_1} &= \left(\varepsilon_a + \xi_a \cdot \frac{f_b - f_a - E_b \cdot (\varepsilon_b - \varepsilon_a)}{E_a - E_b},\; f_a + \xi_a \cdot \frac{E_a \cdot E_b \left(\varepsilon_a - \varepsilon_b\right) + E_a \cdot \left(f_b - f_a\right)}{E_a - E_b}\right) \\
\mathbf{P_2} &= \left(\varepsilon_b + \xi_b \cdot \frac{f_b - f_a - E_a \cdot (\varepsilon_b - \varepsilon_a)}{E_a - E_b},\; f_b + \xi_b \cdot \frac{E_a \cdot E_b \left(\varepsilon_a - \varepsilon_b\right) + E_b \cdot \left(f_b - f_a\right)}{E_a - E_b}\right) \\
\mathbf{P_3} &= \left(\varepsilon_b,\, f_b\right)
\end{aligned}
\qquad 4.22
$$

Where ε_a, f_a and E_a are the boundary conditions for the beginning of the curve, while ε_b, f_b and E_b are the corresponding values for the end of it. Factors ξ_a and $\xi_b \in [0,1]$ define the location of the intermediate control points, $\mathbf{P_1}$ and $\mathbf{P_2}$, between the ends of the curve, $\mathbf{P_0}$ and $\mathbf{P_3}$, and the intersection between the asymptotes (see $(\varepsilon_{int}, f_{int})$ in Figure 4.10).

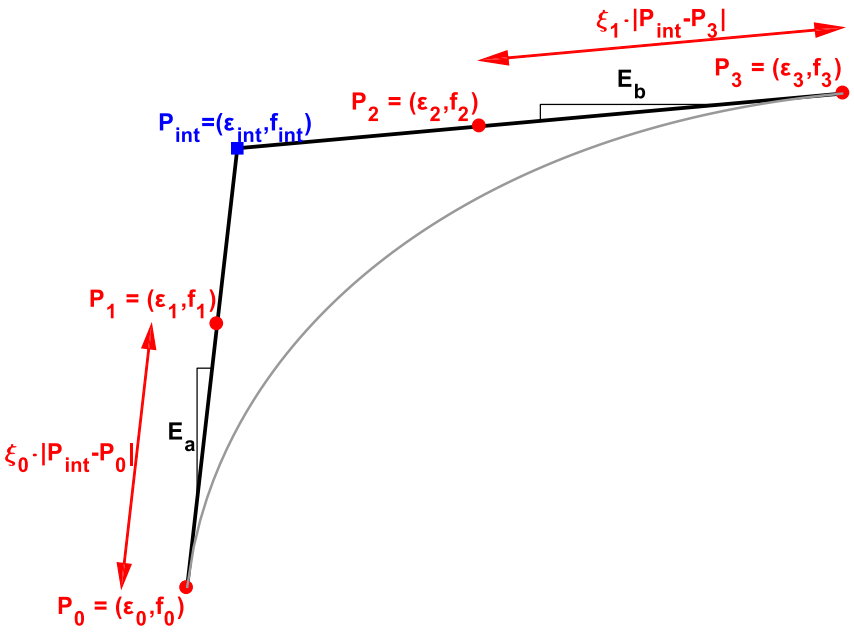

Figure 4.10. Bauschinger Effect Representation Using Rational Cubic Bezier Curves

For a strain ε^* within the Bauschinger curve, the corresponding stress can then be computed as follows:

(i) First, replace the strain at the control points, Equation 4.22, into the parametric definition of the curve, Equation 4.21:

$$\varepsilon^* = \frac{(1-t^*)^3 w_0 \varepsilon_a + 3(1-t^*)^2 t^* w_1 \left(\varepsilon_a + \xi_a \cdot \frac{f_b - f_a - E_b(\varepsilon_b - \varepsilon_a)}{E_a - E_b} \right)}{(1-t^*)^3 \cdot w_0 + 3\cdot(1-t^*)^2 t^* \cdot w_1 + 3\cdot(1-t^*)t^{*2} \cdot w_2 + t^{*3} w_3} + \frac{3\cdot(1-t^*)t^{*2} w_2 \left(\varepsilon_b + \xi_b \cdot \frac{f_b - f_a - E_a(\varepsilon_b - \varepsilon_a)}{E_a - E_b} \right) + t^{*3} w_3 \varepsilon_b}{(1-t^*)^3 \cdot w_0 + 3\cdot(1-t^*)^2 t^* \cdot w_1 + 3\cdot(1-t^*)t^{*2} \cdot w_2 + t^{*3} w_3} \quad 4.23$$

(ii) Rearrange the terms as a cubic equation for t^*:

$$a_3 \cdot t^{*3} + a_2 \cdot t^{*2} + a_1 \cdot t^* + a_0 = 0 \quad 4.24$$

Where:

$$a_3 = -w_0 \left(\varepsilon_a - \varepsilon^* \right) + 3w_1 \left(\varepsilon_a + \xi_a \frac{f_b - f_a - E_b \cdot (\varepsilon_b - \varepsilon_a)}{E_a - E_b} - \varepsilon^* \right) - 3w_2 \left(\varepsilon_b + \xi_b \frac{f_b - f_a - E_a (\varepsilon_b - \varepsilon_a)}{E_a - E_b} - \varepsilon^* \right) + w_3 \left(\varepsilon_b - \varepsilon^* \right) \quad \text{(a)}$$

$$a_2 = 3w_0 \left(\varepsilon_a - \varepsilon^* \right) - 6w_1 \left(\varepsilon_a + \xi_a \frac{f_b - f_a - E_b \cdot (\varepsilon_b - \varepsilon_a)}{E_a - E_b} - \varepsilon^* \right) + 3w_2 \left(\varepsilon_b + \xi_b \frac{f_b - f_a - E_a (\varepsilon_b - \varepsilon_a)}{E_a - E_b} - \varepsilon^* \right) \quad \text{(b)} \quad 4.25$$

$$a_1 = -3w_0 \left(\varepsilon_a - \varepsilon^* \right) + 3w_1 \left(\varepsilon_a + \xi_a \frac{f_b - f_a - E_b \cdot (\varepsilon_b - \varepsilon_a)}{E_a - E_b} - \varepsilon^* \right) \quad \text{(c)}$$

$$a_0 = w_0 \left(\varepsilon_a - \varepsilon^* \right) \quad \text{(d)}$$

(iii) Solve the cubic equation. Cardano's method (Weisstein, 2002) produces the following three roots for the equation:

$$t^* = \begin{cases} p + \sqrt[3]{r+\sqrt{\Delta}} + \sqrt[3]{r-\sqrt{\Delta}} \\ p - \frac{1}{2}\cdot\left(\sqrt[3]{r+\sqrt{\Delta}} + \sqrt[3]{r-\sqrt{\Delta}}\right) + \frac{1}{2}i\sqrt{3}\cdot\left(\sqrt[3]{r+\sqrt{\Delta}} - \sqrt[3]{r-\sqrt{\Delta}}\right) \\ p - \frac{1}{2}\cdot\left(\sqrt[3]{r+\sqrt{\Delta}} + \sqrt[3]{r-\sqrt{\Delta}}\right) - \frac{1}{2}i\sqrt{3}\cdot\left(\sqrt[3]{r+\sqrt{\Delta}} - \sqrt[3]{r-\sqrt{\Delta}}\right) \end{cases} \qquad 4.26$$

Where:

$$p = \frac{-a_2}{3\cdot a_3} \qquad \text{(a)}$$

$$q = \frac{a_1}{3a_3} - p^2 \qquad \text{(b)} \qquad 4.27$$

$$r = p^3 + \frac{a_1 a_2 - 3\cdot a_0 a_3}{6\cdot a_3^2} \qquad \text{(c)}$$

$$\Delta = q^3 + r^2 \qquad \text{(d)}$$

(iv) Based on the discriminant Δ, see Equation 4.27d, select the appropriate root:

a. If Δ =0, all three solutions of Equation 4.26 are real, two of which are equivalent:

$$t^* = \begin{cases} p + 2\cdot\sqrt[3]{r} \\ p - \sqrt[3]{r} \end{cases} \qquad 4.28$$

Select the solution in the interval [0,1]

b. If $\Delta > 0$, only one solution of Equation 4.26 is real

$$t^* = p + \sqrt[3]{R+\sqrt{\Delta}} + \sqrt[3]{R-\sqrt{\Delta}} \qquad 4.29$$

c. If $\Delta < 0$, all three solutions are real and different:

$$t^* = \begin{cases} 2\cdot\sqrt{-q}\cdot\cos\left(\dfrac{\theta}{3}\right)+p \\ 2\cdot\sqrt{-q}\cdot\cos\left(\dfrac{\theta+2\pi}{3}\right)+p \\ 2\cdot\sqrt{-q}\cdot\cos\left(\dfrac{\theta+4\pi}{3}\right)+p \end{cases} \qquad 4.30$$

Where:

$$\theta = \cos^{-1}\left(\frac{r}{\sqrt{-q^3}}\right) \qquad 4.31$$

And select the solution in the interval [0,1]

(v) Once t^* is calculated, the stress f^* is determined from the definition of the curve and the stress at the control points:

$$f^* = \frac{\mathbf{b_0}(t)^T \cdot diag(\mathbf{f_p}) \cdot \mathbf{w_p}}{\mathbf{b_0}(t)^T \cdot \mathbf{w_p}} \qquad 4.32$$

Where $diag(\mathbf{f_p})$ is the diagonalization function applied over vector $\mathbf{f_p}$.

$$\mathbf{b_0}(t) = \begin{bmatrix} (1-t)^3 \\ 3t(1-t)^2 \\ 3t^2(1-t) \\ t^3 \end{bmatrix} \quad \text{(a)} \qquad \mathbf{w} = \begin{bmatrix} w_0 \\ w_1 \\ w_2 \\ w_3 \end{bmatrix} \quad \text{(b)}$$

$$\mathbf{f_p} = \begin{bmatrix} f_a \\ f_a + \xi_a \cdot \dfrac{E_a \cdot E_b(\varepsilon_a - \varepsilon_b) + E_a \cdot (f_b - f_a)}{E_a - E_b} \\ f_b + \xi_b \cdot \dfrac{E_a \cdot E_b(\varepsilon_a - \varepsilon_b) + E_b \cdot (f_b - f_a)}{E_a - E_b} \\ f_b \end{bmatrix} \quad \text{(c)} \qquad 4.33$$

(vi) Finally, the tangent modulus is computed using the chain rule of differentiation. The result is presented in matrix form for brevity:

$$\frac{df}{d\varepsilon}\left(\varepsilon^{*}\right)=\frac{df}{dt}\frac{dt}{d\varepsilon}=\frac{df}{dt}\cdot\left(1\Big/\frac{d\varepsilon}{dt}\right)$$
$$\frac{df}{d\varepsilon}\left(\varepsilon^{*}\right)=\frac{\left(\mathbf{b}_1{}^{\mathrm{T}}(t^{*})\cdot diag(\mathbf{f}_{\mathbf{p}})\cdot\mathbf{w}_{\mathbf{p}}\right)\left(\mathbf{b}_0{}^{\mathrm{T}}(t^{*})\cdot\mathbf{w}_{\mathbf{p}}\right)-\left(\mathbf{b}_0^{\mathrm{T}}(t^{*})\cdot diag(\mathbf{f}_{\mathbf{p}})\cdot\mathbf{w}_{\mathbf{p}}\right)\left(\mathbf{b}_1{}^{\mathrm{T}}(t^{*})\cdot\mathbf{w}_{\mathbf{p}}\right)}{\left(\mathbf{b}_1{}^{\mathrm{T}}(t^{*})\cdot diag(\boldsymbol{\varepsilon}_{\mathbf{p}})\cdot\mathbf{w}_{\mathbf{p}}\right)\left(\mathbf{b}_0{}^{\mathrm{T}}(t^{*})\cdot\mathbf{w}_{\mathbf{p}}\right)-\left(\mathbf{b}_0^{\mathrm{T}}(t^{*})\cdot diag(\boldsymbol{\varepsilon}_{\mathbf{p}})\cdot\mathbf{w}_{\mathbf{p}}\right)\left(\mathbf{b}_1{}^{\mathrm{T}}(t^{*})\cdot\mathbf{w}_{\mathbf{p}}\right)} \quad 4.34$$

Where:

$$\mathbf{b}_1(t)=\begin{bmatrix}-3(1-t)^2\\-6t(1-t)+3(1-t)^2\\-3t^2+6t(1-t)\\3t^2\end{bmatrix}\ \text{(a)}\qquad \boldsymbol{\varepsilon}_{\mathbf{p}}=\begin{bmatrix}\varepsilon_a\\\varepsilon_a+\xi_a\cdot\dfrac{f_b-f_a-E_b\cdot(\varepsilon_b-\varepsilon_a)}{E_a-E_b}\\\varepsilon_b+\xi_b\cdot\dfrac{f_b-f_a-E_a\cdot(\varepsilon_b-\varepsilon_a)}{E_a-E_b}\\\varepsilon_b\end{bmatrix}\ \text{(b)}\quad 4.35$$

4.4.1.1. Parameters of the Bezier function

The proposed function for the Bauschinger effect includes six parameters to control the shape of the curve, while still satisfying the boundary conditions. Two parameters, ξ_a and ξ_b, define the location of the intermediate control points, $\mathbf{P_1}$ and $\mathbf{P_2}$, along the asymptotes defined by the slope at the ends of the curve, see Figure 4.10. While four weighting factors: w_0, w_1, w_2 and w_3, define the relative influence of each control point on the shape of the curve.

To calibrate the parameters of the proposed function, a least-squared minimization of the difference between experimental and analytical Bauschinger curves was used. The experimental curves were extracted from cyclic tests on #4 machined bars, also used in the calibration of the general parameters of the constitutive stress-strain relationship and described in the following section. As for the analytical curves, the stress-strain response

from the iterative formulation (see Bauschinger Effect section) for a variety of boundary conditions and relative areas under the curve, Ω, see Equation 4.14, was assumed as the "true" response to match with the proposed solution.

Following calibration and sensitivity analyses of all six parameters (ξ_a, ξ_b, w_0, w_1, w_2 and w_3), a good approximation of the experimental results and the Bauschinger curves computed with the iterative formulation, was attained by keeping a constant value for five of the parameters and computing the one remaining, w_3, as a function of Ω, see Equation 4.36.

$$\begin{aligned} &\xi_a = \xi_b = 0.9 \\ &w_0 = 1.0 \quad ; \quad w_1 = 1.3 \quad ; \quad w_2 = 0.7 \\ &w_3(\Omega) = 643.4 \cdot e^{-100 \cdot \Omega} \end{aligned} \qquad 4.36$$

Figure 4.11 shows the optimal values of w_3, fitting both experimental and analytical Bauschinger curves (the latter computed with the iterative formulation), against Ω. With a coefficient of determination $R^2 = 0.89$, the regression analysis for w_3 provides satisfactory results.

Figure 4.12 shows some experimental stress-strain responses compared to the predicted values using both the original and the proposed formulations for the Bauschinger effect. To facilitate visualization, the curves in the figure were shifted to start at zero stress and zero strain, and loading in the positive direction. Figure 4.12 shows the predicted response of a Bezier curve matching experimental results as accurately as the iterative formulation.

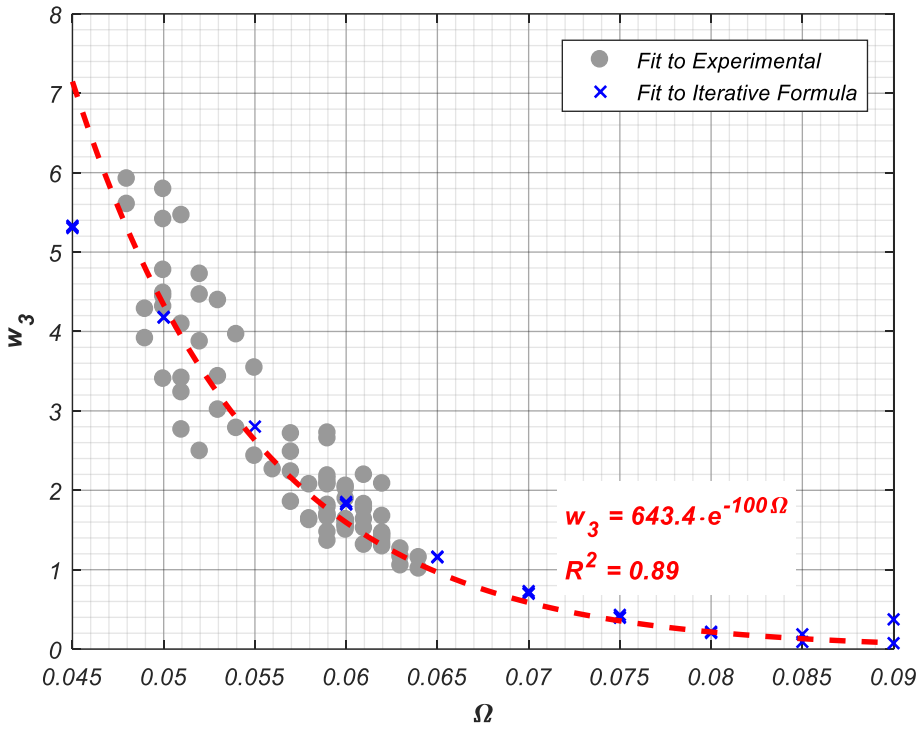

Figure 4.11. Regression Analysis of Bezier Curve Parameter w_3 vs Ω

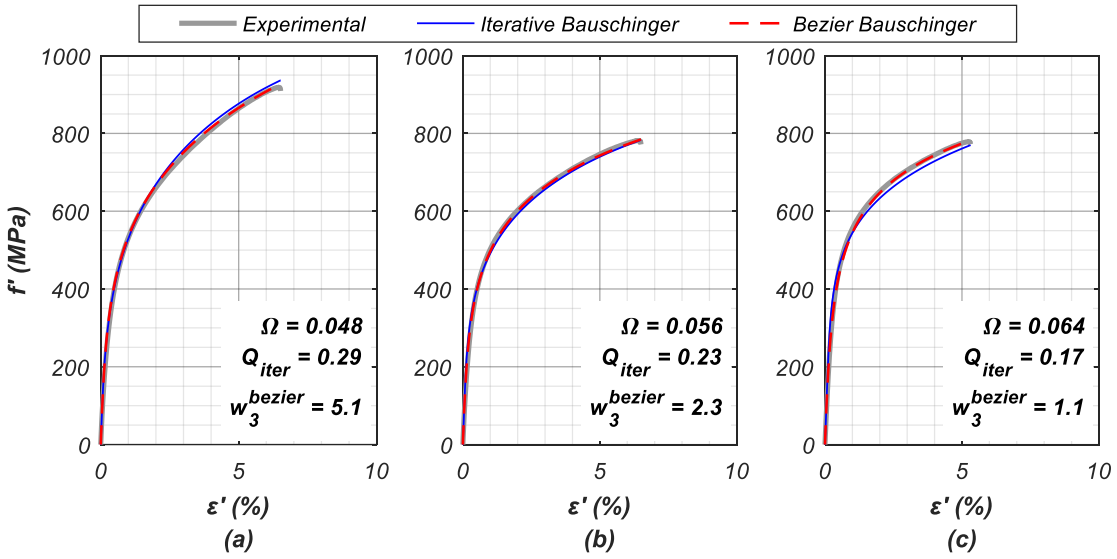

Figure 4.12. Sample Bauschinger Curves Recorded Experimentally against Prediction with Iterative Formulation, and Prediction with Proposed Bezier Function

Furthermore, Figure 4.13 compares the predicted stress-strain response, for multiple values of Ω, from both the original and the proposed formulations. As seen in the figure, both formulations have very similar results, with only some small differences at values of Ω close to the upper limit of 0.1, see Equation 4.14.

The original formulation of the constitutive stress-strain relationship assumed a fixed value Q = 0.35, see Equation 4.13, for Bauschinger curves following a minor or simple reversal. Similarly, the Bezier formulation uses a constant value w_3 = 11.8 following a minor or simple reversal.

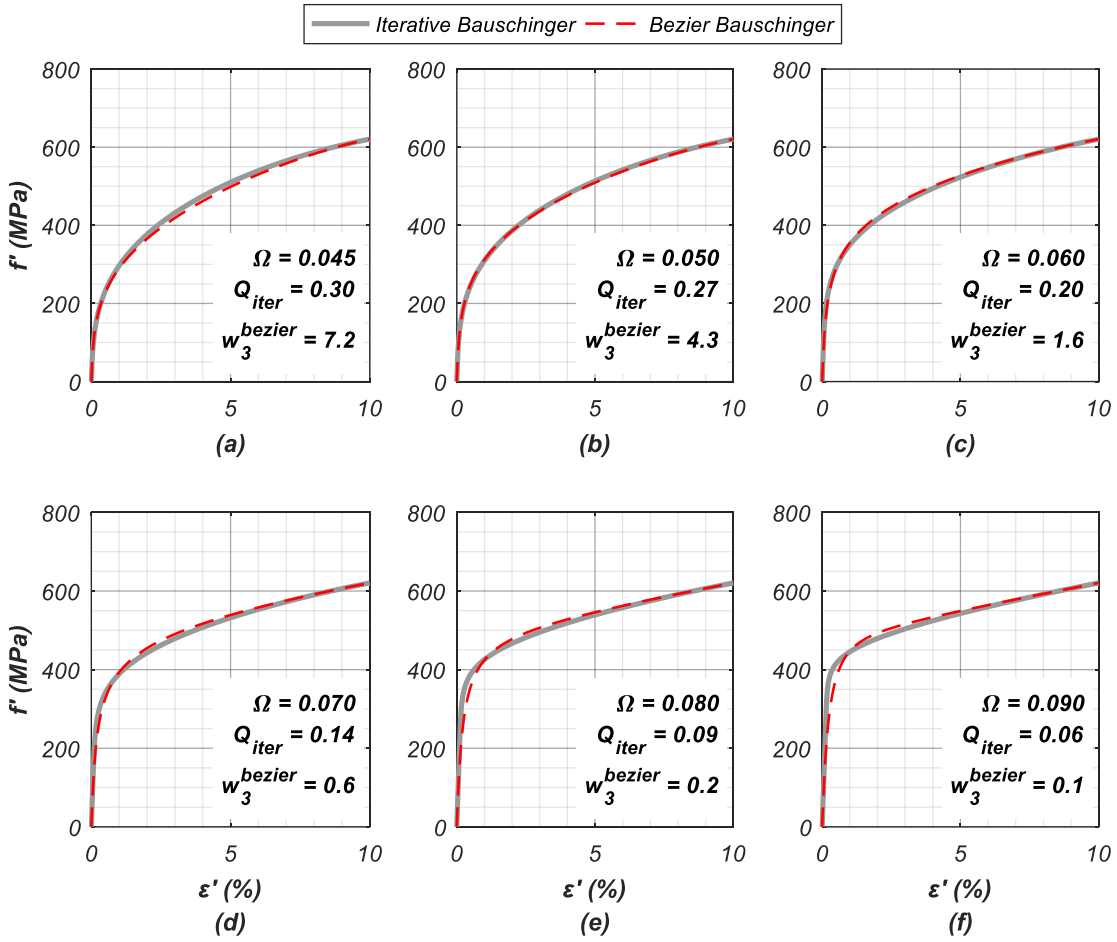

Figure 4.13. Comparison of Bauschinger Effect Predicted with Iterative and Proposed Formulation for Different Values of Ω

4.4.2. Post-Fracture Response

As mentioned in the description of the original model, the Dodd-Restrepo constitutive stress-strain relationship is not well defined for strains beyond the tensile strength, f_u. Because of this, the stress-strain response shows an abrupt loss in capacity after the onset of necking in tension, or crack development in compression, see Figure 4.14. This behavior of the constitutive stress-strain relationship not only misrepresents the material response but carries convergence issues for large scale models using the material model.

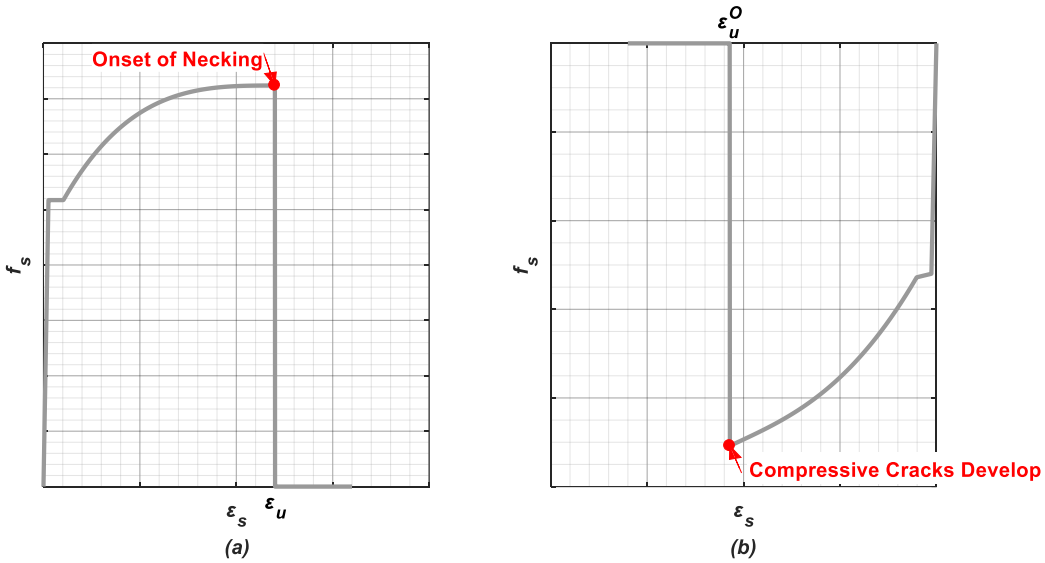

Figure 4.14. Response of Original Model Formulation Following Uniform Strain in Both Loading Directions: (a) Response After Onset of Necking; (b) Response After Cracks in Compression have Developed

The constitutive stress-strain relationship implemented herein includes a parabolic post-necking response for a smooth loss in capacity until the fracture strain defined by the user, ε_{fract}, is reached, see Figure 4.15a. Once ε_{fract} is exceeded, the material model loses all capacity in either loading direction. In compression on the other hand, the model assumes

a linear hardening branch following the uniform strain in natural coordinates, see Figure 4.15b. The increased capacity in compression is consistent with the behavior of the material when geometric non-linearities, such as buckling, are ignored (Nadai, 1950).

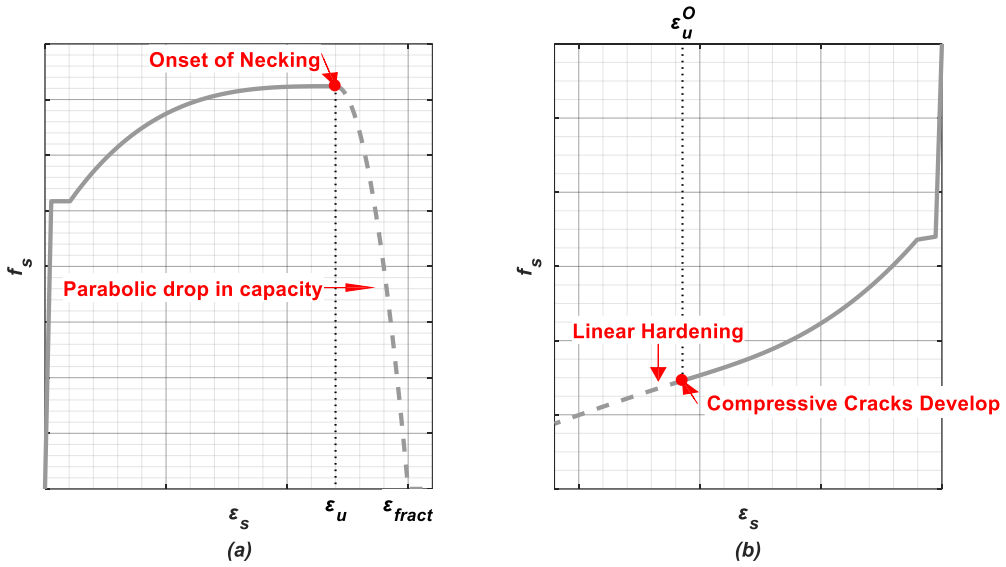

Figure 4.15. Response of New Model Formulation Following Uniform Strain in Both Loading Directions: (a) Response After Onset of Necking; (b) Response After Cracks in Compression have Developed

For reversals within the parabolic post-necking response, a Bauschinger curve is used to connect the reversal point to the backbone stress-strain response at the uniform strain in compression, see Figure 4.16a. A reversal from this curve will transition back to the parabolic post-necking response using another Bauschinger curve, see Figure 4.16b.

For reversals from the linear hardening branch in compression, the implemented material model unloads to zero stress at the plastic strain for the beginning of the linear hardening branch, see Figure 4.17a. Once zero stress is reached, the material loses capacity in either loading direction, see Figure Figure 4.17a. Reversals from the unloading curve,

before zero stress is reached, follow the same unloading path to return to the linear hardening branch, see Figure 4.17b.

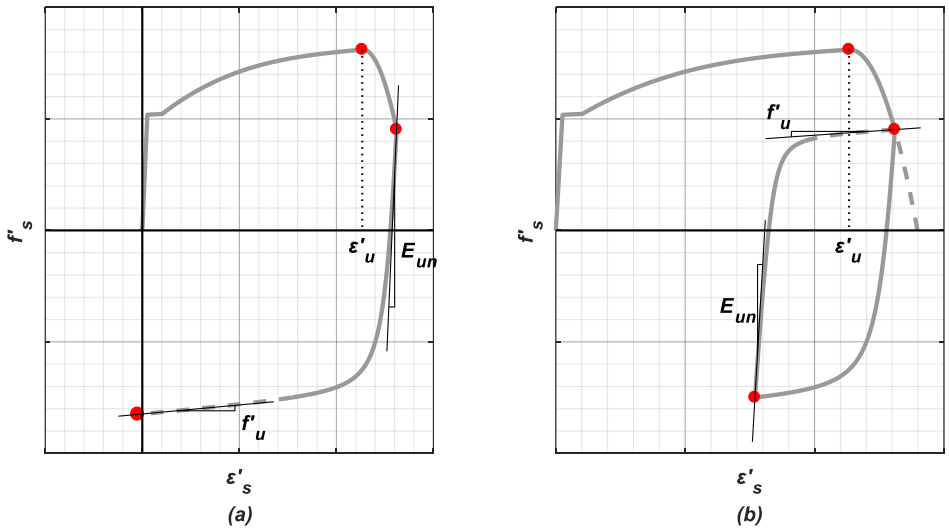

Figure 4.16. Response of New Model Formulation for Reversals after Onset of Necking in Natural Coordinates: (a) Reversal from Parabolic Post-Necking Branch (b) Reversal from Bauschinger Curve Starting in Post-Necking Parabolic Branch

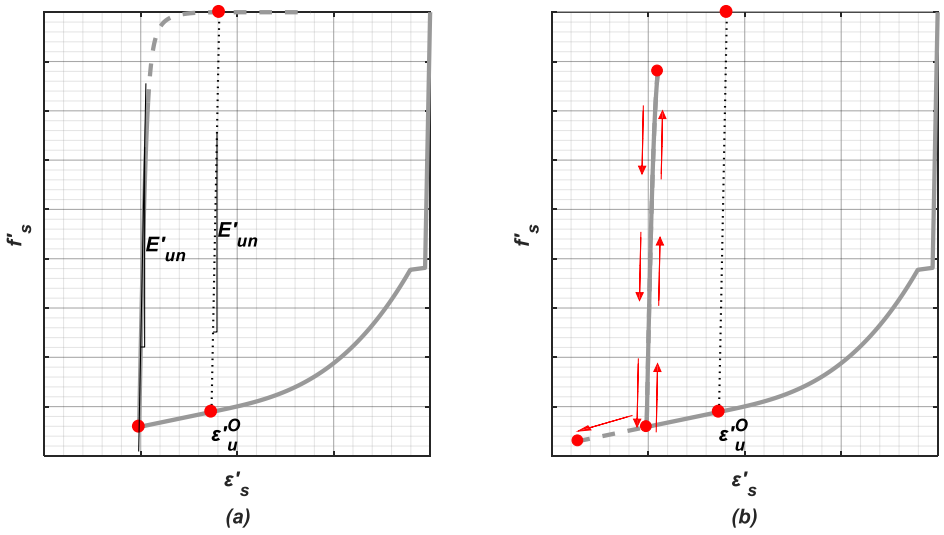

Figure 4.17. Response of New Model Formulation for Reversals after Compressive Crack Development, in Natural Coordinates: (a) Reversal from Compressive Hardening Branch (b) Reversal from Unloading after Compressive Hardening Branch

4.4.3. Tangent and Secant Modulus

An option to select the modulus, *E*, returned by the material model at each analysis step was implemented into the constitutive stress-strain relationship. Despite its simplicity, this feature can have a significant effect reducing convergence issues of full-scale structural models. At large strain amplitudes, and within the yield plateau, the constitutive stress-strain relationship yields small values for the tangent modulus, E_T, which can result in singular stiffness matrices, at the section or element level, for models based on fiber discretization. This problem is particularly relevant for flexibility-based elements (i.e. *forceBeamColumn* in OpenSees), which require inverting stiffness matrices at each analysis step.

The implemented constitutive stress-strain relationship provides three alternatives for the modulus returned at each step: 1) The tangent Modulus, E_T, of the last analysis step; 2) The original Young's Modulus, E_0; 3) A secant modulus, E_{sec}, from the slope between the last analysis step and the preceding strain reversal, ε_r, see Figure 4.18.

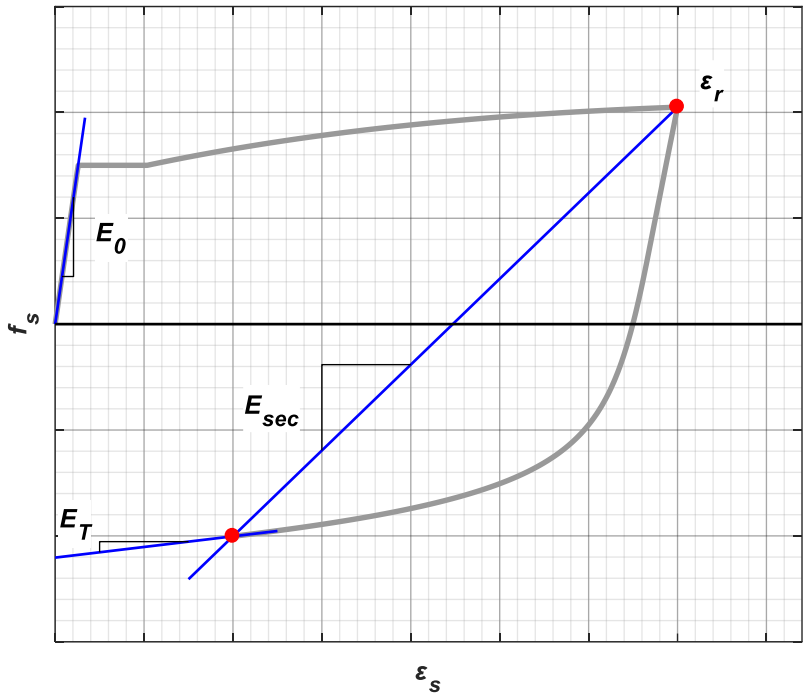

Figure 4.18. Alternative Definitions of Modulus Returned by New Implementation of the Constitutive Stress-strain relationship

4.5. Calibration of Model Parameters

4.5.1. Coupon Testing

To calibrate the parameters of the constitutive stress-strain relationship, two straight, never coiled #4 bars, conforming to the ASTM A615 (2016) and A706 (2016) standards for Grade 60 reinforcing steel, were acquired for testing from three different manufacturers, labeled henceforth as mills A, B and C.

A total of fifty-four 250 mm long coupons were extracted for testing, divided into six groups of nine coupons according to manufacturer and ASTM standard they comply with. The mechanical properties of each material were determined from two coupons per steel category, tested under pure tension in its original unmachined form, see Figure 3.1b.

The remaining coupons were machined in the middle to a 9 mm diameter section with a length to diameter ratio of 2, see Figure 3.1a. This machining was performed to minimize geometric non-linearities in the hysteretic response (i.e. buckling), thus isolating the nonlinear effects from the material itself. One of the machined coupons per steel category was also tested in pure tension, to evaluate any change in the measured mechanical properties, while the rest was tested under cyclic strain histories.

Table 3.2 compares the mechanical properties measured from tensile tests on unmachined and machined coupons, with each steel category labeled by a letter-number combination, indicating the manufacturer (A, B or C) and the ASTM standard it complies with (6 for ASTM A615 or 7 for ASTM A706). As seen in Table 3.2, the mechanical properties identified for machined and unmachined coupons can differ significantly within the same steel category. This difference could be explained by multiple factors, including the different accuracy in the value for the cross-section area of the coupons, the variation in chemical composition and residual stress distribution between the core and surface of the reinforcing bars, and the lack of stress concentrations in the smooth surface of a machined coupon.

For cyclic testing, four randomized strain histories (SH1, SH2, SH3 and SH4) were generated for testing with a nominal strain rate $\dot{\varepsilon}$ = 0.001/sec, see Figure 3.3. The use of randomized strain histories was preferred over traditional "sawtooth" shaped ones to replicate strain responses recorded experimentally in a full-scale structure tested under seismic load (Schoettler et al. 2012). Within each steel category, four coupons were tested under the strain histories at the original strain rate, while two additional coupons were

tested under strain histories SH1 and SH2 at a rate $\dot{\varepsilon}$ = 0.02/sec to assess strain rate effects. Figure 4.19 compares the cyclic stress-strain response of the coupons tested under strain history SH2 at the original strain rate. As seen in Figure 4.19, the hysteretic response from different steel categories are very distinctive, which is also apparent from the peak stress, $|f_{max}|$, and dissipated energy, U, values indicated in the figure.

Previous work by the author (Carreño et al. under-review) offers a detailed description of the experimental procedure and results of the coupon testing. For this work, the results of the calibration analysis on the parameters of the implemented constitutive stress-strain relationship are presented directly. From all the cyclic tests performed, only the results for strain histories at a strain rate $\dot{\varepsilon}$ = 0.001/sec are used in the calibration (four coupons per steel category), as strain rate effects can be neglected for simplicity, as found in Carreño et al. (under-review).

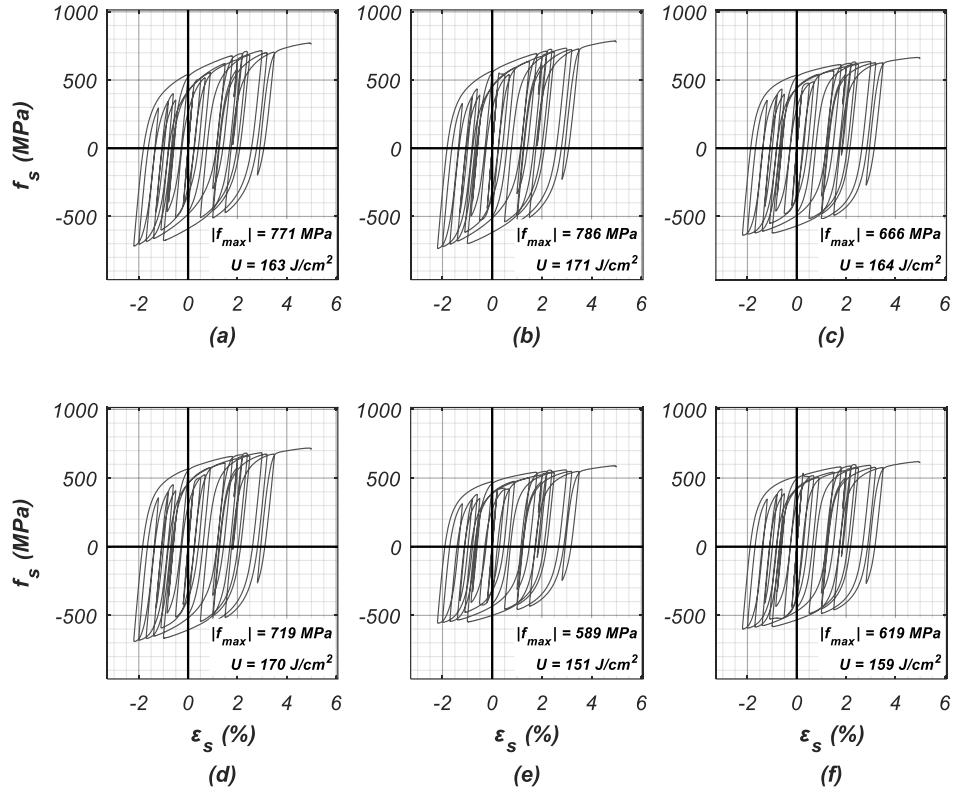

Figure 4.19. Cyclic Response Under Strain History SH2, at Strain Rate $\dot{\varepsilon}$ = 0.001/sec, of Coupons from Steel Categories: (a) A6; (b) B6; (c) B7; (d) A7; (e) C7; (f) C6

4.5.2. Preliminary Analysis

As mentioned in the original formulation of the constitutive stress-strain relationship, the Dodd-Restrepo steel model is defined by eight parameters: E_0, f_y, ε_{sh}, ε_u, f_u, $\varepsilon_{sh,1}$, $f_{sh,1}$, and Ω_{fac}, seven of which can be directly identified from the backbone curve of the material, see Figure 4.3. Instead of input parameters $\varepsilon_{sh,1}$ and $f_{sh,1}$, the implemented constitutive stress-strain relationship can use the exponent P as input to represent the strain hardening branch, see Equation 4.3. The use of parameter P, in lieu of $\varepsilon_{sh,1}$ and $f_{sh,1}$, is recommended due to the stability of the parameter for a variety of reinforcing steel types, as observed by the author in multiple coupon tests (e.g. Table 3.2).

The parameter Ω_{fac} in the constitutive stress-strain relationship, defining the shape of the Bauschinger effect, was originally calibrated for Grade 300 and Grade 430 New Zealand steel (NZS 3402: 1989), to a default value $\Omega_{fac}=1.0$. This calibrated value however, may not be representative of reinforcement typically used today in the United States, such as the Grade 60 ASTM A615 (2016) and A706 (2016) reinforcing bars used in this study. Based on experimental results by Wilson and Bate (1986, see Figure 4.20) Dodd and Restrepo (1995) suggested a negative correlation between Ω_{fac} and the carbon content of the material. At an average of 0.22%, the carbon content in the coupons tested by Dodd and Restrepo (1995) is consistently lower than in the coupons used in this study, see Table 3.3, thus the current calibration analysis is expected to result in values of Ω_{fac} less than 1.0, see Figure 4.20.

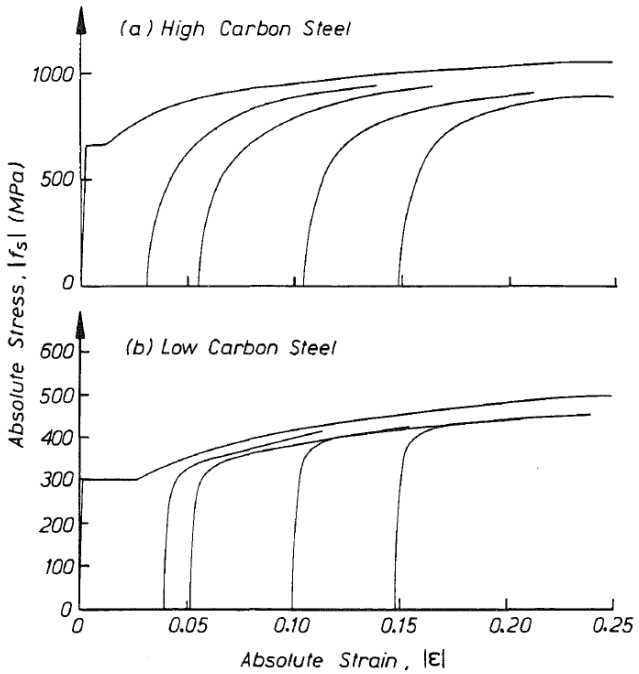

Figure 4.20. Backbone and Bauschinger Curves in Terms of Absolute Value of Stress and Strain for Low and High Carbon Steel (adapted from Wilson and Bate, 1986)

4.5.3. Calibration Results

The calibration of parameters from the constitutive stress-strain relationship was performed using MATLAB's Optimization Toolbox (MathWorks, 2016), by minimizing the error between measured and predicted hysteretic responses of the machined coupons, according to the definition:

$$error(\mathbf{x}) = \sqrt{\frac{\sum_{i=1}^{n}\left(f_{m,i} - f_{p,i}(\mathbf{x})\right)^2}{\sum_{i=1}^{n} f_{m,i}^2}} \qquad 4.37$$

Where $f_{m,i}$ is the measured stress at step i, and $f_{p,i}(\mathbf{x})$ is the corresponding stress predicted by the constitutive stress-strain relationship using the material parameters in vector **x**. This measure of error has been normalized by the measured stress history, $f_{m,i}$, and the results expressed in percentage.

Table 4.1 shows the average and coefficient of variation (c.o.v) of the calibrated material parameters found for each steel category. Results for the Young's Modulus, E_0, show little variation within each steel category and in-between them, with an overall average of E_0= 221360 MPa and a corresponding coefficient of variation (c.o.v.) of 2.5%. The yield and tensile strengths, f_y and f_u, show a relatively small variability within each category, with average c.o.v. values of 3.1% and 1.8% respectively. In between categories however, the difference in strengths can be significant, with the average yield strength as low as 438 MPa and as high as 582 MPa, a difference of 28% between sets with the same nominal strength. Similarly, the tensile strength found for different steel groups ranged between 629 and 829 MPa, a difference of 27%.

A comparison between the calibrated strength values, see Table 4.1, with those obtained from monotonic tests on machined coupons, see Table 3.2, shows noticeable variations in some steel categories, particularly for the yield strength, at an average difference of 7%. The largest discrepancy in f_y was observed in Category A6 at 18%, justified by the multiple ways this parameter influences the cyclic response in the constitutive stress-strain relationship, including the definition of major reversals and the extent of the linear unloading branches following a strain reversal. Dodd and Restrepo (1995) indicated the extent of these post-reversal branches can range between 0.7 and 1.3 times f_y in tested coupons, with the constitutive stress-strain relationship assuming a value of 1.0 f_y for simplicity, see Figure 4.4. In the case of steel coupons in category A6, the linear unloading branches extend longer than 1.0 f_y, thus the calibration analysis returns larger values of f_y to better fit the overall cyclic response. The differences between calibration analysis, Table 4.1, and tensile tests, Table 3.2, for the tensile strength, f_u, are significantly smaller at an average of 3%. Additionally, the values of f_u obtained show a positive correlation to the carbon content C(%), as seen in Figure 4.21.

Table 4.1. Average and Coefficient of Variation (c.o.v) of Calibrated Parameters for the Constitutive Stress-strain relationship per Steel Category

CATEGORY	E_0 MPa	f_y MPa	ε_{sh}	ε_u	f_u MPa	P	Ω_{fac}	Error
A6	215320	539	0.78%	11.0%	829	4.1	0.73	7.9%
	(3%)	(7.2%)	(16.2%)	(4.6%)	(2.1%)	(7.7%)	(3.9%)	(18.7%)
B6	218564	582	0.88%	10.9%	828	3.2	0.79	7.1%
	(1.7%)	(4.6%)	(11.1%)	(6.7%)	(1.5%)	(8.9%)	(3.8%)	(18%)
A7	222316	526	0.82%	10.1%	728	2.9	0.90	5.9%
	(0.8%)	(2.2%)	(23.7%)	(18%)	(0.7%)	(15.3%)	(5.8%)	(12.7%)
B7	227261	498	1.12%	13.8%	704	3.6	0.96	5.8%
	(1.8%)	(1.3%)	(22.8%)	(5.7%)	(2.3%)	(7%)	(5.5%)	(10.7%)
C7	219441	438	1.27%	15.9%	629	3.4	0.95	5.7%
	(0.7%)	(0.9%)	(23.1%)	(7.5%)	(1.3%)	(24.4%)	(1.8%)	(7.2%)
C6	225281	506	1.73%	13.3%	657	3.7	0.96	5.4%
	(1.5%)	(2.7%)	(29.9%)	(13%)	(3.2%)	(10.6%)	(1.4%)	(13.1%)

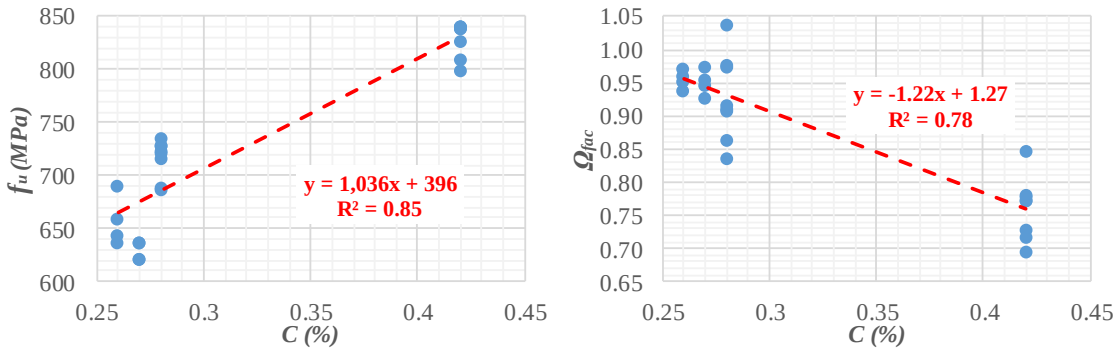

(a) (b)

Figure 4.21. Calibrated Parameter Ω_{fac} and f_u vs Carbon Content, C(%), for all Coupons Tested Under Cyclic Strain Histories: (a) f_u; (b) Ω_{fac}

A higher variability within steel categories is observed for ε_{sh}, with an average c.o.v. at 21%. This variability is expected due to the small influence of the parameter on the response predicted by the constitutive stress-strain relationship, see Sensitivity Analysis section. Given the large dispersion within each steel group, differences in ε_{sh} between categories are relatively small, with a constant value of ε_{sh} for all groups likely providing reasonable predictions of the stress-strain response, see Recommended Model Parameters section.

The uniform strain, ε_u, shows some variability within steel groups, with an average c.o.v. of 9.3%, see Table 4.1. The difference between categories is however noticeable, ranging from 10% to 16%. The results obtained for this parameter however, may not be representative of reinforcement in real structures, as the monotonic tests in tension showed a significant increase in ductility of machined over unmachined coupons, see Table 3.2.

The exponent for the strain hardening branch of the backbone curve, P, shows relatively high variability within steel categories, with an average c.o.v. of 12.3%. Given its limited influence in the hysteretic response of the constitutive stress-strain relationship after the first major strain reversal, an overall average among all steel categories, $P \approx 3.5$, could provide a good fit of the material model to experimental results.

The last parameter of the constitutive stress-strain relationship, controlling the shape of the Bauschinger curve, Ω_{fac}, has stable results within steel categories and distinctive values in-between them, see Table 4.1. Furthermore, the parameter shows a negative correlation to the carbon content, as anticipated by Dodd and Restrepo (1995), see Figure 4.21.

The calibration results presented herein were determined with the implementation of the constitutive stress-strain relationship using a Bezier curve for the Bauschinger effect. It was also verified that an analysis with the original iterative formulation yields almost identical results.

4.6. Sensitivity Analysis

Completing the study of the model parameters, a sensitivity analysis is performed over each cyclic record. In this analysis, the increment in error between measured and predicted stress-strain response is calculated for variations in each model parameter by a fraction of its optimal value, see Equation 4.38. The analysis was performed for each of the cyclic records, with Figure 4.22 showing the overall average.

$$e_{norm}(\mathbf{x}_{opt} + \mathbf{\Delta x_{opt}}) = \frac{error(\mathbf{x_{opt}} + \mathbf{\Delta x_{opt}})}{error(\mathbf{x_{opt}})} \qquad 4.38$$

Where error(**x**) is the function as defined in Equation 4.37, where $\boldsymbol{x_{opt}}$ is a vector containing the optimal parameters of the constitutive stress-strain relationship for the current record, and $\boldsymbol{\Delta x_{opt}}$ a vector with the variation in one of the optimal parameters being evaluated.

Results from Figure 4.22 shows both parameters P and ε_{sh} have an almost negligible effect on the predicted stress-strain response, within the ±25% range of variation evaluated in the figure. Following P and ε_{sh}, the uniform strain, ε_u, shows only small increments in the fit error within a ±10% variation of the parameter, with a relative error increment of 11% on average. For changes in the parameter of 25% or higher however, the fit error shows a significant relative increase, over 39% on average.

The response of the constitutive stress-strain relationship shows a similar sensitivity to both the Young's Modulus, E_0, and the yield strength, f_y, see Figure 4.22. The sensitivity to these variables is relatively high, with a variation of ±25% in either of them resulting in twice the optimal fit error. As seen in the previous section however, the Young's Modulus is very stable between different steel groups, with a c.o.v. of 2.5% among all the calibration results. Assuming a 5% maximum error in the estimation of E_0, when using the mean value E_0= 221360 MPa obtained in the previous section, the fit error will be, on average, only 14% higher than the minimum value. The yield strength, f_y, on the other hand, can vary significantly between steel coupons of the same grade (see Calibration of Model Parameters section), with differences of as much as 28% between tested coupons from different manufacturers. Considering that an error of ±10% in the estimation of the yield strength results on an average relative increase of 33% in the fit error, a good estimate of f_y is essential for the material model to predict an accurate stress-strain response.

The parameters the constitutive stress-strain relationship shows the most sensitivity to are Ω_{fac} and f_u, see Figure 4.22, with a ±25% variation in the optimal values increasing the fit error by a factor of 2.8 and 4.6, on average, respectively. From the calibration analysis results, both these parameters not only show great stability within each steel category, but can also be correlated to the carbon content C(%), see Figure 4.21. Given the high sensitivity of the constitutive stress-strain relationship, with a ±5% variation from the optimal value increasing the fit error by 19% for Ω_{fac} and 37% for f_u, an accurate estimate of these parameters is of great importance when using the Dodd-Restrepo material model.

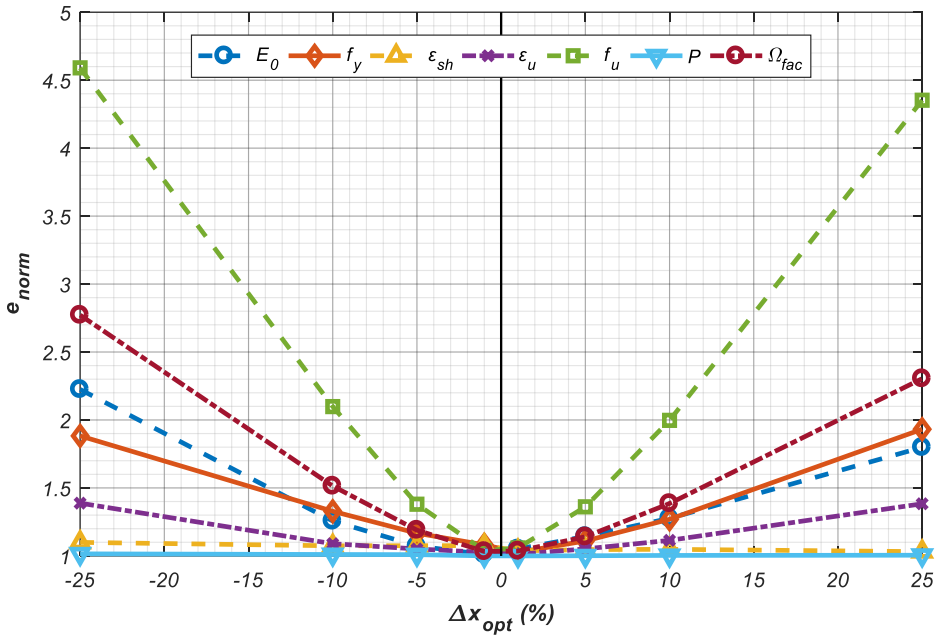

Figure 4.22. Average of Sensitivity Analysis Results from all Coupons Tested Under Cyclic Strain Histories

4.7. Recommended Model Parameters

Based on the results from calibration and sensitivity analyses, a set of parameter values of the Dodd-Restrepo constitutive stress-strain relationship are recommended for Grade 60 ASTM A615 (2016) and A706 (2016) steel reinforcement. Given the stability of the calibrated results for the Young's modulus among all tested coupons, an average value E_0 = 221 GPa can be used for machined coupons. For the Young's Modulus a correction factor shall be applied on the recommended value of E_0 to account for the differences observed between machined and unmachined coupons, see Table 3.2. These differences are mainly justified by the use of nominal instead of exact cross-section areas to compute the stress in unmachined coupons. From the average ratio of E_0 between machined and unmachined coupons in Table 3.2, the recommended Young's Modulus for the unmachined case is E_0 = 200 GPa.

A unique value is also recommended for parameters ε_{sh} and P in the constitutive stress-strain relationship, given the low sensitivity of the predicted cyclic response to these parameters. Based on the overall average results from calibration analysis, a value of ε_{sh}=1.1% and P = 3.5 can be used.

The calibration results for ε_u obtained from machined coupons in Table 4.1, may not be representative of unmachined steel bars, as observed from tensile tests on machined and unmachined coupons, see Table 3.2. Because of this, the results from pure tension tests of unmachined coupons are used for the recommended value of ε_u. Given the similarity between the uniform strains from each steel group in Table 3.2, with a small coefficient of variation at 5%, the overall average ε_u=10.6% is recommended for unmachined steel bars. The 5% c.o.v. between steel categories satisfies the limits to keep the stress-strain fit error small according to the sensitivity analysis of ε_u, which requires to use an estimate within 10% of the optimal value, see Figure 4.22. Since the results obtained herein stem from small diameter reinforcement, #4 bars, the recommended value for ε_u should decrease with larger diameter of reinforcement (see section 3.2.3 in Caltrans SDC, 2013).

For parameters f_u and Ω_{fac}, a correlation to the carbon content in the material, C(%), is found, with the following regression equations, see Figure 4.21:

$$f_u\left(MPa\right) = 1036 \cdot C(\%) + 396 \quad \text{(a)}$$
$$\Omega_{fac} = -1.22 \cdot C(\%) + 1.27 \quad \text{(b)} \qquad 4.39$$

Given the limited experimental data available in this study, the use of equations 4.39a and b can only provide rough estimates for parameters f_u and Ω_{fac}. For more accurate regression functions a larger database is required for statistically significant results.

Since the chemical composition of the reinforcement is not usually available to research and engineering professionals, recommended values are suggested on the basis of the typical carbon content per ASTM specification. For ASTM A706 (2016) Grade 60 steel, for which the standard defines an upper limit of 0.3% for the carbon content to enhance weldability, a typical value of C(%) = 0.28 results in recommended values for f_u and Ω_{fac} at 686 MPa and 0.93 respectively. In the case of the ASTM A615 (2016) standard, since no limitations are specified on the carbon content in the material, a higher variability in the value of C(%) is expected for specimens under the standard. Assuming an average carbon content C(%) = 0.36 for Grade 60 ASTM A615 bars, see Table 3.3, results in recommended values f_u = 769 MPa and Ω_{fac} = 0.83.

For the yield strength, f_y, the calibration analysis showed high variability between the tested steel categories, with differences as much as 28% between extreme values, and no evident correlation with other mechanical or chemical properties of the material. Furthermore, the predicted hysteretic responses showed significant sensitivity to changes in f_y, reaching twice the minimum fit error for a 25% deviation from the optimal f_y, see Figure 4.22. Based on these observations, and the limited number of coupons tested for this study, it was determined that to recommend values of f_y a more comprehensive statistical survey is required. The report by Bournonville et al. (2004) details a statistical analysis on 23,768 heats of steel from 29 mills in the United States and Canada, including a wide variety of bar sizes, grades and ASTM standards. Table 3.11 summarizes the results for f_y and f_u of Gr 60 ASTM A615 and A706 specimens extracted from this report. Based on these statistical results, the average value f_y=478 MPa is recommended for both ASTM

A615 and A706 Grade 60 reinforcement. When using the Dodd-Restrepo constitutive stress-strain relationship and the yield strength of the material is not available, a sensitivity analysis using the percentile values indicated in Table 3.11 is recommended.

Table 4.2 summarizes the recommended values suggested for each of the parameters in the Dodd-Restrepo constitutive stress-strain relationship.

Table 4.2. Recommended Parameter Values for Dodd-Restrepo Constitutive Stress-strain relationship

Parameter	Recommended Value	
E_0	200 GPa (29,000 ksi)	
f_y[§]	478 MPa (69 ksi)	
ε_{sh}[**]	1.1%	
ε_u	10.6%	
f_u[††]	769 MPa (112 ksi)	(ASTM A615)
	686 MPa (99 ksi)	(ASTM A706)
P	3.5	
Ω_{fac}[‡‡]	0.83	(ASTM A615)
	0.93	(ASTM A706)

[§] A sensitivity analysis using percentiles in Table 3.11 is recommended given the high variability in f_y

[**] Parameter value may decrease for bar diameters larger than the #4 coupons tested. However, the cyclic response is not significantly influenced by this parameter.

[††] Parameter the constitutive stress-strain relationship is most sensitive to. Use Equation 4.39 for a rough estimate if carbon content is known. Alternatively, consider performing a sensitivity analysis based on the percentile values for f_u in Table 3.11.

[‡‡] Constitutive stress-strain relationship shows high sensitivity to this parameter, consider using Equation 4.39 for a rough estimate if carbon content C(%) is known.

4.8. Verification of Recommended Parameters

The parameters proposed for the constitutive stress-strain relationship in Table 4.2, are verified with experimental test results independent from the calibration analyses. A study performed in 2011 at UC San Diego's Charles Lee Powell Laboratories studied the cyclic response of reinforcing bars under different unsupported lengths, evaluating the effect of buckling. A series of #4 Grade 60 ASTM A706 unmachined bar coupons, from a different batch than those used in the calibration analysis, were tested under cyclic strain histories for unsupported lengths of 3, 6 and 9 bar diameters, $d_{b\ell}$. The stress-strain response from two coupons with the lowest unbraced length (3 $d_{b\ell}$), and therefore the smallest non-linear geometry effects, is compared to the results of the constitutive stress-strain relationship using the recommended model parameters. As seen in Figure 4.23, the hysteretic response of the recommended parameter values in Table 4.2 significantly overestimate the stress in experimental results. This difference comes from the overestimation of the tensile strength, f_u, in the tested steel coupons, measured at 620 MPa from a monotonic test in tension, which lies below the 25th percentile indicated by Bournonville et al. (2004), see Table 3.11. When the parameter f_u is modified to 620 MPa, the predicted stress-strain response attains a very close fit of the experimental results, see Figure 4.24.

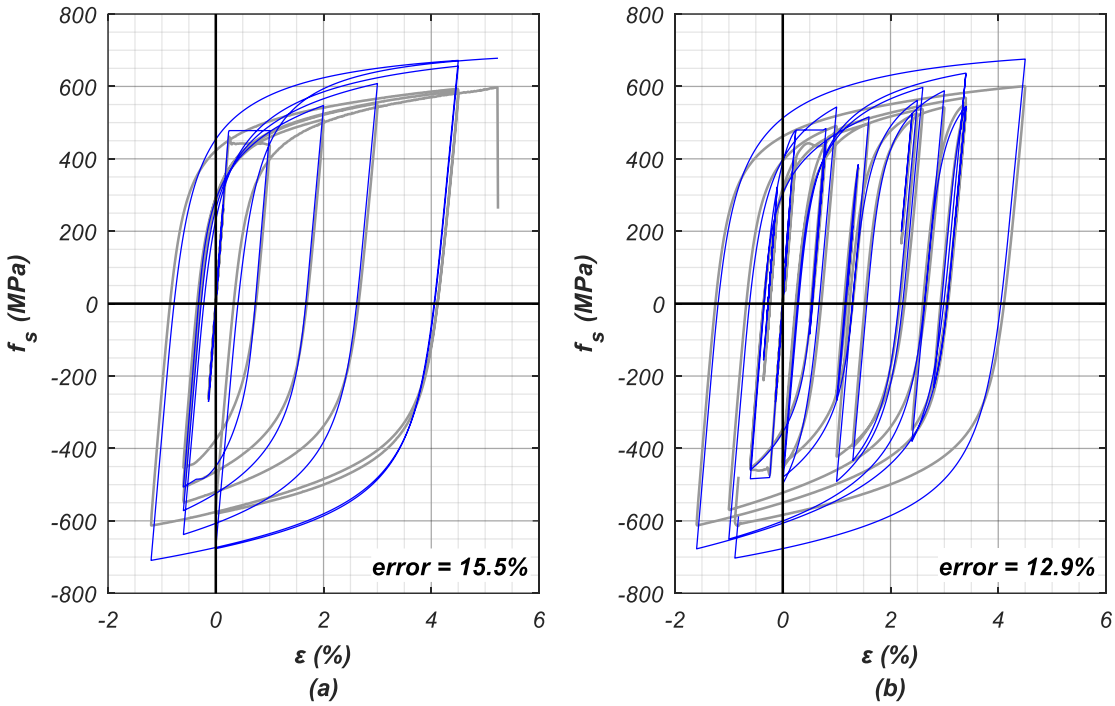

Figure 4.23. Verification Example, Experimental vs. Predicted Response Using Recommended Model Parameters in Table 4.2.

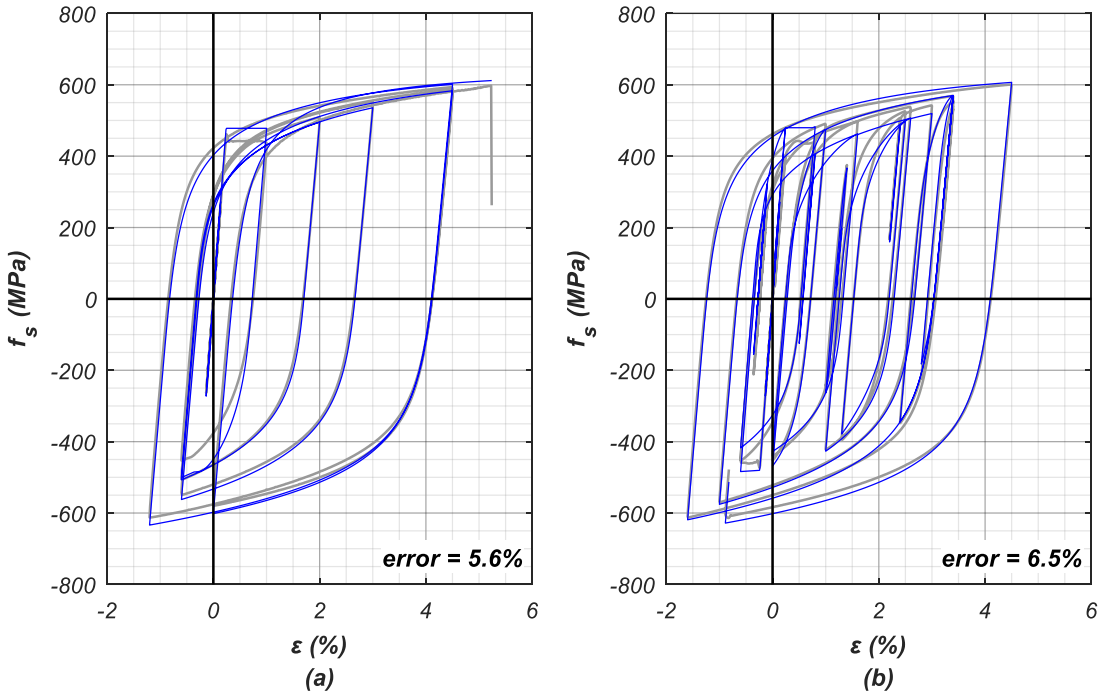

Figure 4.24. Verification Example, Experimental vs Predicted Response Using Recommended Model Parameters in Table 4.2, and f_u = 620 MPa from Tensile Test

4.9. Analysis of Large Scale Model

A full-scale bridge column tested under seismic load at UC San Diego's Large High-Performance Outdoor Shake Table (LHPOST) in 2010 (Schoettler et al. 2012), was modeled in OpenSees using two material models for the reinforcing steel: *STEEL02* and *SteelDRC*. *STEEL02* corresponds to the commonly used constitutive stress-strain relationship by Giuffrè-Menegotto-Pinto (Menegotto and Pinto, 1973), while *SteelDRC* is the improved Dodd-Restrepo model implemented in this study. The response from each model was then compared to the experimental results, both at the global and local level.

The full-scale bridge column in Figure 4.25 was designed according to Caltrans design guidelines and post-tensioned to the shake table for a fixed-base configuration. A large concrete mass ($W_{top} = 2.5 \cdot 10^{10}$ kN-m^2/g) was positioned at the free top of the column to account for the superstructure mass.

Figure 4.25. Full-Scale Bridge Column Tested Under Seismic Loading at UC San Diego's Large High-Performance Outdoor Shake Table (Schoettler et. al 2012)

Based on the known dimensions, reinforcement configuration (Figure 4.26), and properties of the concrete and steel reinforcement, see Table 4.3, a fiber-discretization model, using a single force-based element for the column was developed in OpenSees (McKenna et al. 2000). The model uses a corotational geometric transformation to account for second order effects (e.g. P-Δ) and a modified Radau hinge integration (Scott, 2011) with the equivalent plastic hinge length as defined by Paulay and Priestley (1992), see Equation 4.40.

$$L_p = 0.08 \cdot L + \frac{0.022}{MPa} \cdot d_{b\ell} \cdot f_{y\ell} \qquad 4.40$$

Where L_p is the equivalent plastic hinge length, L is the length of the columns, $d_{b\ell}$ is the diameter of the longitudinal bars, and $f_{y\ell}$ is the yield strength of the longitudinal reinforcement.

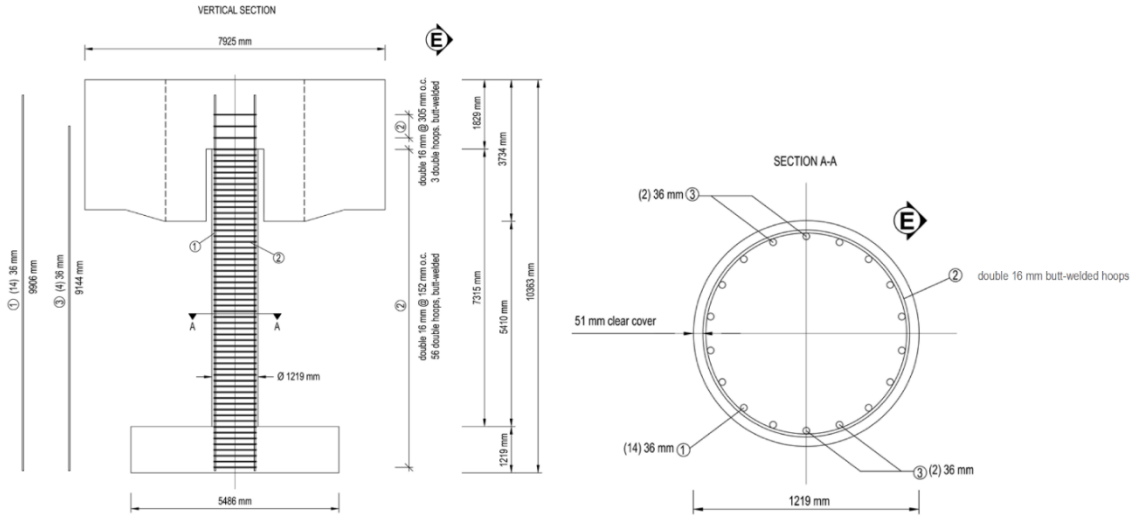

Figure 4.26. Reinforcement Configuration in Full-Scale Column (Schoettler et al. 2012)

Table 4.3. Material Properties of Large-Column Test (Schoettler et al. 2012)

Material	Properties
Concrete	f'_c = 42 MPa ε_{c0} = 0.26% E_c = 22900 MPa
Longitudinal Reinforcement	f_y = 519 MPa E_s = 196000 ε_{sh} = 1.1% ε_u = 12.2% f_u = 707 MPa
Transverse Hoops	f_y = 338 MPa ε_u = 12.5% f_u = 592 MPa

Two models, one per constitutive stress-strain relationship for the reinforcing steel, were subjected to a time-history analysis using the base acceleration records from all ten consecutive earthquakes used in the testing of the bridge column. The results for earthquakes 3 through 9 are presented herein, given the little non-linear behavior observed in first two records, and the mass at the top of the column impacting the safety restraints during the last earthquake.

To analyze the effect of the constitutive stress-strain relationship used for the reinforcing steel in the global response, Figure 4.27 compares the predicted displacement histories at the top of the column to the experimental results. The predicted peak displacements from each model closely resemble the experimental results, see Table 4.4, with the biggest difference observed in the residual values after each record. While the *STEEL02* model shows very small residuals after each earthquake, the *SteelDRC* model

can capture some larger residual displacements, although a close match to the experimental results is only achieved after two of the records (earthquakes 3 and 8).

The models are also compared in terms of the base shear vs displacement response, see Figure 4.28. From the figure, similar responses are observed from the two OpenSees models, although results from *SteelDRC* show less "pinching". The experimental base-shear of the column is highly influenced by the rotation of the mass at the top, producing the particular shape observed in Figure 4.28, and higher amplitudes than the analytical responses, see Table 4.4.

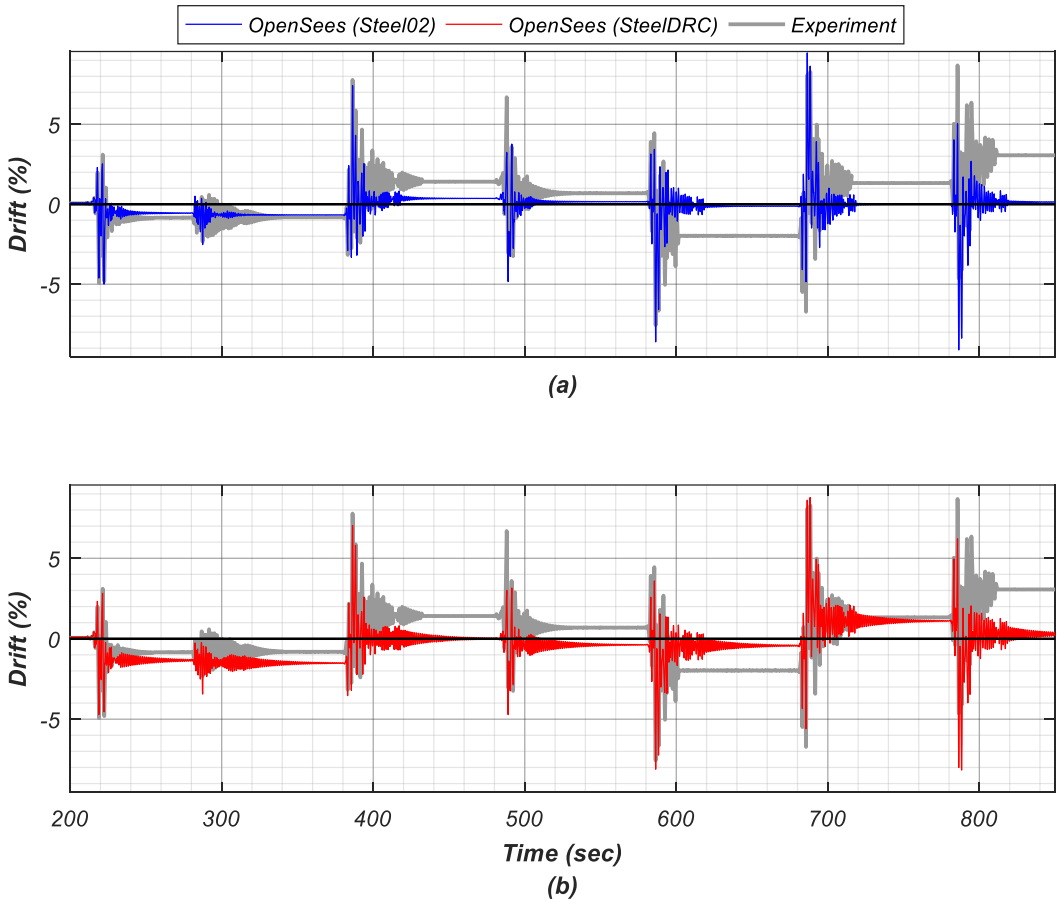

Figure 4.27. Drift History at the Top of the Bridge Column for Earthquakes 3 to 9: (a) Experimental vs OpenSees with Steel02; (b) Experimental vs OpenSees with SteelDRC

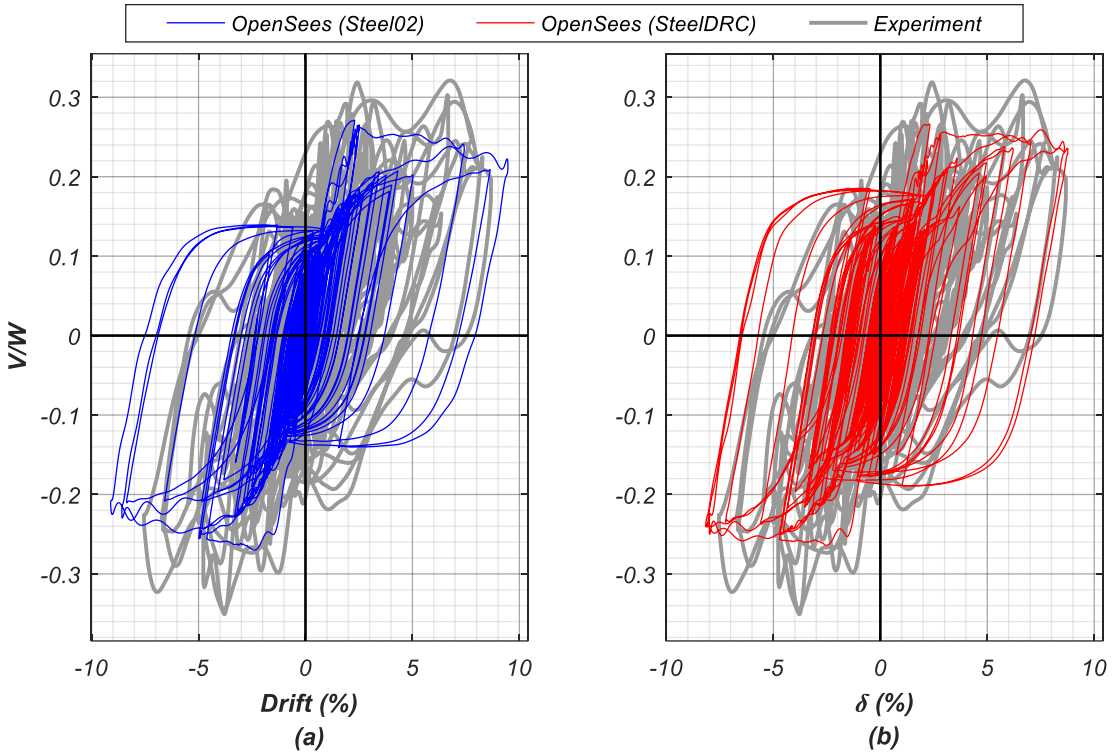

Figure 4.28. Normalized Base Shear vs Drift at the Top of the Column for Earthquakes 3 to 9: (a) Experimental vs OpenSees with Steel02; (b) Experimental vs OpenSees with SteelDRC

For the effect of the constitutive stress-strain relationship on the local response of the model, the Moment-Curvature response at the base of the column is shown in Figure 4.29. Unlike the base-shear response, the rotation of the concrete block at the top of the column has little effect in the experimental moment. Both OpenSees Models under-estimate the Moment and Curvature values found experimentally, see Table 4.4, which could be corrected by changing the equivalent plastic hinge length L_p, for the curvature, and increasing the stress capacity of the confined concrete core for the moment. Similar to the base-shear response, the *SteelDRC* model shows less "pinching" in the response.

Results in this section show that the *SteelDRC* implementation can be used reliably in larger scale models with highly non-linear behavior and multiple cycles, with results comparable to those obtained with the commonly used *STEEL02* model.

It is noted that reinforced concrete elements using *SteelDRC*, unlike with *STEEL02*, can suffer from localization issues (Coleman and Spacone, 2001), given the representation of softening and fracture of the material at large strains by the constitutive stress-strain relationship.

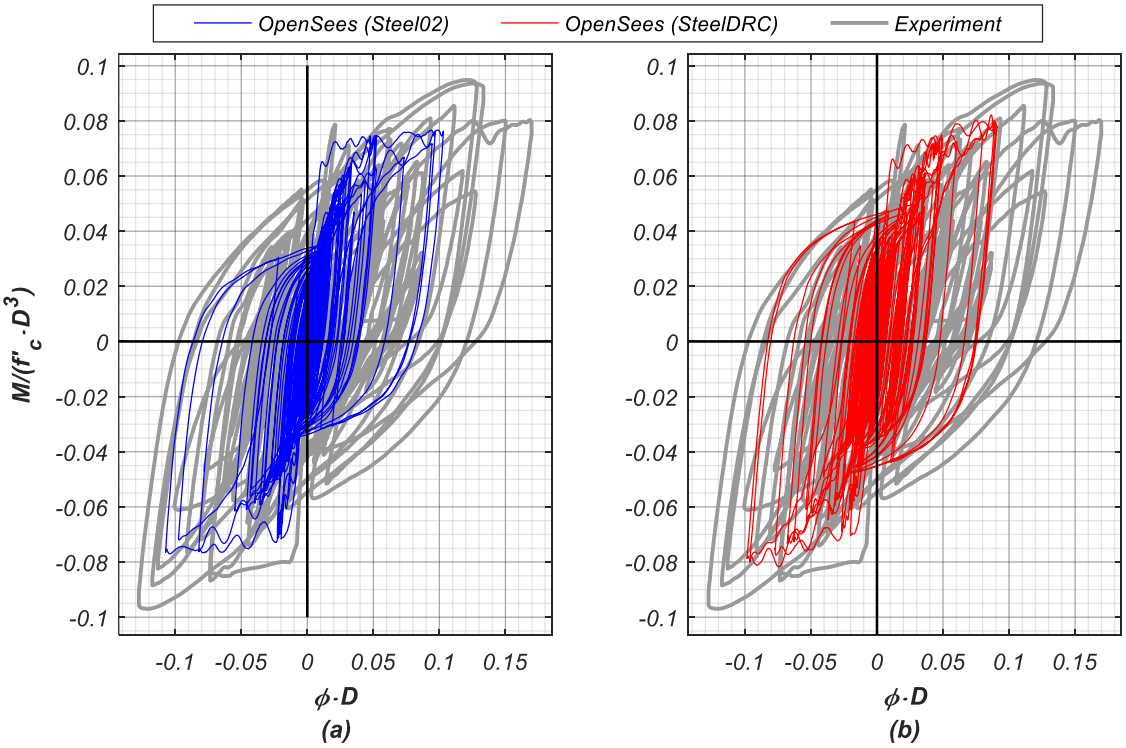

Figure 4.29. Normalized Moment vs Normalized Curvature at the Base of the Column for Earthquakes 3 to 9: (a) Experimental vs OpenSees with Steel02; (b) Experimental vs OpenSees with SteelDRC

Table 4.4. Peak Global and Local Response Values for Bridge-Column. Comparison of Experimental and OpenSees Models Results

	Δ (m)		Base shear (kN)		Moment (kN-m)		Curvature (1/m)	
	min	max	min	max	min	max	min	max
Experimental	-0.55	0.64	-887	813	-7378	7215	-0.105	0.140
OpenSees (SteelDRC)	-0.60	0.64	-668	674	-6218	6248	-0.081	0.074
OpenSees (Steel02)	-0.67	0.69	-683	686	-5859	5833	-0.088	0.085

4.10. Conclusions

In this study, a series of improvements to the constitutive stress-strain relationship by Dodd and Restrepo, including a closed-form Bauschinger curve, a post-necking stress-strain response, and alternative definitions for the output tangent modulus, are implemented into OpenSees in the uniaxial material model *SteelDRC*.

Based on cyclic tests on #4 Grade 60 bars from three different manufacturers, and complying with two ASTM standards (A615, 2016, and A706, 2016), the parameters of the Dodd-Restrepo constitutive stress-strain relationship were calibrated by minimizing the least squared error between the measured and predicted stress histories. The sensitivity of the predicted stress-strain response to variations of each parameter was also assessed, finding that parameters ε_{sh}, P and ε_u have the least influence in the predicted cyclic response, while the parameters the predicted response is most sensitive to are, in ascending order: E_0, f_y, Ω_{fac} and f_u. Calibration analysis results also showed that two material parameters, f_u and Ω_{fac}, can be correlated to the carbon content, which is consistent with observations made by Dodd and Restrepo (1995). A set of recommended parameter values for Grade 60 reinforcement, dependent on the ASTM Standard (A615 or A706), is summarized in Table 4.2. A verification example, using steel coupons not involved in the

calibration analysis, shows the close fit to the measured hysteretic response attained by the material model when the tensile strength of the material is estimated accurately. When only limited information is available for the tensile and yield strength of the reinforcement in a structure, performing a sensitivity analysis in the Finite Element model is recommended, using the statistical results extracted from Bournonville et al. (2004), see Table 3.11.

Using a large-scale structural model, the Dodd-Restrepo constitutive stress-strain relationship implemented in OpenSees, *SteelDRC*, is evaluated against the commonly used formulation by Giuffrè-Menegotto-Pinto, *STEEL02*, comparing responses at the global and local level. Experimental results from a full-scale bridge column, tested under seismic load (Schoettler et al. 2012), are used to evaluate the accuracy of OpenSees models using each reinforcing steel implementation. Results from this analysis show that the implementation of the constitutive stress-strain relationship provides reliable results for large scale-highly non-linear structural models undergoing multiple cycles. Furthermore, the results obtained with *SteelDRC* are comparable with results from *STEEL02*.

Chapter 4, in full, is currently being prepared for submission for publication of the material. Carreño, Rodrigo; Lotfizadeh, Koorosh; Conte, Joel P.; and Restrepo, José I. The dissertation author was the primary investigator and author of this paper.

Chapter 5.

EXPERIMENTAL WORK ON LARGE DIAMETER STEEL REINFORCEMENT

5.1. General

This chapter covers the design and implementation of a loading apparatus capable of cyclically testing large diameter reinforcing steel bars under large strain amplitudes. The main objective is to characterize the plastic buckling-straightening fatigue (PBSF) life of the bars, commonly known as “low-cycle fatigue”. The innovative use of a modified sulfur-based concrete to grip the bars is explained along with the many aspects required to perform the experimental work. Experimental issues and the solutions implemented are also covered. The material properties and geometrical characteristics of the tested large diameter bars are detailed herein. The geometrical characteristics are explored to investigate their effect on the fatigue life of the bars. The procedure to generate the loading protocols for the experimental work is described, along with the main experimental results obtained.

The design of the loading apparatus and loading protocols used for testing was part of the work by Mr. David Duck, a current PhD student. The experimental work and processing of the results was carried-out jointly by the author and Mr Duck, thus an extended version of this Chapter will be included in his PhD Dissertation (see Duck et al. 2018)

5.2. Test setup

5.2.1. Bar Gripping

To avoid issues with bar gripping experienced by other authors who attempted similar experimental work, an innovative approach was taken by embedding the ends of the bars into a highly-confined modified sulfur and aggregate mix, referred to as sulfur concrete henceforth. As described in ACI 548.2R (1993), sulfur concrete is a thermoplastic material prepared by hot-mixing modified sulfur and mineral aggregates. The three main characteristics of sulfur concrete that made it an ideal material for the gripping mechanism are: 1) it solidifies and gains strength rapidly upon cooling, 2) can be remelted and reused, and 3) has a high strength and fatigue resistance. The rapid gain of strength after cooling allows for a relatively fast turnaround between tests using a single test setup, that otherwise would not be possible.

Compression tests on a series of sulfur concrete mix design cylinders were performed to obtain the best grip. Different amounts of 3/8-in. diameter smooth beach pebbles and crushed aggregates were mixed with different ratios of plasticized, silica filled modified sulfur, see Figure 5.1. A mix consisting of 33.8% (by weight) crushed aggregate, 35.7% (by weight) smooth beach pebbles, and 33.5% (by weight) modified sulfur, which

recorded a compressive strength of 6.3 ksi after 2 days was used for the lower pipe grip (LPG), while a mix of 55.9% and 44.1% of crushed aggregate and modified sulfur, with a recorded compressive strength f'_c= 8.5 ksi after 10 days, was used for the upper pipe grip (UPG).

(a) (b) (c)

Figure 5.1. Sulfur Concrete Mix Design Materials: (a) 3/8 in. Diameter Smooth Beach Pebbles; (b) 3/8 in. Diameter Rough Crushed Aggregate (c) Plasticized, Hot-Pour Silica Filled, Modified Sulfur

5.2.2. Loading Apparatus Specifications

A crucial aspect of the research effort was the design of a loading frame capable of testing large-diameter #18 Grade 60 bars under large strain amplitude cyclic loading, see Figure 5.2. The test apparatus had to be sufficiently rigid to sustain the buckling of the #18 bars while providing near full fixity. A finite element model analysis in SAP2000 showed that, when the plastic moment from the #18 reinforcement is applied to the pipe system, it will remain well within the elastic range, with a maximum expected rotation at the top of

the pipe of 1.61×10^{-4} radians, or about 8.05% of the maximum allowable rotation of 0.002 radians, see Duck et al. (2018)

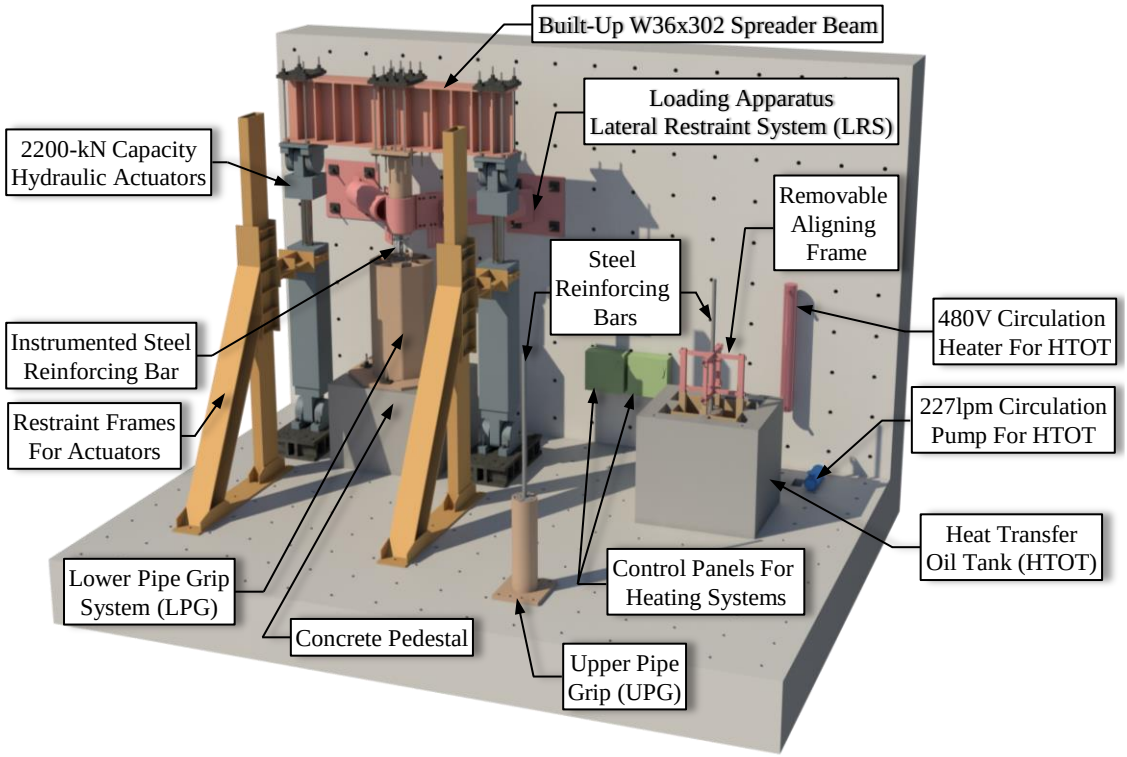

Figure 5.2. 3D Rendering of Loading Frame Apparatus (Duck et al. 2018)

To provide sufficient stiffness to the upper pipe grip, a lateral bracing system allowing the movement and removal of the pipe, was required. Given the issues faced by other authors attempting similar experimental work, the bracing system for the loading frame was designed to resist the moment applied by the buckled bars without allowing excessive out-of-plane movement. A system consisting of an outer sleeve through which the pipe grip could slide was chosen, see Figure 5.3. Friction between the pipe and the sleeve was reduced by providing a greased brass interface (see Duck et al. 2018)

Figure 5.3. View of Bottom Pipe with Heater Terminals and Lateral Bracing System Connected to Strong-Wall

Given the high confinement provided by the pipes and using results from bond slip tests performed by Murcia-Delso et al. (2011), the minimum embedment length of $25d_{b\ell}$ recommended by AASHTO (2014) to develop the #18 bars embedded in 5,000 psi concrete was reduced to $19d_{b\ell}$ for the design of the upper pipe. Given the complexity of the LPG, a larger development length equal to $28d_{b\ell}$ was used in the design, to allow for future use in the testing of high-strength Grade 80 bars. Similar to Mander (1983), 4-in. thick circular steel end blocks with a 2.5 in. center hole were placed around the test specimens on both pipe grips at the surface of the sulfur concrete to restrain the bars when buckling occurs, see Figure 5.4. These blocks simulate the restraint provided by the transverse reinforcement in a column and the cone formed at the base of RC columns after cyclic loading. The steel blocks were supported by L-shaped brackets welded around the inside of the pipes, see Figure 5.5.

Axial load was applied using two 500-kip capacity servocontrolled hydraulic actuators connected by a heavily-reinforced, built-up, W36x302 spreader beam, see Figure 5.2.

Figure 5.4. Circular End-Blocks

Figure 5.5. L-shaped Brackets Welded Inside the Pipes to Support the Circular End Blocks

5.2.3. Development of the Earthquake Smeared Strain History Protocol

To develop a strain history for use in the bar buckling test apparatus, a strain history was derived from the experimental results of a full-scale bridge column tested at the single axis Large High-Performance Outdoor Shake Table (LHPOST) at the University of California - San Diego (Schoettler et al., 2012), see Figure 5.6.

Figure 5.6. Overall View of Full-Scale Reinforced Concrete Column Tested at the Large High-Performance Outdoor Shake Table at the University of California – San Diego (Schoettler et al., 2012)

Smeared longitudinal strains and curvatures were computed from the vertical displacement sensors placed on the North and South faces (perpendicular to the direction of shaking). The vertical displacement sensors were spaced 8 in. apart, starting 2 in. above the column base and extending for 48 in. (i.e. one column diameter). Above this, 24 in. and 31 in. spacings were used, see Figure 5.7 and 5.80. The 2-in. spacing at the column base was left to minimize the effect of fixed-end rotations, caused by strain penetration of the column bars anchored in the foundation, in the curvatures and strains derived from these sensors. The fixed-end rotation was monitored using two pairs of vertical displacement sensors, which spanned the horizontal crack expected to develop at the column-foundation interface (Schoettler et al. 2012).

The experimental work was completed after several longitudinal bars fractured in the plastic hinge region of the column, while the others showed significant signs of buckling, see Figure 5.9.

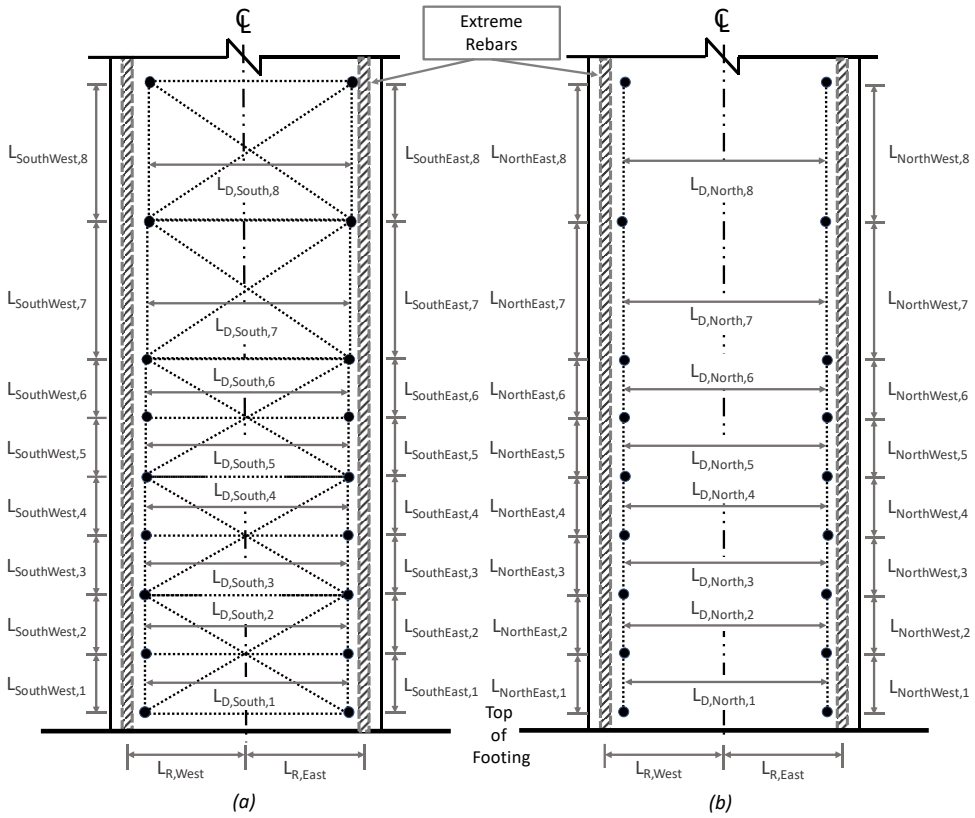

Figure 5.7. Schematics of Column Deformation Panels on: (a) South Face; (b) North Face (Duck et al. 2018)

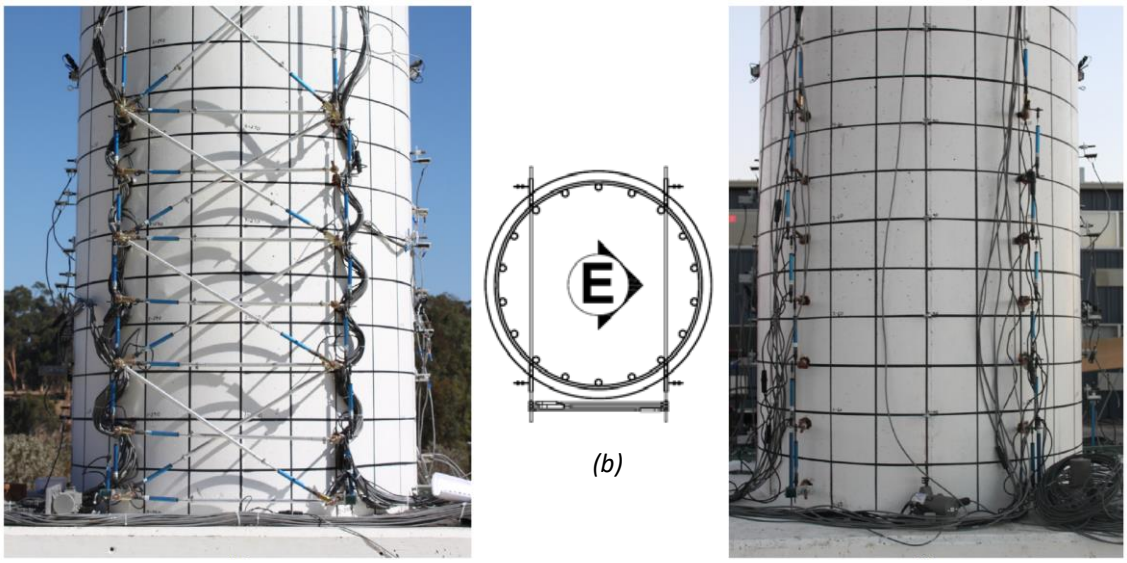

Figure 5.8. Curvature, Shear, and Fixed-End Rotation Linear Potentiometers of the Full-Scale Column: (a) Instrumented South Face (b) Plan View of Column and Linear Potentiometers; (c) Instrumented North Face (Schoettler et al., 2012)

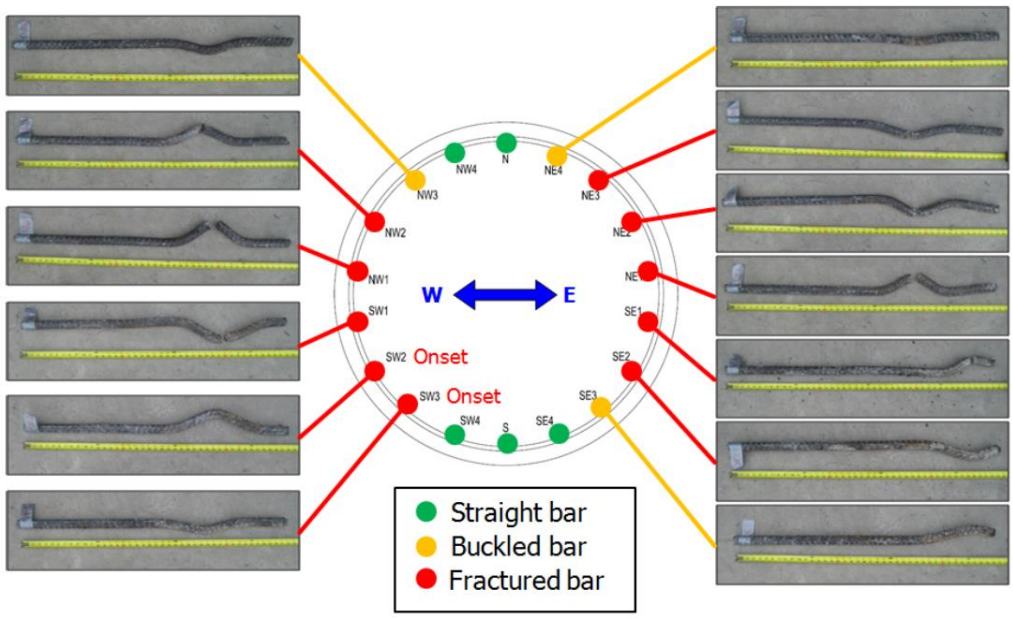

Figure 5.9. Longitudinal Bars Extracted from Column after Completion of Experimental Work (Schoettler et al., 2012)

The classical approach to obtain longitudinal strains and strain histories from one such column, has been the use of an equivalent plastic hinge length, L_p, following the form:

$$L_p = \alpha \cdot L + \beta \cdot f_{ye} \cdot d_{bn} \qquad 5.1$$

where L is the column shear span, f_{ye} is the expected yield strength and d_{bn} is the nominal diameter of the column longitudinal bar. The first term on the right side of Equation 5.1 corresponds to the contribution of the spread of plasticity along the column height to L_p, while the second term in the equation accounts for the strain penetration effect. Supported on the experimental work carried out in columns at the University of Canterbury in the late 1970s and 1980s, Paulay and Priestley (1992) proposed the coefficients α = 0.08 and β = 0.15/ksi for Equation 5.1. These coefficients have been adopted by SDC (2013).

Figure 5.10a depicts a laterally loaded column that has been displaced well past yielding to a displacement Δ. Figure 5.10b and c show the bending moment diagrams and corresponding curvature diagrams at two stages of loading: (i) at first yield and (ii) at a stage well into the plastic range where a plastic hinge has developed in the column. Figure 5.10d shows the idealized curvature diagram used by Paulay and Priestley (1992) to define the equivalent plastic hinge length for the second loading stage. In this approach, the maximum curvature in the idealized curvature diagram is made equal to the peak curvature, ϕ_k, computed for the test column at a stage of loading well into the plastic range. This assumption makes it possible to determine coefficients α and β and the equivalent plastic hinge length L_p (Restrepo et al., 2006).

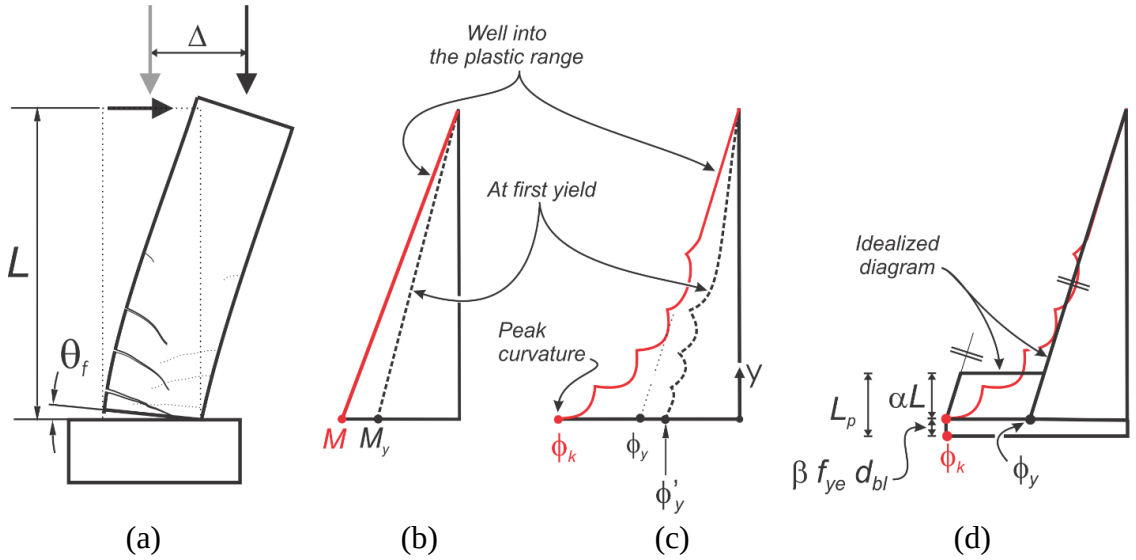

Figure 5.10. Definition of Peak Curvature-based Equivalent Plastic Hinge Length L_p: (a) Column; (b) Bending Moment Diagram; (c) Curvature diagram; (d) Idealized Curvature Diagram (Duck et al. 2018)

Figure 5.11 compares coefficients α and β calculated using the approach proposed by Paulay and Priestley for the test column with the coefficients proposed by these researchers. The values of coefficient α calculated for the experiment, see Figure 5.11a, increase with the drift ratio (or with the displacement ductility). That is, as the column undergoes further plastic displacements, the portion of the equivalent plastic hinge length spreading over the column increases as the displacement ductility increases. The correlation of coefficient α with ductility had also been pointed out by Restrepo et al. (2006). This means that a constant coefficient α seems to be only a fair approximation. The values of coefficient β calculated for the test column, see Figure 5.11b, are largely uncorrelated with the imposed drift ratio (or displacement ductility), an observation also made by Restrepo et al. (2006), which justifies the use of a constant value for this coefficient. Nevertheless, in this test, the values of coefficient β are much lower than that

those recommended by Paulay and Priestley. Restrepo et al. (2006) had reported values of β greater than the proposed value of β = 0.15/ksi.

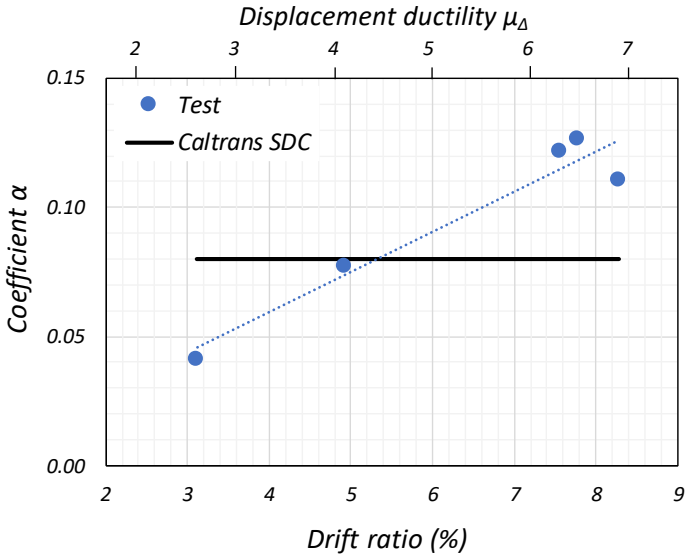

(a)

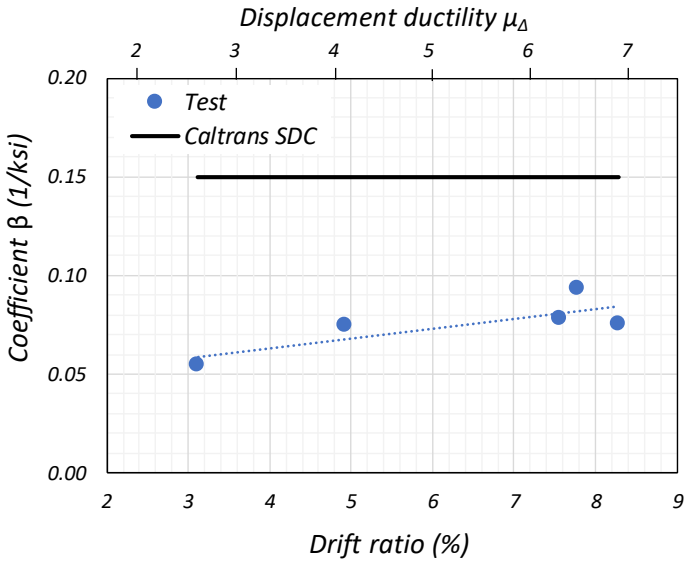

(b)

Figure 5.11. Comparison of Equivalent Plastic Hinge: (a) Coefficient α; (b) Coefficient β. (Duck et al. 2018)

The significant correlation between coefficient α and displacement ductility implies that the equivalent plastic hinge length, L_p, is also correlated with displacement ductility, something that is not recognized in Equation 5.1, see Figure 5.12.

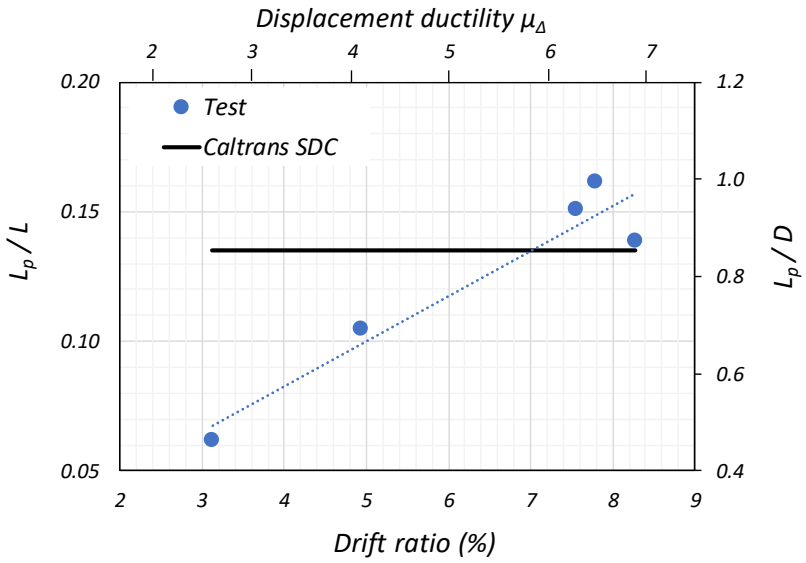

Figure 5.12. Comparison of Equivalent Plastic Hinge Lengths (Duck et al. 2018)

The development of longitudinal bar strain histories from the approach proposed by Paulay and Priestley (1992), using a ductility independent equivalent plastic hinge length, will therefore distort the strain amplitudes at low and at large displacement ductilities, which will have an effect in the prediction of the strain amplitudes to determine the life of a bar. A more suitable approach is to calculate longitudinal strain histories using a smeared strain compatible equivalent plastic hinge length, $L_{p\varepsilon}$. In this approach, the equivalent plastic hinge experiences a smeared curvature, $\bar{\phi} < \phi_k$, see Figure 5.13, such that the test strains recorded on the extreme longitudinal bars in tension and compression,

each smeared over length $L_{p\varepsilon}$, equals the strains computed from a moment-curvature analysis at curvature $\bar{\phi}$, Figure 5.14.

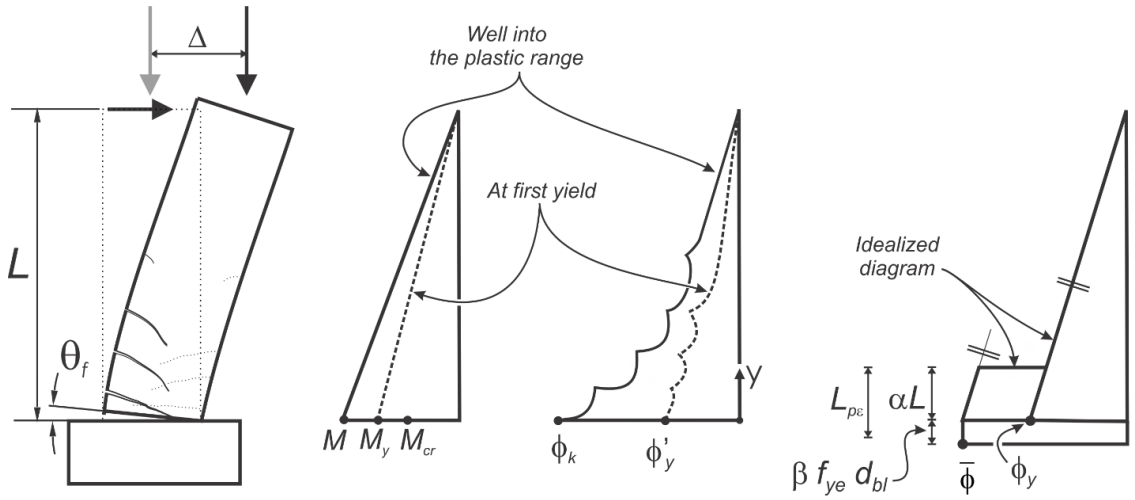

(a) (b) (c) (d)

Figure 5.13. Definition of Smeared Curvature-based Equivalent Plastic Hinge Length $L_{p\varepsilon}$: (a) Column; (b) Bending Moment Diagram; (c) Curvature diagram; (d) Idealized Curvature Diagram (Duck et al. 2018)

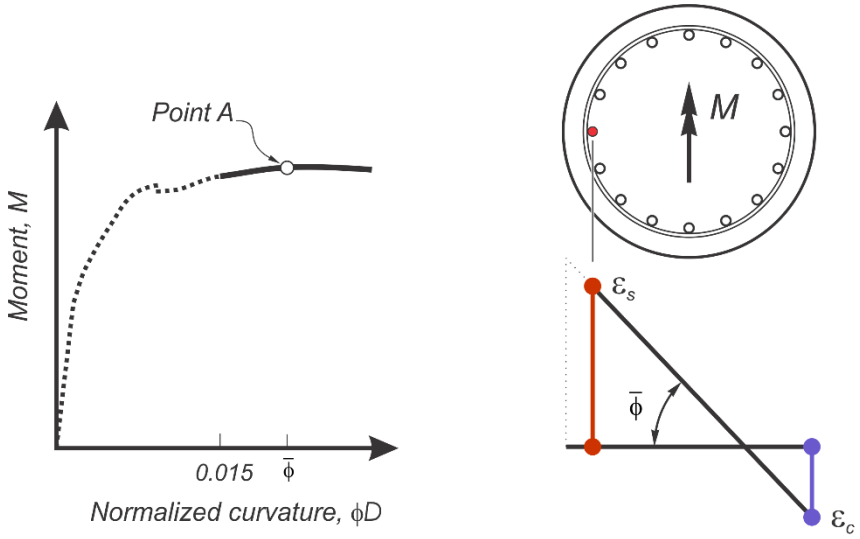

(a) (b)

Figure 5.14. Definition of Smeared Curvature-based Equivalent Plastic Hinge Length $L_{p\varepsilon}$: (a) Domain Used in the Theoretical Moment-Curvature Response; (b) Cross Section, Curvature and Key Strains at Point A (Duck et al. 2018)

An optimization procedure of the experimental data recorded during column testing (Schoettler et al. 2012) resulted in the coefficient values α = 0.248 and β = 0.15/ksi for the smeared curvature-based equivalent plastic hinge length, resulting in $L_{p\varepsilon}$ = 0.3L = 1.82D, or $L_{p\varepsilon}$ = 2.24L_p. As expected, the use of the smeared curvature and smeared strains results in a length $L_{p\varepsilon}$ significantly greater than L_p and 0.5D, a value often cited for the equivalent plastic hinge length, which clearly indicates the two equivalent plastic hinge length definitions are not interchangeable. The advantage of the smeared curvature equivalent plastic hinge length is that, at constant value, it can predict very closely the test tensile and compressive strains smeared over the length $L_{p\varepsilon}$ for the entire range of drift ratios and displacement ductilities, see Figure 5.15.

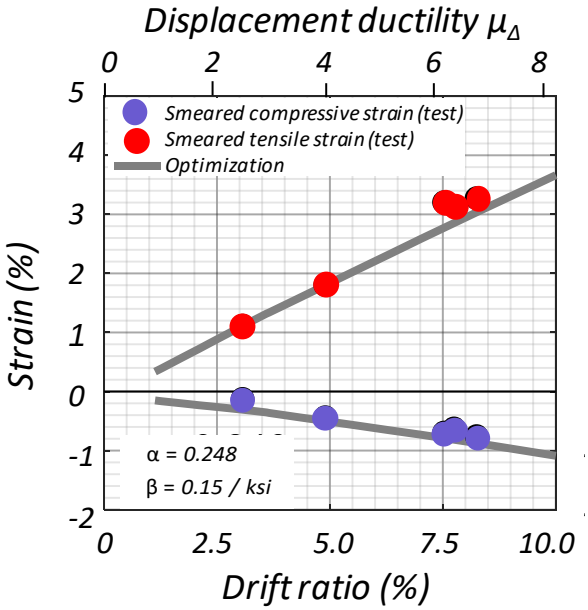

Figure 5.15. Smeared Tensile and Compressive Strains Measured along $L_{p\varepsilon}$ against Predicted Values from Idealized Curvature Distribution using $L_{p\varepsilon}$ at different Displacement Levels (Schoettler et al. 2012)

Figure 5.16a shows the smeared strain history computed using length $L_{p\varepsilon}$ for an extreme longitudinal bar in the test column reported by Schoettler et al. (2012) during the first eight ground motions, see Figure 5.16a. This strain history was simplified to capture the most relevant reversed cycles, see Figure 5.16b, and then simplified further to generate the "random" protocol used for testing of the rebar specimens, see Figure 5.16c.

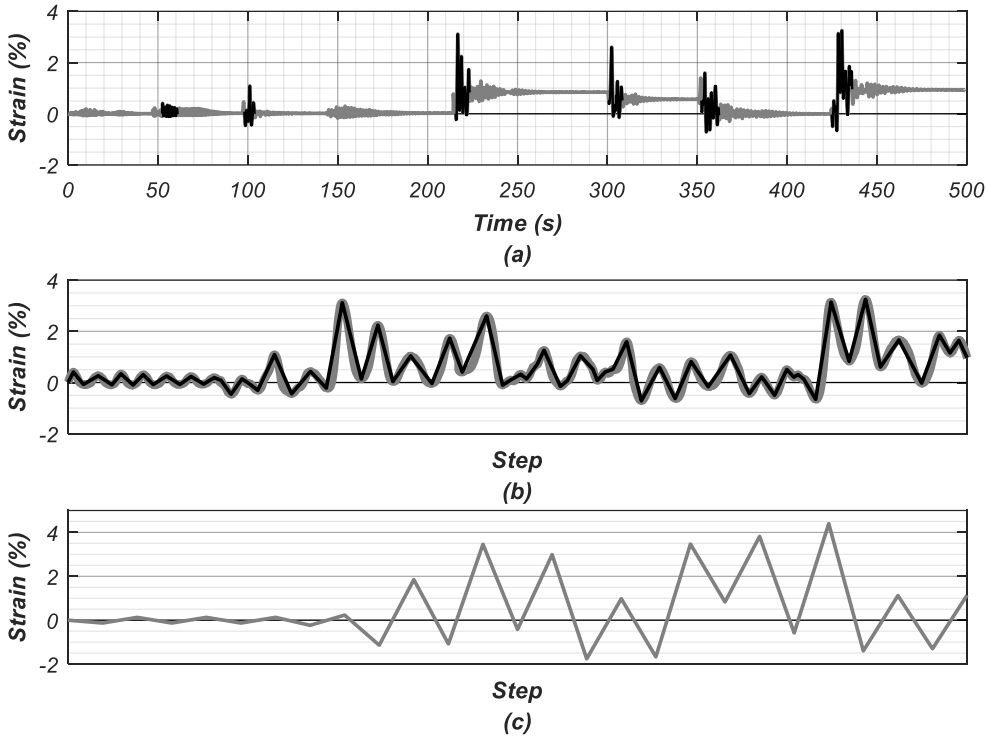

Figure 5.16. Strain History of Long. Bars from Testing of Full-Scale Bridge Column: (a) Complete Strain History; (b) Condensed Strain History; (c) Simplified Strain History used for Testing

5.2.4. Mean Strain History Protocols

Besides the "random" strain history depicted in Figure 5.16c, a series of constant amplitude tests were also performed for the various aspect ratios, $\ell/d_{b\ell}$, of the rebar specimens used in the experimental work. These tests were performed to establish a

relationship between deformation amplitude and the number of cycles to failure, to allow for comparison with current fatigue models. All constant amplitude strain histories began with a series of three elastic cycles with an amplitude equivalent to half the expected yield strain of the bars. After the elastic cycles, constant amplitude cycles with strain amplitudes ranging from 2.8% to 4.5%, were used until fatigue failure of the specimens. The complete histories are shown in Figure 5.17.

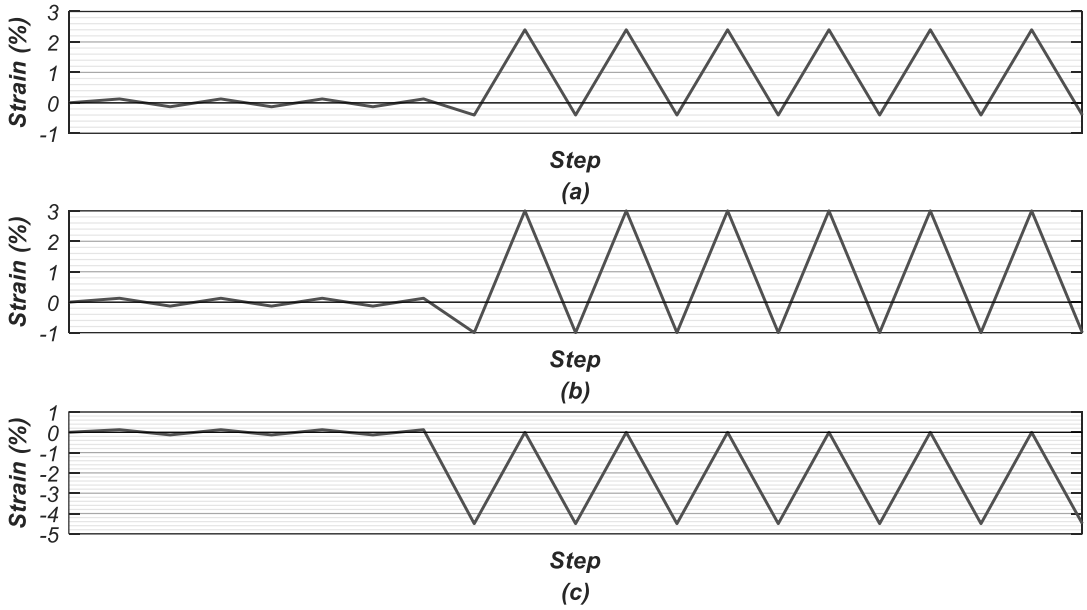

Figure 5.17. Constant Amplitude Strain Histories

5.3. Reinforcing bar Properties

Four monotonic tensile tests were performed on ASTM A706 Grade 60 bars from two different manufacturers (MFR-A and B) to obtain their mechanical properties. Testing procedures were according to ASTM E8 (2016) using a closed-loop active hydraulic SATEC universal testing machine. Two sets of bars were tested per manufacturer, where MFR-A corresponds to the bars provided by Manufacturer-A and MFR-B corresponds to

bars provided by Manufacturer-B. Complete monotonic stress-strain responses of the bars, up to fracture, were recorded for all specimens. Strain measurements were obtained using both a 2-in. gage length extensometer and an in-house designed clip gage. Stresses were obtained by dividing the force exerted by the machine, by the nominal bar area. The results of all four tests are plotted in Figure 5.18 and the material properties tabulated in Table 5.1.

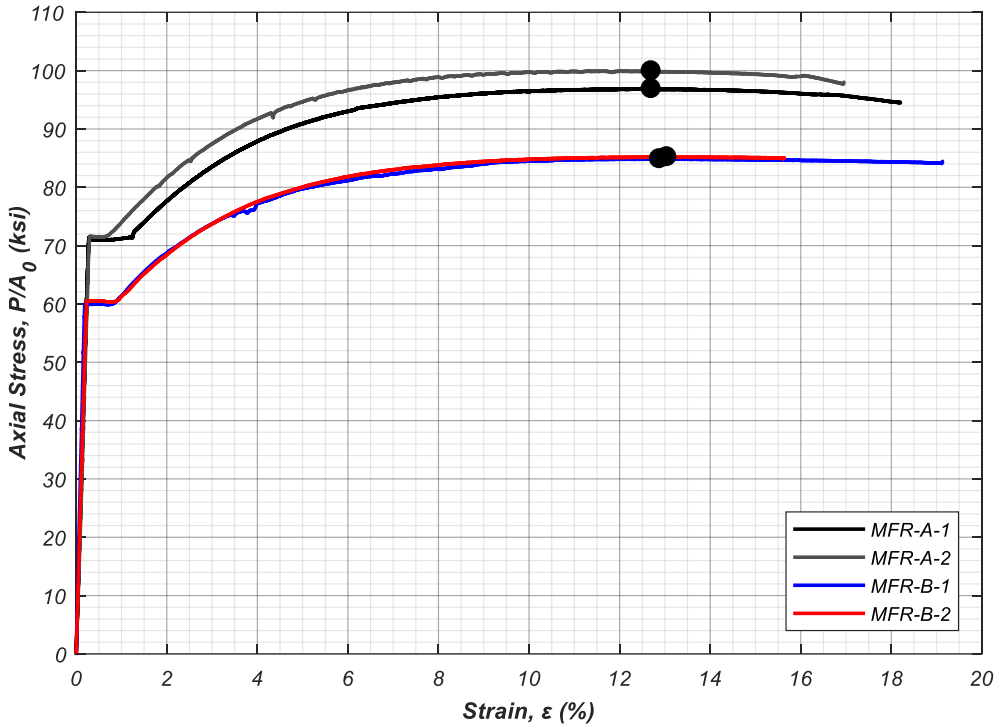

Figure 5.18. Monotonic Tensile Tests of Four ASTM A706 Grade 60 Bars from Two Manufacturers in Engineering Coordinates

The average yield stress, f_y, of the bars from MFR-A was 71.3 ksi which satisfies the ASTM A706 requirements for Grade 60 bars ($f_y \leq 78$ ksi). On the other hand, the average yield stress for the two MFR-B bars was 60.2 ksi, barely exceeding the minimum strength of 60 ksi prescribed in the A706 standard. The upper and lower yield strengths are also tabulated, per ASTM E8 (2016), see Table 5.1. The average tensile strength, f_u, for

MFR-A bars was 98.4 ksi ($1.38 \cdot f_y$) and 85 ksi ($1.41 \cdot f_y$) for MFR-B bars, thus meeting the ASTM requirement for the tensile-to-yield strength (T/Y) ratio $f_u \geq 1.25 \cdot f_y$. The average engineering uniform strain, ε_u, equaled 12.4% for MFR-A and 13.1% for MFR-B. Per ASTM E8 (2016), the uniform strain corresponds to the strain at maximum force sustained by the bar just prior to necking and includes both elastic and plastic strains. The power term, P, obtained from a least-squared optimization between each recorded strain hardening branch and the formulation for this curve proposed by Mander (1983) is also tabulated. The elastic energy, W_y, defined as the area under the monotonic curve up to ε_y, is numerically integrated and shown in Table 5.1

The equivalent carbon content from the mill certificates provided by the manufacturers is tabulated in Table 5.2. Both equivalent carbon contents meet the 0.55% limit established by ASTM A706 (2016), at 0.470% and 0.436% for MFR-A and MFR-B respectively.

Table 5.1. Material Properties from Monotonic Tensile Tests in Engineering Coordinates

	f_y (ksi)									
	Upper	Lower	Avg	ε_y (%)	ε_{sh} (%)	f_u (ksi)	ε_u (%)	P	T/Y	W_y (kip/in^2)
MFRA-1	71.4	70.9	71.0	0.280	1.01	96.8	12.7	3.2	1.36	10.2
MFRA-2	71.6	71.5	71.6	0.300	0.660	99.9	12.0	3.6	1.40	10.9
MFRB-1	60.0	59.9	59.9	0.190	0.847	84.8	12.9	3.2	1.42	5.84
MFRB-2	60.6	60.3	60.5	0.230	0.887	85.2	13.2	3.4	1.41	7.36

Table 5.2. Chemical Composition and Equivalent Carbon Content (C.E.) of Reinforcing Steel Bars

	C (%)	Mn (%)	P (%)	S (%)	Si (%)	Cu (%)	Ni (%)	Cr (%)
MFR-A	0.29	0.91	0.02	0.023	0.29	0.44	0.13	0.16
MFR-B	0.26	0.98	0.007	0.021	0.21	0.21	0.08	0.09

	Mo (%)	Sn (%)	V (%)	Nb (%)	Al (%)	Cb (%)	C.E.
MFR-A	0.03	0.014	0.043	0.003	0.003	-	0.470
MFR-B	0.02	-	0.049	-	-	0.001	0.436

5.4. Instrumentation

Given the importance of establishing a relationship between global and local strains to define strain amplitude and damage to the bar, each bar was well instrumented. Smeared strains for each specimen were measured using at least two diametrically-opposite clip gages with a fixed gage length equal to half the bar's unsupported length, see Figure 5.19. Cyclic tests were controlled by the readings from the clip gage to match the desired testing protocols, see Figure 5.16 and 5.17. The clip gages were designed in-house specifically for this project and consisted of 1.5mm (0.063in) thick aluminum 7075-T6 arches mounted on a steel frame. Each clip gage arch was instrumented with two strain gages, one on the convex face and one on the concave face of the arch. The thickness and dimensions of the arches were such that at a maximum expected bar elongation of 6%, the maximum axial strain in the arches remained less than 50% of the aluminum yield strain. This design criterion ensured a good measurement resolution and that the clip gages would be reusable. While the main objective of the clip gages was to accurately measure large deformations, even when the bars buckled, their design ensured an excellent resolution even for strains

less than the bar's yield strain. A set of clip gages was built for unsupported lengths of $6d_{b\ell}$ and $8d_{b\ell}$. Once built, each clip gage was calibrated using monotonic tensile tests on a closed-loop active hydraulic SATEC universal testing machine. The clip gage data obtained from these tests was compared to the data obtained from a 2 in. MTS extensometer to obtain the calibration factors between the axial strain of the clip gage arches and the axial strain of the bar. Figure 5.20 shows a comparison of a tensile monotonic test between the extensometer and the calibrated clip gage. The four contact points of the clip gages with the specimens where along the bar's vertical ribs at the theoretical inflection points of the buckled shape, using hardened steel tips.

Local strains on the bar were measured by 5mm (0.197in) long electrical-foil strain gages. Two sets of two diametrically-opposite strain gages were placed for all specimens at the theoretical inflection points of the buckled shape, orthogonal to the face of the bar's vertical ribs. A series of strain gages were placed at the bars' mid-height to obtain the longitudinal strain profile in the critical section of the buckled bar. The maximum compressive and tensile engineering strains, corresponding to the concave and convex faces of the buckled bar, as well as the curvature at the mid-section of the tested specimens, were computed from a least-squares fit of the strain gauge records collected during each test, using Bernoulli's hypothesis. Under the assumption that plane sections remain plane, finding the average strain and curvature of a deformed section is equivalent to computing the parameters of the plane containing the deformed section. By using sets of three strain gages, the coordinates of three points are known and the parameters of the plane equation can be solved from a simple linear system with equal number of equations and unknowns.

Since each set of three strain gauges results in a different response for the average strain and curvature in the mid-section, the more representative combination was selected. This selection was based on the authors' engineering judgement, to determine the extreme values of strain in the concave and convex side of the buckled bar.

Rotations of the upper and lower grip pipes as well as of the loading spreader beam were measured using three pairs of inclinometers placed orthogonal to each other (total of six inclinometers). The relative horizontal displacements between the UPG and the lateral restraint system (LRS) sleeve were measured through four linear potentiometers place on the sleeve and bearing against the upper grip pipe. The potentiometers were placed on the North, South, East, and West faces of the sleeve. The vertical displacement of the spreader beam connecting the actuators was measured by four cable-extension displacement transducers, referred from here on as string potentiometers, placed atop the strong floor, away from the actuators, one on each corner of the beam.

Figure 5.19. Specimen Instrumentation

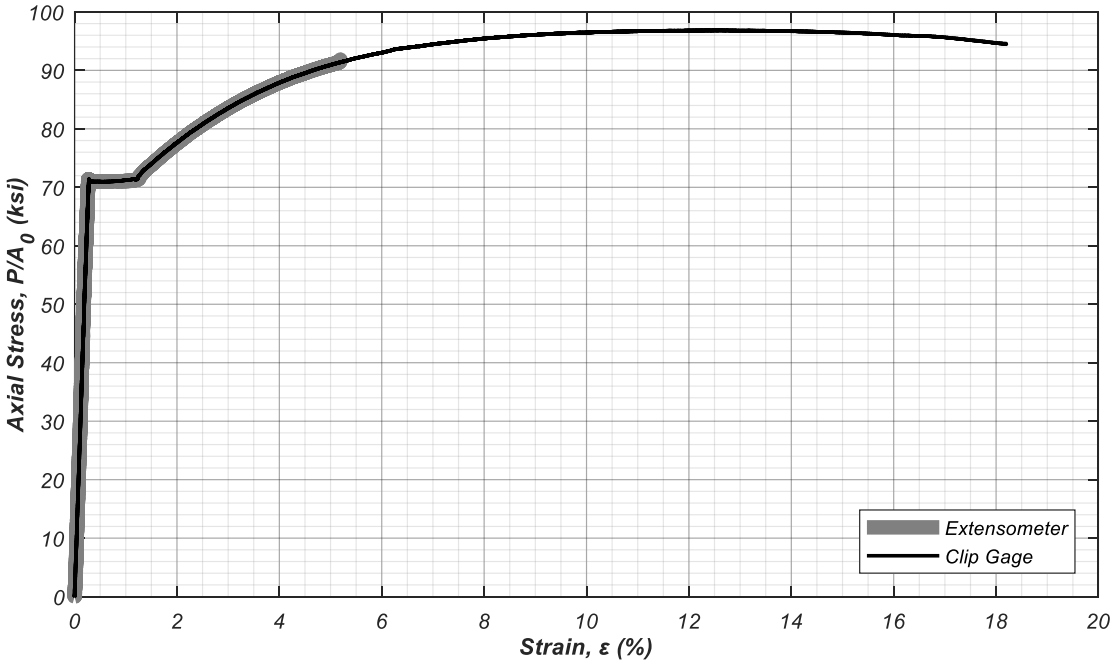

Figure 5.20. Monotonic Tensile Test Used to Calibrate Clip Gage Using Extensometer

5.5. Test Setup

5.5.1. Day 1: Bar Embedment in Upper Pipe Grip (UPG)

Once all the previously described components of the loading frame were fabricated and assembled, the first step in the test setup was to fill the pipe grips with the sulfur concrete. The sulfur was first crushed into a fine powder and mixed with the aggregate, in the amounts previously discussed. The UPG was filled with the sulfur concrete mix and placed inside the concrete tank filled with the heat transfer fluid, and the heating system turned on. After approximately 4 hours of heating the sulfur in the mix has melted, and any previously tested bar still embedded in the pipe was removed. The bar removal was achieved by welding a 1.5 in threaded rod (or a large bolt) at the top of the bar, placing a metal plate through it and a nut to prevent it from moving up, then a pair of hydraulic jacks were installed between the circular steel block at the top of the pipe and the plate, pushing the bar out, see Figure 5.21.

To facilitate the embedment of a new bar specimen, while the sulfur is still liquid, the circular block was removed from the pipe and a 4” hole was drilled in the sulfur, all the way to the bottom of the pipe, using an auger. Once the augering was completed, the circular block was re-positioned at the top of the pipe and the aligning metal frame installed over the tank, see Figure 5.2. The rebar specimen was placed inside the pipe vertically aligned, with a typical embedment length between 39 in and 44 in., although two successful tests were performed with a development length of only 32 in. The 4-in. thickness of the steel blocks was not accounted for in the development length of the bars. Air voids were

removed using a formwork vibrator attached to the embedded bar and sulfur concrete was added until the molten material reached the required height. At this point the concrete tank heating system was turned off. The pipe was left inside the tank overnight to cool down.

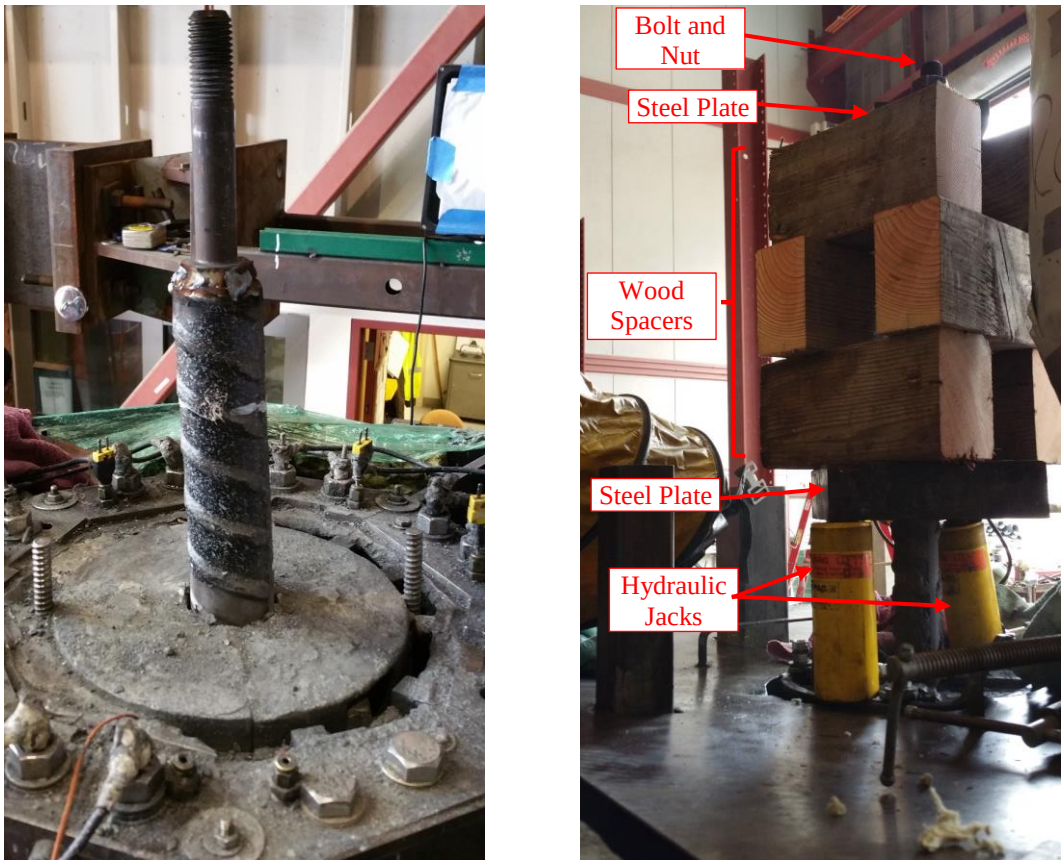

(a) (b)

Figure 5.21. Removal of Tested Bar from Sulfur Mix: (a) Welded Bolt at the Top of the Fractured Bar; (b) Hydraulic Jacks Pushing Rebar out

5.5.2. Day 2: Bar Embedment in Lower Pipe Grip (LPG)

The following day the aligning frame and upper pipe grip were removed from the tank. Oil on the outside of the pipe was removed and the pipe was flipped vertically, with the free end of the bar pointing downward. The heating system for the Lower Pipe Grip

was turned on and left running for approximately 4 hours. Once the sulfur in the LPG had melted any tested bar still embedded was removed following a similar procedure to the one used in the UPG, see Figure 5.21. Following the bar removal, the circular block was extracted from the lower pipe, to drill a 4” diameter, 60” deep hole in the sulfur with the auger, facilitating future embedment.

With the sulfur in the lower pipe still molten, the upper pipe was hoisted through the sleeve of the LRS, see Figure 5.2, and the bar aligned to go through the center hole in the circular block re-installed at the top of the pipe, see Figure 5.4. The bar was then embedded a few inches into the LPG, using the self-weight of the upper pipe alone. The required bar embedment is then achieved by connecting the spreader beam to the base of the upper pipe and pushing down with the hydraulic actuators at each end of the beam. Development lengths used for the lower grip ranged from 48 in. to 52 in. and did not consider the portion of the bar inside of the steel block. The sulfur concrete mix was then added to the lower pipe in a similar manner as with the upper pipe. After the bar was embedded, air voids in the sulfur concrete were removed by attaching a formwork vibrator to the bar. The heating system for the LPG was turned off and the sulfur concrete was let cool overnight.

It is worth noting that, while the sulfur concrete has a very rapid strength gain, it also has a very low thermal conductivity. Hence, the outer region of the sulfur concrete inside the pipes would cool at a faster rate than the core of the material. This phenomenon, plus the time it took for the oil around the LPG to cool, lead the researcher to wait at least 24hrs prior to testing after embedding the lower end of the bars, to allow for all materials

to reach room temperature and ensure the sulfur concrete had gained the required strength. Two tests were performed less than 24hrs after embedding to test this assumption. In both cases, the bars pulled out of the sulfur concrete.

5.5.3. Day 3: Instrumentation

With the bars embedded into both pipe grips and after post-tensioning the rods connecting the spreader beam to the base of the upper pipe, the specimens were instrumented. First, the strain gages were placed on the bar's theoretical inflection points and mid-height, as described in section 5.4. A total of four punch marks were then made on the vertical ribs of the bar, at the theoretical inflection points, marking the location where the four steel tips of the clip gages would attach to the bar. These punch marks also helped the tips to remain in place when the bar elongated or shortened during testing. For several tests, two horizontal string pots were attached at the mid-height of the bar to measure out of plane displacements. The horizontal linear potentiometers on top of the sleeve were then attached and placed against the side of the upper pipe to measure their relative displacement, see Figure 5.22. Finally, the orthogonal pairs of inclinometers on the upper and lower pipes and loading beam were installed.

With all the instrumentation installed, an overall system check was performed to balance and shunt the strain gages and ensure all instrumentation was functioning properly.

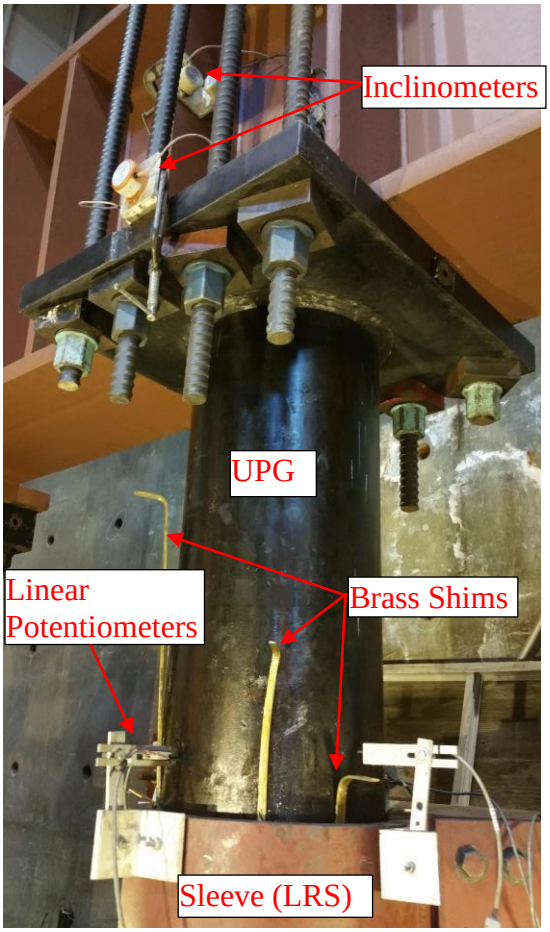

Figure 5.22. Linear Potentiometers and Clinometers Measuring Relative Motion Between Upper Pipe Grip (UPG) and Lateral Restraint System (LRS)

5.5.4. Day 4: Testing and Disassembly

Cyclic testing was performed, using the clip-gauge readings as reference for the testing protocol, see Figure 5.16 and 5.17. Once testing was completed and the specimen fractured due to plastic buckling-straightening fatigue, the spreader beam was detached from the UPG, so the pipe could be removed and placed inside the concrete heating tank. This was the final stage of the test setup.

The described four-day testing procedure was the product of multiple adjustments to the methodology initially planned for this project, as multiple challenges arose during the experimental work. Bar embedment into highly confined sulfur concrete proved to be the most challenging aspect of the experimental work, and different approaches were taken to try and perform this task as efficiently as possible.

5.6. Results

5.6.1. General

A total of thirty-five tests were performed, with Table 5.3 summarizing the main properties and outcome of the tests. Steel reinforcing bars from two different manufactures were used for the experimental work. Specimen01 thru Specimen29 were from the same batch from manufacturer A, while Specimen30 thru Specimen35 were from the same batch from manufacturer B. Unsupported lengths of $8d_{b\ell}$ and $6d_{b\ell}$ were used in the specimens tested, based on the expected distance between points of inflection, d_{POI}, corresponding to one-half of the unsupported length, in the reinforcement of bridge columns designed according to Caltrans Specifications. A total of three tests, specimens 27 to 29, were performed with an aspect ratio equal to 1.5 to remove nonlinear geometrical effects (Restrepo -Posada, 1992) and mainly for academic purposes.

For the commissioning of the loading apparatus, two monotonic tests were performed first to ensure the test setup was able to properly apply and transfer the loads required to fail a specimen under uniaxial tensile load. After the commissioning tests, a series of random history and constant amplitude tests were performed, with different aspect

ratios, to compare the effects of buckling on the fatigue life of the bars. As previously explained, given the initial difficulties with the embedment of the bars and in collecting accurate data from cyclic loading, results from specimens 3 thru 13 were not used for analysis.

The effects of a larger aspect ratio and bar buckling on the fatigue life of the bars are clearly visible when comparing the cyclic response of bars with different aspect ratios tested with the same constant amplitude strain history: Figure 5.24 shows the cyclic response for Specimen16 with an unsupported length of 8 $d_{b\ell}$, while Figure 5.25 shows the response of Specimen20 with an aspect ratio of 6. While both specimens show a progressive reduction in stress for the same strain target, the strength degradation due to the formation and propagation of fatigue cracks occurs at an earlier stage and at a faster rate for the bar with the larger aspect ratio. This leads to a reduced fatigue life for the bar with the largest aspect ratio, as summarized in Table 5.4.

Strain penetration was visible in all tests and must be accounted for when interpreting the results of the experimental work. For instance, as the unsupported length of the bar increases due to strain penetration, the stress at buckling continues to decrease with each successive cycle. While strain penetration is to be expected in a RC column, if buckling occurs at the base of the column, strain penetration will occur only at the base of the bar. In the current experimental work, the effects of strain penetration are exacerbated as the tested bars experience strain penetration at both the top and bottom of the bars. Moreover, while the steel blocks placed around the bars at the surface of the sulfur concrete simulate the restraint provided by the transverse reinforcement in a column and the cone

formed at the base of RC columns after cyclic loading, they further intensify the effects of strain penetration. The combined strain penetration (top plus bottom) at the end of testing equaled to 1.6 in. for Specimen19 (8.88% of original unsupported length), 0.9 in. for Specimen20 (6.67% of original unsupported length), and 1.25 in. for Specimen24 (9.26% of original unsupported length).

5.6.2. Typical Modes of Failure

Except for the specimens tested under monotonic tension that exhibited necking prior to failure, the specimens tested under Buckling-Straightening conditions developed one or more cracks on the concave side. All observed cracks began at the root of the transverse deformations of the bar and propagated toward the convex side of the bar. These cracks resulted in failure once there was not enough material to transfer the applied loads. No necking was observed prior to failure of these specimens. Figure 5.23 shows the fracture surface of two of the specimens tested.

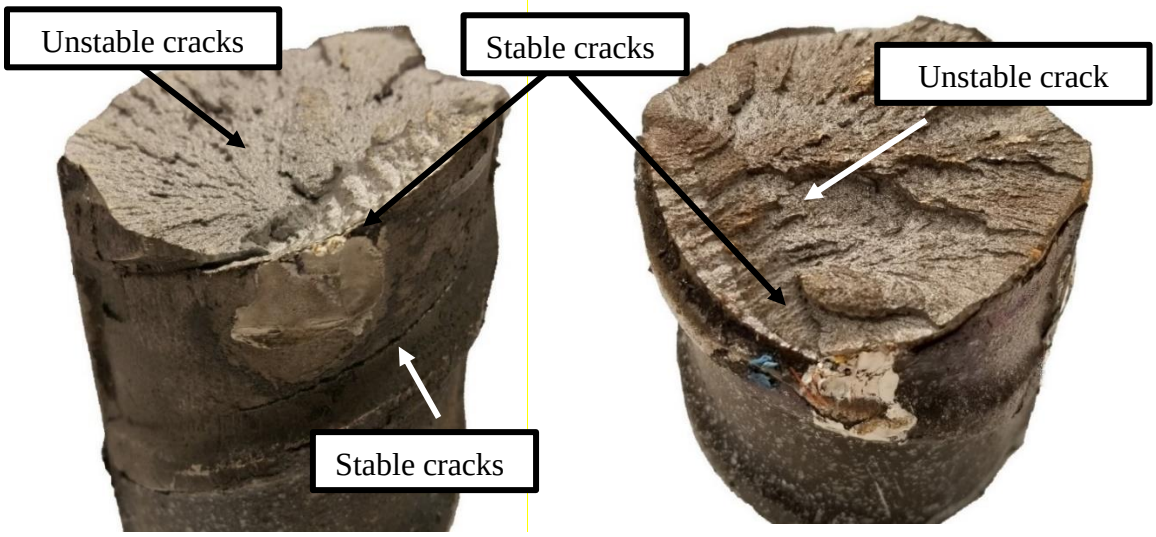

Figure 5.23. Fracture Surfaces Due to Plastic Buckling-Straightening Fatigue: (a) Specimen15; (b) Specimen16

Table 5.3. Summary of Experimental Program

	Aspect Ratio ($s/d_{b\ell}$)	MFR	Test Type[§§]	Test Outcome	Notes
Specimen01	8.56	A	Monotonic	Fractured Bar	Strain data from SG
Specimen02	5.56	A	Monotonic	Fractured Bar	Strain data from SG
Specimen03	10.00	A	Cyclic - RH	Fractured Bar	Strain data from SG
Specimen04	7.78	A	Cyclic - RH	Fractured Bar	Strain data from SG
Specimen05	7.78	A	Cyclic - RH	Fractured Bar	Strain data from SG
Specimen06	8.00	A	Cyclic - RH	Fractured Bar	Strain data from vertical SP
Specimen07	7.78	A	Cyclic - RH	Bar Pullout	Strain data from vertical SP
Specimen08	7.89	A	Cyclic - RH	Duct Pullout	Strain data from vertical SP
Specimen09	7.56	A	Cyclic - RH	Bar Pullout	Strain data from vertical SP
Specimen10	8.36	A	Cyclic - RH	Fractured Bar	Strain data from vertical SP
Specimen11	8.00	A	Cyclic - RH	Fractured Bar	Strain data from CG / CG leg slipped on second to last cycle
Specimen12	8.22	A	Cyclic - RH	Bar Pullout	Strain data from (2) CG
Specimen13	8.00	A	Cyclic - RH	Fractured Bar	Strain data from (2) CG
Specimen14	8.06	A	Cyclic - CA	Fractured Bar	Strain data from (2) CG
Specimen15	8.00	A	Cyclic - CA	Fractured Bar	Strain data from (2) CG
Specimen16	8.00	A	Cyclic - CA	Fractured Bar	Strain data from (2) CG
Specimen17	8.11	A	Cyclic - CA	Fractured Bar	Strain data from (2) CG / CG pushed out by buckled bar
Specimen18	8.00	A	Cyclic - CA	Fractured Bar	Strain data from (4) CG
Specimen19	8.00	A	Cyclic - RH	Fractured Bar	Strain data from (4) CG
Specimen20	6.00	A	Cyclic - CA	Fractured Bar	Strain data from (4) CG
Specimen21	6.00	A	Cyclic - CA	Fractured Bar	Strain data from (4) CG

[§§] RH: Random strain History, see Figure 5.16. CA: Constant Amplitude strain history, see Figure 5.17

Table 5.3. Summary of Experimental Program (Continued)

	Aspect Ratio ($s/d_{b\ell}$)	MFR	Test Type	Test Outcome	Notes
Specimen22	6.00	A	Cyclic - CA	Fractured Bar	Strain data from (4) CG / No SG at mid-height
Specimen23	6.00	A	Cyclic - CA	Fractured Bar	Strain data from (4) CG
Specimen24	6.00	A	Cyclic - RH	Fractured Bar	Strain data from (4) CG
Specimen25	8.00	A	Cyclic - CA	Fractured Bar	Strain data from (4) CG
Specimen26	8.00	A	Cyclic - CA	Fractured Bar	No instrumentation used
Specimen27	1.67	A	Cyclic - CA	Fractured Bar	Strain data from SG / Bar buckled while embedding -
Specimen28	1.50	A	Cyclic - CA	Bar Pullout	Strain data from SG
Specimen29	1.50	A	Cyclic - CA	Fractured Bar	Strain data from SG / Gages not reliable on last tensile cycle to
Specimen30	8.11	B	Cyclic - RH	Fractured Bar	Strain data from (4) CG / CG slipped mid-test
Specimen31	7.89	B	Cyclic - CA	Fractured Bar	Strain data from (4) CG
Specimen32	8.00	B	Cyclic - CA	Fractured Bar	Strain data from (4) CG

Table 5.4. Summary of Constant Amplitude Tests

Strain History	ε_{max} (%)	ε_{min} (%)	ε_{amp}*** (%)	Specimen	Aspect Ratio ($s/d_{b\ell}$)	MFR	$2N_f$	W_{ft} (kip/in2)
1	3.0	-0.5	1.75	Specimen14	8	A	13	19.4
2	2.4	-0.4	1.4	Specimen15	8	A	29	36.0
				Specimen16	8	A	23	24.0
				Specimen20	6	A	41	56.6
				Specimen22	6	A	37	47.6
3	3.0	-1.0	2.0	Specimen18	8	A	9	16.2
				Specimen31	8	B	17	23.2
				Specimen23	6	A	17	33.1
4	0.0	-4.5	2.25	Specimen25	8	A	5	10.9
				Specimen32	8	B	7	12.7
				Specimen21	6	A	7	18.0

*** $\varepsilon_{amp}=(\varepsilon_{max}-\varepsilon_{min})/2$

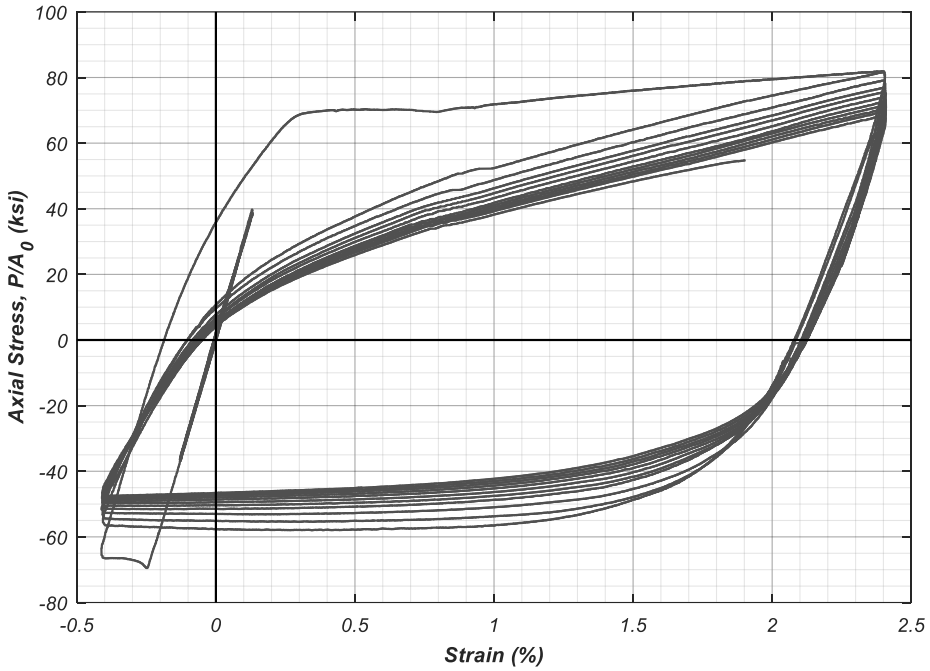

Figure 5.24. Axial Stress-Strain Response of #18 Bar with Unsupported Length of 8 $d_{b\ell}$ Subjected to Constant Amplitude Cycles of +2.4%, -0.4% (Specimen16)

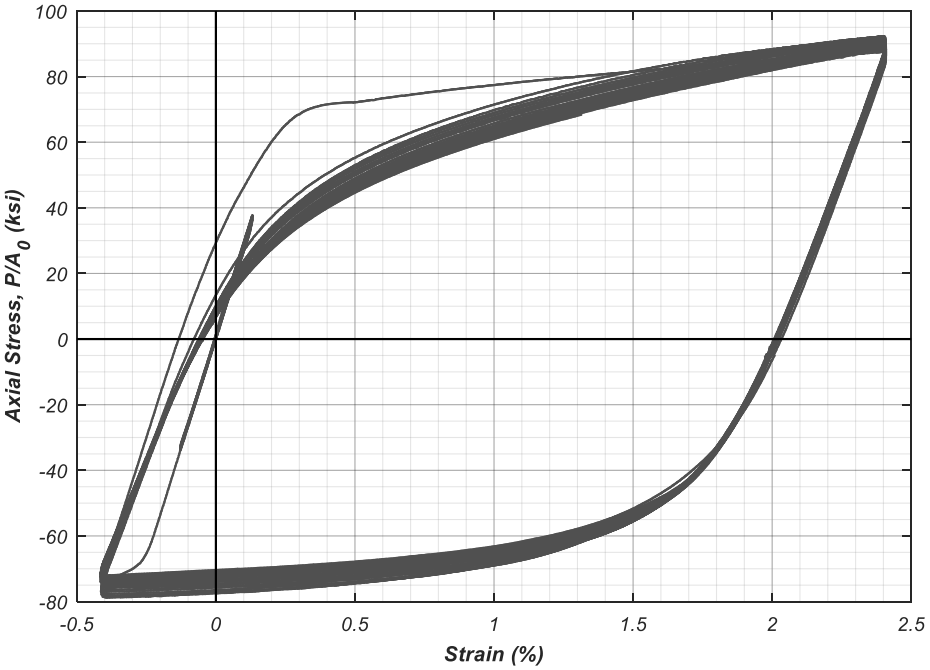

Figure 5.25. Axial Stress-Strain Response of #18 Bar with Unsupported Length of 6 $d_{b\ell}$ Subjected to Constant Amplitude Cycles of +2.4%, -0.4% (Specimen20)

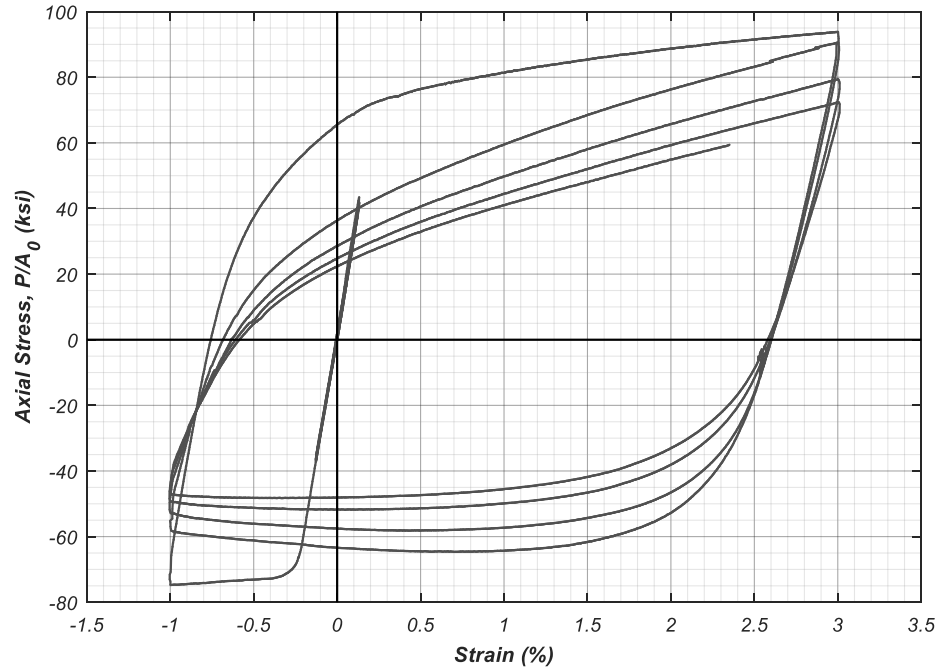

Figure 5.26. Axial Stress-Strain Response of #18 Bar with Unsupported Length of 8 $d_{b\ell}$ Subjected to Constant Amplitude Cycles of +3.0%, -1.0% (Specimen18)

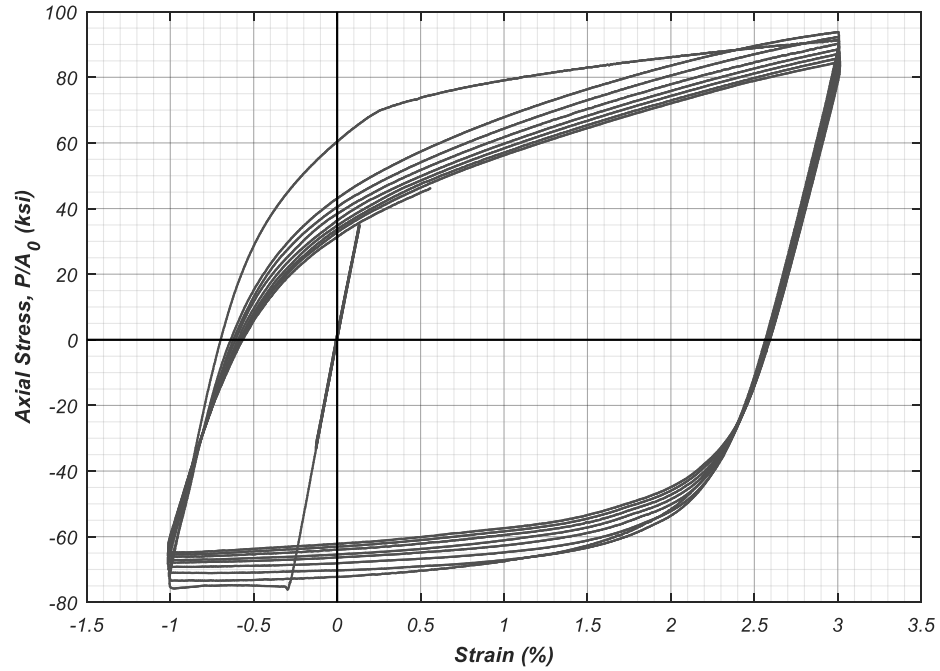

Figure 5.27. Axial Stress-Strain Response of #18 Bar with Unsupported Length of 6 $d_{b\ell}$ Subjected to Constant Amplitude Cycles of +3.0%, -1.0% (Specimen23)

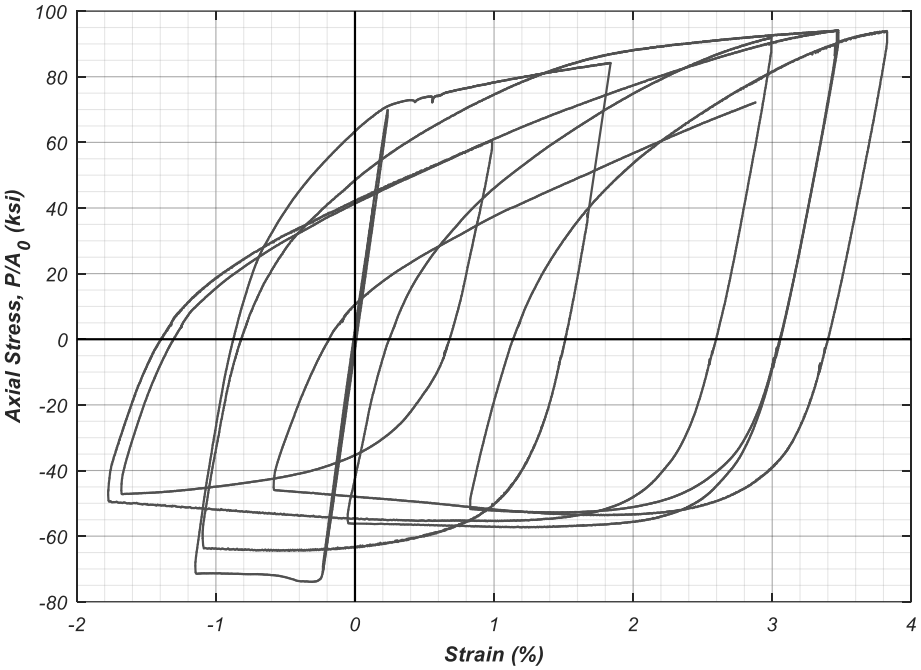

Figure 5.28. Axial Stress-Strain Response of #18 Bar with Unsupported Length of 8 $d_{b\ell}$ Subjected to Random History Cycles (Specimen19)

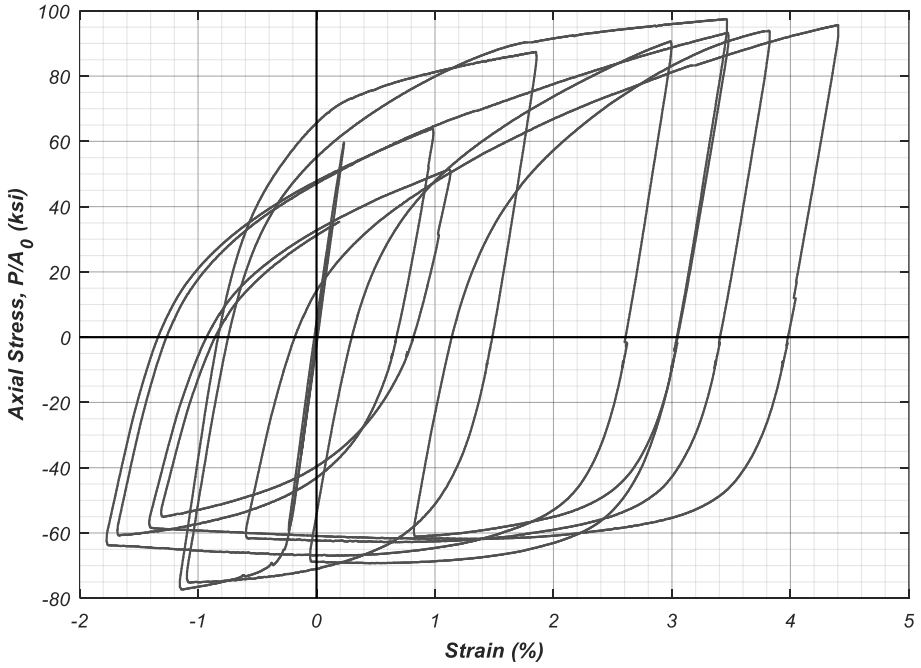

Figure 5.29. Axial Stress-Strain Response of #18 Bar with Unsupported Length of 6 $d_{b\ell}$ Subjected to Random History Cycles (Specimen24)

5.7. Summary

Through the innovative use of sulfur concrete as part of a loading apparatus, the cyclical testing of large diameter reinforcing steel bars under large strain amplitudes was successfully achieved after multiple unsuccessful attempts by others. These tests allowed to obtain the missing characterization of the plastic buckling-straightening fatigue life of large diameter bars. Results from relevant experimental work were used to derive a random strain history to test the bars in the bar buckling test apparatus. A series of constant amplitude tests were also performed to establish a relationship between deformation amplitude and the number of cycles to failure. Smear strains for all tests were measured using in-house designed clip gages with a fixed gage length equal to half the bar's unsupported lengths. The smeared strains calculated from these displacement sensors more closely approximate the strains assumed in design. Unsupported lengths equivalent to $1.5d_{b\ell}$, $6d_{b\ell}$, and $8d_{b\ell}$ were used for the experimental work. Results from these tests show strength degradation of the bars due to the formation and propagation of fatigue cracks, which occur at an earlier stage and at a faster rate for bars with larger aspect ratios. As a result, bars with larger unsupported lengths tend to have a reduced plastic buckling-straightening fatigue life. The influence of the total strain amplitude, ε_{amp}, on the fatigue life of the bars was also evident. A larger strain amplitude resulted in a reduced fatigue life of the bars. These results match the trends observed by previous research.

Chapter 5, in full, is a reprint of the material as it appears in *SSRP Report 17/10: Plastic buckling-straightening fatigue of large Diameter reinforcing steel bars*, 2018. Duck, David; Carreño, Rodrigo; and Restrepo, José I. The dissertation author was a co-author of the report.

Chapter 6.

LONGITUDINAL BAR – HOOP INTERACTION IN CIRCULAR COLUMNS

6.1. General

A very common mode of failure observed in the testing of circular bridge columns designed per Caltrans specifications is fracture of the longitudinal reinforcement following buckling. After spalling off of the concrete cover and upon large amplitude strain reversals, bars begin to buckle, first unnoticeably to the naked eye, pushing against the hoops and, under some conditions, the hoops yield and buckling of the bar becomes evident. For this reason, a number of researchers have investigated the response of reinforcing bars after buckling. Section 2.2 presents a review of this research effort. Limited research has taken place to assess the response of reinforcing bars that buckle over sets of hoops, with the focus of attention taking place in the buckling of bars in between adjacent sets of hoops. This section describes the method used and results of the investigation carried out to

understand the interaction between the longitudinal and transverse reinforcement in circular bridge columns loaded past the onset of buckling in the longitudinal reinforcement. The main interest here is the determination, with simple equations, of the characteristic dimensions of the buckled shape (e.g. distance between points of inflection, d_{POI}), and maximum strains in the concave side of the reinforcement, as a function of reinforcement configuration (e.g. bar size, spacing.), loading history, and material properties (e.g. yield stress, ultimate stress). This information is key in determining the fatigue life of a bar and is a crucial parameter in the design procedure described in Chapter 7.

For this study, a series of Finite Element models, representing different combinations of column sizes, transverse and longitudinal reinforcement, and material properties (e.g. ultimate stress of longitudinal or transverse reinforcement), were developed in OpenSees (McKenna, et. al. 2000). The response under axial load was then used to identify characteristic dimensions and local strains in the buckled reinforcement, and how they correlate to the parameters under study.

6.2. Description of the Finite Element Model

In the OpenSees Finite Elements (FE) models analyzed, each longitudinal bar and hoop was modeled as a single displacement-based beam-column element, discretized along its length into multiple sub-elements, see Figure 6.1a. The use of displacement-based elements accounts for both the axial and bending capacity of the reinforcement.

The nonlinear behavior of steel is included in the material fibers used to define the cross section of each element, see Figure 6.2b, using the steel model by Dodd and Restrepo (1995). The geometric nonlinearities, of great importance in the buckling phenomenon, are accounted for by corotational geometric transformations in every sub-element of the model (Crisfield, 1997). Shear deformations were accounted for by a linear model, with a shear modulus, G, computed for a Poisson's ratio of $\upsilon = 0.26$. Furthermore, an initial lateral imperfection is introduced to the longitudinal elements, to ensure the occurrence of buckling, see Figure 6.1c. The magnitude of such imperfection, at only 0.01 inch, has a negligible effect on the model response, besides triggering buckling.

Here it is assumed for simplicity that the cover concrete in the column does not influence the response of the longitudinal bars. Often times spalling of the column cover precedes the onset of bar buckling, otherwise initial onset of buckling triggers the spalling. The concrete in the core of the column, however, influences the response of the reinforcement in two ways: it prevents the bars from developing lateral deformations towards the core, and exerts a pressure on the longitudinal bars from the lateral expansion of the confined concrete due to dilation. The latter effect can be significant when the neutral axis depth in the column is deep, which is not the case of bridge columns, which have

moderate longitudinal reinforcement ratios and low axial compression. For this reason, a model of a bare column cage was chosen to conduct the parametric analysis described in this chapter.

For the loading configuration a triangular axial load distributed pattern was applied along each longitudinal element at the hoop locations, with the maximum force at the top and bottom nodes, see Figure 6.2.With this load pattern, the maximum axial force concentrates at the mid-height of the column, in a length of at least three hoop spacings, forcing the first buckling mode at this location. The model includes boundary conditions restraining translation and rotation in the nodes at the bottom of the column, and restraining all but the vertical displacement in the nodes at the top, see Figure 6.2b. With this load pattern and boundary conditions, all longitudinal bars are expected to have equivalent lateral deformations along the radial axis of the column.

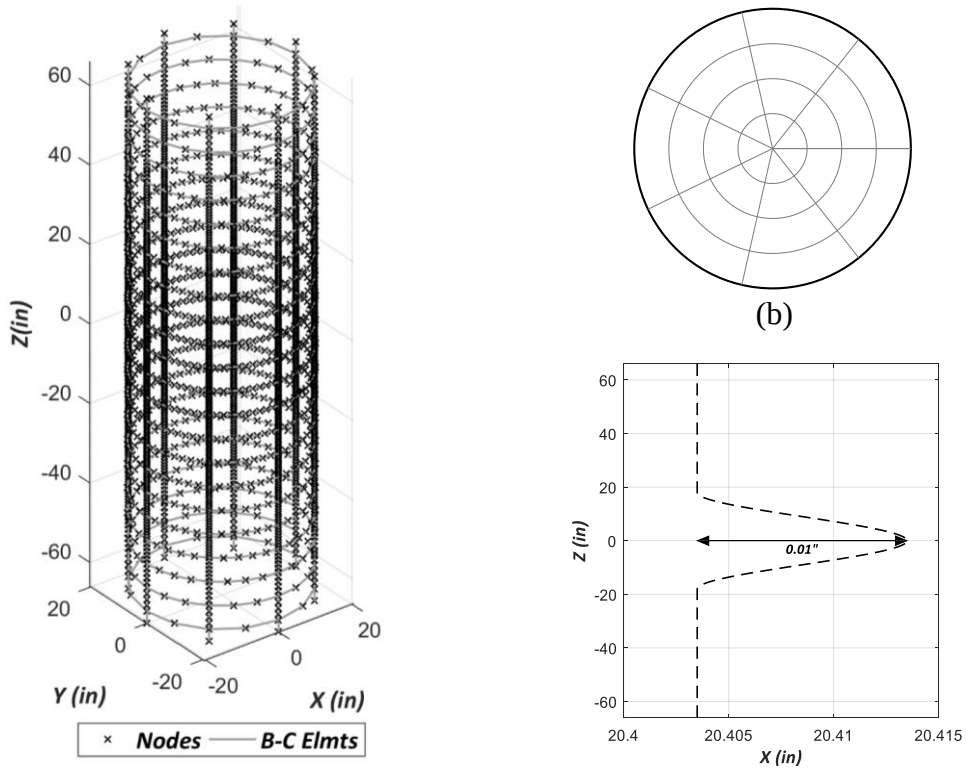

Figure 6.1. OpenSees Model: (a) 3D Model; (b) Reinforcing Bar Cross Section; (c) Longitudinal Bar with Initial Imperfection

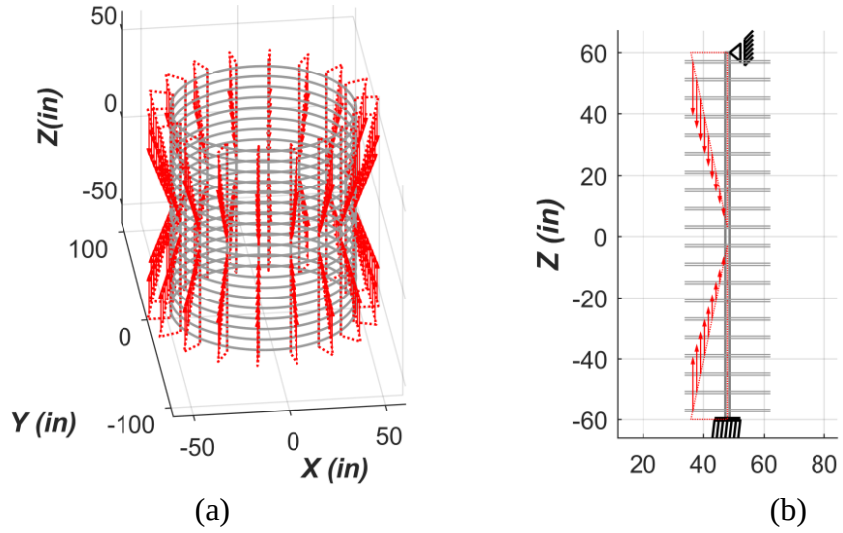

Figure 6.2. Loading Configuration and Boundary Conditions: (a) Model Loading; (b) Single Bar Boundary Conditions

6.3. Variables Investigated

The characteristic dimensions and maximum/minimum local strains in the buckled reinforcement are evaluated for different combinations of geometric and material properties of the column, including: column diameter, bar size, reinforcing steel ratio, hoop distribution, yield to ultimate strength ratio (T/Y) of longitudinal and transverse reinforcement. Additionally, the models were tested under multiple loading histories, see Figure 6.4.

FE models were classified into thirty-three categories for the reinforcement configuration, see Table 6.1, combined with eighteen material property combinations for the longitudinal and transverse reinforcement, see Table 6.3. The effect of the loading protocol was analyzed for a subset of geometric and material property combinations, under three loading protocols.

6.3.1. Reinforcement Configuration

Typical bridge pier designs under Caltrans SDC (2013) have a longitudinal reinforcement ratio, ρ_ℓ, ranging between 1% and 2.5%. Similarly, the volumetric reinforcement ratio, ρ_s, ranges between 0.7% and 1.5% with an on center (o.c.) distance, s, between hoops satisfying the limitations of SDC Section 8.2.5. When possible, a minimum clear spacing of 5 inches between hoops was used in the Finite element models to mimic the construction practice. For academic purposes case 27 and onwards, Table 6.1, use unrealistic large values of ρ_s to evaluate the effect of high ρ_s/ρ_ℓ ratios on the characteristic dimensions and strain distributions in the buckled elements.

Figure 6.3 shows the basic geometry of the column cages investigated and the geometric properties considered. The longitudinal reinforcement consists of equal size bars distributed on the perimeter of the column in a single layer. Single or double hoops were used, spaced a distance *s*, as indicated in Table 6.1.

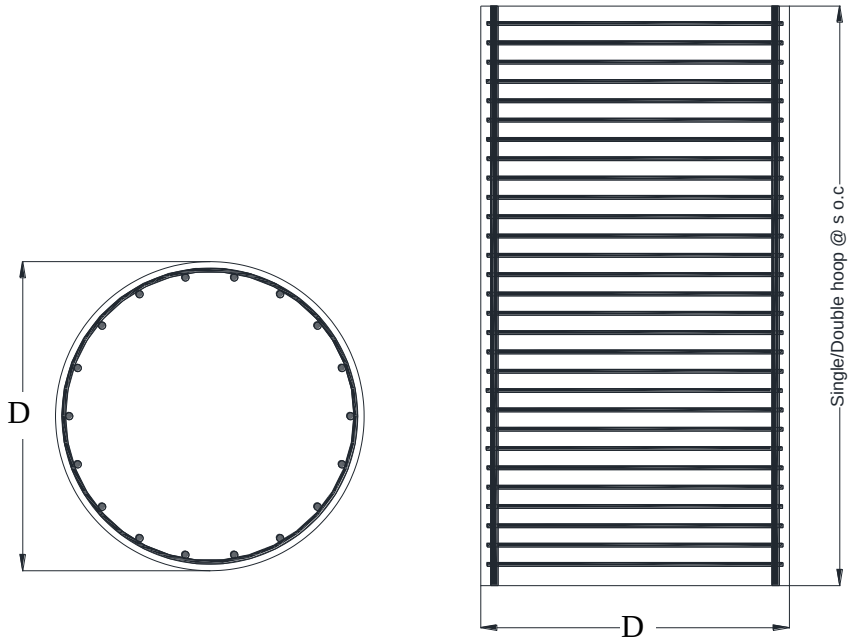

(a) (b)

Figure 6.3. Column Geometry. (a) Column cross section; (b) Column elevation

Table 6.1 Column Model Categories by Reinforcement Configurations

Case	Diameter (ft)	ρ_ℓ (%)	ρ_s (%)	Bar size	n_{bar}	Hoop size	$s/d_{b\ell}$	ρ_s/ρ_ℓ
1	4	0.99	0.70	#14	8	#6 (single)	3.5	0.7
2	4	1.55	0.70	#18	7	#6 (single)	2.7	0.5
3	4	1.55	0.70	#11	18	#6 (single)	4.3	0.5
4	4	1.55	1.00	#11	18	#5 (double)	4.3	0.6
5	8	0.99	0.70	#14	32	#9 (single)	3.5	0.7
6	8	0.99	0.70	#18	18	#9 (single)	2.7	0.7
7	8	0.99	1.00	#14	32	#8 (double)	4.1	1.0
8	8	0.99	1.00	#18	18	#8 (double)	3.1	1.0
9	8	1.55	0.70	#18	28	#9 (single)	2.7	0.5
10	8	1.55	1.00	#18	28	#8 (double)	3.1	0.6
11	8	1.55	1.30	#18	28	#9 (double)	3.1	0.8
12	8	1.55	0.70	#14	50	#9 (single)	3.5	0.5
13	8	1.55	1.00	#14	50	#8 (double)	4.1	0.6
14	8	1.99	0.70	#18	36	#9 (single)	2.9	0.4
15	8	1.99	1.00	#18	36	#8 (double)	3.1	0.5
16	8	2.49	0.70	#18	45	#9 (single)	2.7	0.3
17	8	2.49	1.00	#18	45	#8 (double)	3.1	0.4
21	8	1	0.45	#18	18	#5 (double)	2.5	0.5
22	8	1.99	0.90	#18	36	#7 (double)	2.4	0.5
23	8	2.49	1.12	#18	45	#8 (double)	2.7	0.4
24	8	1.55	1.09	#18	28	#8 (double)	2.7	0.7
25	8	1.99	1.39	#18	36	#9 (double)	2.7	0.7
26	8	1.99	1.39	#14	64	#9 (double)	3.5	0.7
27	8	2.49	1.74	#18	45	#10 (double)	2.7	0.7
28	8	1.55	1.55	#18	28	#10 (double)	3.0	1.0
29	8	1.99	1.99	#18	36	#10 (double)	2.3	1.0
30	8	1.99	1.99	#14	64	#10 (double)	3.1	1.0
31	8	2.49	2.49	#18	45	#11 (double)	2.3	1.0
32	8	1	1.40	#18	18	#9 (double)	2.7	1.4
33	8	1.55	2.17	#18	28	#11 (double)	2.7	1.4
34	8	1.99	2.79	#18	36	#11 (double)	2.0	1.4
35	8	1.99	2.79	#14	64	#11 (double)	2.7	1.4
36	8	2.49	3.49	#18	45	#11 (double)	1.7	1.4

6.3.2. Material Properties

Uniaxial fibers in the FE model used the constitutive stress-strain relationship developed by Dodd and Restrepo (1995). Most of the parameters of this formulation can be extracted from the monotonic response of the material, see Figure 4.3. Additional parameters of the model control the shape of strain hardening backbone curve and the Bauschinger effect (P and Ω_{fac}, respectively). Work by Restrepo-Posada et al. (1994) suggests that Ω_{fac} is correlated to the carbon content in the steel, see Figure 4.20.

Table 6.2. Material Properties P, T/Y and Ω_{fac} vs Carbon Content (C)

Coupon #	Manufacturer ID	ASTM	Bar Size	*C* (%)	*P*	Ω_{fac}
1	1	A615	4	0.42%	3	0.83
2	1	A706	4	0.28%	3	0.98
4	2	A706	4	0.27%	2.9	0.91
5	3	A615	4	0.42%	3.2	0.77
6	3	A706	4	0.28%	3.1	0.96

With the exception of Set 0, all material property combinations used in the FE models (Table 6.3) were based on the average, 10 percentile, and 90 percentile yield strength (f_y) found by Bournonville, et.al (2004) for Grade 60 ASTM A706 steel. Each value of f_y was combined with typical T/Y ratios (from 1.25 to 1.5), and with correlated values for *P* and Ω_{fac}. For the remaining material parameters, typically more stable between different steel batches, constant values were used, see Equation 6.1.

Set 0 in Table 6.3 matches the experimental material properties of reinforcement used in the Full Scale Bridge Column tested at UC San Diego (Schoettler, et al. 2012). Results from Set 0 are used to verify the computational model results against experimental

values. Note that in the test the transverse reinforcement, with a yield strength of 54.4 ksi, does not comply with Grade 60 reinforcement specifications.

For material properties not listed in Table 6.3 the values indicated in 6.1 are used, consistent with experimental results of ASTM A706 steel specimens. Note that the strain at onset of strain hardening in transverse reinforcement, $\varepsilon_{sh,t}$, is only slightly larger than the yield strain, ε_{yt}, to account for the lack of yield plateau in the work-hardened hoops.

Table 6.3. Column Model Combinations of Material Properties

	LONGITUDINAL REINFORCEMENT				TRANSVERSE REINFORCEMENT			
set	$f_{y\ell}$ (ksi)	$f_{u\ell}$ (ksi)	P_ℓ	$\Omega_{fac,\ell}$	f_{yt} (ksi)	f_{ut} (ksi)	P_t	$\Omega_{fac,t}$
0	75.2	102.4	3.2	0.89	54.4	85.9	3.9	1.06
1	66	89	3.1	0.88	70	95	3.1	0.89
2	66	95	3.4	0.95	70	95	3.1	0.89
3	66	102	3.7	1.04	70	95	3.1	0.89
4	70	89	2.9	0.82	70	95	3.1	0.89
5	70	95	3.1	0.89	70	95	3.1	0.89
6	70	102	3.5	0.97	70	95	3.1	0.89
7	75	95	2.9	0.81	70	95	3.1	0.89
8	75	95	2.9	0.81	70	89	2.9	0.82
9	75	102	3.2	0.89	70	95	3.1	0.89
10	70	95	3.1	0.89	66	89	3.1	0.88
11	70	95	3.1	0.89	75	102	3.2	0.89
12	66	89	3.1	0.88	66	89	3.1	0.88
13	66	89	3.1	0.88	75	102	3.2	0.89
14	75	102	3.2	0.89	66	89	3.1	0.88
15	75	102	3.2	0.89	75	102	3.2	0.89
16	66	82.5	2.8	0.80	70	95	3.1	0.89
17	66	99	3.6	1.00	70	95	3.1	0.89

$$
\begin{aligned}
E_{s\ell} &= 29{,}000 \text{ ksi} && \text{(a)} \\
\varepsilon_{u\ell} &= 13\% && \text{(b)} \\
\varepsilon_{sh,\ell} &= 4\,\varepsilon_{y\ell} && \text{(c)} \\
E_{st} &= 29{,}000 \text{ ksi} && \text{(d)} \\
\varepsilon_{ut} &= 12\% && \text{(e)} \\
\varepsilon_{sh,t} &= 1.1\,\varepsilon_{yt} && \text{(f)}
\end{aligned}
\qquad 6.1
$$

6.3.3. Loading Protocol

In addition to the reinforcement configuration and material properties, the effect of the loading protocol on the resulting buckled shapes is also evaluated. Two cyclic and one monotonic loading protocols are tested, see Figure 6.4.

Cyclic protocols 1 and 2, with maximum tensile strains of 4.5% and 6%, represent extreme strain histories observed in the reinforcement at the plastic hinge region of RC bridge columns, where the axial load ratio is typically low. In the selected histories, low-amplitude reversals typically seen in seismic responses were omitted to expedite the computational analysis, assuming they do not play a significant role in the buckling parameters under study.

The use of a monotonic strain history in compression, although unrealistic for the reinforcement in a RC bridge column, represents an extreme case to evaluate the effect of the loading protocol.

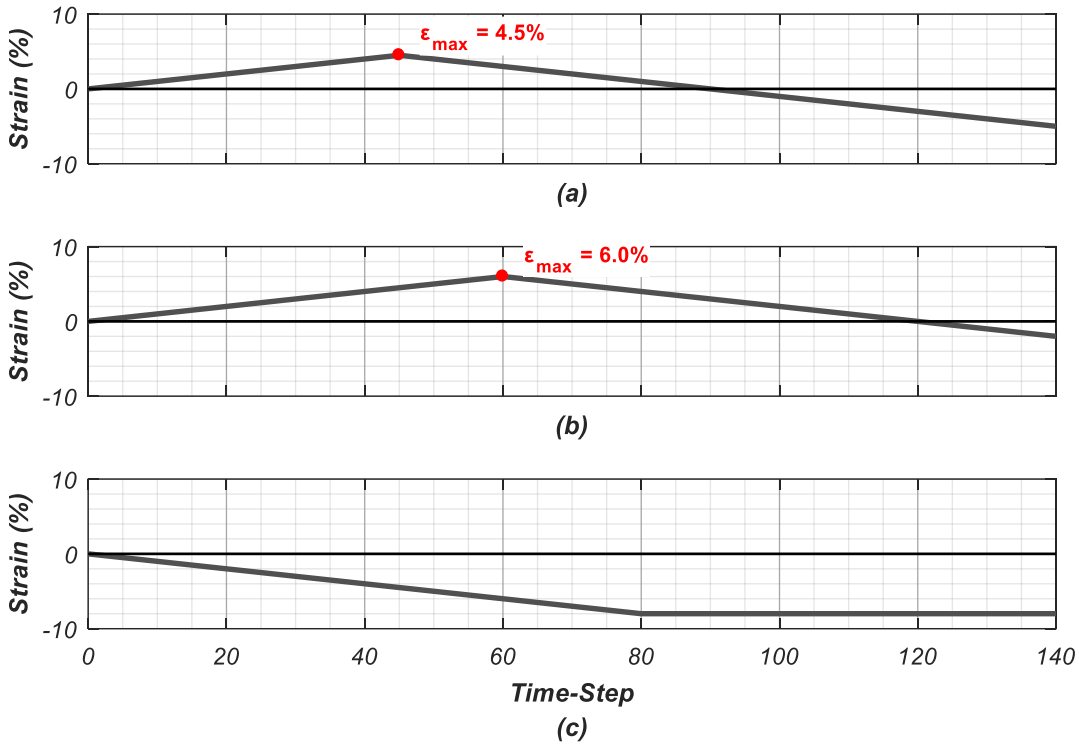

Figure 6.4. Loading Protocols: (a) Protocol 1; (b) Protocol 2; (c) Protocol 3

6.4. Analysis Results

FE model analyses were performed for multiple combinations of reinforcement configuration (Table 6.1) and material properties (Table 6.3) under Loading Protocol 1 (Figure 6.4a), with the objective of defining simple equations for characteristic dimensions and damage indices of the buckled reinforcement. The effect of the Loading protocol was assessed by analyzing a subset of the models under all three protocols, Figure 6.4.

In all the computational analyses displayed herein, longitudinal reinforcement elements underwent significant buckling deformations, well beyond the onset of buckling. Comparison to experimental results corroborate the accuracy of the computational models. Experimental verification is however limited, since very few studies detailing the state of buckled reinforcement from bridge column specimens are available in the public domain.

Using the strain recorded at the concave and convex side of the critical plastic hinge in the buckled shape (ε_{kv} and ε_{kx} respectively) several characteristic states of the analysis are identified:

1) Zero stress, following the maximum reversal in tension, ε_0, corresponding to the plastic strain in the material. This step is represented in the figures by the symbol ×.
2) Bifurcation point, when the difference between ε_{kv} and ε_{kx} becomes greater than 10%, representing the onset of buckling. The strain at this point is called henceforth “Engesser-Considère strain”, ε_{EC}. For the following figures the step is represented by the symbol: ○.

3) Peak Stress in compression is reached, when the segments outside of the buckled shape begin unloading in tension, represented in the figures by the Δ symbol. The smeared strain at this point is identified as "von-Karman strain", ε_{vK}.

4) Natural strain in the concave side, shifted by the plastic strain $\varepsilon'_0(1)$, reaches one-half the uniform strain in compression ($\varepsilon'_{kv} = \varepsilon'_0 - \varepsilon'_u/2$). This step is represented by a □ symbol in the analysis figures.

5) Natural strain in the concave side, shifted by ε'_0, reaches the uniform strain ($\varepsilon'_{kv} = \varepsilon'_0 - \varepsilon'_u$, $DI = 1.0$). The ◊ symbol represents this state in following figures.

6) Analysis step halfway between 4) and 5), used for the measurement of characteristic dimensions in the buckled shape. In following figures represented by the ∗ symbol.

6.4.1. Characteristic Dimensions of Buckled Bars

For this section two main dimensions of the buckled reinforcement are identified: 1) The distance between points of inflection, d_{POI}, and 2) the distance between centers of the rotation in the two plastic hinges at the end of the buckled shape, d_{CR}, see Figure 6.5.

The distance between points of inflection, d_{POI}, is identified from the locations of zero curvature above and below the plastic hinge in the middle of the buckled shape, where the fracture of reinforcement is expected. The distance between centers of rotation, d_{CR}, on the other hand, is computed from the centroids of the curvature distribution between the

point of inflection and the next point of zero curvature, both above and below the middle plastic hinge, see shaded areas in Figure 6.5b.

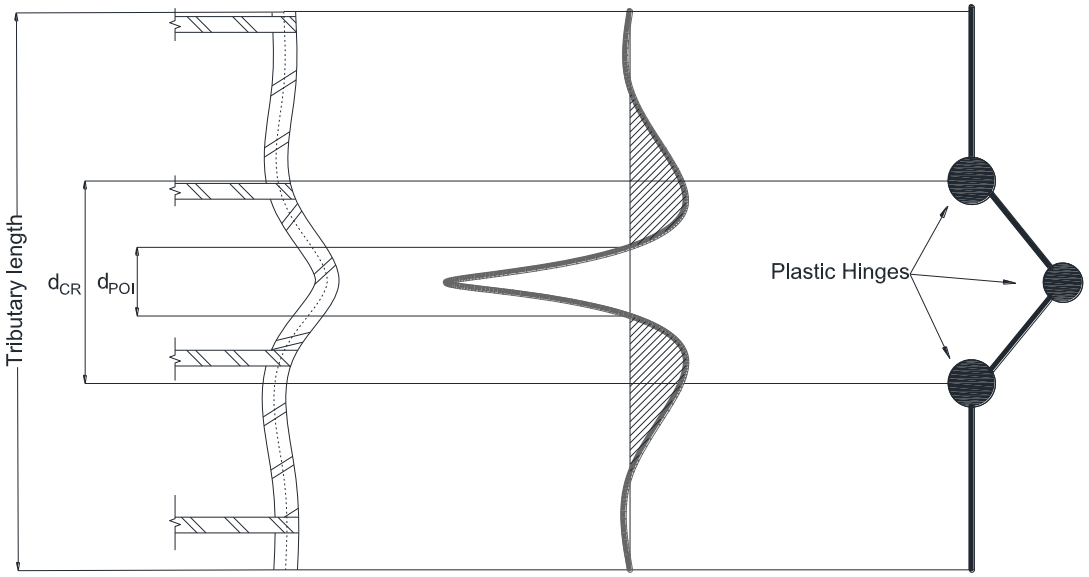

Figure 6.5. Characteristic Dimensions in Buckled Shape: (a) Buckled Reinforcement; (b) Curvature Distribution; (c) Simplified Buckled Shape Model

Figure 6.6 to Figure 6.8 show the results from the Finite Element model matching the reinforcement configuration and material properties of the large column test performed at UC San Diego's Shake Table (Schoettler et al. 2012). Comparison to the experimental results in terms of distance between points of inflection, with an analytical d_{POI} at $3.0 \cdot d_{b\ell}$ and experimental d_{POI} at $3.3 \cdot d_{b\ell}$, yields a difference of only 9%.

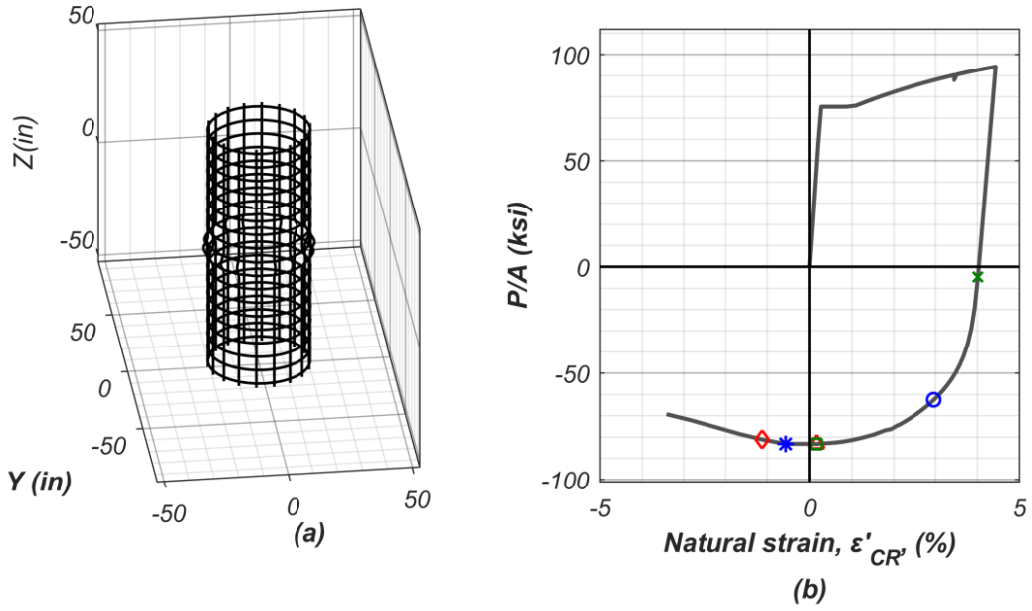

Figure 6.6. Global Response of FE model, Set 0-Case 4-Protocol 1: (a) Tri-dimensional Representation of Buckled Shape; (b) Smeared Natural Strain vs Average Stress in one Longitudinal Bar, including analysis steps from Section 6.4

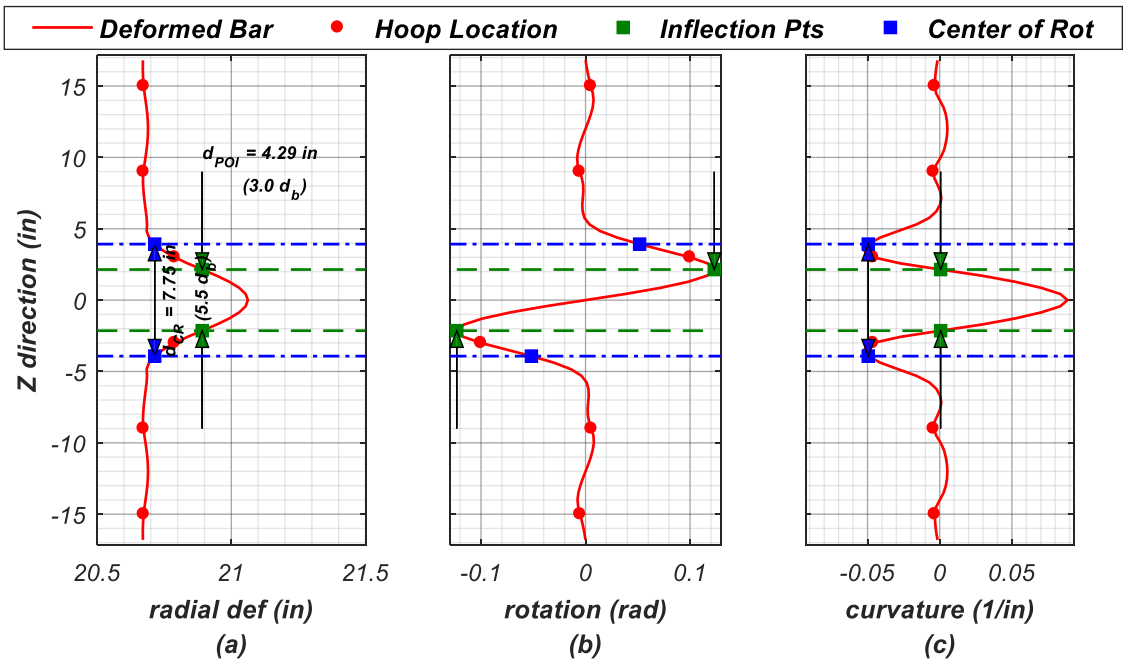

Figure 6.7. Deformed Shape of Buckled Reinforcement at Analysis Step 6) (see Section 6.4). Set 0 – Case 4- Protocol 1: (a) Lateral Deformation; (b) Node Rotations; (c) Curvature Distribution

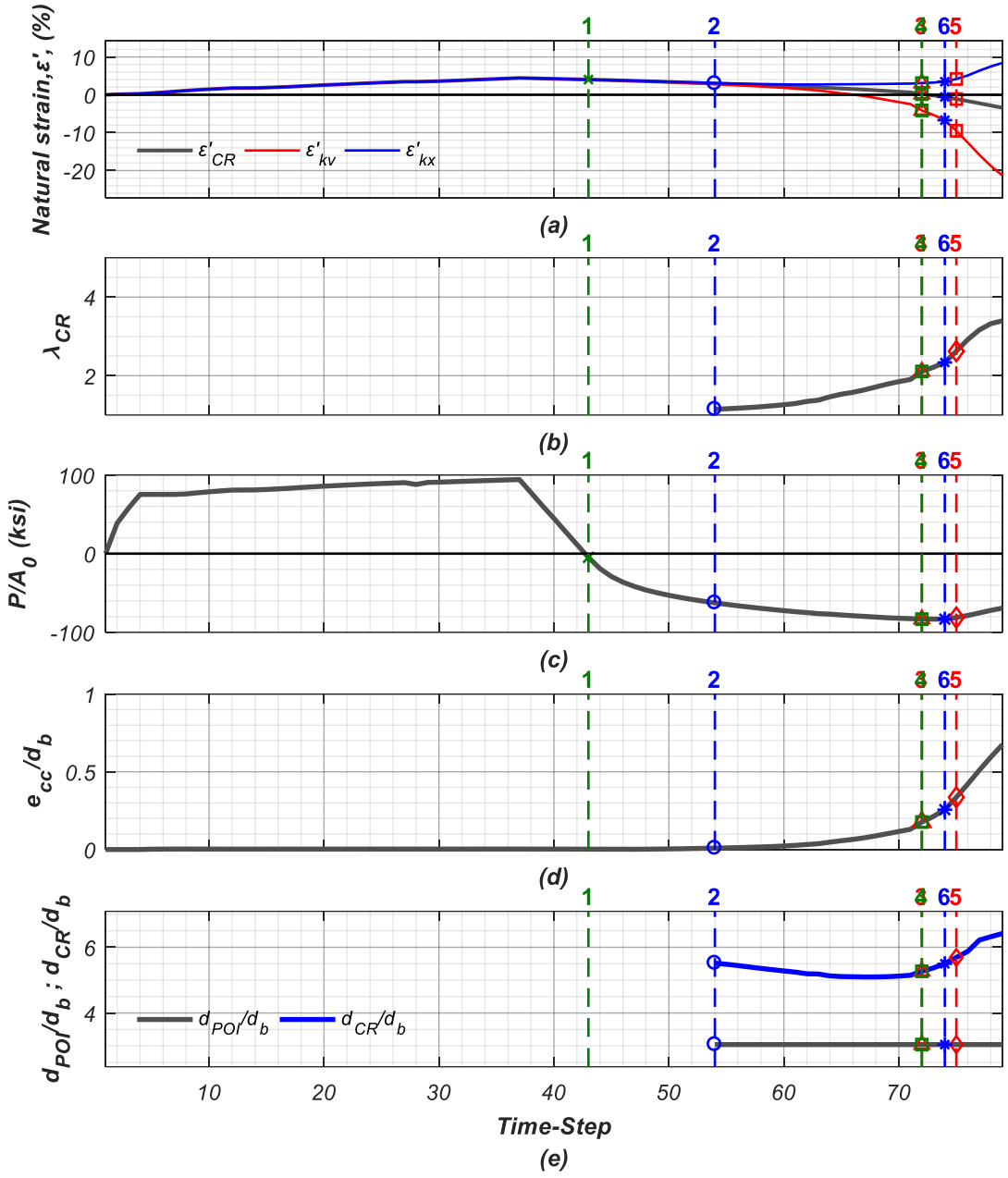

Figure 6.8. Variation of Parameters in Buckled Reinforcement at Each Time-Step. Set 0 – Case 4 – Protocol 1: (a) Strain History Smeared Between CRs, Local Strain in Concave and Convex Face of Reinforcement; (b) Ratio Between Local and Smeared Strains (see 6.4); (c) Average Axial Stress in Reinforcement; (d) Lateral Deformation/Eccentricity of Buckled Bar, e_{cc}, Normalized by Bar Diameter, $d_{b\ell}$; (e) Distance Between POIs and CRs, Normalized by $d_{b\ell}$

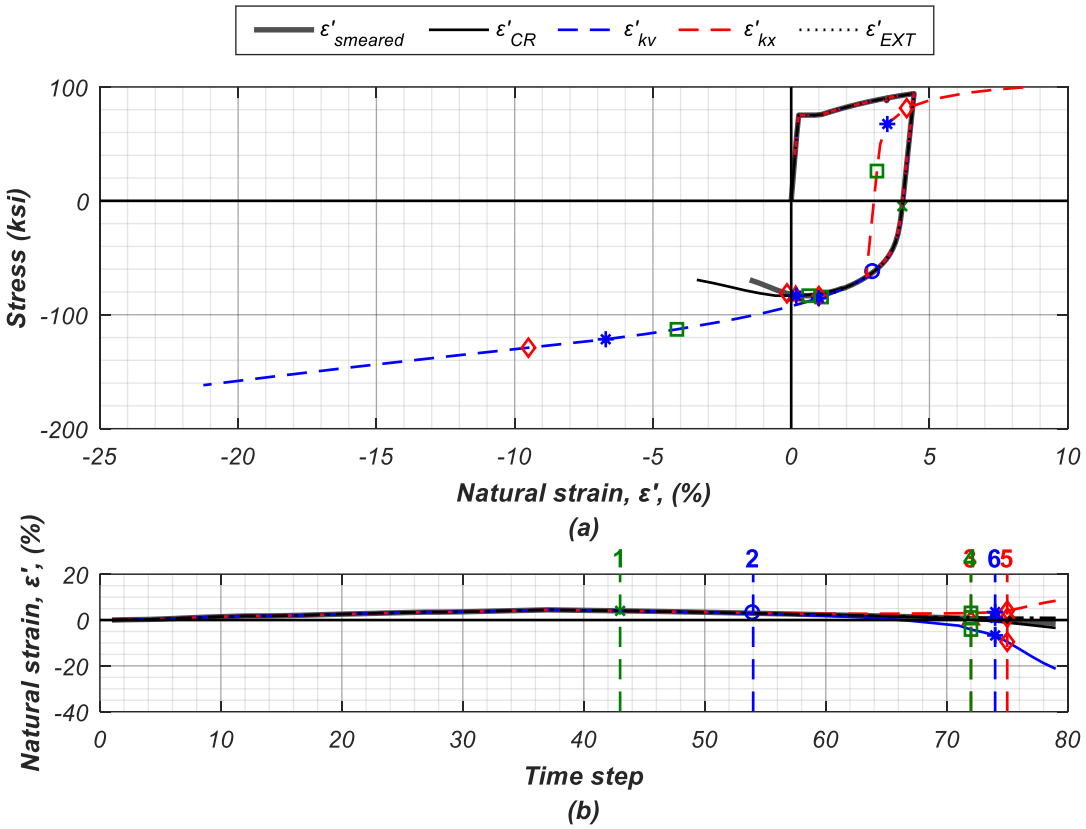

Figure 6.9. Local vs Smeared Response in Buckled Reinforcement. Set 0 – Case 4 – Protocol 1: (a) Natural Strain vs Stress response; (b) Natural Strain Time-History

Table 6.4 and Table 6.5 are the result matrices for the values of d_{POI} and d_{CR} obtained from all cases analyzed under Loading protocol 1. Considering cases 1 through 26, which have the more realistic reinforcement configurations (see Section 6.3.1), the range found for d_{POI} was between 2.1 and 4.2 bar diameters, with an average of 2.7 and a coefficient of variation of 18%. Similarly, the results for d_{CR} range between 4.0 and 8.7 bar diameters, with a mean value of 5.3 and a coefficient of variation of 19%.

Table 6.4. Results of $d_{POI}/d_{b\ell}$ from FE Model under Loading Protocol 1.

CASES \ SETS	0	1	2	3	4	5	6	7	8	9	10	11	12	13	14	15	16	17
1	3.5	3.0	3.0	3.5	3.0	3.0	3.5	3.0	3.0	3.5		3.0	3.0	3.0	3.5	3.0	3.0	3.0
2		3.8	4.2	4.2		4.2	4.2	4.2	4.2	4.2	4.2	4.2	3.8	3.8	4.2	4.2	3.8	4.2
3	3.0	3.0	3.0	3.0	3.0	3.0	3.0	3.0	3.0	3.0	3.0	3.0	3.0	3.0	3.0	3.0	2.4	3.0
4	3.0	3.0	3.0	3.0	3.0	3.0	3.0	3.0	3.0	3.0	3.0	3.0	3.0	3.0	3.0	3.0	3.0	3.0
5	3.0	2.5	2.5	3.0	2.5	2.5	3.0	2.5	2.5	3.0	2.5	2.5	2.5	2.5	3.0	3.0	2.5	2.5
6	2.3	2.7	2.3	2.3	2.3	2.3	2.3	2.3	2.3	2.3	2.3	2.3	2.7		2.3	2.3	2.3	2.3
7	3.0	3.0	3.0	3.0	3.0	3.0	3.0	3.0	3.0	3.0	3.0	3.0	3.0	3.0	3.0	3.0	3.0	3.0
8	2.7		2.2	2.2	2.2	2.2	2.2	2.2	2.2	2.2	2.2	2.2			2.2	2.2	2.2	2.2
9	2.7	2.3	2.3	2.3	2.3	2.3	2.7	2.3	2.3	2.7	2.3	2.3	2.3	2.3	2.7	2.7	2.3	2.3
10	2.7	2.2	2.2	2.7	2.2	2.2	2.7	2.7	2.7	2.7	2.2	2.2	2.2	2.2	2.7	2.7	2.2	2.7
11	2.2	2.2	2.2	2.2	2.2	2.2	2.2	2.2	2.2	2.2	2.2	2.2	2.2	2.2	2.2	2.2	2.2	2.2
12		3.0	3.0	3.0	3.0	3.0	3.0	3.0	3.0	3.0	3.0	3.0	3.0	3.0	3.0	3.0	3.0	3.0
13	3.0	3.0	3.0	3.0	3.0	3.0	3.0	3.0	3.0	3.0	3.0	3.0	3.0	3.0	3.0	3.0	3.0	3.0
14		2.5	2.9	2.9	2.5	2.9	2.9	2.9	2.5	2.9	2.9	2.5	2.9	2.5	2.9	2.9	2.5	2.9
15	2.7	2.2	2.2	2.2	2.2	2.2	2.7	2.2	2.2	2.7	2.2	2.2	2.2	2.2	2.7	2.7	2.2	2.2
16		2.7	3.0	3.0	2.7	3.0	3.0	3.0	3.0	3.0	3.0	3.0	2.7	2.7	3.0	3.0	2.7	3.0
17		2.7	2.7	2.7	2.7	2.7	2.7	2.7	2.7	2.7	2.7	2.7	2.7	2.7	2.7	2.7	2.7	2.7
21	4.0	3.6	3.3	3.6	3.3	3.6	3.6	3.6	3.6	3.6	3.6	3.3	3.3	3.3	3.6	3.6	3.3	3.6
22	2.4	2.1	2.1	2.4	2.1	2.1	2.4	2.1	2.1	2.4	2.1	2.1	2.1	2.1	2.4	2.4	2.1	2.4
23	2.7	2.3	2.3	2.3	2.3	2.3	2.3	2.3	2.3	2.3	2.3	2.3	2.3	2.3	2.3	2.3	2.3	2.3
24	2.3	2.3	2.3	2.3	2.3	2.3	2.3	2.3	2.3	2.3	2.3	2.3	2.3	2.3	2.3	2.3	2.3	2.3
25	2.3	2.3	2.3	2.3	2.3	2.3	2.3	2.3	2.3	2.3	2.3	2.3	2.3	2.3	2.3	2.3	2.3	2.3
26	3.0	2.5	2.5	3.0	3.0	3.0	3.0	3.0	3.0	3.0	2.5	3.0	2.5	2.5	3.0	3.0	2.5	3.0
27	2.3	2.3	2.3	2.3	2.3	2.3	2.3	2.3	2.3	2.3	2.3	2.3	2.3	2.3	2.3	2.3	2.3	2.3
28	2.1	2.1	2.1	2.1	2.1	2.1	2.1	2.1	2.1	2.1	2.1	2.1	2.1	2.1	2.1	2.1	2.1	2.1
29	2.0	2.0	2.0	2.0	2.0	2.0	2.0	2.0	2.0	2.0	2.0	2.0	2.0	2.0	2.0	2.0	2.0	2.0
30	2.7	2.7	2.7	2.7	2.7	2.7	2.7	2.7	2.7	2.7	2.7	2.7	2.7	2.7	2.7	2.7	2.7	2.7
31	2.0	2.0	2.0	2.0	2.0	2.0	2.0	2.0	2.0	2.0	2.0	2.0	2.0	2.0	2.0	2.0	2.0	2.0
32	1.9	3.2	1.9	1.9	1.1	1.1	1.0	1.9	1.9	1.9	1.1	1.1	2.9	3.2	1.9	1.9	1.9	1.9
33	1.9	1.9	1.9	1.9	1.9	1.9	1.9	1.9	1.9	1.9	1.9	1.9	1.9	1.9	1.9	1.9	1.9	1.9
34	1.7	1.7	1.7	1.7	1.7	1.7	1.7	1.7	1.7	1.7	1.7	1.7	1.7	1.7	1.7	1.7	1.7	1.7
35	2.3	2.3	2.3	2.3	2.3	2.3	2.3	2.3	2.3	2.3	2.3	2.3	2.3	2.3	2.3	2.3	2.3	2.3
36	1.4	1.4	1.4	1.4	1.4	1.4	1.4	1.4	1.4	1.4	1.4	1.4	1.4	1.4	1.4	1.4	1.4	1.4

Table 6.5. Results of $d_{CR}/d_{b\ell}$ from FE Model under Loading Protocol 1.

CASES \ SETS	0	1	2	3	4	5	6	7	8	9	10	11	12	13	14	15	16	17
1	7.5	6.4	6.8	7.1	6.6	6.8	7.0	6.7	6.7	7.0		6.6	6.6	6.4	7.1	6.8	6.1	6.2
2		7.6	7.8	8.0		7.7	7.9	7.9	7.8	8.7	7.9	7.6	7.5	7.2	7.9	7.8	7.2	7.7
3	6.1	5.3	5.7	5.9	5.3	5.5	5.7	5.4	5.4	5.5	5.4	5.5	5.5	5.3	5.8	5.5	4.6	5.5
4	5.5	5.0	5.2	5.3	5.1	5.2	5.2	5.1	5.1	5.2	5.2	5.1	5.1	5.0	5.3	5.2	4.7	5.2
5	5.6	5.0	5.1	5.4	5.0	5.1	5.4	5.0	5.0	5.4	5.1	5.0	5.0	4.9	5.3	5.3	4.9	5.1
6	4.7	5.1	4.2	4.5	4.2	4.3	4.5	4.3	4.2	4.4	4.3	4.3	4.9		4.3	4.3	4.0	4.3
7	5.3	5.2	5.3	5.2	5.2	5.2	5.3	5.2	5.2	5.3	5.2	5.2	5.2	5.2	5.3	5.3	5.1	5.3
8	4.4		4.3	4.5	4.2	4.3	4.4	4.3	4.3	4.4	4.3	4.3			4.4	4.3	4.2	4.3
9	5.5	4.4	4.7	5.0	4.4	4.5	5.2	4.6	4.6	5.0	4.5	4.4	4.4	4.3	5.1	5.1	4.4	4.7
10	4.9	4.3	4.4	4.6	4.3	4.4	4.7	4.4	4.4	4.5	4.4	4.4	4.4	4.3	4.5	4.5	4.3	4.6
11	4.3	4.2	4.2	4.3	4.2	4.2	4.3	4.2	4.2	4.3	4.2	4.2	4.2	4.2	4.3	4.3	4.1	4.2
12		6.3	6.6	6.7	6.1	6.2	6.7	6.2	6.2	6.8	6.7	6.3	6.5	6.1	6.9	6.6	6.0	6.5
13	6.9	6.2	6.3	6.2	6.1	6.0	6.2	6.3	6.3	6.5	6.1	6.0	6.1	6.1	6.4	6.3	6.2	6.1
14		5.3	6.0	6.6	5.0	5.8	6.2	5.4	5.3	6.3	6.1	5.3	5.6	4.9	6.5	6.1	5.1	6.1
15	4.6	4.3	4.4	4.6	4.3	4.4	4.7	4.4	4.4	4.5	4.5	4.4	4.3	4.2	4.5	4.5	4.3	4.5
16		6.4	7.0	7.1	5.8	6.5	7.1	6.6	6.7	6.8	6.7	6.6	6.3	6.2	7.3	6.5	5.0	7.3
17		5.3	5.3	5.6	5.0	5.2	5.9	5.2	5.2	5.5	5.0	5.1	5.1	5.2	5.5	5.2	4.8	5.8
21	7.9	6.6	6.7	7.6	6.5	7.0	7.3	6.9	7.2	7.2	6.8	6.9	6.6	6.4	7.2	7.0	6.7	6.9
22	5.4	4.3	4.4	5.1	4.2	4.4	4.6	4.3	4.3	4.6	4.4	4.4	4.3	4.3	4.6	4.5	4.4	4.8
23	5.1	4.6	4.7	5.0	4.6	4.7	4.9	4.7	4.7	4.8	4.6	4.7	4.5	4.6	5.1	4.8	4.5	4.8
24	4.2	4.0	4.0	4.2	4.0	4.1	4.2	4.7	4.7	4.3	4.1	4.1	4.0	4.0	4.2	4.3	4.3	4.0
25	4.2	4.0	4.3	4.4	4.3	4.2	4.4	4.5	4.5	4.3	4.1	4.2	4.0	4.0	4.3	4.3	4.2	4.4
26	5.8	5.6	5.6	5.6	5.6	5.6	5.8	5.7	5.7	5.8	5.7	5.7	5.6	5.6	5.8	5.8	5.6	5.6
27	4.4	4.2	4.5	4.5	4.6	4.2	4.4	4.7	4.7	4.5	4.3	4.2	4.2	4.2	4.5	4.5	4.5	4.4
28	4.0	3.9	3.9	4.0	4.4	4.0	4.0	4.0	4.0	4.0	4.0	4.0	3.9	3.9	4.0	4.0	3.9	4.0
29	4.0	3.6	4.0	4.0	3.8	4.0	3.9	3.9	3.9	4.0	3.9	4.0	3.6	3.6	4.0	4.0	3.6	3.8
30	5.1	4.7	4.8	5.0	4.8	5.0	5.1	5.0	5.0	5.1	5.0	5.0	4.7	4.7	5.1	5.1	4.6	5.0
31	4.1	3.9	3.9	4.1	3.8	4.1	4.0	3.9	3.9	4.1	4.1	4.1	3.9	3.9	4.1	4.1	3.7	4.0
32	3.7	2.6	3.6	3.7	2.6	2.6	2.6	3.7	3.7	3.7	2.6	2.6	2.6	2.6	3.7	3.7	3.6	3.7
33	3.6	3.5	3.6	3.6	3.5	3.6	3.6	3.6	3.6	3.6	3.6	3.6	3.5	3.5	3.6	3.6	3.5	3.5
34	3.3	3.1	3.4	3.7	3.2	3.2	3.5	3.2	3.2	3.2	3.2	3.2	3.1	3.1	3.2	3.2	3.1	3.6
35	4.6	4.4	4.3	4.5	4.6	4.5	4.5	4.7	4.7	4.6	4.5	4.5	4.4	4.4	4.6	4.6	4.5	4.5
36	3.2	3.1	3.0	3.2	3.3	3.2	3.1	3.4	3.4	3.3	3.2	3.2	3.1	3.1	3.3	3.3	3.3	3.1

The effect of the loading protocol on the resulting d_{POI} and d_{CR} was tested using a subset of the FE models (Set 5, Cases 1 - 36) under the strain histories specified in Figure 6.4. A comparison of the results of d_{POI} and d_{CR} for the different protocols found negligible differences between the two cyclic protocols, and slightly larger values for the monotonic case, limited to a 20% increment, see Figure 6.10. Given these results and considering the extreme case a monotonic loading in the reinforcing steel of a bridge column represents, the effect of the loading protocol on the characteristic dimensions of a buckled bar can be neglected.

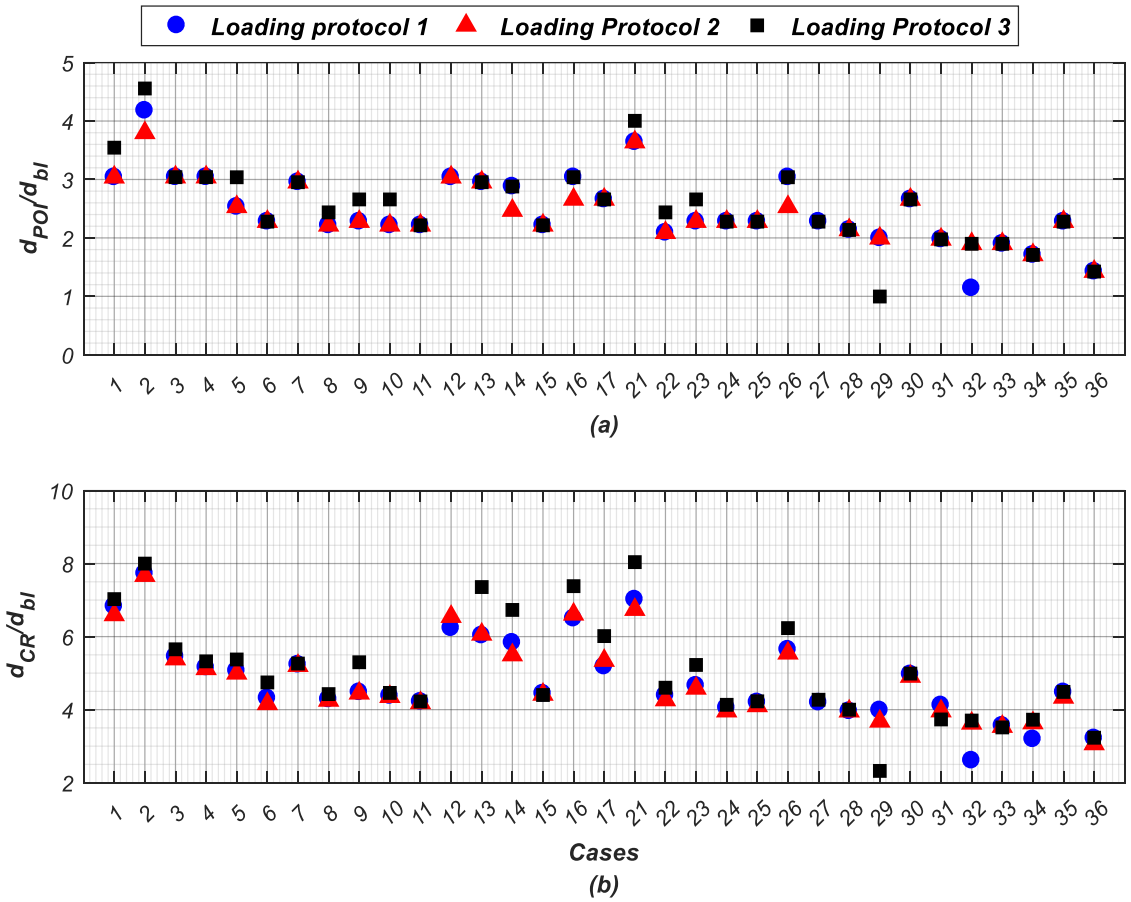

Figure 6.10. Comparison of Loading Protocol Results for Set 5: (a) $d_{POI}/d_{b\ell}$; (b) $d_{CR}/d_{b\ell}$

To evaluate the accuracy of the FE model results, the experimental data and post-mortem information collected from the large bridge column tested at UC San Diego in 2010 (Schoettler et al. 2012), is studied for comparison to the corresponding analytical results.

Following ten strong intensity ground motions, extensive damage was observed in the plastic hinge region of the specimen, including buckling and fracture of the longitudinal reinforcement, with limited crushing of the concrete core, see Figure 6.11.

Figure 6.11. Column Base East Face View after EQ10 (Schoettler et al., 2012).

As part of the post-mortem analysis, longitudinal bar segments from the plastic hinge region were extracted and photographed, providing valuable information on the buckled shape of large diameter bars when interacting with transverse hoops.

For the specimens in Figure 6.12, the distance between inflection points was independently measured by five structural engineers, and a weighted average was obtained to minimize individual bias. The weight assigned to the measurements from each member was based on the precision of the method they used, see Figure 6.13, and the accuracy of

their estimation of buckled shapes artificially generated, for which d_{POI} was known, see Figure 6.14.

(a) (b) (c) (d)

Figure 6.12. Buckled Non-Fractured Reinforcement for Identification of d_{POI} (a) Specimen SW2; (b) Specimen SW3; (c) Specimen NE4; (d) Specimen NW3

The results of the weighted average prove satisfactory, with an average error of **3%** for the measurement of artificial buckled shapes, smaller than the average error in the prediction by any one individual. The weighted average of the distance d_{POI} for each specimen in Figure 6.12 is detailed in Table 6.6.

Table 6.6. Weighted Average Distance Between Points of Inflection

Specimen	Average $d_{POI}/d_{b\ell}$
SW2	4.21
SW3	2.95
NE4	2.98
NW3	3.02
Mean	3.29

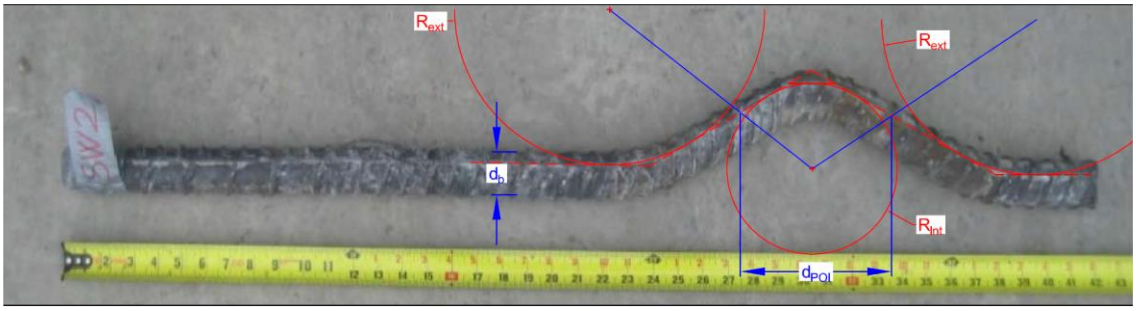

Figure 6.13. Specimen SW2 Measurement of Distance Between Points of Inflection.

Figure 6.14. Artificial Buckled Shape, $d_{POI} = 2.8\ d_{b\ell}$

The average d_{POI} found for the specimens was $3.3 \cdot d_{b\ell}$, which was closely predicted by the corresponding FE model analysis, see Figure 6.7, with a difference of only 9%.

A regression analysis of the results from the FE model analyses found the characteristic dimensions of the buckled shape, d_{POI} and d_{CR}, most closely correlate to the following reinforcement configuration parameters: ρ_s/ρ_ℓ, n_{bar}, and $s/d_{b\ell}$. A simple equation is suggested for each d_{POI} and d_{CR}, Equation 6.2 and 6.3.

$$\frac{d_{POI}}{d_{b\ell}} = 0.54 + \frac{0.82}{\rho_s(\%)} + 0.75 \cdot \left| \sqrt[3]{n_{bar}} - 2.96 \right| + 0.28 \cdot \frac{s}{d_{b\ell}} \qquad 6.2$$

$$\frac{d_{CR}}{d_{b\ell}} = 0.80 + \frac{2.09}{\rho_s(\%)} + 2.05 \cdot \left| \sqrt[3]{n_{bar}} - 2.85 \right| + 0.34 \cdot \frac{s}{d_{b\ell}} \qquad 6.3$$

Figure 6.15a and Figure 6.16a show the fit between the results from Equation 6.2 and 6.3 and the output from the Finite Element models. The lack of bias and small standard deviation of the ratio between FE model solutions and the value predicted by the regression equations ($\mu \approx 1.0$ and $\delta < 12\%$, Figure 6.15b and Figure 6.16b), suggests Equation 6.2 and 6.3 provide an accurate prediction of the dimensions in the buckled shape. Furthermore, the fragility curves for each parameter shows the ratio between "measured" (FE model) and predicted values can be well approximated by a lognormal distribution, particularly in the case of $d_{CR}/d_{b\ell}$.

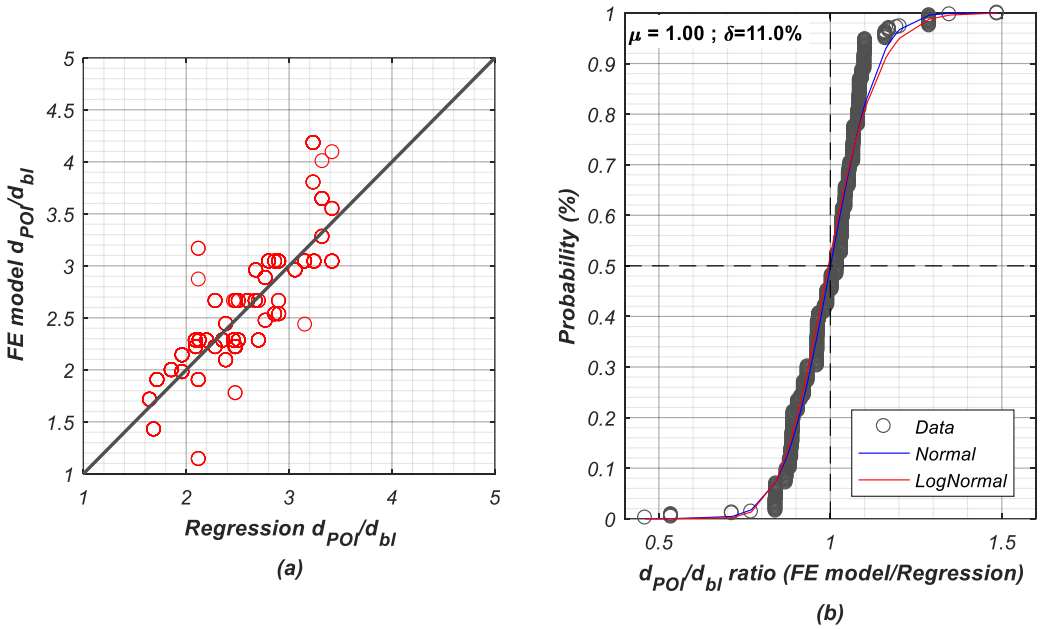

Figure 6.15 Regression Results for $d_{POI}/d_{b\ell}$, 6.2: (a) Regression Results vs FE Model Results; (b) Fragility Curve for Ratio between Regression and FE Model Results

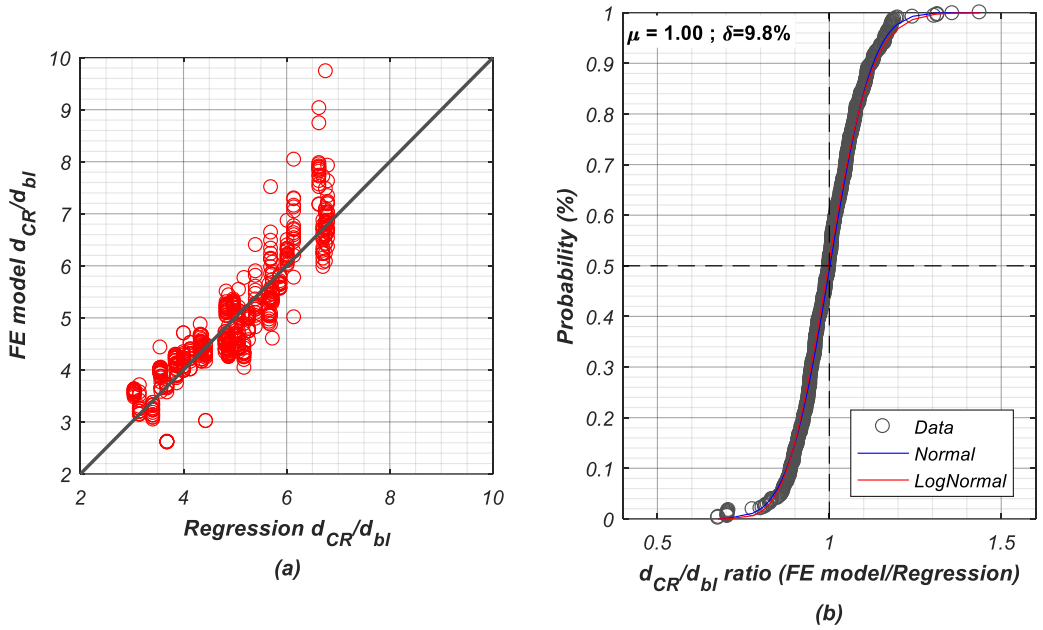

Figure 6.16 Regression Results for $d_{CR}/d_{b\ell}$, 6.3: (a) Regression Results vs FE Model Results; (b) Fragility Curve for Ratio between Regression and FE Model Results

For most predictive variables found in the regression analyses of both characteristic dimensions (d_{POI} and d_{CR}), and limit strains covered in section 6.4.2 (e.g. ε_{vK}), there is a straightforward explanation of their influence on the buckling response of reinforcing bars. The number of longitudinal bars, n_{bar}, however, usually found in the term $\sqrt[3]{n_{bar}}$ throughout regression functions presented in this chapter, needs some additional justification. The effect of n_{bar} in the buckling response is two-fold: first, an increase in n_{bar} at a constant ρ_ℓ will reduce the diameter, and therefore increase the slenderness, of the longitudinal reinforcement; and second, the number of longitudinal bars controls the deformed shape and efficiency of the hoop reinforcement in restraining lateral deformations, a phenomenon called herein the "polygon effect". The influence of n_{bar} on the slenderness of longitudinal reinforcement had little significance for the size of bars typically used in bridge columns, which are large enough to ensure the buckled shape will

span between multiple hoops (for extreme changes in bar size however, this effect cannot be neglected). On the other hand, the "polygon effect" has significant importance for small values of n_{bar}, with the effect reducing as the number of bars increases. For a small number of longitudinal bars, the lateral deformations after the onset of buckling will push the transverse hoops at very discrete locations, forcing the circular hoop to a deformed shape resembling a polygon with vertices at the location of each longitudinal bar. To achieve this deformed shape, the circular hoops will bend at the vertices, producing noticeable "kinks" see Figure 6.17. Transverse hoops are most effective restraining lateral deformations when working in pure tension, not bending, therefore as the number of bars increases, pushing the hoops to deform as a circle, the hoops can restraint lateral deformations more effectively. The "polygon effect" is expected to be significant only for small values of n_{bar}, and become less important as n_{bar} increases, which is consistent with the cubic root, $\sqrt[3]{n_{bar}}$, found in the regression results.

(a) (b)

Figure 6.17. Polygon Effect Observed in Plastic Hinge of Type II shaft (source: Lotfizadeh and Restrepo, in-preparation)

6.4.2. Relation Between Local and Smeared Strains

The compressive strain in the concave side of buckled steel reinforcement, ε_{kv}, is a critical index of damage, and ultimately controls the strain at fracture. Because of this, the estimation of the critical local strain, ε_{kv}, in terms of the strain smeared along the plastic hinge length of a RC member, is essential to assess damage and predict fracture of longitudinal reinforcement. As with the geometry of the buckled shape in section 6.4.1, the relation between local and smeared strains in buckled bars is dependent on the reinforcement configuration of the RC member, as well as the material properties of transverse hoops and longitudinal bars.

For the analyses in this section, a parameter λ_{CR} is defined as the ratio between the natural strain in the concave fiber, ε'_{kv}, and the smeared natural strain between centers of

rotation of the buckled shape, ε'_{CR}, see Equation 6.4. The use of natural over engineering strains accounts for the change in geometry of the steel bar at large deformations and takes advantage of the symmetric tension/compression response of the material in natural coordinates (see Figure 4.1). Both local and smeared strain in λ_{CR} are shifted by the peak strain in tension, ε'_{st}, following the change in uniform (natural) strain of steel, ε'_{u}, found by Dodd and Restrepo (1995), see Figure 6.18.

$$\lambda_{CR} = \frac{\varepsilon'_{st} - \varepsilon'_{kv}}{\varepsilon'_{st} - \varepsilon'_{CR}} = \frac{\Delta\varepsilon'_{kv}}{\Delta\varepsilon'_{CR}} \quad \text{(a)}$$

$$\lambda_{POI} = \frac{\varepsilon'_{st} - \varepsilon'_{kv}}{\varepsilon'_{st} - \varepsilon'_{POI}} = \frac{\Delta\varepsilon'_{kv}}{\Delta\varepsilon'_{POI}} \quad \text{(b)} \qquad 6.4$$

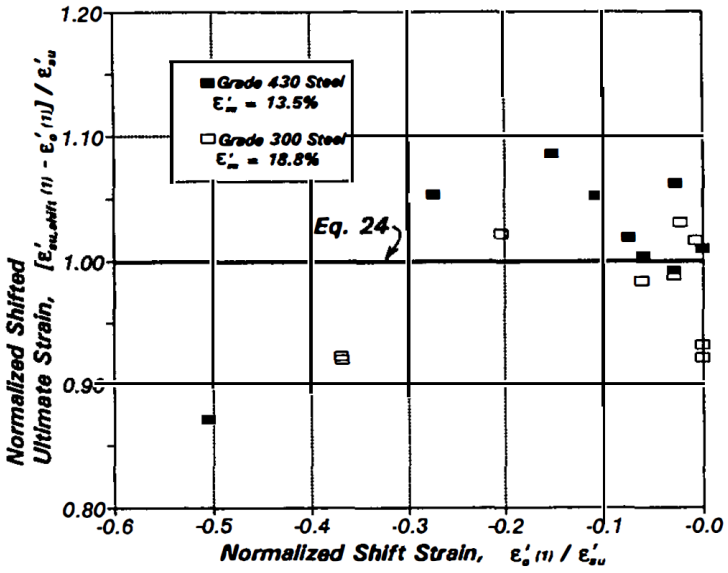

Figure 6.18. Effect of Shift Strain on True Strain at Ultimate Tensile Load (Dodd and Restrepo, 1995)

As stated by Wang and Restrepo (1996), and by Moyer and Kowalsky (2003), the buckling of reinforcement in a RC member is highly dependent on the deformations in tension, and any longitudinal bar buckling will occur for relatively large values of ε'_{st}, see Section 2.2 for details.

From the results of the FE model analyses, the relation between the smeared strain amplitude, $\Delta\varepsilon'_{CR}$, and λ_{CR} at each analysis step following the onset of buckling (state 2 of the analysis, see Section 6.4) was determined for each reinforcement configuration/material property combination (Table 6.1 and Table 6.3 respectively). As seen in the results for Set 0 – Case 4 in Figure 6.19, the relation between the smeared strain and λ_{CR} can be approximated by a linear function, see Equation 6.5. The parameters defining the line, c_1 and $\Delta\varepsilon'_{EC}$, can be determined from a regression analysis of the FE model results.

$$\lambda_{CR} = 1+c_1 \cdot \left(\Delta\varepsilon'_{CR} - \Delta\varepsilon'_{EC}\right) \qquad 6.5$$

Where $\Delta\varepsilon'_{EC} = \varepsilon'_{st} - \varepsilon'_{EC}$ is the amplitude between peak tensile strain and the onset of buckling (Engesser - Considère strain).

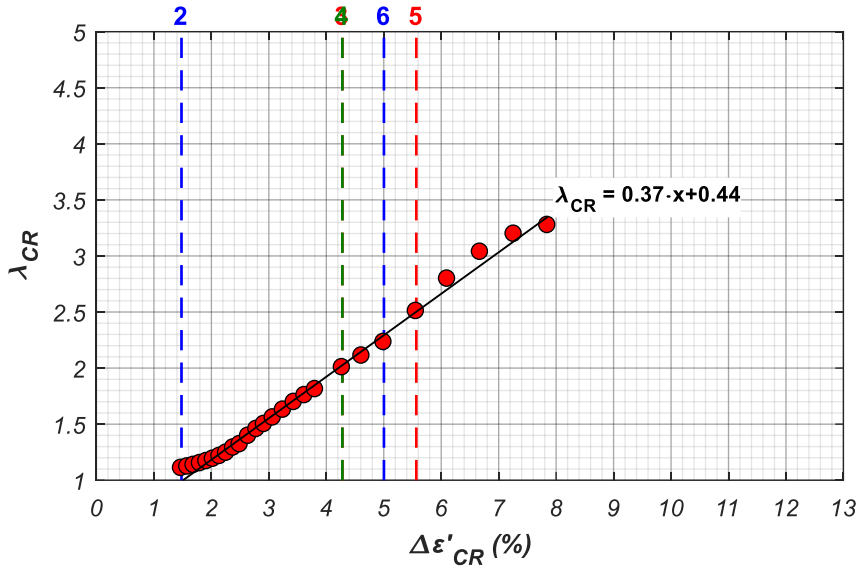

Figure 6.19. Smeared Strain between Centers of Rotation (CR), Shifted by Peak Tensile Strain ε'_{st}, vs Ratio of Local Strain in Concave Fiber over Smeared Strain (λ_{CR}, see 6.4). Set 0 – Case 4 – Protocol 1

Based on Equation 6.4a and 6.5, an upper limit for the strain amplitude between centers of rotation, $\Delta\varepsilon'_{CR}$, is determined for the condition of the damage index, DI, remaining below 1.0 in fibers in the concave side of the reinforcement, $\Delta\varepsilon'_{kv} \leq \varepsilon'_{su}$, see Equation 6.6.

$$\Delta\varepsilon'_{CR} \leq \frac{1}{2}\cdot\left(\sqrt{\left(\frac{1}{c_1}-\Delta\varepsilon'_{EC}\right)^2+4\cdot\frac{\varepsilon_u}{c_1}} \; - \; \left(\frac{1}{c_1}-\Delta\varepsilon'_{EC}\right)\right) \qquad 6.6$$

Similar to the analysis of the characteristic dimensions d_{POI} and d_{CR} a simple, yet accurate, regression function is generated to predict the value of $\Delta\varepsilon'_{EC}$ in Equation 6.5 from the reinforcement configuration and material properties of the column, see Equation 6.7 and Figure 6.20. The mean and standard deviation of the ratio between finite element model

and the regression analysis results, at μ=1.0 and σ=8.8%, indicate the good accuracy attained by the regression function.

$$\Delta\varepsilon'_{EC} = 0.062 + 0.33 \cdot \rho_s - 0.0044 \cdot \frac{s}{d_{b\ell}} - 0.023 \cdot \frac{T}{Y} \qquad 6.7$$

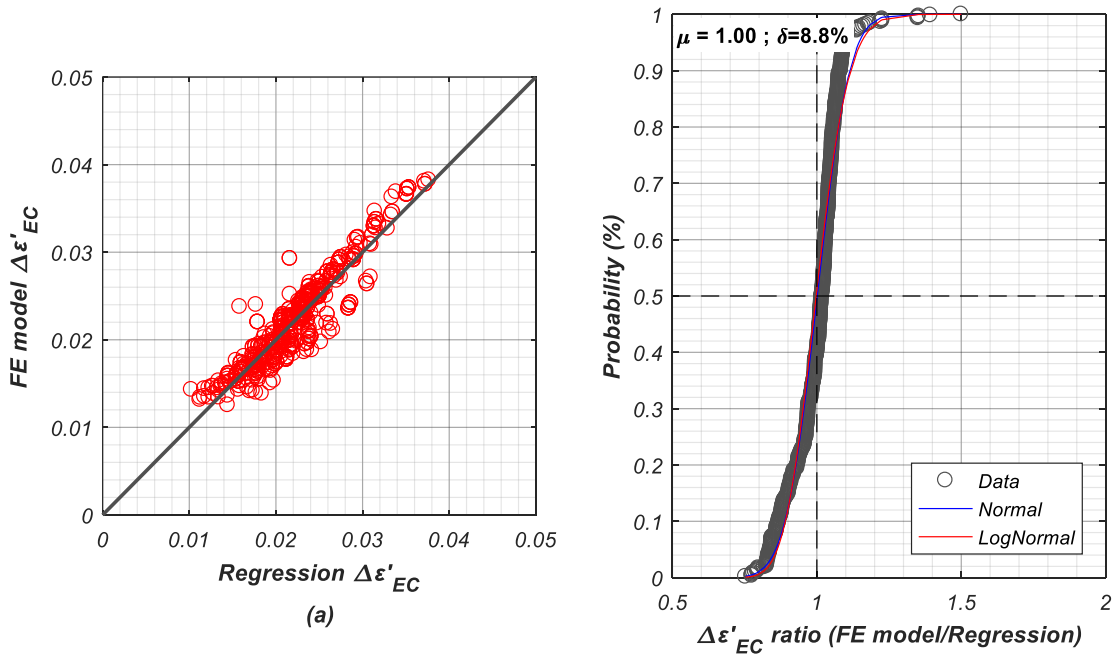

Figure 6.20 Regression Results for $\Delta\varepsilon'_{EC}$, 6.7: (a) Regression Results vs FE Model Results; (b) Fragility Curve for Ratio between Regression and FE Model Results

Completing the formulation for λ_{CR}, the slope c_1 in Equation 6.5 is determined by regression analysis, see Equation 6.8. Only the cases where c_1 was greater than 10 and the stability condition $\rho_s/\rho_\ell > 0.48$ was satisfied, see section 6.4.3, were considered for the analysis. Only within these limits for c_1 the value λ_{CR} is expected to control the design for plastic buckling-straightening fatigue. For values of c_1 under 10, the buckling of reinforcement is significantly delayed, therefore large strain concentrations in the concave side, ε'_{kv}, are not a concern, whereas reinforcement configurations with $\rho_s/\rho_\ell \leq 0.48$ will

likely have an unstable post-buckling behavior, see section 6.4.3, thus requiring a redesign to prevent premature fracture.

$$c_1 = 25.1 \cdot \left(\frac{\rho_s}{\rho_l} \cdot \sqrt[3]{n_{bar}} \right)^{-1} + 41.8 \cdot \frac{T}{Y} + 9.9 \cdot \frac{s}{d_{bl}} - 68.0 > 0 \qquad 6.8$$

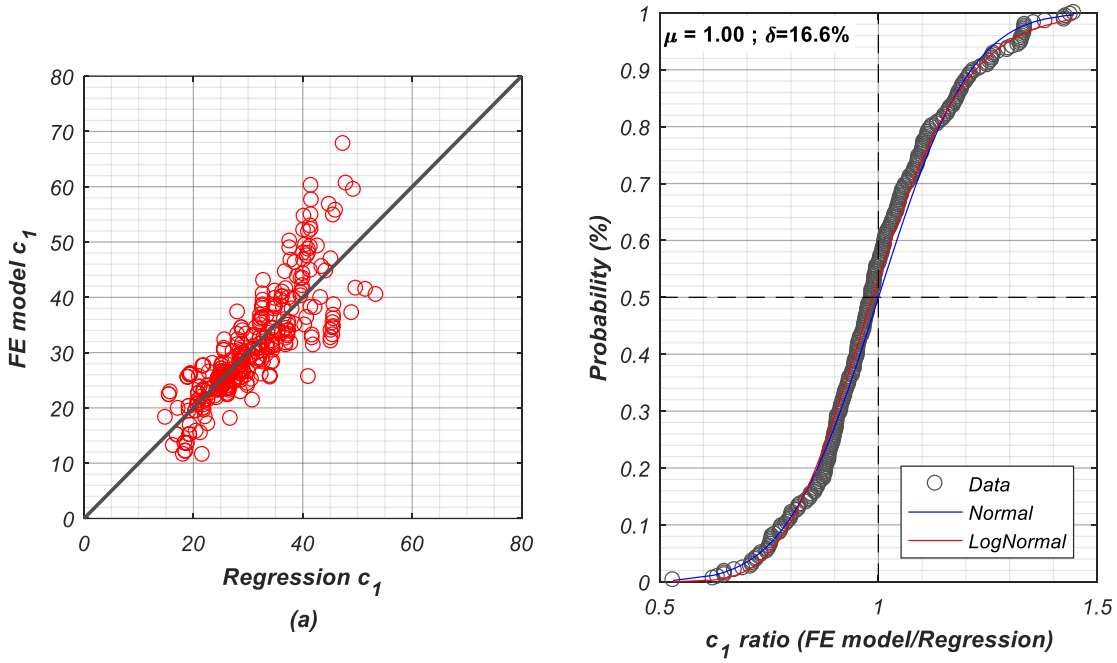

Figure 6.21 Regression Results for c_1, 6.8: (a) Regression Results vs FE Model Results; (b) Fragility Curve for Ratio between Regression and FE Model Results

A simplified regression equation for c_1, including only variables typically available to the design engineer is presented in Equation 6.9. The equation includes a constant bias, overpredicting c_1 in 95 percent of the analyzed models. This formulation is intended for the design of transverse reinforcement to prevent the limit state of plastic buckling-straightening fatigue for the longitudinal reinforcement, see Chapter 7. .

$$c_1 = \frac{39.1}{\frac{\rho_s}{\rho_\ell} \cdot \sqrt[3]{n_{bar}}} + 29.0 \qquad 6.9$$

In a design procedure, the strain in the reinforcement of the critical element section, obtained from a Moment-Curvature (M-ϕ) analysis, corresponds to the smeared value along the strain compatible equivalent plastic hinge length of the member, $L_{p\varepsilon}$, described in section 5.2.3. By simple geometry, the relation between engineering strain smeared along the equivalent plastic hinge of the member, ε_s, and engineering strain between centers of rotation of the buckled shape, ε_{CR}, is as follows:

$$L_{p\varepsilon} \cdot (1+\varepsilon_s) = d_{CR} \cdot (1+\varepsilon_{CR}) + (L_{p\varepsilon} - d_{CR}) \cdot (1+\varepsilon_{EXT}) \qquad 6.10$$

Combining Equation 6.10 for the states of maximum tension and subsequent buckling in compression, ε_s equals ε_{st} and ε_{sc} in Figure 6.22, results in the following relation:

$$L_{p\varepsilon} \cdot \Delta\varepsilon_{t\text{-}c} = d_{CR} \cdot \Delta\varepsilon_{CR} + (L_{p\varepsilon} - d_{CR}) \cdot \Delta\varepsilon_{EXT} \qquad 6.11$$

Where $\Delta\varepsilon_{t\text{-}c} = \varepsilon_{st} - \varepsilon_{sc}$ is the engineering strain amplitude smeared along the plastic hinge length $L_{p\varepsilon}$, $\Delta\varepsilon_{CR}=\varepsilon_{st}\text{-}\varepsilon_{CR}$ is the engineering strain amplitude smeared between centers of rotation of the buckled shape, and $\Delta\varepsilon_{EXT} = \varepsilon_{st}-\varepsilon_{EXT}$ is the engineering strain amplitude outside the buckled shape of the bar. ε_{st} is the maximum engineering strain in tension preceding the onset of buckling, see Figure 6.22. Rearranging the terms in Equation 6.11, the strain amplitude between centers of rotation, $\Delta\varepsilon_{CR}$, can be computed as follows:

$$\Delta\varepsilon_{CR} = \frac{L_{p\varepsilon} \cdot \Delta\varepsilon_{t\text{-}c} - (L_{p\varepsilon} - d_{CR}) \cdot \Delta\varepsilon_{EXT}}{d_{CR}} \qquad 6.12$$

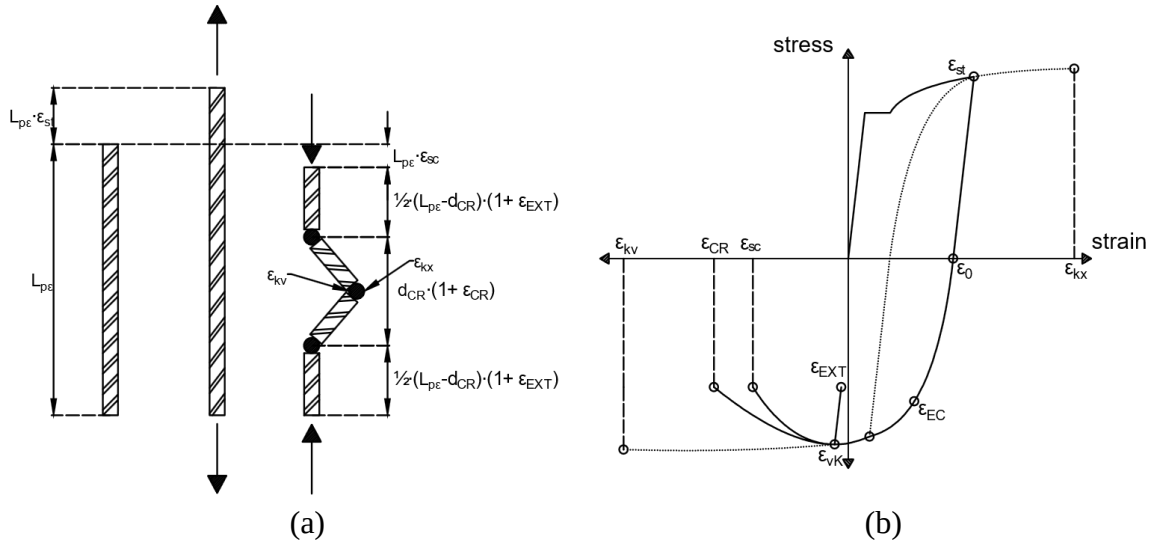

Figure 6.22. Strain Distribution in Buckled Reinforcement: (a) Dimensions of Buckled Element; (b) Stress-Strain Response of Buckled Bar

From Figure 6.22b, the strain smeared along the plastic hinge length of the reinforced concrete column, ε_{sc}, matches the smeared strain between centers of rotation, ε_{CR}, until the strain at the peak compressive stress, ε_{vK}, defined herein as the von Karman strain, is reached. Once ε_{vK} is exceeded, the bar segments outside the buckled portion start to unload in tension, thus ε_{sc} and ε_{CR} start to diverge. Assuming that for a well-designed RC member the drop in compressive stress following ε_{vK} is small, the value of $\Delta\varepsilon_{EXT}$ can be approximated by $\Delta\varepsilon_{vK}$ in 6.12 to compute $\Delta\varepsilon_{CR}$, see Figure 6.22b.

The natural strain amplitude at the peak compressive stress, $\Delta\varepsilon'_{vK}$, can be determined from a regression analysis of the FE model results, see Equation 6.13. For a reliable performance against plastic buckling-straightening fatigue (PBSF), the strain

demand of reinforcing bars shall remain below the von Karman strain amplitude, preventing large strain concentrations between centers of rotation of the buckled shape.

$$\Delta\varepsilon'_{vK} = 0.11 + \min(0.054, 0.032 \cdot \rho_s(\%)) - 0.0175 \cdot \left| \sqrt[3]{n_{bar}} - 2.93 \right| - 0.054 \cdot \frac{T}{Y} \qquad 6.13$$

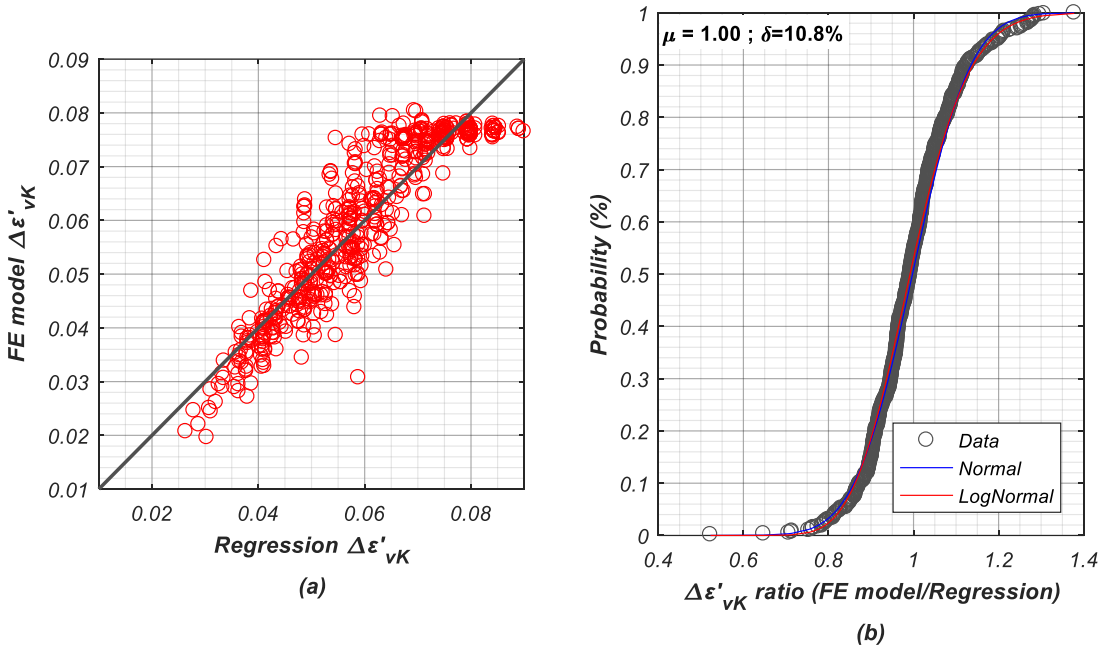

Figure 6.23 Regression Results for ε'_0-ε'_{vK}, 6.13: (a) Regression Results vs FE Model Results; (b) Fragility Curve for Ratio between Regression and FE Model Results

As with the characteristic dimensions of the buckled shape (d_{POI} and d_{CR}), the strain estimates obtained from regression analyses should consider the effect of the loading protocol. Figure 6.24 shows the results for $\Delta\varepsilon'_{EC}$ and $\Delta\varepsilon'_{vK}$ for all reinforcement configurations with one combination of material properties (Set 5 – Case 1 to 36) for the three loading protocols described in section 6.3.3. Unlike the distances d_{POI} and d_{CR} described in Section 6.4.1, the effect of the loading protocol cannot be neglected in the values of $\Delta\varepsilon'_{EC}$ and, to a lesser extent, $\Delta\varepsilon'_{vK}$. Figure 6.24a shows that an increase in tensile

strains, ε_{st}, corresponding to 4.5%, 6.0% and 0% for loading protocols 1, 2 and 3, increases the distance $\Delta\varepsilon'_{EC}$. A correction factor dependent on ε_{st} should therefore be included in Equation 6.7. The significant difference in the results of $\Delta\varepsilon'_{EC}$ and $\Delta\varepsilon'_{vK}$ for the monotonic loading protocol is expected, given the difference in the stress-strain response preceding the onset of buckling in steel that has not experienced initial strain hardening. However, for typical bridge column members with low axial load ratio, the critical reinforcement is expected to undergo large plastic deformations in tension before the onset of buckling. The following correction to Equation 6.7 is suggested:

$$\Delta\varepsilon'_{EC} = 0.044 + 0.33\cdot\rho_s - 0.0044\cdot\frac{s}{d_{b\ell}} - 0.023\cdot\frac{T}{Y} + 0.39\cdot\varepsilon_{st} \qquad 6.14$$

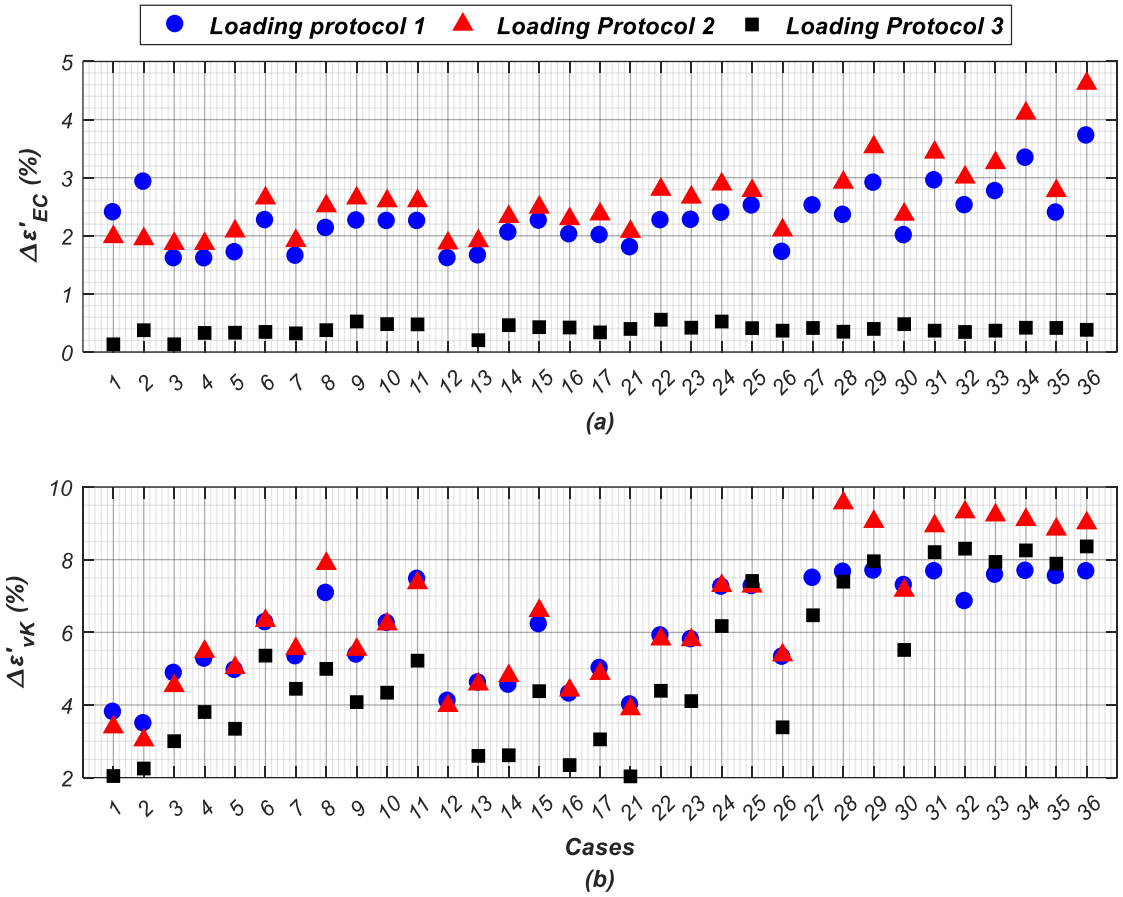

Figure 6.24. Comparison of Loading Protocol Results for Set 5: (a) $\Delta\varepsilon'_{EC}$; (b) $\Delta\varepsilon'_{vK}$

The effect of the loading protocol on the value of $\Delta\varepsilon'_{vK}$ is much less pronounced, and no clear trend was observed, see Figure 6.24b. Because of this, no corrections to Equation 6.13 are deemed necessary.

6.4.3. Stability of Post-Buckling Response

Among all the reinforcement configuration and material property combinations analyzed as part of this Chapter, a small set of the stress-strain responses – 6 percent of all analyses –showed a rapid decrease in the stress capacity after the peak in compression, f_{vK},

was reached, see Figure 6.25. This is an undesirable behavior for the design of the plastic hinge region of a column, with a non-ductile response before fracture and large strain concentrations in a short span of the reinforcement (e.g. d_{CR}). This section introduces a simple formulation, based on statistical analysis of the FE model results, to predict the stability of the post-peak response in reinforcing bars, based on the reinforcement configuration used.

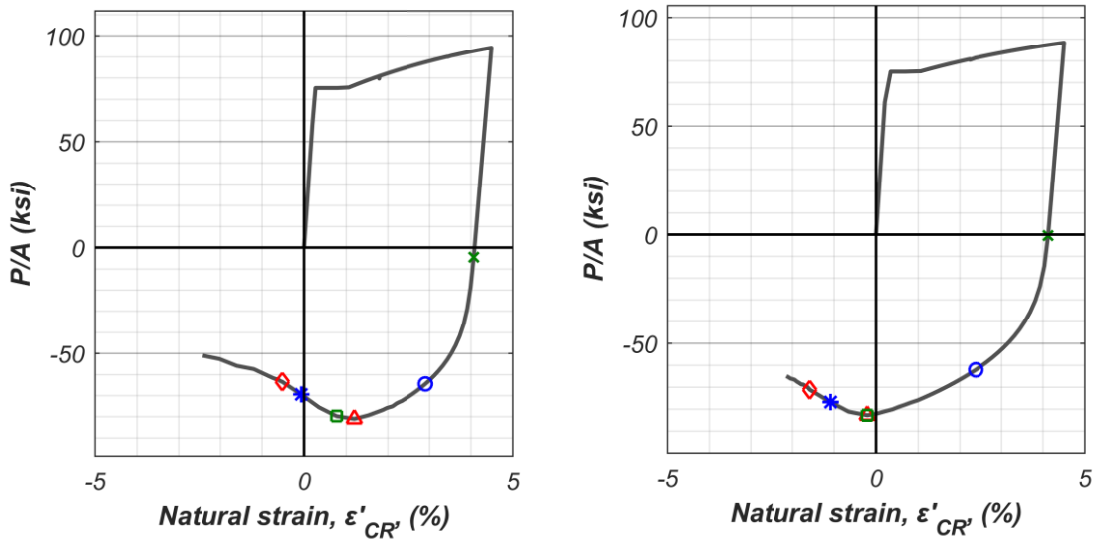

(a) (b)

Figure 6.25. Stress-Strain Response with Rapid Decrease in Capacity after f_{vK}: (a) Set 0 – Case 12; (b) Set 7 – Case 16

For the purposes of this study, a post-peak response is considered stable when one of two conditions are met:

1) The strain amplitude between the peak stress in compression and the plastic strain in tension, ε'_{vK}-ε'_{0}, is greater than 5%. This is a conservative limit for the

amplitude of strains in the reinforcement of bridge columns under a design level earthquake, see Figure 6.26a.

2) The magnitude of the stress in compression following f_{vK} decreases less than 10% before the uniform strain, ε_u, is attained in the concave fiber of the buckled shape (ε'_0-$\varepsilon'_{kv} \geq \varepsilon'_u$, $DI = 1$), see Figure 6.26b.

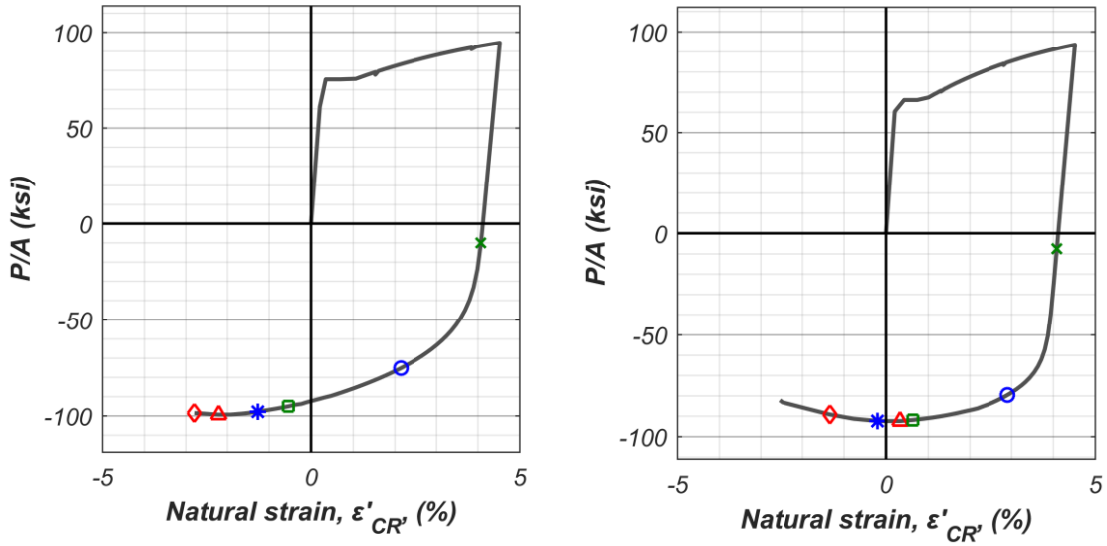

(a) (b)

Figure 6.26. Stable Post-Peak Stress-Strain Response: (a) ε'_0-$\varepsilon'_{vK} \geq 5\%$ (Set 0-Case 25); (b) Post-Peak Stress Reduction Less Than 10% (Set 3 – Case 10)

From a logistic binary regression, commonly used to predict variables with only two possible outputs, in this case between a "Stable" and "Unstable" post-peak response, a probability function for the "Stable" condition is obtained:

$$P(Stable) = \frac{1}{1+\exp(7.2-21.2\cdot \rho_s / \rho_\ell)} \qquad 6.15$$

Figure 6.27 shows the fit between the probability function in 6.15 and the observed behavior from the Finite element models. Assuming, conservatively, that a reinforcement configuration will yield a Stable post-peak response only if P(Stable) > 95%, results in the following limit condition:

$$\begin{cases} \text{Stable Post-Peak} & \text{if } \dfrac{\rho_s}{\rho_\ell} \geq 0.48 \\ \text{Unstable Post-Peak} & \text{Otherwise} \end{cases} \qquad 6.16$$

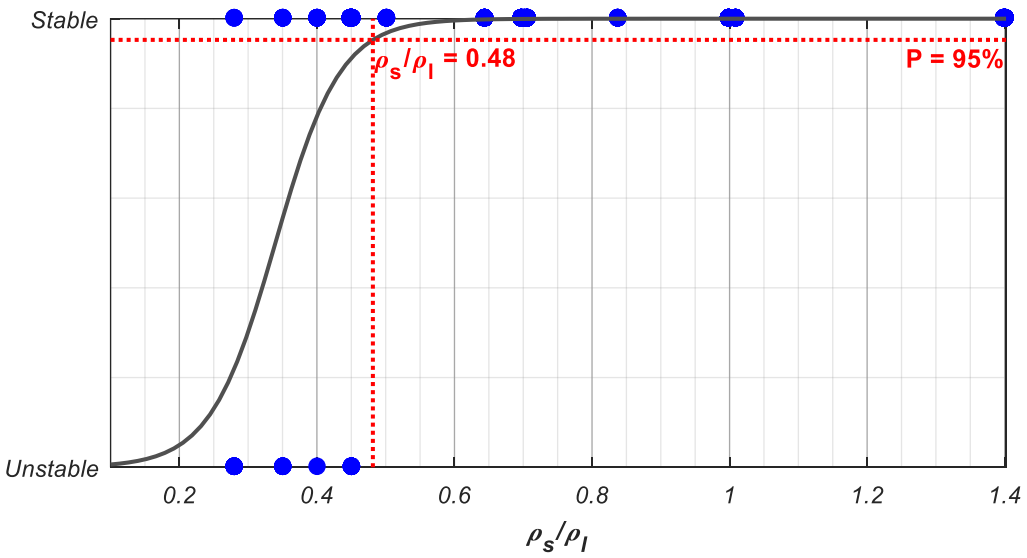

Figure 6.27. Observed Stable or Unstable Post-Peak Response with Logistic Binary Regression Function

6.5. Summary

In this chapter the analysis of more than 500 finite element model realizations were performed. The models capture the behavior of reinforcing bars well beyond the onset of buckling, taking into account the interaction with transverse hoops. Typical reinforcement configurations and material properties of bridge columns designed in accordance to Caltrans SDC were considered.

A statistical analysis of the computational results showed that characteristic dimensions of the buckled shape (e.g. d_{POI}, d_{CR}), and the relation between smeared and local strains after the onset of buckling, are highly correlated to the reinforcement configuration parameters ρ_s, $\sqrt[3]{n_{bar}}$, and $s/d_{b\ell}$, as well as T/Y, the tensile to yield strength ratio of the longitudinal reinforcement. Equations 6.2 to 6.16, resulting from the regression analysis of the FE model results, are presented herein to predict the geometry of the buckled reinforcement (e.g. d_{POI}, d_{CR}), characteristic strain limits (e.g. $\varepsilon_{E\text{-}C}$, ε_{vK}), and amplification factors between smeared and local strains (λ_{CR}).

Based on regression analyses, the effect of the loading protocol on reinforcing bars has a negligible effect on the geometric properties of the buckled shape (d_{POI}, d_{CR}). Conversely, the strain amplitude at the onset of buckling, $\Delta\varepsilon_{EC}$, shows a significant correlation to ε_{st}, see Equation 6.14.

Results from the FE model analyses closely match the behavior observed in the longitudinal reinforcement of a bridge column designed according to Caltrans SDC and tested at UC San Diego's large outdoor shake-table (Schoettler et al., 2012). The column showed significant plastic buckling-straightening fatigue in the plastic hinge region.

Comparison of analytical and experimental response was performed in terms of the geometry of the buckled bars, in particular d_{POI}, the information most readily available from the experimental results.

Finally, based on binary regression of the analytical results, a simple limit for the ratio between transverse and longitudinal reinforcement ratios, ρ_s/ρ_ℓ, is established to prevent an undesirable drop in the stress capacity of reinforcing bars after the peak compressive stress is reached, see Equation 6.16.

Chapter 6, in full, is a reprint of the material as it appears in *SSRP Report 17/10: Plastic buckling-straightening fatigue of large Diameter reinforcing steel bars*, 2018. Duck, David; Carreño, Rodrigo; and Restrepo, José I. The dissertation author was a co-author of this report and first author of the specific Chapter.

Chapter 7.

DESIGN AND VERIFICATION PROCEDURES FOR PLASTIC BUCKLING – STRAIGHTENING FATIGUE (PBSF) OF LONGITUDINAL REINFORCEMENT

7.1. General

Caltrans SDC (2013) specifies minimum design requirements necessary to meet the performance goals for Ordinary Bridges. The purpose of this specification is to update current Structure Design manuals with new and existing seismic design criteria, based on multiple documented research efforts. SDC v.1.7 (2013) addresses some of the most recent seismic design philosophies, using displacement demand/capacity for the design of ductile members, and capacity design for elements not intended to develop plastic deformations (e.g. bent-caps).

According to Caltrans SDC, the Collapse Limit State in a ductile bridge column can be defined by one of two strain limits in the Moment-Curvature analysis of the plastic hinge region: crushing of the concrete core, or fracture of the longitudinal reinforcement. The code defines a reduced ultimate strain for the longitudinal reinforcement, $\varepsilon_u{}^R$, which

does not explicitly account for Buckling-Straightening fatigue fracture of bars, often observed in bridge column specimens subjected to seismic loads (Schoettler et al. 2012).

In this section, a design procedure based on SDC specifications is suggested for the ductile design of RC bridge columns, with the fracture of longitudinal reinforcement due to buckling-straightening fatigue considered explicitly. Additionally, a verification procedure is described, to be used when all reinforcement configuration parameters are known.

7.2. Current Design Procedure

As per Caltrans SDC, the capacity and demand of ordinary bridge systems is evaluated in terms of the lateral displacement. This section describes a step-by-step procedure for the design of a fixed based bridge columns following SDC specifications.

1) Definition of the geometry of the column (e.g. length, diameter) and initial configuration of the longitudinal reinforcement, $\rho_{\ell,}$ meeting the limits set forth by SDC, Equation 7.1.

$$A_{st,\max} = 0.04 \cdot A_g \quad \text{(a)}$$
$$A_{st,\min} = 0.01 \cdot A_g \quad \text{(b)} \qquad 7.1$$

2) Compute the expected nominal moment capacity, M_{ne}, using expected material properties of steel and concrete.

3) Compute over-strength shear demand, V_0, and design the shear reinforcement configuration, ρ_s, according to Section 3.6 in SDC, using nominal material properties.

$$V_0 = 1.2 \cdot \frac{M_p^{col}}{L} \approx 1.2 \cdot \frac{M_{ne}}{L} \quad \text{(a)}$$

$$\phi \cdot V_n \geq V_0 \quad \text{(b)} \qquad 7.2$$

Where The resistance factor ϕ for shear is 0.9 (Section 3.2.1 in SDC)

Verify the conditions for minimum and maximum shear reinforcement are met, Equation 7.3 (see SDC section 3.6).

$$V_s \leq 8 \cdot \sqrt{f'_c(psi)} \times A_e \quad \text{(a)}$$

$$\rho_s \geq \frac{0.1}{f_{yh}(ksi)} \quad \text{(b)} \qquad 7.3$$

4) Determine the equivalent lateral stiffness of the column, K, using either a Pushover analysis, Moment-curvature (M-ϕ) response (see Equation 7.4a), or effective section properties (see Equation 7.4b), as per section 5.6 in SDC:

$$K = \frac{3 \cdot M_y}{\phi_y \cdot L^2} \quad \text{(a)}$$

$$K = \frac{3 \cdot E_c I_{eff}}{L^2} \quad \text{(b)} \qquad 7.4$$

5) Based on the effective lateral stiffness, *K*, and tributary weight of the column, *W*, compute the first predominant period of the column system.

$$T_1 = 2 \cdot \pi \cdot \sqrt{\frac{W}{g \cdot K}} \qquad 7.5$$

6) Compute the displacement demand for period T_1 from the design response spectrum (Chapter 2 in SDC). Transform modal displacement demands into displacement at the top of the column using the modal shape and participation factor of the first mode.

$$\Delta_d = S_d\left(T_1\right) \cdot \Gamma_1 \cdot \varphi_1^{top} \qquad 7.6$$

Where Γ_1 is the modal participation factor of the first mode and φ_1^{top} the component of the first mode shape at the top of the column.

7) Determine the plastic displacement demand on the member, Δ_p in Equation 7.7a, and compute the equivalent plastic hinge length, L_p, as per section 7.6.2 in SDC.

$$\Delta_p = \Delta_d - \Delta_Y^{col} \qquad \text{(a)}$$

$$\Delta_Y^{col} = \frac{L^2}{3} \cdot \phi_Y \qquad \text{(b)} \qquad 7.7$$

8) Using the plastic rotation concept, θ_p, compute the plastic curvature, ϕ_p, along the equivalent plastic hinge length to reach Δ_p.

$$\Delta_p = \theta_p \cdot \left(L - \frac{L_p}{2} \right) \qquad \text{(a)}$$

$$\phi_p = \frac{\Delta_p}{L_p \cdot \left(L - \frac{L_p}{2} \right)} \qquad \text{(b)} \qquad 7.8$$

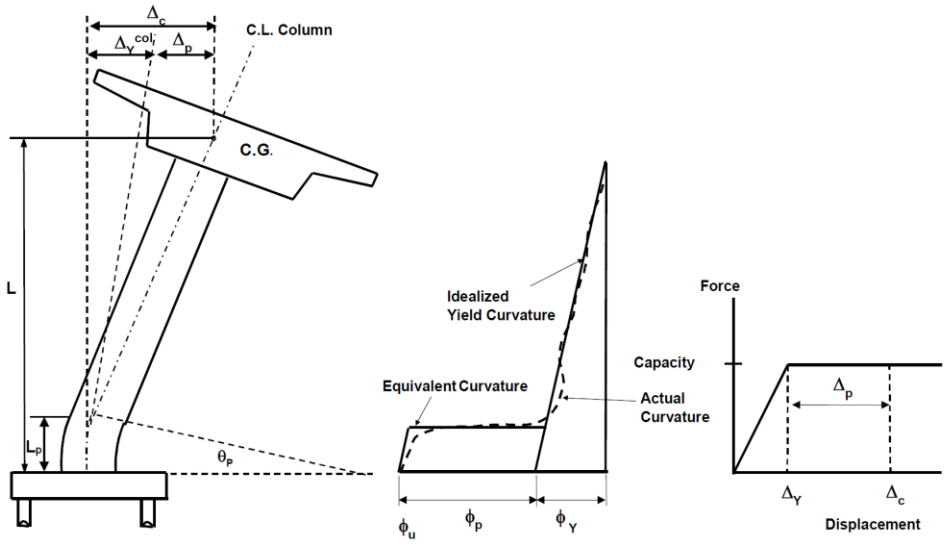

Figure 7.1. Displacement Capacity of Cantilever Column with Fixed Base (SDC v.1.7)

9) Perform a monotonic *M-ϕ* analysis of the critical section of the column, considering expected material properties and confinement of the concrete core, see Figure 7.2.

10) Identify ϕ_u for the strain limit states of the concrete core and longitudinal reinforcement, Equation 7.9. Verify the minimum displacement ductility demand on the column (see Equation 7.10)

$$\varepsilon_{cc} \geq \varepsilon_{cu} \quad \text{(a)}$$
$$\varepsilon_s \leq \varepsilon_{su}^R \quad \text{(b)} \qquad 7.9$$

$$\mu_c = \frac{\Delta_c}{\Delta_Y^{col}} \geq 3 \qquad 7.10$$

11) If the plastic curvature capacity from the M-ϕ curve, ϕ_u-ϕ_Y^{col}, is greater than the demand in Equation 7.8b, move to step 12). If curvature capacity is insufficient, modify design depending on the controlling limit state (e.g. if core concrete crushes, consider increasing transverse reinforcement for higher confinement) and return to Step 4).

12) With the Plastic moment capacity from the M-ϕ curve, M_p^{col} in Figure 7.2, compute overstrength moment, M_0, and the shear demand, V_0.

$$M_0 = 1.2 \cdot M_p^{col} \quad \text{(a)}$$

$$V_0 = \frac{M_0}{L} \quad \text{(b)} \qquad 7.11$$

13) Verify shear design, Equation 7.2b. If transverse reinforcement is sufficient, continue with seismic detailing (Chapter 8 in SDC). If transverse reinforcement is insufficient, repeat shear design and return to Step 9).

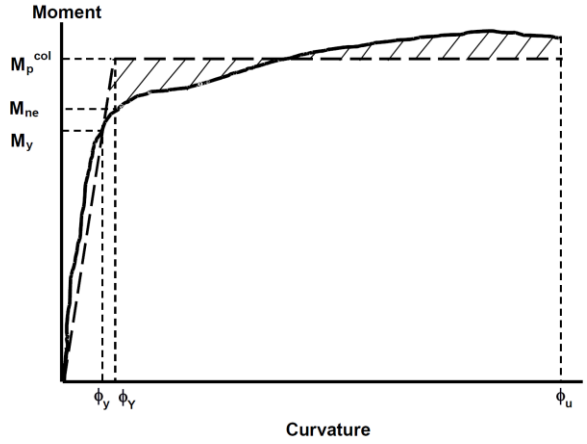

Figure 7.2. Moment- Curvature curve (M-ϕ). Column section at the plastic hinge (SDC v.1.7)

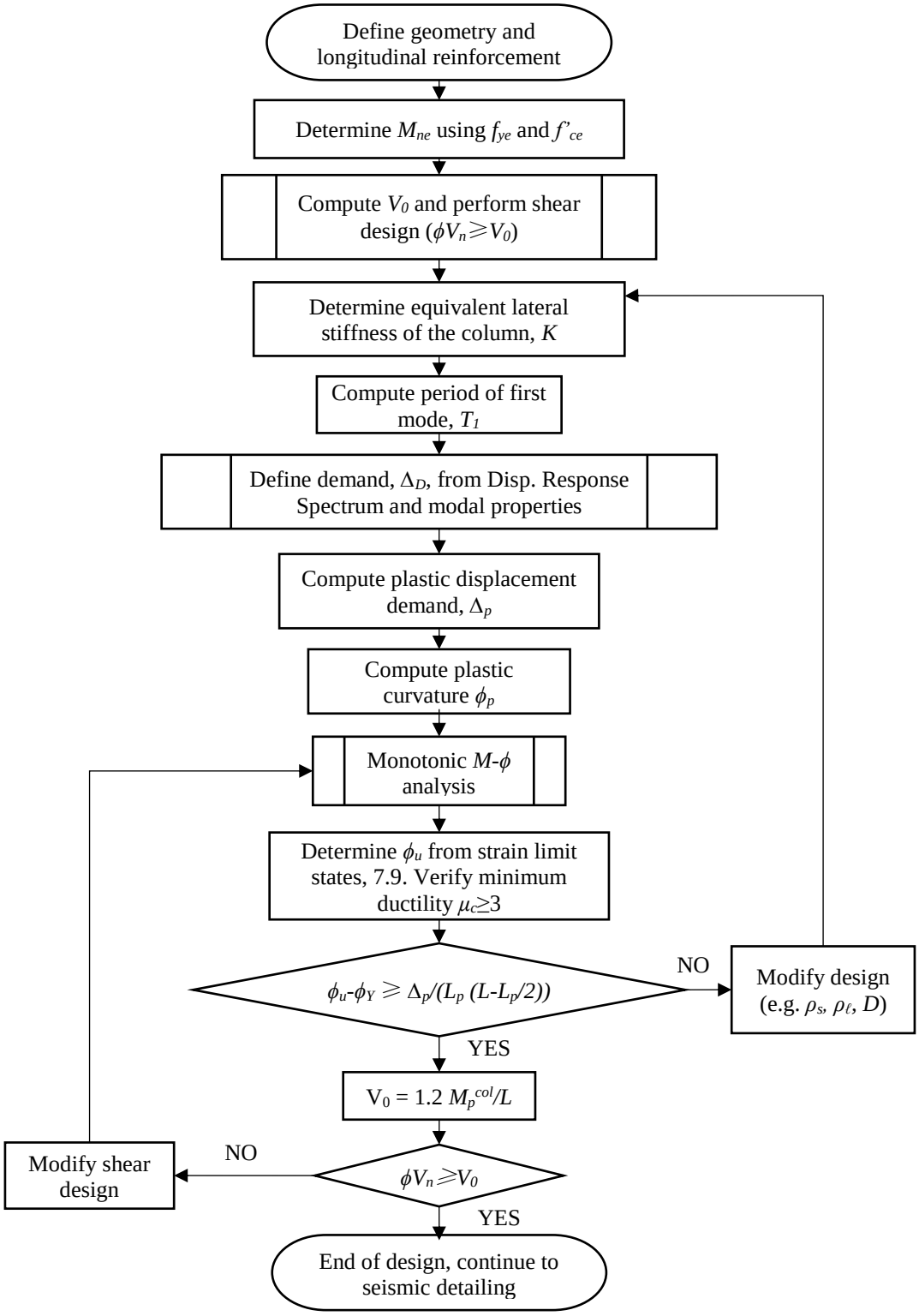

Figure 7.3. Design Flowchart for Ductile Cantilever Bridge Column, as per SDC v.1.7 (2013)

7.3. Proposed Design procedure

To account for plastic buckling-straightening fatigue of reinforcing bars, the first step is to consider the cyclic nature of the bar response. Instead of using a monotonic M-ϕ analysis, as indicated by Caltrans SDC (2013), it is recommended to perform the M-ϕ analysis in both directions, assigning to the reinforcement the combined strain amplitude from both analyses, $\Delta\varepsilon_{t\text{-}c} = \varepsilon_{st}\text{-}\varepsilon_{sc}$. This approach uses the strain amplitude, $\Delta\varepsilon_{t\text{-}c}$, as it is a better indicator of damage in the reinforcement than the strain in either direction separately, see Dodd and Restrepo (1995).

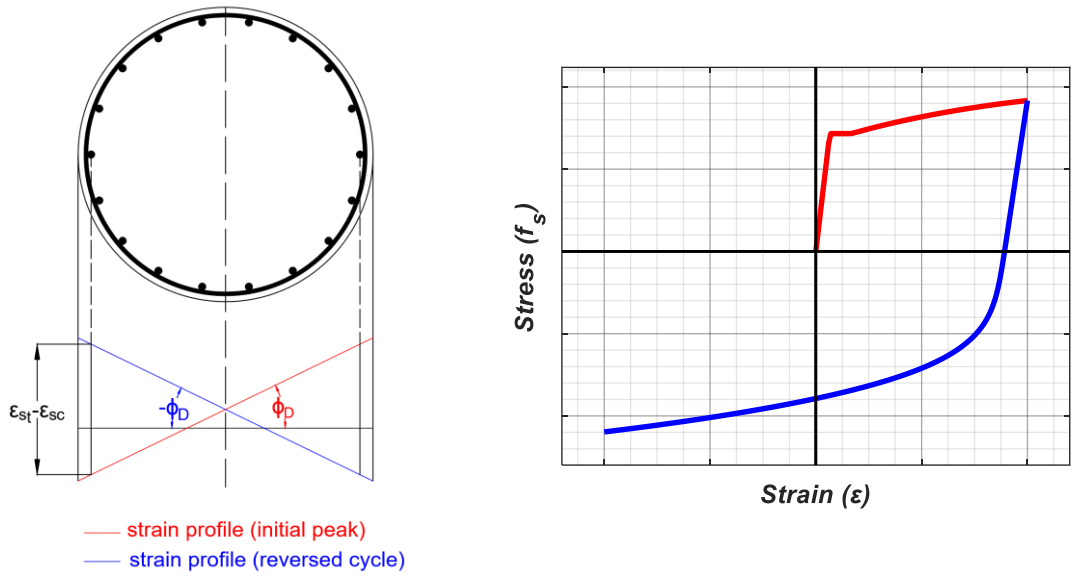

(a) (b)

Figure 7.4. Pseudo-Cyclic Method: (a) Strain Profile for Each Seismic Direction; (b) Stress-Strain Response of Extreme Reinforcement for Initial and Reversed Direction

For a bridge column with constant axial force (e.g. interior column, see Figure 7.5), only one M-ϕ analysis is required, as the response is symmetric in both directions. In the

case of variable axial force (e.g. exterior column, see Figure 7.5), at least one M-ϕ analysis is required for each loading direction.

To include the plastic buckling-straightening fatigue phenomenon in the design procedure as per Caltrans SDC (2013), the following steps can be introduced after the column shear design is completed (step 3 in section 7.2):

3-i) Compute the minimum transverse reinforcement, $\rho_{s,PBSF1}$, to prevent the strain amplitude demand, $\Delta\varepsilon'_{t\text{-}c}$ from exceeding the von Karman strain amplitude, $\Delta\varepsilon'_{vK}$. A simplified regression for $\Delta\varepsilon'_{vK}$, assuming strain amplitudes in engineering and natural coordinates are equivalent in the range of values typically used ($\Delta\varepsilon'_{vK} \approx \Delta\varepsilon_{vK}$), and a constant bias for a conservative design, is presented in Equation 7.12. With this bias, the value of $\Delta\varepsilon_{vK}$ is underpredicted in 95% of the FE model results analyzed in Chapter 6. The resulting limit for the transverse reinforcement, $\rho_{s,PBSF1}$, is then computed as per Equation 7.13.

$$\Delta\varepsilon_{vK} = 0.02 + \min\left(0.054, 0.032 \cdot \rho_s(\%)\right) - 0.0175 \cdot \left|\sqrt[3]{n_{bar}} - 2.93\right| \qquad 7.12$$

$$\rho_{s,PBSF1}(\%) \geq \frac{\Delta\varepsilon_{t\text{-}c} - 0.02}{0.032} + 0.55 \cdot \left|\sqrt[3]{n_{bar}} - 2.93\right| \qquad 7.13$$

This formulation is limited for a spacing between hoops under $4.5d_{b\ell}$.

3-ii) Determine the minimum transverse reinforcement ratio, $\rho_{s,PBSF2}$, required to prevent the concave fibers of reinforcement from reaching a damage index of 1, $\Delta\varepsilon_{kx} = \varepsilon_u$, before exceeding the von Karman strain amplitude, $\Delta\varepsilon_{vK}$. Equation 6.6, combined

with the condition $\Delta\varepsilon_{t\text{-}c} = \Delta\varepsilon_{CR}$ when $\Delta\varepsilon_{t\text{-}c} \le \Delta\varepsilon_{vK}$ results in an upper limit for the strain amplitude demand:

$$\Delta\varepsilon_{t\text{-}c} \le \frac{1}{2}\cdot\left(\sqrt{\left(\frac{1-c_1\cdot\Delta\varepsilon_{EC}}{c_1}\right)^2+4\cdot\frac{\varepsilon_u}{c_1}} - \frac{1-c_1\cdot\Delta\varepsilon_{EC}}{c_1}\right) \qquad \Delta\varepsilon_{t\text{-}c} \le \Delta\varepsilon_{vK} \qquad 7.14$$

Replacing the right-hand side of Equation 7.14 with a first order approximation results in a simple relation:

$$\Delta\varepsilon_{t\text{-}c} \le \sqrt{\frac{\varepsilon_u}{c_1}} \qquad 7.15$$

Finally, with the simplified (biased) regression of c_1 in Equation 6.9, a limit for the transverse reinforcement is defined as follows:

$$\rho_{s,PBSF2} \ge \frac{39.1\cdot\rho_\ell}{\sqrt[3]{n_{bar}}\cdot\left(\frac{\varepsilon_u}{\Delta\varepsilon_{t\text{-}c}^{\,2}} - 29\right)} \qquad 7.16$$

3-iii) Additionally, a minimum transverse reinforcement is required for a stable stress-strain response after the von Karman strain amplitude, $\Delta\varepsilon_{vK}$, is exceeded:

$$\rho_{s,PBSF3} \ge 0.48\cdot\rho_\ell \qquad 7.17$$

3-iv) Select the maximum between transverse reinforcement computed for the shear demand, $\rho_{s,shear}$, and plastic buckling-straightening fatigue: $\rho_{s,PBSF1}$, $\rho_{s,PBSF2}$, and $\rho_{s,PBSF3}$.

$$\rho_s = \max\left(\rho_{s,shear}, \rho_{s,PBSF1}, \rho_{s,PBSF2}, \rho_{s,PBSF3}\right)$$
$$\frac{s}{d_{b\ell}} \le 4.5 \qquad 7.18$$

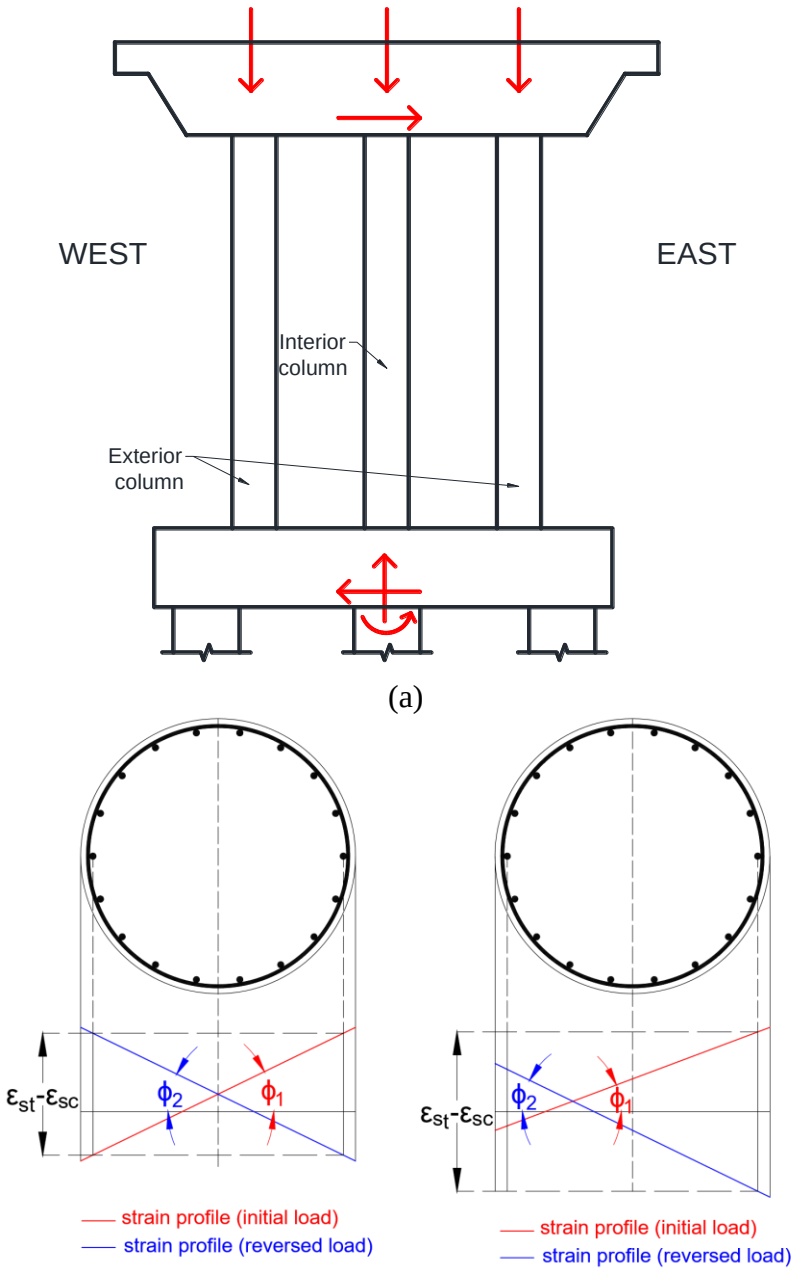

Figure 7.5. Strain Profile for Columns in a Bridge Bent: (a) Elevation View of Bent Frame; (b) Strain Profile in Interior Column; (c) Strain Profile in Exterior Column

7.4. Design Verification

For the verification of an existing bridge column design, with all reinforcement configuration parameters known, the unbiased regression equations from Chapter 6. can be used. The following procedure is suggested to verify the design of a bridge column against plastic buckling-straightening fatigue of reinforcing bars:

1) Compute the von-Karman strain amplitude, $\Delta\varepsilon_{vK}$, from Equation 6.13. If the tensile to yield strength ratio of the longitudinal reinforcement is unknown, assume T/Y = 1.4, see Equation 7.19.

$$\Delta\varepsilon'_{vK} = 0.030 + \min(0.054, 0.032 \cdot \rho_s(\%)) - 0.0175 \cdot \left| \sqrt[3]{n_{bar}} - 2.93 \right| \qquad 7.19$$

2) Compute the limit strain amplitude for a damage index of 1.0 preceding the von Karman strain, as seen in Equation 7.15. From the unbiased regression of c_1, see Equation 6.8, and assuming T/Y= 1.4 when the tensile to yield strength ratio is unknown, compute $\Delta\varepsilon_{DI=1}$ as per Equation 7.21.

$$c_1 = 25.1 \cdot \left(\frac{\rho_s}{\rho_\ell} \cdot \sqrt[3]{n_{bar}} \right)^{-1} + 9.9 \cdot \frac{s}{d_{bl}} - 9.5 > 0 \qquad 7.20$$

$$\Delta\varepsilon_{DI=1} = \sqrt{\frac{DI \cdot \varepsilon_u}{c_1}} \qquad 7.21$$

3) Determine the maximum strain amplitude demand allowed by the longitudinal reinforcement as the minimum of the two strain amplitude limits:

$$\Delta\varepsilon_{t\text{-}c}^{MAX} = \min(\Delta\varepsilon_{vK}, \Delta\varepsilon_{DI=1}) \qquad 7.22$$

For a column with constant axial force, the corresponding maximum curvature allowed in the critical section is computed as follows:

$$\phi_u = \frac{\Delta\varepsilon_{t\text{-}c}^{MAX}}{0.95 \cdot D} \qquad 7.23$$

Where $0.95D$ is the approximate distance between the longitudinal reinforcement at both extremes of the critical section of the column.

4) Compute the lateral deformation due to plastic rotations in the plastic hinge region of the column, Δ_p.

Based on the work by Guerrini and Restrepo (in-press) the extent of plasticity, ℓ_{pr}, in a cantilever bridge column is characterized by the flexure-shear interaction. For slender columns, with weak flexure-shear interaction, the extent of plasticity, ℓ_1, is computed as follows:

$$\ell_1 = \frac{\left(\frac{T_0}{A_{st} f_y} - \frac{T'_y}{A_{st} f_y}\right)\omega_\ell - \frac{P_u}{A_g f'_c}\left(\alpha_0 - \alpha'_y\right)}{\frac{T_0}{A_{st} f_y}\omega_\ell + \frac{P_u}{A_g f'_c}\left(1 - \alpha_0\right)} \cdot L \qquad 7.24$$

Where Guerrini and Restrepo (in-press) defined each parameter in terms of the material properties and reinforcement configuration of the column, see Appendix A for details.

In case of Strong Flexure-Shear interaction, the extent of plasticity, ℓ_2, can be computed as follows:

$$\ell_2 = \begin{cases} 1.52 \cdot \sqrt{\left(\dfrac{T_0}{A_{st} f_y} - \dfrac{T_y}{A_{st} f_y} \right) \dfrac{f_y}{f_{yh}} \dfrac{\rho_\ell}{\rho_s}} \cdot D & x \le 1.12D \\ \left(0.94 \cdot \left(\dfrac{T_0}{A_{st} f_y} - \dfrac{T_y}{A_{st} f_y} \right) \dfrac{f_y}{f_{yh}} \dfrac{\rho_\ell}{\rho_s} + 0.62 \right) \cdot D & x > 1.12D \end{cases} \quad 7.25$$

Based on the type of level of flexure-shear interaction, defined in terms of the column slenderness *L/D* herein, the lateral displacement capacity due to plastic rotations in the plastic hinge region can be computed as follows:

- If $L/D \geq 4.5$ (Weak Flexure-Shear Interaction)

$$\Delta_p = 0.3\ell_1 \cdot \phi_u \left(L - 0.15 \cdot \ell_1 \right) \quad 7.26$$

- If $L/D < 4.5$ (Strong Flexure-Shear Interaction)

$$\Delta_p = \begin{cases} 0.314 \cdot L \left(\varepsilon_{dem} + \varepsilon_0 \right) \left(\left(0.34\eta + 3.18 \right) \cdot \tan^{-1} \left(1.78 \dfrac{\ell_2}{D} \right) - 0.61 \cdot \eta \dfrac{\ell_2}{D} \right) & \ell_2 \le 1.12 \cdot D \\ \left(\varepsilon_{dem} + \varepsilon_0 \right) \left(\left(1.1 - 0.095\eta \right) L + 0.36 \cdot D \left(\left(\dfrac{L}{D} \left(1 + 0.52\eta \right) + 1.12 + 0.58\eta \right) \left(\dfrac{\ell_2}{D} - 1.12 \right) - \left(0.42\eta \dfrac{L}{D} + \dfrac{1}{2} + 0.73\eta \right) \left(\left(\dfrac{\ell_2}{D} \right)^2 - 1.12^2 \right) + 0.28\eta \left(\left(\dfrac{\ell_2}{D} \right)^3 - 1.12^3 \right) \right) \right) & \ell_2 > 1.12 \cdot D \end{cases} \quad 7.27$$

Where:

$$\eta = \frac{\varepsilon_{dem} - \hat{\varepsilon}_y}{\varepsilon_{dem} + \varepsilon_0} \frac{f_{yh}}{f_0 - f_y} \frac{\rho_s D^2}{A_s^*} \quad 7.28$$

The details of the derivation of Equation 7.27 can be found in Appendix A.

5) Compute lateral displacement contributions from bond-slip and linear-elastic deformations in the column.

From Paulay and Priestley (1992), the plastic rotation at the base of the column due to strain penetration can be estimated as follow:

$$\theta_{sp} = \phi_u \cdot \frac{0.15}{ksi} f_y \cdot d_{b\ell} \qquad 7.29$$

Where f_y is the yield strength of the longitudinal reinforcement and $d_{b\ell}$ the corresponding bar diameter.

Since the rotation θ_{sp} occurs at the interface between column and footing, the lateral displacement due to strain penetration, Δ_{sp}, can be computed as follow:

$$\Delta_{sp} = \theta_{sp} \cdot L \qquad 7.30$$

Since the contribution from linear-elastic deformations in the column is small, it can be computed simply as:

$$\Delta_e = \frac{1}{3}\phi_y L^2 \qquad 7.31$$

Where the curvature at yield, ϕ_y, can be estimated using the formulation proposed by Priestley (2003):

$$\phi_Y = \frac{2.25 \cdot \varepsilon_{ye}}{D} \qquad 7.32$$

Where ε_{ye} is the expected yield strain of the longitudinal reinforcement.

6) Compute the ultimate displacement capacity, Δ_u, and displacement ductility, μ_Δ, and verify they are greater than the seismic demand, Δ_D and μ_D.

$$\Delta_u = \Delta_p + \Delta_{sp} + \Delta_e \geq \Delta_D \qquad \text{(a)}$$

$$\mu_\Delta = \frac{\Delta_u}{\Delta_Y} \geq \mu_D \qquad \text{(b)} \qquad 7.33$$

7.5. Design and verification Example

7.5.1. Design Example

Consider the bridge column tested at UC – San Diego's Large Outdoor Shake table (Schoettler et al., 2012), with a longitudinal reinforcement ratio ρ_ℓ = 1.55%, corresponding to 18 #11 bars with a measured uniform strain ε_u=12.2%. A strain amplitude for the longitudinal reinforcement of $\Delta\varepsilon_{t\text{-}c}$=4% was extracted from experimental results for a drift ratio of 7.5%, see Figure 5.15. According to the proposed design procedure, the minimum transverse reinforcement required to prevent plastic buckling-straightening fatigue can be computed as follows:

$$\rho_{s,PBSF}=\max\left(\frac{0.04\text{-}0.02}{0.032}+0.55\cdot\left|\sqrt[3]{18}\text{-}2.93\right|,\frac{39.1\cdot 1.55\%}{\sqrt[3]{n_{bar}}\cdot\left(\frac{0.122}{0.04^2}\text{ - }29\right)},0.48\cdot 1.55\%\right)=0.8\% \quad 7.34$$

The actual volumetric ratio of the column, at ρ_s=0.953%, meets the requirements presented herein to prevent a PBSF type of failure.

7.5.2. Verification Example

In the following, a step-by-step procedure to verify the lateral displacement capacity of the column, with ρ_s=0.953% and s = 6 (in), is described:

1) Compute the von Karman strain amplitude:

$$\Delta\varepsilon'_{vK}=0.030+\min(0.054,0.032\cdot 0.953)-0.0175\cdot\left|\sqrt[3]{18}-2.93\right|=5.5\%$$

2) Compute the smeared limit strain for a damage index of 1.0, assuming it occurs before the von Karman strain is reached

$$\Delta\varepsilon_{DI=1} = \sqrt{\frac{0.122}{25.1\cdot\left(\frac{0.953}{1.55}\cdot\sqrt[3]{18}\right)^{-1} + 9.9\cdot\frac{6.0}{1.41} - 9.5}} = 5.0\%$$

3) Define the maximum strain amplitude demand, $\Delta\varepsilon_{t\text{-}c}^{MAX}$, and the corresponding curvature, ϕ_u.

$$\Delta\varepsilon_{t\text{-}c}^{MAX} = \min(5.5\%\ ,\ 5.0\%) = 5.0\%$$

$$\phi_u = \frac{0.050}{0.95\cdot 48"} = 0.0011\cdot\frac{1}{in}$$

4) Compute the lateral deformation due to plastic rotations in the plastic hinge region of the column.

Since $L/D = 6 \geq 4.5$, assume weak flexure-shear interaction:

$$\ell_1 = \frac{(0.81-0.45)\cdot 0.19 - 0.053\cdot(0.35-0.46)}{0.81\cdot 0.19 + 0.053\cdot(1-0.35)}\cdot 24' = 9.5' = 114"$$

Where the parameters used for the computation of ℓ_1 are extracted from the empirical relationships proposed by Guerrini and Restrepo (in-press) as follow:

$$\frac{T'_y}{A_{st}\cdot f_y} = 1.5\left(1.8\cdot 0.0155 - 0.0020\frac{6.1\cdot ksi}{MPa} - 0.25\right)(2.1\cdot 0.053 - 0.08) + 0.48 - 1.10\cdot 0.0155$$
$$= 0.45$$

$$\frac{T_0}{A_{st}\cdot f_y} = 1.5\left(4\cdot 0.0155 - 0.0025\cdot\frac{6.1\cdot ksi}{MPa} - 0.22\right)(1.25\cdot 0.053 - 0.17) + 0.82 - 3.3\cdot 0.0155$$
$$= 0.81$$

$$\alpha'_y = 0.53\cdot 0.053 + 0.43 = 0.46$$

$$\alpha_0 = 0.5\cdot 0.053 + 0.32 = 0.35$$

The lateral displacement due to plastic rotation is then computed as follow:

$$\Delta_p = 0.3 \cdot 114" \cdot \frac{0.0011}{in} \cdot \left(288" - 0.15 \cdot 114"\right) = 10.2"$$

5) Compute the contributions of strain penetration and elastic deformations in the lateral displacement of the column:

$$\theta_{sp} = \frac{0.0011}{in} \frac{0.15}{\text{ksi}} \cdot 75.2 \cdot \text{ksi} \cdot 1.41" = 0.0175 \text{ rad}$$

$$\Delta_{sp} = 0.0175 \text{ rad} \cdot 288" = 5.04"$$

$$\phi_Y = \frac{2.25 \cdot 0.0026}{48"} = \frac{1.22 \cdot 10^{-4}}{\text{in}}$$

$$\Delta_y = \frac{1}{3} \cdot \frac{1.22 \cdot 10^{-4}}{\text{in}} \left(288"\right)^2 = 3.37"$$

6) Compute the ultimate displacement capacity and ductility:

$$\Delta_u = 10.15" + 5.04" + 3.37" = 18.61"$$

$$\mu_\Delta = \frac{18.61}{3.37} = 5.5$$

During testing, the maximum lateral displacement recorded before the first longitudinal bar fracture was $\Delta_{measured}$ = 21.8" ($\delta_{measured}$ = 7.6%). The relative difference between predicted and measured lateral displacement/drift is thus 16%.

Additionally, the verification analysis is performed on the same column for a range of transverse reinforcement ratios, ρ_s, between 0.34% and 1.35%, with the resulting drift and displacement ductilities presented in Figure 7.6. The limits for ρ_s correspond to the volumetric ratios when replacing the transverse hoops with either #3 or #6 bars (lower and upper limit respectively).

Figure 7.6 shows that equivalent volumetric ratios, ρ_s, with single or double hoop configurations will yield different results as the transverse reinforcement increases, with the more closely spaced single hoops providing better protection against PBSF failure (although constructability becomes an issue for very small spacing). From the analytical formulation presented herein, large values of ρ_s will result in high displacement capacities (e.g. $\mu_\Delta \geqslant 9$ for #6 single hoops). In practice, the ductility capacity of bridge columns is capped by failure modes not considered by the current formulation (e.g. sideway buckling of longitudinal bars). Because of this, the curves in Figure 7.6 are only drawn as continuous lines until a limit displacement ductility μ_Δ=9, a commonly observed capacity of bridge columns tested experimentally.

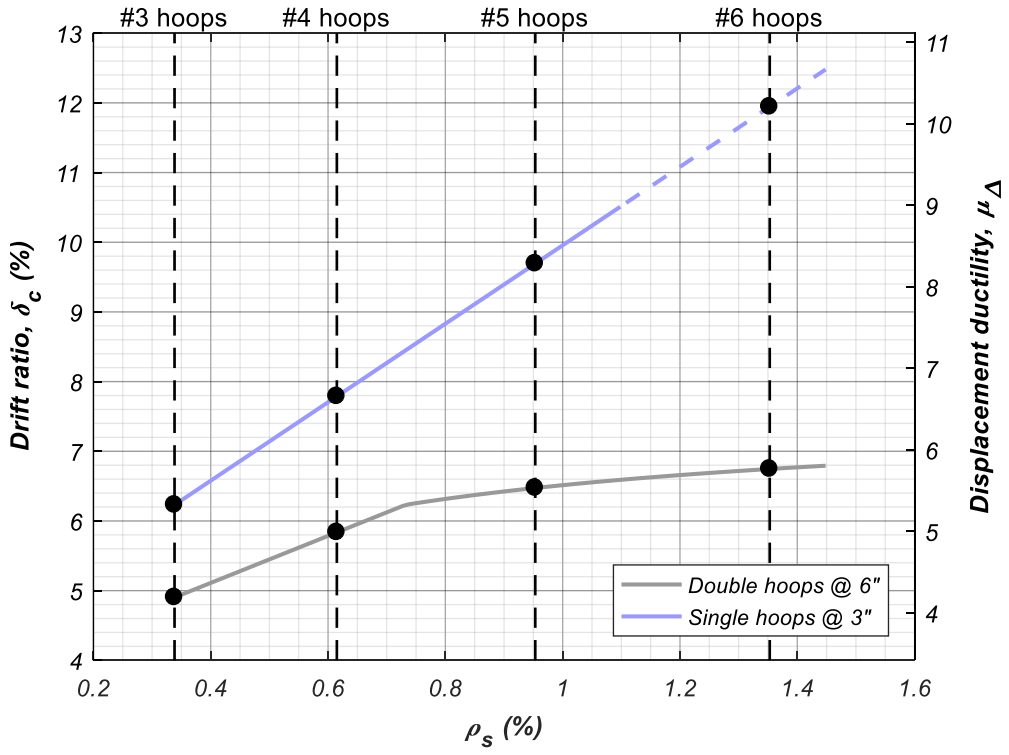

Figure 7.6. Drift and Displacement Ductility Capacity for a PBSF Damage Index of 1.0 vs ρ_s (Double Hoops @ 6" or Single Hoops @ 3")

7.6. Prediction of experimental results

To complete the verification of the methodology proposed herein, experimental results of reinforced concrete circular bridge columns tested under cyclic load were extracted from the literature. In all columns under consideration, the main failure mechanism observed was fracture of longitudinal reinforcement, following the onset of bar buckling. Table 7.1 shows the lateral displacement recorded in each column before the fracture of the first longitudinal bar, $\Delta_{u,m}$, as well as the column properties required by the verification procedure in section 7.4.

The experimental test results in Table 7.1 include two full scale columns, one tested under seismic excitation (Schoettler et al. 2012), and the other under quasi-static reversed cyclic load (Lotfizadeh and Restrepo, in-preparation). The remaining test columns were scaled to either one-half (Trejo et al. 2014, and Goodnight et al. 2015) or 35% scale (Stephan et al. 2003), with section diameters between 18" and 36".

The test columns considered include a wide variety of reinforcement configurations, with ρ_ℓ between 0.83% and 3.10%, ρ_s between 0.82% and 1.74%, and reinforcement ratio ρ_s/ρ_ℓ ranging from 0.3 to 1.0, see Table 7.1.The relative axial load applied also shows some variability between cases, ranging between 5% and 20% of $f'_c A_g$, see Table 7.1.

Specimens tested by Goodnight et al. (2015) and Trejo et al. (2014) used spirals for the transverse reinforcement, unlike the single and double hoops of the analytical models used in regression analysis. This discrepancy in the reinforcement configuration, however, showed little effect on the accuracy of the verification procedure described in section 7.4.

Table 7.1. Column Properties and Maximum Lateral Displacement

Source	Spec	ρ_s (%)	ρ_ℓ (%)	n_{bar}	$s/d_{b\ell}$	D (in)	L (in)	ε_y (%)	ε_u (%)	$f_{y\ell}$ (ksi)	$f_{u\ell}$ (ksi)	f_{yt} (ksi)	f'_c (ksi)	$\frac{P_u}{f'_c \cdot A_g}$ (%)	$\Delta_{u,m}$ (in)
Goodnight et al. 2015	9	0.92	1.60	16	2.67	24	96	0.24	11.9	68.1	92.8	74.1	6.81	5.5	6.7
	13	1.60	1.60	16	3.67	24	96	0.24	13.3	68.1	94.8	69.9	6.10	6.2	6.5
	14	0.50	1.60	16	5.33	24	96	0.24	13.3	68.1	94.8	64.6	6.64	5.7	6.4
	15	0.70	1.60	16	3.67	24	96	0.24	13.3	68.1	94.8	64.6	7.23	5.2	6.7
	16	1.30	1.60	16	2.00	24	96	0.24	13.3	68.1	94.8	64.6	6.71	5.6	8.3
	19	1.30	1.70	10	2.67	18	96	0.25	11.8	68.1	92.4	65.6	6.33	10.0	6.9
	20	1.30	1.70	10	2.67	18	96	0.25	11.8	68.1	92.4	65.6	6.47	5.0	7.0
	21	1.30	1.70	10	2.67	18	132	0.25	11.8	68.1	92.4	65.6	6.39	5.0	11.9
	22	1.30	1.70	10	2.67	18	132	0.25	11.8	68.1	92.4	65.6	6.53	10.0	12.6
	23	1.30	1.70	10	2.67	18	156	0.25	11.8	68.1	92.4	65.6	6.61	5.0	19.4
	24	1.30	1.70	10	2.67	18	156	0.25	11.8	68.1	92.4	65.6	6.47	10.0	14.3
Trejo et al. 2014	25	1.00	2.10	16	2.29	24	96	0.24	11.4	69.7	95.5	63.9	6.29	5.0	7.2
	26	1.00	2.10	16	2.29	24	96	0.24	11.4	69.7	95.5	63.9	5.89	10.0	6.0
	27	1.00	1.60	16	2.67	24	96	0.24	11.8	68.7	93.7	63.9	6.15	10.0	5.5
	28	1.30	1.70	10	2.67	18	96	0.24	11.8	68.7	93.7	63.9	6.24	15.0	8.0
	29	1.30	1.70	10	2.67	18	96	0.24	11.8	68.7	93.7	63.9	5.91	20.0	8.1
	30	1.30	3.10	10	2.00	18	96	0.24	10.9	70.5	97.7	63.9	6.05	15.0	7.4
	C1	0.82	1.10	16	4.00	24	144	0.26	13.1	66.7	93.7	72.8	4.77	5.0	7.5
	C2	0.82	0.83	12	4.00	24	144	0.31	10.7	86.2	114.3	85.6	4.84	5.0	7.5
	C3	0.82	2.19	22	3.33	24	144	0.26	14.0	67.2	100.6	72.8	3.59	5.0	10.0
	C4	0.82	1.58	16	3.33	24	144	0.31	12.3	85.7	114	85.6	4.66	5.0	10.0
	C5	0.82	2.19	22	3.33	24	72	0.26	14.0	67.2	100.6	72.8	3.58	5.0	4.4
	C6	0.82	1.58	16	3.33	24	72	0.31	12.3	85.7	114	85.6	3.85	5.0	4.4
Schoettler et al. 2012		1.00	1.55	18	4.26	48	288	0.26	12.2	75.2	102.4	54.8	6.10	5.3	21.8
Stephan et al. 2003		1.74	2.54	84	2.50	36	114	0.23	10.5	61.8	103.2	60	9.30	6.3	6.8
Lotfizade and Restrepo, in-preparation		1.00	1.74	14	2.95	48	216	0.35	9.2	87	114.3	87.8	5.17	8.9	20.5

Figure 7.7 compares measured and predicted values for the maximum drift at the top of each column before the occurrence of bar fracture.

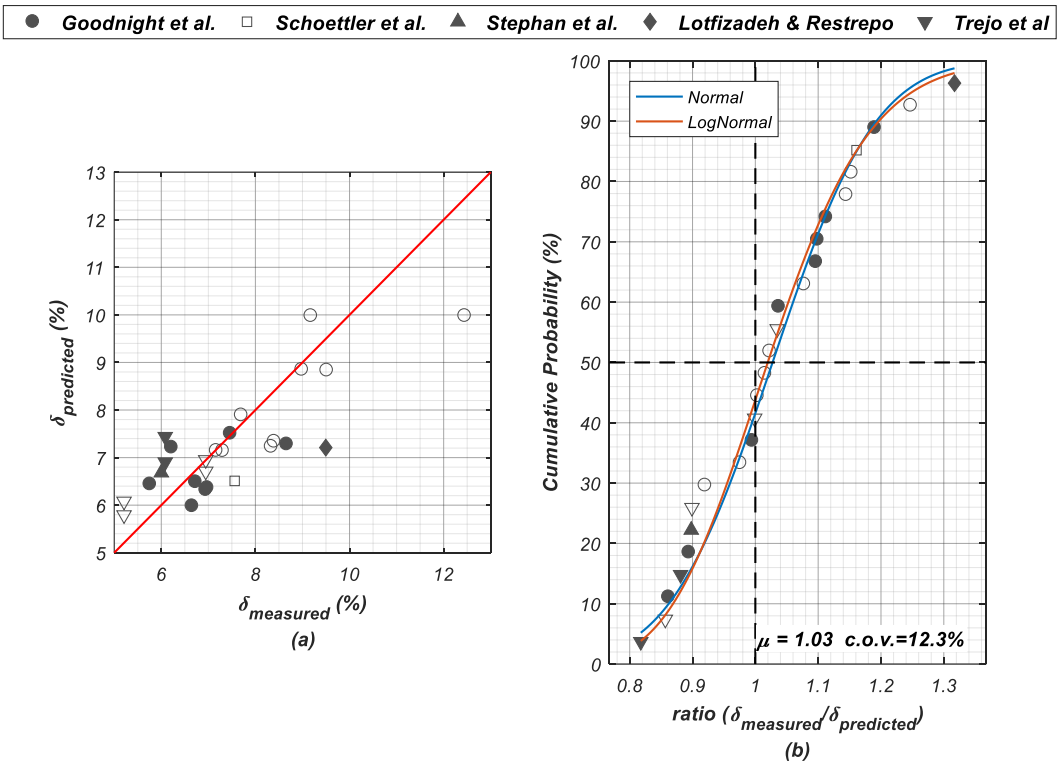

Figure 7.7. Predicted Lateral Drift Ratio at the Top of the Column: (a) Experimental vs Predicted Lateral Drift; (b) Fragility Curve of Ratio between Experimental and Predicted Results

As seen in Figure 7.7, the verification process slightly under-predicts the measured lateral drift before bar fracture, with an average ratio of experimental to predicted drift of $\mu = 1.03$. The small coefficient of variation (c.o.v) for the distribution of ratios, at $\delta = 12.3\%$, suggests a high precision of the method developed herein. Furthermore, the fragility curves in Figure 7.7b indicate that the lateral drift ratios can be well approximated by a Log-normal distribution.

Chapter 7, in full, is a reprint of the material as it appears in SSRP Report 17/10: *Plastic buckling-straightening fatigue of large Diameter reinforcing steel bars*, 2018. Duck, David; Carreño, Rodrigo; and Restrepo, José I. The dissertation author was a co-author for this report and first author of the specific Chapter.

Chapter 8.

CONCLUSIONS

Research efforts in this dissertation focused on the behavior of longitudinal steel reinforcement under large cyclic strain reversals, such as those experienced in the plastic hinge region of bridge columns.

For the first stage of this research, a series of reinforcing steel coupons from different manufacturers were tested under randomized cyclic strain histories. Based on the hysteretic response of such coupons, the parameters of two popular uniaxial constitutive stress-strain relationships: the Giuffrè-Menegotto-Pinto (GMP) and the Dodd-Restrepo (DR) steel models, were calibrated for Grade 60 reinforcement complying with either the ASTM A615 (2016) or ASTM A706 (2016) standards. The calibration study included sensitivity analyses for each parameter and verification examples, based on coupon tests not used in the calibration, yielding satisfactory results.

The lack of a robust implementation of the Dodd-Restrepo constitutive stress-strain relationship in structural analysis software has prevented its wider use in engineering practice. To address this issue, a new implementation of the material model, including a closed-form formulation of the Bauschinger effect among several improvements, was

developed for the OpenSees software framework (McKenna et al., 2000) as *SteelDRC*. The implemented uniaxial material was used in a large-scale structural model subjected to high intensity earthquake loads, showing similar results and convergence speed during the analysis compared to the popular *Steel02* model in OpenSees.

Cyclic testing was performed on large diameter steel reinforcement using an innovative gripping system based on a modified sulfur-based concrete mix. The test results collected for #18 ASTM A706 Grade 60 reinforcement provided the first successful experimental evaluation of the fatigue life of reinforcing bars of this size. Unsupported lengths equivalent to $1.5d_{b\ell}$, $6d_{b\ell}$, and $8d_{b\ell}$ were used for the experimental work. Results show a relation between the strength degradation of the bars, due to the formation and propagation of fatigue cracks, with the unsupported length.

A series of finite element model realizations were performed to assess the buckling behavior of reinforcing bars interacting with transverse hoops. Multiple configurations of reinforcement (transverse and longitudinal) and material properties were tested. From regression analyses, it was found that both the geometry (e.g. d_{POI}) and characteristic strain limits (e.g. Engesser-Considère strain, $\varepsilon_{E\text{-}C}$) of the buckled reinforcement are highly correlated to the following parameters: ρ_s, $\sqrt[3]{n_{bar}}$, $s/d_{b\ell}$ and ρ_s/ρ_{ℓ}. The presence of a factor $\sqrt[3]{n_{bar}}$ in the prediction variables for the response of buckled reinforcement can be explained by the "polygon effect", under which hoops are less effective restraining lateral deformations of few reinforcing bars, where hoops work in bending, with the effect becoming less and less important as the number of bars increases, hence the cubic-root limiting the effect for large n_{bar}. Regression analyses also showed that the loading protocol

had little effect on the geometry of the buckled shape, as well as the strain amplitude when the peak stress in compression is reached (von Karman strain, $\Delta\varepsilon_{vK}$). The strain smeared between the centers of rotation of the buckled shape, ε_{CR}, and the local strain in the concave side of the bar, ε_{kv}, was shown to closely follow a linear relation, the constants of which can be computed in terms of parameters $\rho_s / \rho_\ell \sqrt[3]{n_{bar}}$ and $s/d_{b\ell}$.

For an adequate response against plastic buckling-straightening fatigue, a logistic binary regression of the FE model results produced a limit for ρ_s/ρ_ℓ of 0.48 to ensure the post-buckling response of the reinforcement is stable. A stable post-buckling response was defined by one of the two conditions: the von Karman strain amplitude, $\Delta\varepsilon_{vK}$, being greater than 5%, or the loss in stress capacity is less than 10% following the peak stress, $f_{vK.}$

A design procedure was proposed to prevent PBSF failure in the longitudinal reinforcement by imposing a stable post-buckling response, $\rho_s/\rho_\ell>0.48$, and both the von Karman strain amplitude, $\Delta\varepsilon_{vK}$, and strain amplitude for a damage index DI=1, $\Delta\varepsilon_{DI=1}$, greater than the strain demand, $\Delta\varepsilon_{t\text{-}c}$. Additionally, it is recommended to limit the spacing between hoops to 4.5 bar diameters, $s/d_{b\ell} \leq 4.5$.

A verification procedure is also proposed for existing bridge columns designs. A step-by-step procedure is described to determine the drift ratio and displacement ductility capacity of a bridge column for a PBSF Damage Index of 1, to compare against the seismic displacement demand.

REFERENCES

ACI Committee, 5. (1993). 548.2R Guide for Mixing and Placing Sulfur Concrete in Construction.

Ajovalasit, A. (2012). The measurement of large strains using electrical resistance strain gages. *Experimental Techniques, 36*, 77-82.

American Association of State Highway and Transportation Officials (AASHTO), LRFD Bridge Design Specifications. (2014). *7th Edition*.

ASTM E606 Standard Test Method for Strain-Controlled Fatigue Testing. (2012). ASTM International.

ASTM E8 Standard Test Methods for Tension Testing of Metallic Materials. (2016). ASTM International.

ASTM International. (2016). *ASTM A615/A615M-16 Specification for Deformed and Plain Carbon-Steel Bars for Concrete Reinforcement.* West Conshohocken, PA: ASTM International. doi:10.1520/a0615_a0615m-16

ASTM International. (2016). *ASTM A706/A706M-16 Specification for Deformed and Plain Low-Alloy Steel Bars for Concrete Reinforcement.* West Conshohocken, PA: ASTM International. doi:10.1520/a0706_a0706m-16

Atalay, M. B., Mahin, S. A., Bertero, V. V., & Rea, D. (1972). Rate of Loading Effects on Uncracked and Repaired Reinforced Concrete Members.

Bae, S., Mises, A. M., & Bayrak, O. (2005). Inelastic buckling of reinforcing bars. *Journal of Structural Engineering, 131*(2), 314-321.

Bao, Y., Kunnath, S. K., El-Tawil, S., & Lew, H. S. (2008). Macromodel-based simulation of progressive collapse: RC frame structures. *Journal of Structural Engineering, 134*(7), 1079-1091.

Bate, D. V. (1987). Bauschinger effects in strain aged steels. *Materials Forum, 10,* 33-42.

Bauschinger, J. (1886). On the change of the elastic limit and the strength of iron and steel, by drawing out, by heating and cooling, and by repetition of loading (summary). *Minutes of Proceedings of the Institution of Civil Engineers with Other Selected and Abstracted Papers, 87,* 463.

Bayrak, O., & Sheikh, S. A. (2001). Plastic hinge analysis. *Journal of Structural Engineering, 127*, 1092-1100.

Bernstein, S. (1912). Démonstration du théorème de Weierstrass fondée sur le calcul des probabilités. *Communications of the Kharkov Mathematical, XIII*.

Berry, M. (2003). Estimating flexural damage in reinforced concrete columns. *Master Thesis, Dept. of Civil and Environmental Engneering, Univ. of Washington*.

Berry, M. P., & Eberhard, M. O. (2005). Practical performance model for bar buckling. *Journal of Structural Engineering, 131*, 1060-1070.

Bezier, P. (1970). *Numerical Control - mathematics and applications.* Wiley.

Bosco, M., Ferrara, E., Ghersi, A., Marino, E. M., & Rossi, P. P. (2016). Improvement of the model proposed by Menegotto and Pinto for steel. *Engineering Structures, 124*, 442-456.

Bournonville, M., Dahnke, J., & Darwin, D. (2004). *Statistical analysis of the mechanical properties and weight of reinforcing bars.* Tech. rep., University of Kansas Center for Research, Inc.

Bresler, B., & Gilbert, P. H. (1961). Tie requirements for reinforced concrete columns. *Journal Proceedings*, *58*, pp. 555-570.

Brown, J., & Kunnath, S. K. (2004). Low-cycle fatigue failure of reinforcing steel bars. *ACI materials journal, 101*, 457-466.

Byrd, R. H., Hribar, M. E., & Nocedal, J. (1999). An interior point algorithm for large-scale nonlinear programming. *SIAM Journal on Optimization, 9*(4), 877-900.

Caltrans, S. D. (2010). Caltrans seismic design criteria version 1.6. *California Department of Transportation, Sacramento*.

Caltrans, S. D. (2013). Caltrans seismic design criteria, v. 1.7. April.

Carreño, R. P., & Restrepo, J. I. (in-preparation). Plastic Buckling-Straightening Fatigue Limit State for Longitudinal Reinforcement in Circular Bridge Columns.

Carreño, R., Lotfizadeh, K., Conte, J. P., & Restrepo, J. I. (in-preparation). Implementation of Improved Dodd-Restrepo Constitutive Stress-Strain Relationship.

Carreño, R., Lotfizadeh, K., Conte, J. P., & Restrepo, J. I. (under-review). Material Model Parameters for the Giuffrè-Menegotto-Pinto Uniaxial Steel Stress-Strain Model.

Chen, W.-F., & Lui, E. M. (1987). *Structural stability: theory and implementation.* Elsevier New York.

Ciampi, V., Eligehausen, R., Bertero, V., & Popov, E. P. (1982). *Analytical model for concrete anchorages of reinforcing bars under generalized excitations.* Berkeley: Earthquake Engineering Research Center.

Co, T. S. (2014, 6). *YF-series Post-Yield Strain Gage Manual.* Retrieved from http://www.tml.jp/e/product/strain_gauge/catalog_pdf/YEF_YF_YHFseries.pdf

Coleman, J., & Spacone, E. (2001). Localization issues in force-based frame elements. *Journal of Structural Engineering, 127*(11), 1257--1265.

Considere, A. (1891). Résistance des pièces comprimées. *Annexe au compte rendu du congr{\`e}s International des proc{\'e}d{\'e}s de construction. Paris*.

Corporation, M. T. (2009). *MTS 318 Load Unit Product Information Manual.* Eden. Retrieved from http://w.mts-systems.de/cs/groups/public/documents/library/mts_004909 1.pdf

Cosenza, E., & Prota, A. (2006). Experimental behaviour and numerical modelling of smooth steel bars under compression. *Journal of Earthquake Engineering, 10*, 313-329.

Crisfield, M. A. (1997). *Non-linear finite element analysis of solids and structures.* Wiley. Retrieved from https://books.google.com/books?id=INtRAAAAMAAJ

Dafalias, Y. (1975). On cyclic and anisotropic plasticity. *A general model*.

Dhakal, R. P., & Maekawa, K. (2002). Modeling for postyield buckling of reinforcement. *Journal of Structural Engineering, 128*(9), 1139-1147.

Dhakal, R. P., & Maekawa, K. (2002). Path-dependent cyclic stress--strain relationship of reinforcing bar including buckling. *Engineering Structures, 24*, 1383-1396.

Dodd, L. L., & Restrepo-Posada, J. I. (1995). Model for predicting cyclic behavior of reinforcing steel. *Journal of structural engineering, 121*, 433-445.

Duck, D. E., Carreño, R., & Restrepo, J. I. (2018). *SSRP-17/10: Plastic Buckling-Straightening Fatigue of Large Diameter Reinforcing Steel Bars (Vol I & II).* University of California, San Diego. La Jolla: Dept. of Structural Engineering.

El-Bahy, A., Kunnath, S. K., Stone, W. C., & Taylor, A. W. (1999). Cumulative seismic damage of circular bridge columns: Benchmark and low-cycle fatigue tests. *ACI Structural Journal, 96*, 633-641.

Engesser, F. (1889). *Die knickfestigkeit gerader stäbe.* W. Ernst & Sohn.

Fei, J., & Darwin, D. (1999). *Fatigue of high relative rib area reinforcing bars.* Tech. rep., University of Kansas Center for Research, Inc.

Feng, Y., Kowalsky, M. J., & Nau, J. M. (2014). Finite-element method to predict reinforcing bar buckling in RC structures. *Journal of Structural Engineering, 141*, 04014147.

Filippou, F. C., Bertero, V. V., & Popov, E. P. (1983). Effects of bond deterioration on hysteretic behavior of reinforced concrete joints.

Fragiadakis, M., Pinho, R., & Antoniou, S. (2008). Modelling inelastic buckling of reinforcing bars under earthquake loading. *Computational Structural Dynamics and Earthquake Engineering: Structures and Infrastructures Book Series*, *2*, 347.

Giuffrè, A., & Pinto, P. (1970). Il comportamento del cemento armato per sollecitazioni cicliche di forte intensità. *Giornale del Genio Civile*.

Goldberg, J. E., & Richard, R. H. (1963). Analysis of nonlinear structures. *Journal of the Structural Division ASCE, 89*(4), 333-352.

Gomes, A., & Appleton, J. (1997). Nonlinear cyclic stress-strain relationship of reinforcing bars including buckling. *Engineering Structures, 19*, 822-826.

Goodnight, J. C., Feng, Y., Kowalsky, M. J., & Nau, J. M. (2015). *The Effects of Load History and Design Variables on Performance Limit States of Circular Bridge Columns - Volume 2: Experimental Observations.* Juneau, AK: Alaska Department of Transportation and Public Facilities. Retrieved from http://www.dot.state.ak.us/stwddes/research/assets/pdf/4000-072v2.pdf

Guerrini, G., & Restrepo, J. I. (in-press). Extend of Plasticity in Reinforced Concrete Column. *ACI*.

Hanson, J. M., Burton, K. T., & Hognestad, E. (1968, September). Fatigue Tests of Reinforcing Bars Effect of Deformation Pattern. *PCA Research and Development Laboratories, 10*, 2-13.

Haselton, C. B., Goulet, C. A., Mitrani-Reiser, J., Beck, J. L., Deierlein, G. G., Porter, K. A., . . . Taciroglu, E. (2008). *An assessment to benchmark the seismic performance of a code-conforming reinforced-concrete moment-frame building.* Berkeley: Pacific Earthquake Engineering Research Center.

Johnston, B. G. (1983). Column buckling theory: historic highlights. *Journal of Structural Engineering, 109*, 2086-2096.

Kashani, M. M., Barmi, A. K., & Malinova, V. S. (2015). Influence of inelastic buckling on low-cycle fatigue degradation of reinforcing bars. *Construction and Building Materials, 94*, 644-655.

Kato, B. (1973). Predictable properties of material under incremental cyclic loading. *IABSE Symposiums, Theme III, 13*, pp. 119-124.

Kim, S. H., & Koutromanos, I. (2016). Constitutive model for reinforcing steel under cyclic loading. *Journal of Structural Engineering, 142*, 04016133.

Kokubu, M., & Okamura, H. (1969). Fatigue behavior of high strength deformed bars in reinforced concrete bridges.

Kolozvari, K., Orakcal, K., & Wallace, J. W. (2018). New opensees models for simulating nonlinear flexural and coupled shear-flexural behavior of RC walls and columns. *Computers and Structures, 196*, 246-262.

Krantz, S. G. (1999). *Handbook of Complex Variables.* Boston, MA: Springer Science \& Business Media.

Kunnath, S. K., Heo, Y., & Mohle, J. F. (2009). Nonlinear uniaxial material model for reinforcing steel bars. *Journal of Structural Engineering, 135*, 335-343.

Lotfizadeh, K., & Restrepo, J. I. (in-preparation). *High-Strength Steel Reinforcement in Critical Regions of Earthquake-Resistant Bridges.* La Jolla, California.

Lu, Y., & Panagiotou, M. (2013). Three-dimensional cyclic beam-truss model for nonplanar reinforced concrete walls. *Journal of Structural Engineering, 140*(3).

MacGregor, J. G., Jhamb, I. C., & Nuttall, N. (1971). Fatigue strength of hot rolled deformed reinforcing bars. *Journal Proceedings, 68*, pp. 169-179.

Madsen, I. (1941). *Report of crane girder tests.*

Mander , J. B., Priestley, M. N., & Park, R. (1984). *Seismic Design of Bridge Piers.* University of Canterbury. Civil Engineering.

Mander, J. B. (1983). Seismic Design of Bridge Piers. *Ph.D Dissertation*.

Manjoine, M. J. (1944). Influence of rate of strain and temperature on yield stress of mild steel. *J. Appl. Mech., 11*, 211-218.

Marsh, M. L., Wernli, M., Garrett, B. E., Stanton, J. F., Eberhard, M. O., & Weinert, M. D. (2011). NCHRP Report 698: Application of Accelerated Bridge Construction Connections in Moderate-to-High Seismic Regions. *Transportation Research Board, Washington, DC.*

Massone, L. M., & López, E. E. (2014). Modeling of reinforcement global buckling in RC elements. *Engineering Structures, 59*, 484-494.

Massone, L. M., & Moroder, D. (2009). Buckling modeling of reinforcing bars with imperfections. *Engineering Structures, 31*, 758-767.

MathWorks. (2016). MATLAB Optimization Toolbox 2016b. Natick, MA, USA.

MathWorks. (2018). *Constrained Nonlinear Optimization Algorithms*. Retrieved from https://www.mathworks.com/help/optim/ug/constrained-nonlinear-optimization-algorithms.html

Mattock, A. H. (1967). *Rotational Capacity of Reinforced Concrete Beams' by W. G. Corley.* Journal of the Structural Division. ASCE.

Mau, S. T., & El-Mabsout, M. (1989). Inelastic buckling of reinforcing bars. *Journal of engineering mechanics, 115*, 1-17.

Mazzoni, S., McKenna, F., Scott, M. H., Fenves, G. L., & others. (2006). OpenSees command language manual. *Pacific Earthquake Engineering Research (PEER) Center*.

McKenna, F., Fenves, G. L., & Scott, M. H. (2000). Open system for earthquake engineering simulation. *University of California, Berkeley,CA*.

Menegotto, M., & Pinto, P. (1973). Method of analysis for cyclically loaded RC plane frames including changes in geometry and non-elastic behavior of elements under combined normal force and bending. *Proc. of IABSE symposium on resistance and ultimate deformability of structures acted on by well defined repeated loads*, (pp. 15-22).

Meyers, M. A., & Chawla, K. K. (2009). *Mechanical behavior of materials* (Vol. 2). Cambridge University Press Cambridge.

Mirza, S. A., & MacGregor, J. G. (1979). Variability of mechanical properties of reinforcing bars. *Journal of the Structural Division, 105*.

Mitra, N., & Lowes, L. N. (2007). Evaluation, calibration, and verification of a reinforced concrete beam--column joint model. *Journal of Structural Engineering, 133*(1), 105-120.

Montgomery, D. C., & Runger, G. C. (2010). *Applied statistics and probability for engineers.* John Wiley and Sons.

Monti, G., & Nuti, C. (1992). Nonlinear cyclic behavior of reinforcing bars including buckling. *Journal of Structural Engineering, 118*(12), 3268-3284.

Moyer, M. J., & Kowalsky, M. J. (2003). Influence of tension strain on buckling of reinforcement in concrete columns. *ACI Structural Journal, 100*, 75-85.

Mullapudi, T. R., & Ayoub, A. (2010). Modeling of the seismic behavior of shear-critical reinforced concrete columns. *Engineering Structures, 32*(11), 3601-3615.

Murcia-Delso, J., Stavridis, A., & Shing, B. (2011). Modeling the bond-slip behaviour of confined large-diameter reinforcing bars. *III ECCOMAS thematic conference on computational methods in structural dynamics and earthquake engineering.*

Nadai, A. (1950). *Theory of flow and fracture of solids* (Vol. 1). New York: McGraw-Hill Book Co. Inc.

Nakamura, H., & Higai, T. (2002). Modeling of Nonlinear Cyclic Behavior of Reinforcing Bars. *ACI Special Publication*, 273-296.

Nonaka, T. (1973). An elastic-plastic analysis of a bar under repeated axial loading. *International Journal of Solids and Structures, 9*, 569-580.

Oldfather, W. A., Ellis, C. A., & Brown, D. M. (1933). Leonhard Eulerś elastic curves. *Isis, 20*, 72-160.

Osgood, W. R. (1951). The effect of residual stress on column strength. *Proc. 1st US Nat. Cong. Appl. Mech*, (p. 415).

Papadrakakis, M., & Loukakis, K. (1988). Inelastic cyclic response of restrained imperfect columns. *Journal of engineering mechanics, 114*, 295-313.

Papia, M., Russo, G., & Zingone, G. (1988). Instability of longitudinal bars in RC columns. *Journal of Structural Engineering, 114*, 445-461.

Paulay, T., & Priestley, M. J. (1992). Seismic design of reinforced concrete and masonry buildings.

Piegl, L., & Tiller, W. (1997). *The NURBS book.* Berlin, Germany: Springer-Verlag.

Priestley, M. J. (2003). *Myths and fallacies in earthquake engineering, revisited.* IUSS press.

Prota, A., De Cicco, F., & Cosenza, E. (2009). Cyclic behavior of smooth steel reinforcing bars: experimental analysis and modeling issues. *Journal of Earthquake Engineering, 13*, 500-519.

Ramberg, W., & Osgood, W. R. (1943). *Description of stress-strain curves by three parameters.* Washington D.C.: National Advisory Committee for Aeronautics.

Restrepo, J. I. (2007). Advanced Seismic Design Course Notes. Department of structural Engineering, University of California, San Diego.

Restrepo, J. I. (2010). *Results from a Full-scale Bridge Column Shake Table Test.* unpublished.

Restrepo, J. I., Park, R., & Buchanan, A. H. (1993). *Seismic behaviour of connections between precast concrete elements.* University of Canterbury, Department of Civil Engineering.

Restrepo, J. I., Seible, F., Stephan, B., & Schoettler, M. J. (2006). Seismic testing of bridge columns incorporating high-performance materials. *ACI Structural Journal, 103*, 496.

Restrepo-Posada, J. I. (1992). Seismic Behaviour of Connections Between Precast Concrete Elements. Christchurch, New Zealand: University of Canterbury.

Restrepo-Posada, J. I., Dodd, L. L., Park, R., & Cooke, N. (1994). Variables affecting cyclic behavior of reinforcing steel. *Journal of Structural Engineering, 120*, 3178-3196.

Rodriguez, M. E., Botero, J. C., & Villa, J. (1999). Cyclic stress-strain behavior of reinforcing steel including effect of buckling. *Journal of Structural Engineering, 125*, 605-612.

Schoettler, M. J., Restrepo, J. I., Guerrini, G., Duck, D. E., & Carrea, F. (2012). A full-scale, single-column bridge bent tested by shake-table excitation. *Center for Civil Engineering Earthquake Research, Department of Civil Engineering, University of Nevada*.

Scott, M. H. (2011). *Force-Based Beam-Column Element - OpenSeesWiki.* Retrieved from OpenSeesWiki: http://opensees.berkeley.edu/wiki/index.php/File:IntegrationTypes.pdf

Shanley, F. R. (1947). Inelastic column theory. *Journal of the Aeronautical Sciences, 14*(5), 261-268.

Shanley, F. R. (2012). The column paradox. *Journal of the Aeronautical Sciences*.

Slavin, C. M., & Ghannoum, W. M. (2015). *Defining Structurally Acceptable Properties of High-Strength Steel Bars through Material and Column Testing, PART I: MATERIAL TESTING REPORT.* techreport, University of Texas at Austin.

Standards Association of New Zealand. (1989). NZS 3402: Steel bars for the reinforcement of concrete. 16.

Stanton, J. F., & McNiven, H. D. (1979). *The development of a mathematical model to predict the flexural response of reinforced concrete beams to cyclic loads, using system identification.* Berkeley: Earthquake Engineering Research Center.

Stephan, B., Restrepo, J. I., & Seible, F. (2003). Seismic behavior of bridge columns built incorporating MMFX steel. *SSRP*, 9.

Tanaka, H. (1990). Effect of lateral confining reinforcement on the ductile behaviour of reinforced concrete columns.

Tanaka, H., & Park, R. (1987). Prediction of the ultimate longitudinal compressive concrete strain at hoop fracture using energy considerations. *Bulletin of the New Zealand National Society for Earthquake Engineering, 20*, 290-305.

Templin, R. L., Sturm, R. G., Hartmann, E. C., & Holt, M. (1938). Column strength of various aluminum alloys. *Tech. Paper, 1*.

Trejo, D., Barbosa, A. R., & Link, T. (2014). *Seismic Performance of Circular Reinforced Concrete Bridge Columns Constructed with Grade 80 Reinforcement.* Corvallis, OR: Oregon Department of Transportation. Retrieved from http://www.oregon.gov/odot/programs/pages/research.aspx

von Kármán, T. (1910). Untersuchungen über Knickfestigkeit. In *Mitteilungen über Forschungsarbeiten auf dem Gebiete des Ingenieurwesens insbesondere aus den Laboratorien der technischen Hochschulen* (pp. 1-44). Springer Berlin Heidelberg. doi:10.1007/978-3-662-01994-8_1

Wang, Y. C. (2000). *Retrofit of reinforced concrete members using advanced composite materials.* University of Canterbury nz. University of Canterbury. Civil Engineering.

Wang, Y. C., & Restrepo, J. I. (1996). *Strength enhancement of concentrically loaded reinforced concrete columns using TYFO S fibrwrap jackets.* Department of Civil Engineering, University of Canterbury.

Wang, Y. C., & Restrepo, J. I. (2001). Investigation of concentrically loaded reinforced concrete columns confined with glass fiber-reinforced polymer jackets. *Structural Journal, 98*, 377-385.

Weisstein, E. W. (2002). Cubic formula. *omega, 86*, 87.

Wilson, D. V., & Bate, P. S. (1986). Reversibility in the work hardening of spheroidised steels. *Acta Metallurgica, 34*(6), 1107-1120.

Yang, H., Wu, Y., Mo, P., & Chen, J. (2016). Improved nonlinear cyclic stress--strain model for reinforcing bars including buckling effect and experimental verification. *International Journal of Structural Stability and Dynamics, 16*, 1640005.

Zahn, F. A. (1985). Design of reinforced concrete bridge columns for strength and ductility.

Zong, Z. (2011). Uniaxial material model incorporating buckling for reinforcing bars in concrete structures subjected to seismic loads. *Ph.D. Dissertation, University of California, Davis*.

Zong, Z., Kunnath, S., & Monti, G. (2013). Material model incorporating buckling of reinforcing bars in RC columns. *Journal of Structural Engineering, 140*, 04013032.

APPENDIX A

LATERAL DISPLACEMENT IN CIRCULAR BRIDGE COLUMNS WITH WEAK AND STRONG FLEXURE-SHEAR INTERACTION

The development of plasticity in reinforced concrete columns under lateral forces can be characterized as having either weak or strong flexure-shear interaction. Weak flexure-shear interaction typically occurrs in slender and lightly reinforced columns, for which the effect of shear forces in the deformation is small, and classical flexure theory can be applied. In columns with weak flexure-shear interaction, a nearly horizontal crack pattern is observed in the plastic region at large deformations, see Figure A.1a. In elements with strong flexure-shear interaction, the plastic region shows a diagonal crack pattern, forming diagonal concrete struts, no longer well represented by classical flexure theory. Diagonal cracks from strong flexure-shear interaction are divided into two regions: a fanned diagonal compression field (FDCF) and a parallel diagonal compression field (PDCF). The FDCF starts with a nearly horizontal crack at the base, with cracks at

increasing angles from the horizontal converging toward the compressive force resultant in the critical section, see Figure A.1b. After a critical crack angle is reached, the remaining cracks in the plastic region remain parallel at the critical angle, corresponding to the PDCF, see Figure A.1b.

(a) (b)

Figure A.1. Crack Patterns Observed Experimentally: (a) Column with Weak Flexure-Shear Interaction (Schoettler et al. 2012); (b) Column with Strong Flexure-Shear Interaction (Restrepo et al. 2006)

For columns with weak-flexure shear interaction, Guerrini and Restrepo (in-press) established an equation to compute the extent of plasticity, ℓ_1, defined as the length of the column where the bending moment exceeds the first-yield moment, M'_y:

$$\ell_1 = \frac{\left(\frac{T_0}{A_{st} f_y} - \frac{T'_y}{A_{st} f_y}\right)\omega_\ell - \frac{P_u}{A_g f'_c}\left(\alpha_0 - \alpha'_y\right)}{\frac{T_0}{A_{st} f_y}\omega_\ell + \frac{P_u}{A_g f'_c}\left(1-\alpha_0\right)} \cdot L \qquad \text{A.1}$$

Where T_0 and T'_y correspond to the resultant tensile force in the column sections at moments M_0 and M'_y. P_u is the compressive axial force applied to the column, α_0 and α'_y are the distance between the tension forces T_0 and T'_y and the center of the column, normalized by the lever arm between compressive and tensile force resultants, jd_0 and jd_y.

$\omega_\ell = \rho_\ell f_y / f'_c$ is the mechanical reinforcement ratio. All of these parameters were determined empirically by Guerrini and Restrepo (in-press) and summarized in Table A.1.

Table A.1. Empirical Relationships for Circular Columns (Guerrini and Restrepo, in-press)

Parameter	Empirical Formula
$\frac{T'_y}{A_{st} \cdot f_y}$	$1.5 \cdot \left(1.80\rho_\ell - 0.0020\frac{f'_c}{MPa} - 0.25\right)\left(2.10\frac{P_u}{A_g f'_c} - 0.08\right) + 0.48 - 1.10\rho_\ell$
$\frac{jd'_y}{D}$	0.62
α'_y	$0.53\frac{P_u}{A_g f'_c} + 0.43$
$\frac{T_0}{A_{st} \cdot f_y}$	$1.5 \cdot \left(4.00\rho_\ell - 0.0025\frac{f'_c}{MPa} - 0.22\right)\left(1.25\frac{P_u}{A_g f'_c} - 0.17\right) + 0.82 - 3.30\rho_\ell$
$\frac{jd_0}{D}$	0.5
α_0	$0.50\frac{P_u}{A_g f'_c} + 0.32$

An analysis of circular columns with weak-flexure shear interaction tested experimentally found that, using plastic rotation theory with an equivalent plastic hinge length $L_p = 0.3\ell_1$ resulted in good approximations of the lateral displacement capacities observed experimentally, see Section 7.6.

For element with strong flexure-shear interaction, Guerrini and Restrepo (in-press) determined the extent of plasticity, ℓ_2, based on a free body diagram of the plastic region, see Figure A.2. To simplify the analysis, the shear capacity of concrete was neglected and the distance between compressive and tensile force resultants, *jd*, was assumed constant throughout the extent of plasticity, at $jd = 0.56D$ for circular columns. It was also assumed

that classical flexure theory applies at the ends of the plastic region, thus the parameters for sections with moment M'_y and M_0 can be determined using Table A.1.

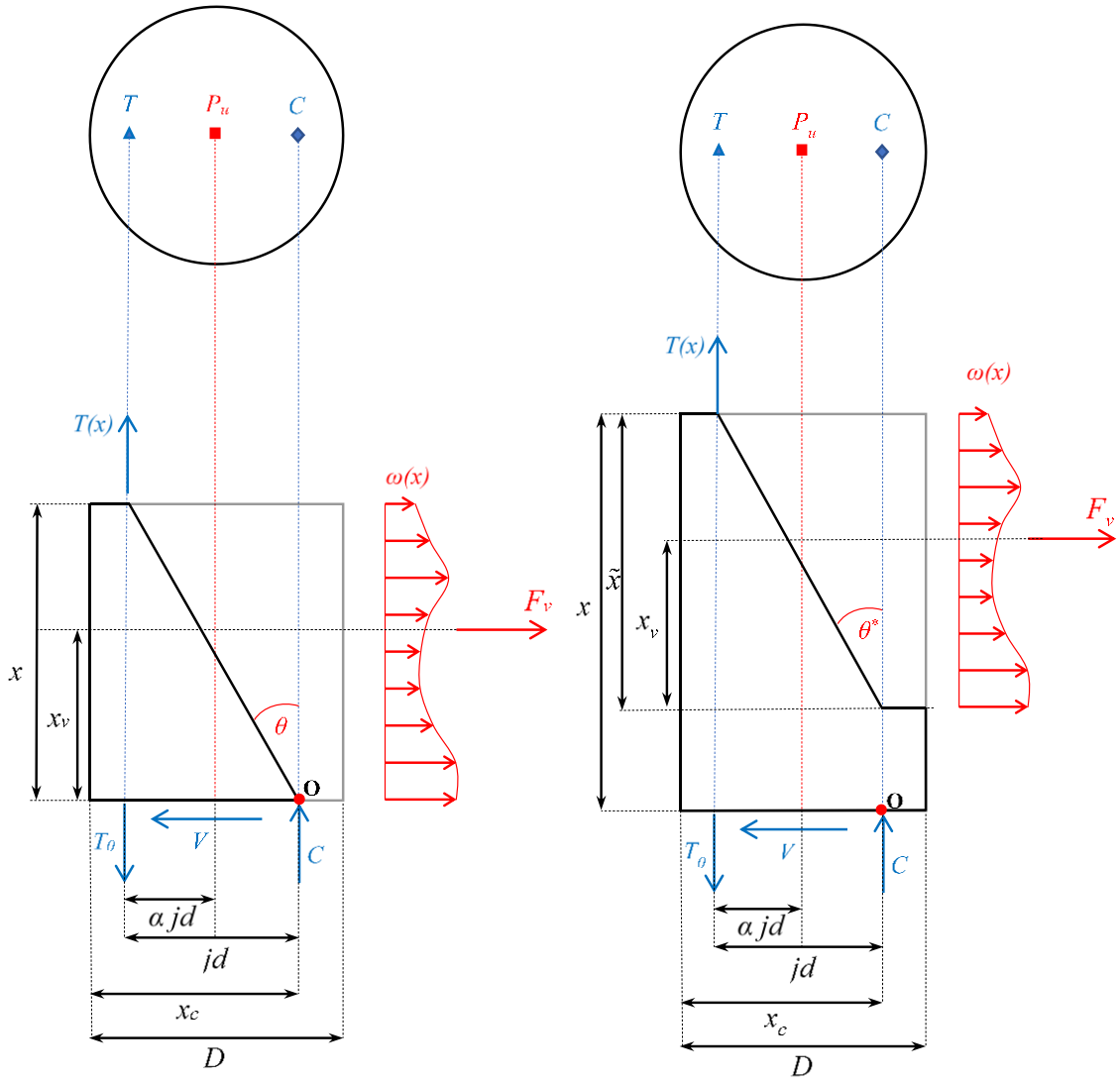

Figure A.2. Free-Body Diagram of Plastic-Hinge Region with Strong Flexure-Shear Interaction: (a) Crack in the Fanned Diagonal Compression Field (FDCF); (b) Crack in the Parallel Diagonal Compression Field (PDCF)

For the angle θ^* defining the transition between the FDCF and PDCF, Guerrini and Restrepo (in-press) assumed a value θ^*=26.6°, which satisfies the condition cotan(θ^*)=2.

To determine the extent of plasticity in the column, the magnitude and location of the force provided by the hoops crossing the diagonal cracks must be determined. Assuming all hoops in the plastic region are yielding, the force F_v and location x_v can be determined as follow, see Figure A.3:

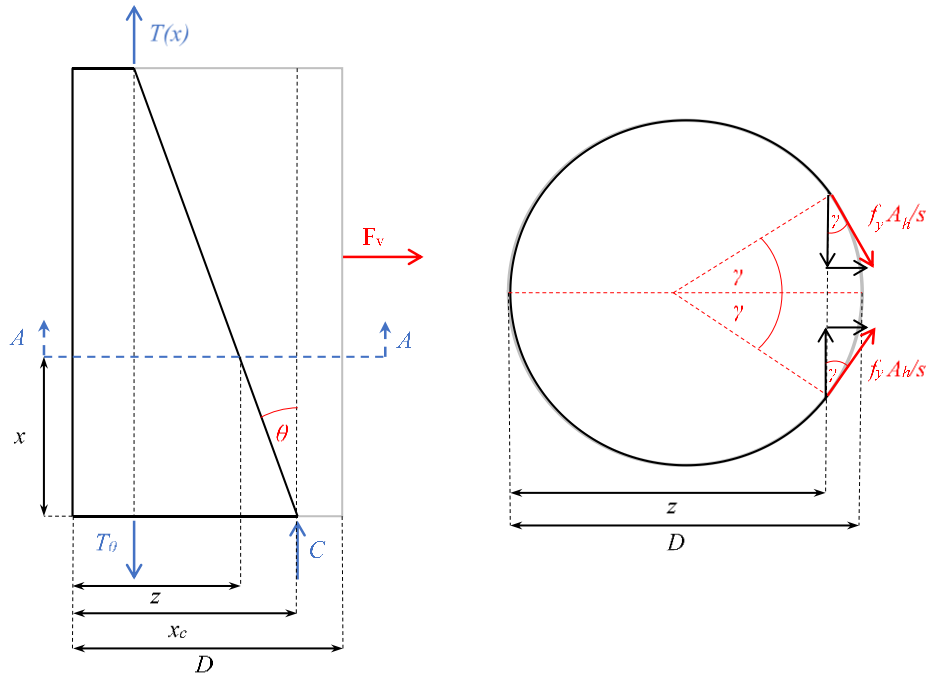

(a) (b)

Figure A.3. Lateral Force Provided by the Hoops: (a) Elevation; (b) Section A-A

$$\omega(x) = 2 \cdot \frac{f_{yh} \cdot A_h}{s} \sin\gamma \qquad \text{(a)} \qquad \text{A.2}$$

$$\sin\gamma = \sqrt{1 - \left(\frac{2 \cdot z}{D} - 1\right)^2} \qquad \text{(b)}$$

$$F_v = \begin{cases} \int_0^x \dfrac{f_{yh}A_v}{s}\sin\gamma\, dx & x \le 2\,jd \\ \int_0^{2\,jd} \dfrac{f_{yh}A_v}{s}\sin\gamma\, d\tilde{x} & x > 2\,jd \end{cases} \quad \text{(a)}$$

$$F_v(x) \approx 0.84\,\frac{f_{yh}A_v}{s}\cdot\min(x, 2\,jd) \quad \text{(b)} \qquad \text{A.3}$$

$$x_v = \begin{cases} \dfrac{1}{F_v}\cdot\int_0^x \dfrac{f_{yh}A_v}{s}\sin\gamma\cdot x\, dx & x \le 2\,jd \\ \dfrac{1}{F_v}\int_0^{2\,jd} \dfrac{f_{yh}A_v}{s}\sin\gamma\cdot\tilde{x}\, d\tilde{x} & x > 2\,jd \end{cases} \quad \text{(a)}$$

$$x_v(x) \approx 0.45\cdot\min\left(x, 2\,jd\right) \quad \text{(b)} \qquad \text{A.4}$$

Using the simplified formulas for F_v and x_v in Equations A.3b and A.4b, a moment equilibrium around O, see Figure A.2, results in the following distribution of the tensile resultant within the extent of plasticity:

$$T(x) = \begin{cases} T_0 - 0.34\,f_{yh}\rho_s\cdot x^2 & x \le 2\,jd \\ T_0 - 0.84\cdot f_{yh}\rho_s D\cdot\left(x - 0.62\cdot D\right) & x > 2\,jd \end{cases} \qquad \text{A.5}$$

With the extent of plasticity, ℓ_2, calculated as the value of x where the yield resultant T'_y is reached, see Equation A.6.

$$\ell_2 = \begin{cases} 1.52\cdot\sqrt{\left(\dfrac{T_0}{A_{st}f_y} - \dfrac{T_y}{A_{st}f_y}\right)\dfrac{f_y}{f_{yh}}\dfrac{\rho_\ell}{\rho_s}}\cdot D & \ell_2 \le 2\,jd \\ \left(0.94\cdot\left(\dfrac{T_0}{A_{st}f_y} - \dfrac{T_y}{A_{st}f_y}\right)\dfrac{f_y}{f_{yh}}\dfrac{\rho_\ell}{\rho_s} + 0.62\right)\cdot D & \ell_2 > 2\,jd \end{cases} \qquad \text{A.6}$$

The tensile resultant distribution along the extent of plasticity, *T(x)*, is then transformed into stress of the longitudinal reinforcement by assuming all bars in tension

reach their yield strength at moment M'_y, and the area of steel in tension remains constant throughout the extent of plasticity:

$$f(x)=\begin{cases} f_0-\dfrac{0.34\,f_{yh}\rho_s}{A_{st}^*}\cdot x^2 & x\le 2\,jd \\ f_0-\dfrac{0.84\cdot f_{yh}\rho_s D}{A_{st}^*}\cdot\left(x-0.62\cdot D\right) & x>2\,jd \end{cases} \qquad \text{A.7}$$

Where:

$$\begin{aligned} A_{st}^{\ *} &= A_{st}\cdot\frac{T_y}{A_{st}\cdot f_y} \\ &= A_{st}\cdot\left[1.5\cdot\left(1.8\rho_\ell-0.002\cdot\frac{f'_c}{MPa}-0.25\right)\left(2.1\frac{P_u}{A_g f'_c}-0.08\right)+0.48-1.1\cdot\rho_\ell\right] \end{aligned} \qquad \text{A.8}$$

Based on the stress distribution, see Equation A.7, the strain in the longitudinal reinforcement in tension can be approximated by a linear function, see Equation A.9 and Figure A.4.

$$\varepsilon(x)=\begin{cases} \left(\varepsilon_{dem}+\varepsilon_0\right)\left(1-0.34\cdot\eta\cdot\left(\dfrac{x}{D}\right)^2\right) & x\le 2\,jd \\ \left(\varepsilon_{dem}+\varepsilon_0\right)\left(1-0.84\cdot\eta\cdot\left(\dfrac{x}{D}-0.62\right)\right) & x>2\,jd \end{cases} \qquad \text{A.9}$$

Where ε_{dem} is the strain demand in the critical section of the column and ε_0 the plastic strain in compression. η is a unitless variable defined as follows:

$$\eta=\frac{\varepsilon_{dem}-\hat{\varepsilon}_y}{\varepsilon_{dem}+\varepsilon_0}\frac{f_{yh}}{f_0-f_y}\frac{\rho_s D^2}{A_s^*} \qquad \text{A.10}$$

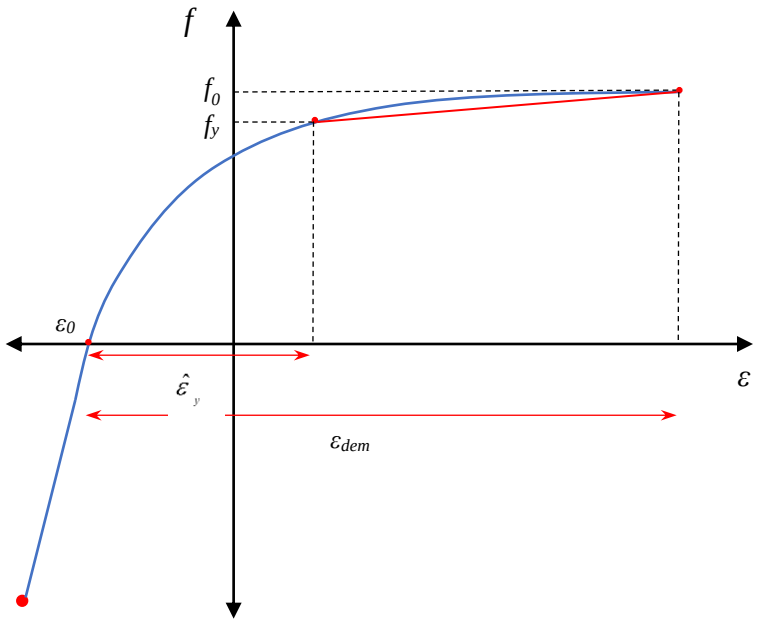

Figure A.4. Approximated Stress-Strain Relation for Longitudinal Reinforcement

Once the strain distribution along the reinforcement in tension is known, the lateral displacement at the top of the column can be estimated from the cumulative rotation from diagonal crack openings within the extent of plasticity, see Figure A.5.

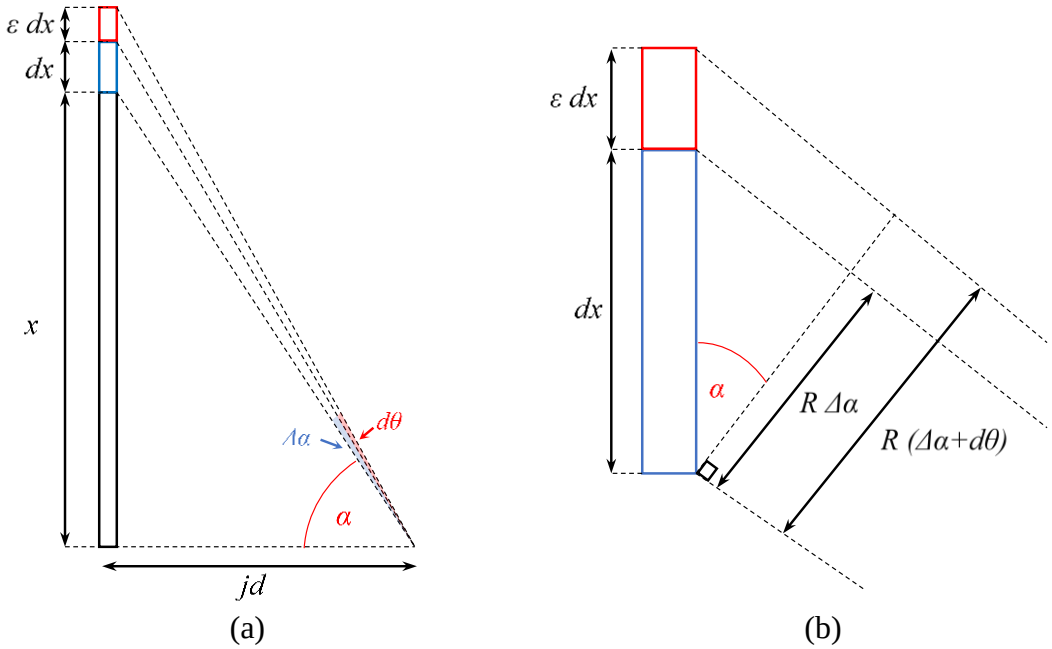

(a) (b)

Figure A.5. Rotation Increment from Diagonal Cracks in Element with Strong Flexure-Shear Interaction: (a) Global View of Reinforcement; (b) Close up of Infinitesimal Bar Length, dx, and Elongation, ε dx

The rotation increment will vary depending on the strain distribution in the longitudinal reinforcement, *ε(x)*, and the region within the diagonal compression field (fanned or parallel):

$$d\theta = \frac{\varepsilon \cdot jd}{(jd)^2 + x^2} dx = 0.56 \frac{\varepsilon}{D} \frac{dx}{\left(\frac{x}{D}\right)^2 + 0.314} \qquad x \le 1.12D$$

$$d\theta^* = \frac{\varepsilon}{5\,jd} dx = 0.36 \frac{\varepsilon}{D} dx \qquad x > 1.12D \qquad \text{A.11}$$

The lateral displacement at the top of a cantilever column can be computed from the integrals:

$$\Delta = \begin{cases} \int_0^{\ell_2} L \cdot d\theta & \ell_2 \le 2\,jd \\ \int_0^{2\,jd} L \cdot d\theta + \int_{2\,jd}^{\ell_2} (L + 2\,jd - x) \cdot d\theta^* & \ell_2 > 2\,jd \end{cases} \qquad \text{A.12}$$

Which result in Equation A.13:

$$\Delta_p = \begin{cases} 0.314 \cdot L\left(\varepsilon_{dem} + \varepsilon_0\right)\left(\left(0.34\eta + 3.18\right) \cdot \tan^{-1}\left(1.78\dfrac{\ell_2}{D}\right) - 0.61 \cdot \eta \dfrac{\ell_2}{D}\right) & \ell_2 \le 1.12 \cdot D \\ \left(\varepsilon_{dem} + \varepsilon_0\right)\left(\left(1.1 - 0.095\eta\right)L + 0.36 \cdot D\left(\left(\dfrac{L}{D}\left(1 + 0.52\eta\right) + 1.12 + 0.58\eta\right)\left(\dfrac{\ell_2}{D} - 1.12\right) - \left(0.42\eta\dfrac{L}{D} + \dfrac{1}{2} + 0.73\eta\right)\left(\left(\dfrac{\ell_2}{D}\right)^2 - 1.12^2\right) + 0.28\eta\left(\left(\dfrac{\ell_2}{D}\right)^3 - 1.12^3\right)\right)\right) & \ell_2 > 1.12 \cdot D \end{cases} \qquad \text{A.13}$$